NOVEL MEASUREMENT OF SOLIDS CIRCULATION RATE IN PILOT-SCALE DUAL FLUIDIZED BED GASIFIER AT HIGH TEMPERATURE

by

MD. HAFIZUR RAHMAN

B.Sc., Bangladesh University of Engineering and Technology, Dhaka, Bangladesh, 2005

M.Sc., The University of Alberta, Edmonton, Alberta, Canada, 2011

A DISSERTATION SUBMITTED IN PARTIAL FULFILLMENT OF

THE REQUIREMENTS FOR THE DEGREE OF

DOCTOR OF PHILOSOPHY

in

THE FACULTY OF GRADUATE AND POSTDOCTORAL STUDIES

(Chemical & Biological Engineering)

THE UNIVERSITY OF BRITISH COLUMBIA

(Vancouver)

October 2017

Abstract

A number of fluidized bed reactor processes operating at high temperature require that solid particles be circulated back and forth between two reactor vessels. Since the circulation rate strongly affects mass and energy balances, and therefore greatly influences hydrodynamics and performance of the system, a reliable technique for its accurate measurement would be helpful in monitoring and modeling the process. However, there are no reported techniques suitable for measuring this critical hydrodynamic parameter at elevated temperatures typical of gasification systems.

A novel thermal-tracing technique was developed for measuring the solids circulation rate between two vessels. Packets of particles at lower temperatures are injected into a downward-moving packed bed of solids at elevated temperature, creating reduced-temperature zones inside the moving bed. The transit time of the cold-particle-clusters between pairs of thermocouples is determined by cross correlation, allowing the flux to be estimated. The technique was shown to provide sensitive and reproducible data for a cold model unit with injection of dry ice. The technique was then applied to determine solids circulation rates between the bubbling bed gasifier and the riser combustor of a pilot scale dual fluidized bed gasification system. A number of conditions are imposed on the data to eliminate unsatisfactory data at high temperatures. Data which satisfy the discrimination criteria led to measured solids circulation fluxes up to 133 kg/m^{2}s at temperatures up to 856°C in the gasifier test section.

A novel butterfly valve technique was developed to validate the thermal-tracing technique at high temperatures. Closing the valve causes solids to accumulate in the downcomer section of the pilot gasifier. The elevation of the top surface of these solids was tracked with high-temperature capacitance

sensors, facilitating determination of the solids circulation flux between the two reactors of the pilot plant. The fluxes were also estimated using two indirect methods based on pressure balance and energy balance techniques. Agreement among the fluxes obtained from applying these four techniques are reasonable given the difficulty in measuring solids circulation rates.

Lay Summary

More than 80% of world's energy demands are met by fossil fuels, the main sources of greenhouse gas emissions into the atmosphere. Although the dependence on fossil fuels cannot be eliminated in foreseeable future, their importance can be reduced by developing renewable energy technologies such as biomass gasification. The gasification of biomass in a dual fluidized bed (DFB) gasifier can produce high-quality synthesis gas for production of heat, electrical power, fuels and chemicals.

The development of DFB gasification technology could benefit immensely from development of a robust and accurate technique for the determination of the circulation rate of particles between adjacent vessels. A novel 'thermal-tracing' technique was developed for this purpose in this thesis project. This technique was validated by developing a novel butterfly valve technique. Two techniques based on pressure and energy balance considerations are also developed. Satisfactory agreement is observed among the outcomes of these four techniques.

Preface

All the research works (except Appendix C) presented in this thesis were performed by the author under the supervision of Professors Xiaotao Bi, John Grace and Jim Lim of the Department of Chemical and Biological Engineering and Fluidization Research Centre at the University of British Columbia. The author designed test sections, conducted experiments, wrote computer programs for data processing, compiled the results, analyzed the outcomes and prepared this dissertation.

A version of Chapter 2 has been published as follows:

M.H. Rahman, X.T. Bi, J.R. Grace, C.J. Lim, Measurement of solids circulation rate in a high-temperature dual fluidized bed pilot plant, Powder Technology 316 (2017) 658–669.

In addition to conducting the research described in the paper, the author prepared the manuscript, with inputs from the other authors.

The research presented in Chapters 3 and 4 will be used to prepare one or two additional papers for submission to journals for publication.

The author wrote the manuscript of the paper provided in Appendix C.

See footnotes with similar information on the first page of the items mentioned above.

The author also delivered oral presentations based on the work described in this dissertation at the following national and international conferences:

- M.H. Rahman, X.T. Bi, J.R. Grace, C.J. Lim, Measurement of solids circulation rate in a high-temperature dual fluidized bed pilot plant, Fluidization XV Conference, Montebello, QC, Canada, 2016.
- M.H. Rahman, M.C. Stewart, X.T. Bi, J.R. Grace, C. J. Lim, Measurement of solid circulation rate in a high temperature dual fluidized bed using dry ice, iSGA-3 Conference, Vancouver, BC, Canada, 2012.

Table of Contents

List of Tables

List of Figures

List of Symbols

a	Decay constant (-)
$a_{1\text{-}4}$	Coefficients for viscosity estimation (-)
A	Area (m^2)
Ar	Archimedes number (-)
$b_{1\text{-}4}$	Coefficients for heat capacity estimation (-)
C_d	Drag coefficient (-)
C_p	Heat capacity (J/kg-K)
d	Diameter (m)
f	Friction factor (-)
g	Gravitational acceleration (m/s^2)
G_s	Solids circulation flux (kg/m^2-s)
Gr	Grashof number (-)
h	Heat transfer coefficient (W/m^2-K)
H	Total height (m)
k	Thermal conductivity (W/m-K)
L_c	Characteristic length (m)
m	Solids circulation rate (kg/s)
$m_{1\text{-}7}$, $n_{1\text{-}5}$	Coefficients for thermal conductivity estimation (-)
MW	Molecular weight (kg/kmol)
N_{or}	Number of orifices in distributor (-)

Nu	Nusselt number (-)
P	Pressure (kPa)
Pr	Prandtl number (-)
Q	Heat energy (kW)
r	Radius (m)
R	Resistance to heat transfer (K/W)
Ra	Rayleigh number (-)
Re	Reynolds number (-)
t	Time (s)
T	Temperature (K)
U	Superficial gas velocity (m/s)
U_t	Terminal velocity (m/s)
U_b	Bubble velocity (m/s)
x	Distance (m)
z	Height (m)
β	Volume expansion coefficient (K^{-1})
ϵ	Emissivity (-)
ε	Voidage (-)
μ	Dynamic viscosity (Pa-s)
ν	Kinematic viscosity (m^2/s)
ξ	Cyclone friction coefficient (-)
ρ	Density (kg/m^3)

σ	Stefan–Boltzmann constant ($W/m^2\text{-}K^4$)

Subscripts

acc	Acceleration
b	Bubble
BFB	Bubbling fluidized bed
cyc	Cyclone
d	Bottom dense region
e	Exit region
g	Gas
fg	Gas friction
fp	Particle friction
mix	Mixture
mf	Minimum fluidization
nc	Natural convection
p	Solid particle
rad	Radiation
rep	Representative

Acknowledgments

I wish to express my deepest gratitude to Professors Xiaotao Bi, John Grace and Jim Lim for their invaluable guidance throughout the research program. I feel truly honoured and privileged to have been able to work with these world-renowned researchers in the field of fluidization. Beyond their roles as research supervisors, they supported me in many ways during the years of my mother's prolonged illness and the deaths of both of my parents. Professor Grace kindly shared his personal experience, which helped me in part to overcome the grief caused by these two deaths in a span of three months. My supervisors' extraordinary efforts will be gratefully remembered throughout my life!

I would like to thank Professors Patrick Kirchen and Paul Watkinson for serving as the members of the supervisory committee. I am very grateful to Dr. Yonghua Li for assistance with the operation of the experimental facility and the development of safe operational procedures, among other items. Special thanks to Dr. Zhiwei Chen, Dr. Jhon Ramirez and Michael Stewart for their assistance in different stages of the experimental campaign. I thank Gordon Cheng, Charles Cheung, Graham Liebelt and Doug Yuen of the departmental workshop for their efforts in constructing unique and complex experimental equipment. I recognize and appreciate the assistance of the support staff and faculty of the Department.

Funding assistance from Natural Sciences and Engineering Research Council of Canada, Carbon Management Canada, The Dow Chemical Company (DowDuPont Inc.), and the British Columbia Bioenergy Network are recognized with gratitude.

The current and past members of the Fluidization Research Centre including Mohammad Masnadi, Chuan He, Ziliang Wang, Eric Jia, Turki al-Smari, James Butler and Sina Tebianian are recognized for

sharing their experiences and expertise, and, equally importantly, for their friendship. Beyond the workplace, the friendship and words of encouragement of Usman, Mynol and Mahafuz are fondly remembered.

No words are sufficient to portray the endless love and support I had received from my parents until their deaths! They would have been happiest to see me complete the PhD degree. I was born and raised in a small town of one of the world's least developed countries (Bangladesh); without their outstanding care and encouragement, it would not have been possible for me to reach one of world's top 50 universities for the highest academic degree. My younger sisters, Samina and Sadia, have also always been sources of encouragement.

My wife, Farhana, always tries her best with great love and care to support my endeavours. Her patience and understanding was very helpful for me to go for overnight experiments, working late on weekdays and working at the weekend on many occasions. My one-year-old son, Ariz, continues to rejuvenate me after work with his funny activities!

Most importantly, I remain extremely grateful to the almighty Allah, as he has enabled me to overcome many difficulties in my research and personal life to bring this research project to a successful end.

To the memory of my parents,

Md. Syedur Rahman and Shahana Begum

1 Introduction

1.1 Background

With the world population approaching 7.5 billion [1], the importance of reducing dependence on fossil fuels has never been greater. In a recent estimate, the British Petroleum [2] found that more than 80% of world's energy comes from burning coal, oil and natural gas. These fossil fuels are the main sources of greenhouse gas (GHG) emission into the atmosphere. The current level of use of fossil fuel is simply not sustainable, as GHG emissions have a profound impact on climate. The concentrations of GHG gases like carbon-di-oxide and methane have already exceeded by far their natural ranges in the atmosphere. A catastrophic change in climate cannot be avoided if the GHG concentration in the atmosphere exceeds 450 ppm [3]. Although fossil fuels will remain the largest sources of global energy supply in the foreseeable future, their impact can be reduced by increasing the share of renewable energy options in the global energy basket.

Canada possesses the third largest share (9%) of the world's forest resource [4] and is a global leader in biomass utilization. Each year, the Canadian forest product industry generates a huge amount of forest residues. Economic and environmentally sustainable utilization of this form of biomass could be achieved if the forest residues were used to produce high-grade synthesis gas (syngas), replacing syngas produced from fossil fuel sources. For this purpose, biomass particles can be gasified with steam, instead of air, to avoid nitrogen in the product gas and consequently to ensure high heating value of the syngas, which can be used in combined heat and power production plants or for the synthesis of alcohols, liquid fuels or value-added chemicals [5]. In addition, injection of a metal oxide sorbent (such

as CaO) could capture carbon-dioxide to produce high-quality syngas with high hydrogen concentration, while also minimizing, or even eliminating, tar formation. Then this syngas could be used in fuel cells or engines. Thus, biomass gasification offers one of the most promising renewable energy options and, at the same time, could ensure economic use of local forest residues.

Gasification of biomass with steam involves a number of endothermic reactions occurring at temperatures above 700°C in the gasifier. The required heat can be obtained from combustion of part of the char produced in the gasifier. This can be accomplished in two ways – by injecting oxygen to directly burn these char particles in the gasifier, or by burning the char in a separate combustor and circulating an inert heat carrier medium such as sand to transfer heat to the gasifier from the riser [6]. The latter method is preferred, as the injection of air or oxygen into the gasifier lowers the heating value of the syngas [7]. Consequently, the gasification system requires not only a biomass steam gasifier, but also a char combustor. This system can be achieved by combining a bubbling fluidized bed (BFB) as the gasifier and a circulating fluidized bed (CFB) riser as the combustor [8,9]. The resulting system is then known as a “dual fluidized bed” (DFB).

One of the principal advantages of fluidized beds is that particles can be readily circulated between vessels, e.g. between a cracker reactor and a regenerator in the case of fluid catalytic cracking (FCC), or between a calciner and a carbonator in the case of carbon capture. Dual fluidized bed gasifiers, requiring circulation of particles between gasification and combustion reactors, are being developed in several countries as a means of efficient generation of synthesis gases from carbonaceous feedstocks. The dual fluidized bed pilot gasifier located at the University of British Columbia is capable of producing high-

quality synthesis gas (syngas) from a variety of solid fuels, including different types of biomass [9]. A photograph and a schematic diagram of this plant are provided in Figures 1.1 and 1.2, respectively. When biomass is used in a dual fluidized bed with integrated carbon-dioxide capture, it can even become a negative-carbon-emissions energy system [10].

In dual bed gasifiers, inert heat carrier particles (e.g. sand) must be constantly circulated at high flow rates to transfer the heat generated in the CFB combustor to the BFB gasifier in order to support endothermic reactions there. The inert heat carrier also acts as bed material for both reactors. Figure 1.3 shows the directions of the movement of these heat carrier particles in the dual fluidized bed system. The gas travels upward through each of the reactors. A small amount of inert nitrogen gas is supplied to the solids transfer pipe to facilitate the moving packed bed flow of solids through the pipe. Part of this gas flow is dragged down by the solids to the bubbling bed reactor. The rest of this flow travels upward through the solids transfer pipe and joins the combustion flue gas at the riser's cyclone.

Mass and energy balances of individual reactors and the overall system greatly depend on the rate of circulation of the solid heat carrier. Thus the circulation rate of solid particles is one of the most important hydrodynamic parameters, strongly influencing the performance of both the CFB and BFB reactors.

The engineering design of any commercial-scale DFB gasification plant would benefit from accurate determination of the circulation rate of solids between the reactors. If an appropriate technique is developed, it could make a substantial contribution to the development of DFB gasification technology,

while also finding potential applications in other circulating systems, such as fluid cokers and fluid catalytic crackers.

Figure 1.1 Photograph of the dual fluidized bed (DFB) pilot plant at the University of British Columbia.

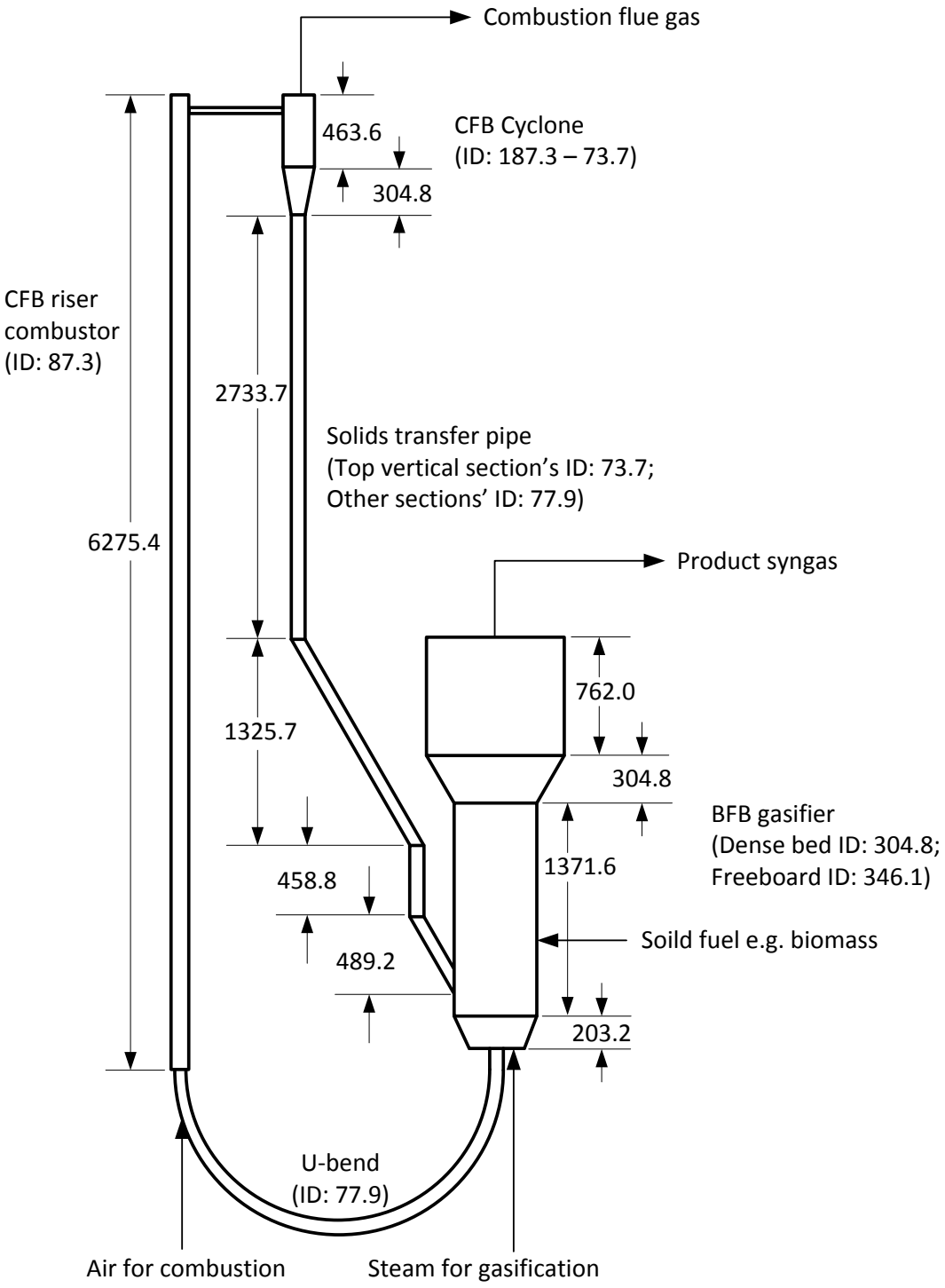

Figure 1.2: Schematic of the dual fluidized bed (DFB) pilot plant. (Dimensions are in mm.)

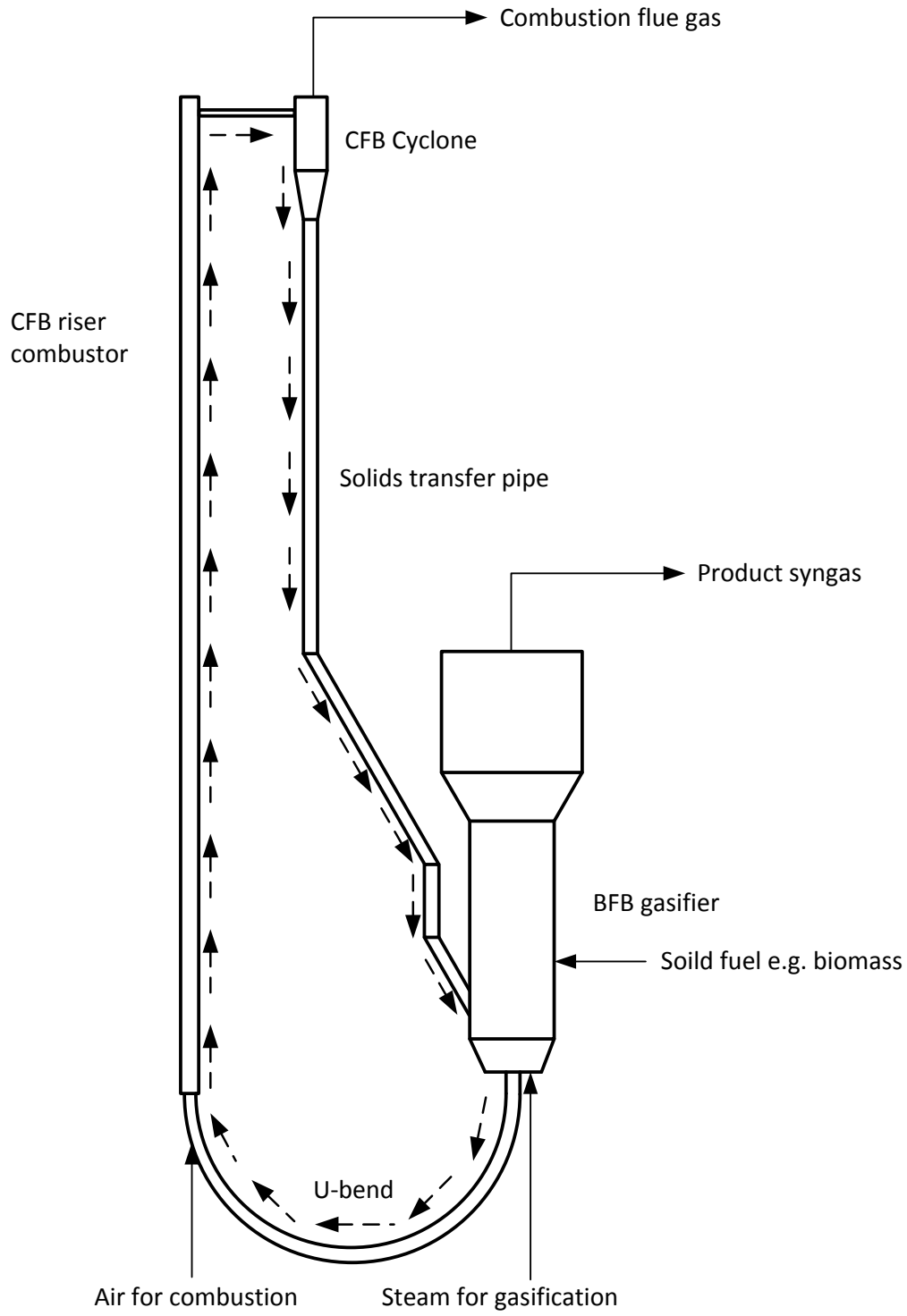

Figure 1.3: The directions of solids circulation in the DFB plant indicated by dashed arrows.

1.2 Literature survey

A number of attempts to measure solids circulation rate in fluidized bed systems have been reported over several decades. Burkell et al. [11] considered five different techniques for measuring solid circulation rates: impact flowmeter, modified orifice meter, porous valve method, time of descent method and calorimetry. None of these methods is fully appropriate for commercial-scale high-temperature DFB gasification systems. When particles struck the pan of the impact flow meter, the resulting force was mechanically transmitted by a sensitive load beam. This is too cumbersome for high-temperature equipment. Application of the flow meter was found to be limited to low solid circulation rates due to overloading of the beam.

A number of acrylic discs were stacked to make the modified orifice meter where differential pressure drops across the stack were measured to determine accumulation of solids. The pressure drops obtained at low circulation rates were too small to be recorded, whereas they fluctuated wildly at high rates.

In its closed position, the porous valve accumulated solids over time. At high circulation rates, the interference caused by closing the valve significantly upset the steady-state operation of the system.

The visual determination of time for the descent of particles required that the test section be made of transparent materials, which is unlikely to be practical for high-temperature large-scale systems. In addition, visibility is affected when particles glow at elevated temperatures.

The calorimetric method was also utilized by Glicksman et al. [12]. In this method, a cooling jacket around the pipe removes heat from the particles flowing downward and the resulting temperature change of the circulating particles is detected. The radial temperature gradient across the pipe and the inability to accurately determine the heat loss from the test section significantly reduced the accuracy of this method. Moreover, additional loss of heat energy from a high-temperature system is undesirable.

Muir et al. [13] developed a novel method for determination of circulation rate which uses a sinker dragged downward by the solids, with the time needed for the sinker to travel a specific distance measured. The drawbacks of this method, in addition to the operating inconvenience, are that it assumes a uniform particle velocity profile across the pipe and negligible relative velocity between the sinker and the particles.

Davies and Harris [14] introduced a novel slot flow meter to measure the solids circulation rate. Solids were collected in a chamber with one or more vertical slots in its sides. The weight of the solids in this chamber was continuously monitored using an electronic balance attached to it. The installation of such a chamber in the downcomer section of the solids circulation loop in a large-scale system is likely to create operational problem. Hence its ability to handle large volumes of solids is questionable. Moreover, any malfunction of the chamber could very quickly cause blockage in the measurement section, leaving the operators no choice but to shut down the plant. The attachment of the electronic scale to the chamber installed inside a high-temperature system would be a great challenge. The scale, its power cable and data cable to the recording computer would have to survive high temperatures. This seems very unlikely to be feasible for currently commercially available scales and cables.

Kreuzeder et al. [15] measured the circulation rate by tracking the rate of change of the height of solids accumulated in an L-shaped section of transfer pipe after shutting off fluidization air. This is a visual determination technique and cannot be applied in high temperature vessels constructed of non-transparent materials unless sight glasses are provided. Moreover, closing a part of transfer pipe is bound to upset the pressure balance, thereby affecting the circulation rate.

Ludlow et al. [16] installed a rotating spiral vane made of fibreglass in a CFB standpipe and measured low flow rates of solids at ambient temperature. Its ability to operate at high temperatures and/or with higher circulation rates is doubtful. Davies et al. [17] reviewed attempts to obtain solids flow rate by using sound pressure waves at ambient temperature. So far as we are aware, this technique has not been applied to any high-temperature system. Recently, Ellis et al. [18] used an acoustic emission sensor to measure solids flow rate at room temperature. Given the ambient noise near commercial reactors and the difficulties in calibrating such a system, this type of sensor is again unlikely to be practical for high-temperature commercial systems.

Monazam et al. [19] developed correlations which predicted solids flow rate as a function of pressure drop over a horizontal section between the riser and the cyclone. Some of the coefficients found in these correlations were quite dependent on the range of conditions used to develop them in a cold flow setup. Patience et al. [20] measured the pressure drop at a similar section and related it to the solids flow rate measured in a transparent section in the downcomer using the time-of-descent method. As mentioned earlier, such a transparent section would be impractical for a high-temperature system. A relationship between the pressure and the solids circulation rate could be established at room

temperature and then this relationship could be used for determining the solids circulation rate at high temperature. However, the usefulness of a calibration curve established at low temperature of working at high temperature is questionable. Song et al. [21] recorded the pressure drop across a venturi constriction near the riser's exit and calibrated it using an optical fibre probe to measure the solids circulation rate at room temperature. This probe, even if fabricated to survive high temperatures, is likely to be unable to distinguish between light reflected from particles and light emitted by particles radiating at that temperature. Lim et al. [22] correlated the solids circulation rate with the pressure gradient in the riser. According to them, the technique is limited if an appropriate value of slip factor cannot be determined. Grieco and Marmo [23] developed correlations between the pressure drop across a control valve and the flow rate of solids through it using a room temperature setup.

The method described by Monazam & Shadle [24] cannot be applied at high-temperature large-scale system since a sudden cut-off of solids flow will severely affect the hydrodynamics and the steady-state operation of the system. Chorpening et al. [25] used a microwave Doppler system to sense the sliding or intermittent flow of particles. This type of sensor is unlikely to be sustainable at high temperature.

Wu et al. [26] developed a solids flow meter and installed it in the lower part of their setup which mimicked the downcomer of a circulating fluidized bed system. When free falling solids hit a plate, the torque generated due to the rotation of the plate around a hinge was recorded which was then utilized to measure the solids flow rate. The device was shown to work well at very low flow rates of solids in a room temperature setup. A high temperature application of this device would at first face the challenge of designing related parts which can survive at high temperature, and then be able to transfer the

torque from the plate to the sensing equipment with reasonable accuracy under high temperature conditions.

The technique developed by Lech [27] depends on measuring the electrostatic charges generated from collisions of particles inside the pipe using ring-shaped sensors in a pneumatic transport test loop. If this technique were to be considered for high temperature application, the effect of temperature on electrostatic charges needed to be investigated as it could significantly affect the accuracy of this technique.

Bodelin et al. [28] developed a technique in which they installed a weighing hopper at the standpipe of their circulating fluidized bed system. The closure of a pneumatic valve accumulated the solids in the hopper, and the weight of these solids was measured. The execution of this experimental procedure resulted in no flow of solids through the standpipe for several minutes. In an industrial scale plant, the disruption of the steady flow of solids for several minutes is unlikely to be acceptable. Also, the force transducer used for transferring the weight information from the hopper to a recording device is unlikely to survive the high temperature of the plant.

Kuramoto et al. [29] used tracer particles coated with fluorescent dyes to measure the circulation rate of solids in a two-dimensional fluidized bed system. The movement of the particles in the downcomer was detected by two optical fibre probes installed at different levels in the downcomer. The difficulty of using an optical fibre probe at high temperature was discussed earlier in this section. In addition, these dyes may not survive at high temperature, and, even if they were to survive, there is a high possibility

that the particles would be further coated by other substances, such as coke, tar or soot, thereby reducing their effectiveness.

Liu and Huan [30] developed a turbine meter to measure the solids flow rate in a standpipe. The flow of solids rotates the blades of the turbine. The rate of turbine's rotation is recorded and correlated to the solids flow rate. Both the turbine and the column in which it was installed were made of plexiglass. In a high temperature industrial-scale setup, the turbine would be subjected to large volumes of solids and turbulent fluctuations which would be challenging for its smooth operation. In addition, the cable needed to pass the information of turbine's rotation to the electrical circuit of the metering device would have to be resistant enough to serve at high temperature. This appears unlikely to be feasible for currently commercially available cables.

Dry et al. [31] used a semi-permeable flapper valve, similar to the one used by Burkell et al. [11], to measure the solids circulation rate in the downcomer of a cold model circulating fluidized bed. At the same time, they measured the differential pressure across four different sections in the system. Finally, they correlated the solids circulation rate with each of these differential pressures. The usefulness of their final correlation to provide the solids circulation rate information at high temperature is questionable since the gas properties changes significantly with temperature, thereby affecting the hydrodynamics of the system.

Motivated by the work of Roy et al. [32] in a liquid-solid system, Bhusarapu et al. [33] tracked the movement of a single radioactive tracer particle in the downcomer section of a circulating fluidized bed

operating at ambient pressure and temperature. The use of radioactive tracer particles could in principle be helpful; however, such systems would not only be expensive, but also demand extraordinary safety measures.

Medrano et al. [34] measured the solid circulation rate between an air reactor and a membrane-assisted fuel reactor in a two-dimensional interconnected reactor system using three techniques – optical technique, pressure difference technique and particle-extraction technique. Among these three techniques, they recommended the pressure difference technique for high-temperature application. Recently, Guio-Perez et al. [35] used ferromagnetic particles as tracer and tracked them with an inductance coil. The method worked well under cold conditions. They concluded that this method is suitable for low-temperature application only.

X-ray, electrical capacitance tomography and electrical resistance tomography require that probes be mounted directly on a wall. However, the reactor vessels are heavily insulated to minimize heat losses from the system. X-rays are unlikely to be able to penetrate pipe walls of commercial-scale reactors made of or insulated with high-temperature alloys or refractory.

1.3 Research objectives

The overall objective of this project was to develop a technique which would enable reliable measurement of the solids circulation rate between a circulating fluidized bed riser combustor and the bubbling fluidized bed gasifier of a dual fluidized bed pilot plant at high temperatures. As described in the previous section, a number of methods have been previously attempted in efforts to track the

movement of particles in the downcomer, either visually or using devices such as optical fibre probes. Most of those attempts were limited to room temperature setups.

After brain-storming different ideas involving the author and his supervisors, it was thought that a tracking mechanism could be made to work at elevated temperature. Thermocouples are widely and reliably used in process plants. They are capable of measuring temperature over broad ranges, including typical operating temperatures of gasifiers (in excess of 800°C). However, the temperature vs. time signal from a thermocouple does not change significantly during steady-state operation of a plant unless some sort of thermal disturbance is created. Injection of some relatively cold particles travelling in plug flow (or nearly so) through a temperature measurement section could act as a suitable tracer, creating the necessary thermal disturbance for the thermocouples to detect and then blending with other particles downstream. This way the passage of the cold tracer particles in the test section can be tracked by using two or more thermocouples installed along the length of the section. Thermal-tracing of injected cold particles and using thermocouples to monitor their passage was considered to be a potentially useful technique.

Validation of the thermal-tracing technique at high temperatures would require the development of a second technique which can measure solids circulation rates directly at these temperatures. The suitability of a butterfly type device, similar to the porous valve developed by Burkell et al. [11] was explored for this task. Brereton [36] successfully used such a butterfly valve in a room-temperature CFB system. Although the closing of this valve cannot be recommended for a large-scale commercial plant, its use for short durations in the pilot scale dual fluidized bed plant was thought to provide a potential

means of confirming the thermal-tracing technique. Therefore, the development of a butterfly valve for high-temperature application was considered to be promising option for validation of the thermal-tracing technique at high temperature.

As mentioned in section 1.2, pressure data have been utilized in several methods, whereas energy balances over a section have been applied in several other cases for the measurement of the solid circulation rates. The application of the thermal-tracing technique and the butterfly valve technique would require steady operation of the dual fluidized bed pilot plant, determined based on a number of temperature, pressure and gas flow measurement devices equipped in the plant. Those data generated from these devices during plant's operation can also be used to estimate the solids circulation rate using a third approach – a pressure balance across the solids circulation loop and an energy balance over the bubbling fluidized bed gasifier.

The specific objectives of this thesis are:

- Development of a novel thermal-tracing technique for application at all temperatures;
- Development of a novel butterfly valve technique for the validation of the thermal-tracing technique at high temperature;
- Estimation of the solids circulation rates using the pressure balance and an energy balance method to compare with the rates measured by the other two novel techniques.

1.4 Thesis outline

Chapter 2 describes the development and application of a novel thermal-tracing technique for the measurement of solids circulation rate. The basic principle of the technique is presented first. A description of the experimental setup and the procedure of preliminary tests at ambient temperature follows. Solids circulation rates obtained from applying the thermal-tracing technique are then compared with results from a simple and independent time-and-weight measurement technique at room temperature. In the next section of Chapter 2, the experimental setup, materials used and test procedure for the high-temperature tests are provided. Then, a simple model is presented to investigate the heat transfer process between the bulk hot solids and the injected cold particles in the test section. The implications of the model predictions on the design of the test section are discussed. The data analysis procedure, including a set of criteria for filtering out unjustifiable values, is described in the following section of the chapter. At the end, the solids circulation rates measured at high temperature in the dual fluidized bed pilot plant using the thermal-tracing technique are presented, together with a discussion of the factors that affect the performance and accuracy of this technique.

Chapter 3 depicts the development and application of a novel butterfly valve technique for the validation of the thermal-tracing technique at high temperature. This chapter contains key dimensions of the butterfly valve test section and justifies the selection of these dimensions. The high-temperature capacitance sensors used for detecting the top surface of accumulated solids on valve's plates are described. In the next section of Chapter 3, the experimental procedure for applying the thermal-tracing and the butterfly valve techniques, one immediately after another, for the measurement of solids circulation rate is provided. The development of the procedure is also portrayed in this section. This is

followed by a comparison of the solids circulation rates obtained from this technique and a thermal-tracing technique in the cold and hot tests.

Chapter 4 outlines assumptions underlying the estimation of the solids circulation rate from the pilot plant's operational data using two indirect methods – a pressure balance method and an energy balance method. Simplifying assumptions, relevant correlations and dimensions of important sections of the dual fluidized bed pilot plant utilized by each of the methods to estimate the solids circulation rate are provided. The circulation rates estimated using these two indirect methods are then compared with those directly measured using the thermal-tracing and the butterfly valve techniques in the two previous chapters. Potential sources of error in estimating solids circulation rates using these techniques are also identified and discussed.

Chapter 5 summarizes overall conclusions from this thesis and recommendations for future work.

A code written in MATLAB to process the raw data obtained from applying the thermal-tracing technique, the detailed engineering designs for the construction of the butterfly valve test section, an article by Daniel et al. (manuscript in preparation) relevant to Chapter 2 are provided, among other items, in the appendices.

2 Development and Application of Thermal-tracing Technique[1]

2.1 Basic principle

The thermal-tracing technique is based on the determination of the velocity at which solids pass through a test section. Two quantities are needed when calculating the solids' velocity: a) distance travelled, and b) time needed to travel that distance. The distance is set by the location of measuring probes. Measurement of travel time in the test section at high temperature is the key. Thermocouples are used for that purpose.

Consider two identical thermocouples separated by a known distance installed in a vertical test section in such a way that their tips fall on the same vertical line, i.e. with the tip of one directly above that of the other. During steady-state operation of the DFB system, the temperature profile of each thermocouple appears flat, with no significant change with time. If the temperature of a small portion of moving bed is impulsively reduced at the top of the test section, then the profile of each thermocouple shows a sudden drop in temperature as the colder parcel of particles passes that tip. The temperature soon returns to the steady-state temperature. The upper thermocouple experiences the temperature drop earlier than the lower one. The time lag is measured as solids travel time between the two

[1] A version of Chapter 2 has been published as follows: M.H. Rahman, X.T. Bi, J.R. Grace, C.J. Lim, Measurement of solids circulation rate in a high-temperature dual fluidized bed pilot plant, Powder Technology 316 (2017) 658–669.

thermocouples. The reduction of the temperature of a portion of moving bed for a brief period using particles at lower temperature, that either leaves no residue or blends with the bed upon completing the job, to allow the bed's movement to be tracked by stationary thermocouples is a novel way of determining the solids circulation rate. Therefore, the proposed technique is considered to be a novel technique for the measurement of the solids circulation rate.

In a DFB system, the best location to install the test section is in the lower part of the solids transfer pipe where the particles travel as a moving packed bed of solids. This location not only minimizes interference of the testing process on the stable operation of each reactor, but also eliminates the need to measure the density of solids in the test section during experimentation. The solids bulk density can be easily determined at room temperature. The test section must have a vertical orientation to maximize the uniformity of the velocity profile of particles descending in the moving bed.

As provided by Equations (2.1) and (2.2), the key relationships are simply:

$$Solids\ velocity, V_s\ \left(\frac{m}{s}\right) = \frac{Distance, \Delta x\ (m)}{Time, \Delta t\ (s)} \tag{2.1}$$

$$Solid\ flux, G_s\ \left(\frac{kg}{m^2.s}\right) = \ Solids\ velocity, V_s\ \left(\frac{m}{s}\right) \times\ Solids\ bulk\ density, \rho_b\ \left(\frac{kg}{m^3}\right) \tag{2.2}$$

An uncertainty analysis is performed to investigate the relative importance of each parameter which is used to estimate solids flux. Equation (2.3) is obtained from Equation (2.2) and used for this analysis.

$$G_s\left(\frac{kg}{m^2.s}\right) = \rho_p\left(\frac{kg}{m^3}\right) \times (1 - \varepsilon_{bed}) \times \frac{\Delta x(m)}{\Delta t(s)} \quad (2.3)$$

where ε_{bed} is the voidage of the moving packed bed in the test section.

Table 2.1 shows the contribution of each parameter in Equation (2.3) to the solids circulation flux.

In most of the experiments of this project, Lane Mountain Sand was used as bed material in the dual fluidized bed system. Its particle density is 2650 kg/m^3, as provided in the website of the producer, Lane Mountain Company, Valley, WA, USA. Rahman [37] used this sand, although of a smaller size, in his Master's research project. In this regard, the Saskatchewan Research Council determined the density of this sand to be 2650 kg/m^3. Based on these two sources, the base value of the sand's particle density is taken to be 2650 kg/m^3 for the uncertainty analysis. The author considers that an uncertainty of approximately 50 kg/m^3, corresponding to a 2% error in the determination of the particle density, is reasonable.

Knowlton [38] showed that aeration gas introduced at a point in an angled standpipe occupies the upper portion of the pipe's volume. Since the aeration gas entered the standpipe at a point below the thermal-tracing test section, it is very likely that a portion of this gas traveled upward through the test section. The point of gas entry is located on an angled section of the standpipe. The aeration gas, travelling mostly along the upper portion of the angled pipe, did not distribute evenly across the cross-sectional area of the vertical test section. Moreover, it was not possible to determine the portion of aeration gas

that traveled upward. Therefore, it was thought that attempting to obtain a base case value of the bed voidage in the test section based on the total aeration rate would not be accurate.

The bulk density of the loose-packed sand particles was measured to be 1445 kg/m^3. When this value was combined with the particle density of sand, the loose-packed voidage was found to be 0.45. This value is taken as the base case value of voidage for the uncertainty analysis in this thesis. Ludlow et al. [16] mentioned that the maximum value of voidage could be as high as 0.5 if the bed inside the standpipe were just fluidized. Although they used a different bed material (cork particles of mean size 812 μm), this value is considered as a maximum in the absence of a more appropriate reference. The difference between these two values, 0.45 and 0.5, is considered here to be reasonable in estimating the uncertainty for the voidage over the thermal-tracing test section. This difference corresponds to an error of 10%.

A typical value of 2.34 s, obtained from measurement, is taken as the base value of the particle's travel time between two planes of measurement. The accuracy of the estimation of particle velocity using the cross-correlation technique can suffer from the limited number of sampling points when a particle travels from one probe to another. A high sampling frequency of 50 Hz was selected to minimize error. For the typical travel time of 2.34 s, a sampling frequency of 50 Hz can lead to a measurement error of 1.2%. Liu et al. [39] reported that the fluctuations in solids concentration were strongly correlated to the fluctuations in solids velocity in a riser. In a downcomer section full of moving bed of solids, lower fluctuations, compared to those in the riser, can be expected. It was thought that the maximum cross-correlation coefficient must be taken from a clear distinct peak in the cross-correlation coefficient vs.

time shift plot. If the plot does not have a clear distinct peak, then error is likely to be introduced from reading the maximum cross-correlation coefficient. Since accurate determination of the combined effects of errors from multiple sources would be difficult, the author assumes an overall error of 10% in the time difference.

The distance between the two planes of measurement in the thermal-tracing test section is known with high precision, and therefore 1% error is considered sufficient. The distance, 0.102 m, is considered as the base value of distance in the uncertainty analysis. The base value of solids circulation flux is estimated from the base values mentioned above. The value is found to be 63.3 kg/m^2-s.

Solid fluxes are calculated at base case conditions, with no change in any parameter and four different conditions by changing one of the parameters at a time based on uncertainty in it [16]. Then deviation of solids flux at each of these conditions with regard to base case conditions is calculated. The bed voidage and the time difference then have more impact than the other parameters when comparing squared deviations. These four squared deviations are then used to estimate a residual-sum-of-squares (RSS) error. This value and the solids flux at the base case condition are then utilized to obtain an overall uncertainty of 12.4%.

Table 2.1: Relative contribution of each parameter's uncertainty to the uncertainty in measuring solids circulation flux. Procedure based on Ludlow et al. [16].

					Effect of change in one variable at a time (others remain the same as in base case)			
Variable	Base case	% Error	Uncertainty		ρ_s	ε_{bed}	Δt	Δx
ρ_s (kg/m3)	2650	2	53		2703	Same	Same	Same
ε_{bed} (-)	0.45	10	0.045		Same	0.50	Same	Same
Δt (s)	2.34	10	0.23		Same	Same	2.57	Same
Δx (m)	0.102	1	0.001		Same	Same	Same	0.103
G_s (kg/m^2-s)	63.3				64.5	58.1	57.5	63.9
				ΔG_s	1.3	-5.2	-5.8	0.6
				$(\Delta G_s)^2$	1.6	26.8	33.1	0.4
RSS Error	7.9							
Overall uncertainty (%)	12.4							

It is assumed that the injection of cold particles does not significantly alter the flow profile of bulk solids inside the test section. The bed density is equal to the bulk density of the solids and is unaffected by the injection of cold particles. The spatial distribution of cold particles inside the moving bed is assumed to remain unchanged as the packet of particles passes through the test section.

2.2 Preliminary cold model tests

The viability of the technique was tested at room temperature before committing time and energy to the design and construction of a test section for high-temperature experimentation. Two columns made of plexiglass were used for the room temperature experiments, one with a diameter of 101.6 mm and the other 88.9 mm. The distances between adjacent thermocouples were 38.1 and 101.6 mm, respectively. A schematic diagram of the setup is given in Figure 2.1.

The test procedure and materials were the same for each of these two columns. Limestone particles with a bulk density of 1411 kg/m^3 and size range of 420-710 μm were used as bed material. Dry ice, carbon dioxide in solid form with a sublimation temperature of -78°C, was manually crushed into fine particles (approximately 1 to 3 mm in diameter) for use as cold tracer particles. The flowability of dry ice particles was examined on an inclined surface of stainless steel before testing in the fluidization column. Care was taken to minimize dry ice contact with ambient air, as its very low temperature attracts moisture. It was observed that prolonged exposure to ambient air could condense enough moisture to encapsulate the dry ice particles, thereby reducing their mobility.

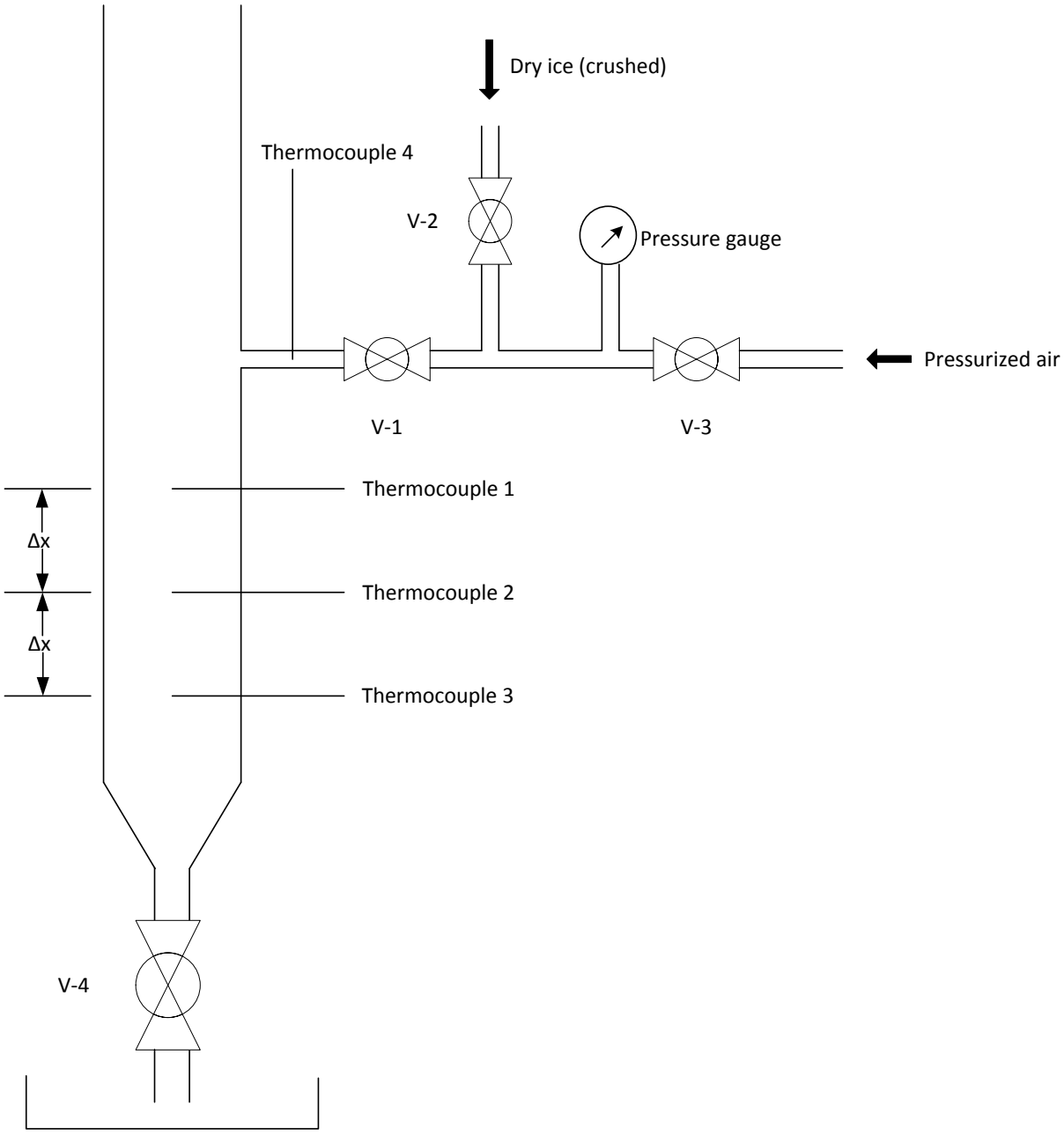

Figure 2.1: Schematic diagram of cold model test column (Column 1 - Δx: 38.1 mm, Diameter: 101.6 mm; Column 2 - Δx: 101.6 mm, Diameter: 88.9 mm).

For each test, the column was filled with bed material such that its top surface was at least 200 mm above the injection line. Then crushed dry ice particles were loaded into the injection pipe and pressurized with air at an absolute pressure of 163 kPa and injection valve V-1 closed. Opening valve V-4 at the bottom of the column released bed material to descend through the column, simulating roughly the flow of the moving packed bed in the lower part of the standpipe of the DFB system. As soon as the bed surface dropped to a height of 150 mm above the injection line, valve V-1 was opened to inject the pressurized dry ice particles into the moving packed bed. As the dry ice sublimed, it cooled the portion of the bed surrounding it. When this cool zone contacted a thermocouple's tip while moving down the column, a drop in temperature was registered. The starting point of the decreasing trend of temperature obtained from a thermocouple's reading was used to determine the time at which the cold packet reached that particular thermocouple. The time required for a cold zone to travel from one thermocouple to another and the distance between these two thermocouples was used to calculate the solids velocity from Equation (2.1), and hence the corresponding solids flux from Equation (2.2). Thus a solids flux was measured between thermocouples 1 and 2, another between 2 and 3, and a third between 1 and 3.

The solids circulation rate was also measured separately with no injection of cold particles by opening the bottom valve to allow the bed materials to exit. The time needed for bed top surface to drop from its initial position to a given height was tracked while the discharged bed particles were collected and weighed. The time and weight were then used to calculate solids flow for direct comparison with the results of the thermal-tracing technique.

Dry ice particles were injected five times into each column. In each test, three thermocouples provided three pairs of time from which the solids flux was estimated, providing three data points from each injection of a packet of cold particles. The sampling time for the cold tests were 30 seconds or longer, which was much longer than the period of the stick-slip fluctuations.

The results from injecting the dry ice tracer are compared with those from time and weight measurements in Figure 2.2. Error bars in the plot reflect 90% confidence intervals of the reported data. Both a -25% and a +25% lines are included to show deviations of thermal tracer injection results from the average time-weight measurement results.

The results show that the thermal-tracing technique was capable of measuring solids flux with reasonable accuracy. All data points fell within the ±25% interval from the weight vs. time measurement data. Sources of error which contributed to the deviations were: 1. Identical injection of dry ice for all tests was impossible due to the manual operation of the injection valve, causing some variation in the volume and degree of dispersal of each injected packet. 2. Some error can be attributed to the limited sensitivity and response characteristics of the thermocouples. Nevertheless, these findings confirmed that the thermal-tracing technique was promising for further development.

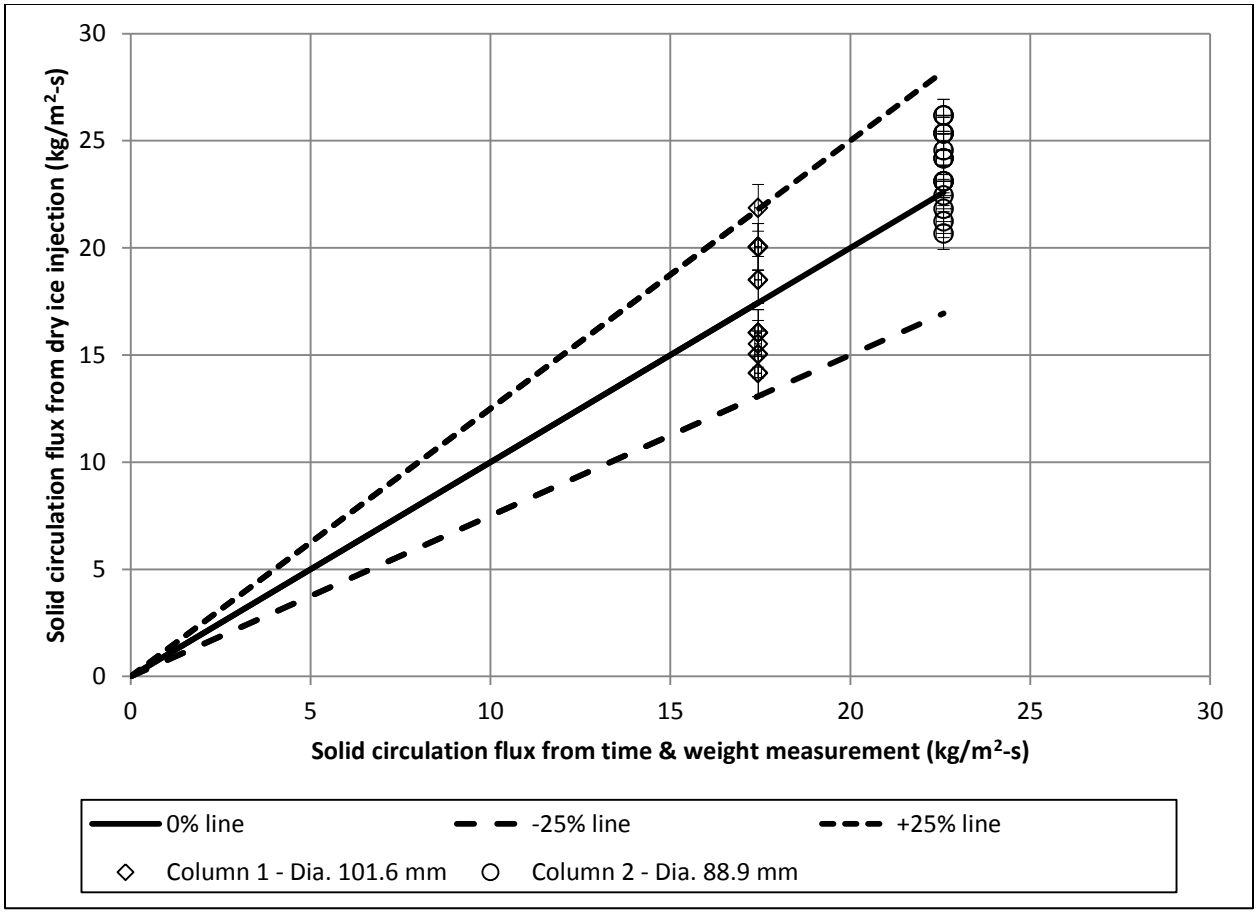

Figure 2.2: Comparison of solids fluxes obtained from dry ice injection with those from weight vs. time measurements at ambient temperature.

2.3 High-temperature experimental set up, materials and procedure

A high-temperature test section was designed and installed in the dual bed gasifier in the solid transfer pipe between the CFB combustor cyclone and BFB gasifier as depicted in Figure 2.3.

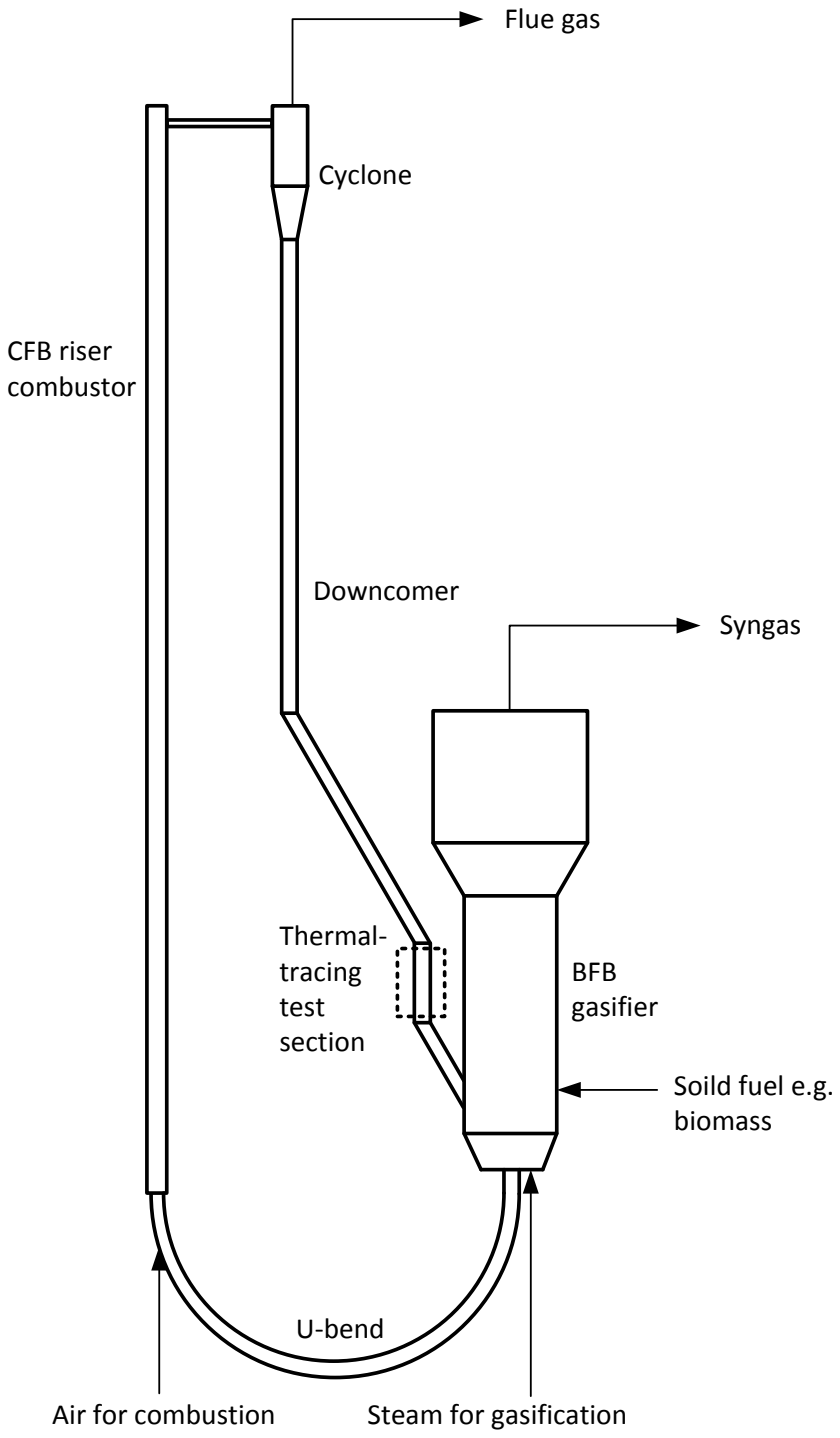

Figure 2.3: Location of thermal-tracing test section in the solids transfer pipe of the DFB pilot plant.

The lower part of the pipe was selected, as a moving packed bed of solids formed there before entering the gasifier. The geometry of the test section is displayed in Figure 2.4.

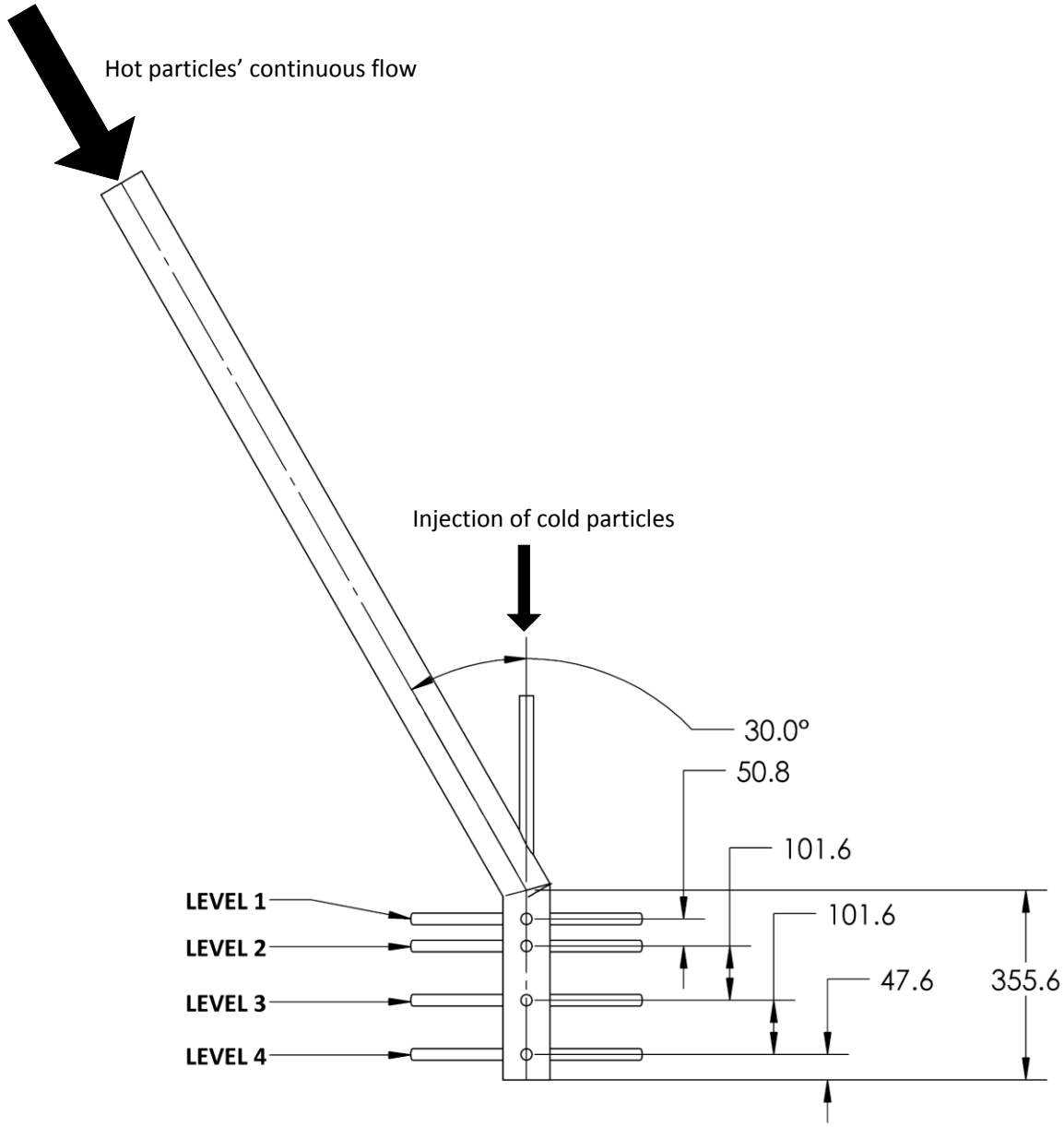

Figure 2.4: High-temperature test section for measuring solids circulation rate by thermal-tracing technique. (Dimensions are in mm.)

For most experiments, hot particles at about 900°C flow continuously through the test section. Hence, 800HT was used as the material of construction instead of stainless steel 316. Hot particles enter the test section at the top of the inclined pipe, which makes a 30° angle with the vertical plane, and exit at the bottom of vertical pipe. Both of these pipes have an internal diameter of 77.9 mm (NPS 3, SCH. 40). A vertical pipe of 20.9 mm internal diameter (NPS ¾, SCH. 40) is connected at the lower portion of the inclined pipe. This pipe carries cold particles from a hopper to the inclined pipe for instantaneous injection during each test. Twelve identical thermocouples of 3.2 mm diameter are mounted at four levels (horizontal planes), one penetrating to the centre of the pipe, the second one-quarter of the pipe diameter and the third is close to the wall. All thermocouples are of K-type, with their junctions exposed to the measurement environment. Exposed junction thermocouples were selected as they provide faster response than regular grounded or ungrounded junction thermocouples. Additional information on the response time of exposed junction thermocouple and the benefits of choosing it over other type of thermocouples are discussed in details in Appendix A. The distance between planes 1 and 2 is 50.8 mm, whereas it is 101.6 mm between planes 2 and 3, and also between planes 3 and 4. The three thermocouples at each measurement level occupied only 4% of the cross-sectional area of the pipe. Hence, it can be assumed that their presence neither appreciably altered solids flow pattern in the pipe, nor significantly affected the stable operation of the system.

The particles for all hot test data reported in this chapter were either:

a) Fluid cracking catalyst, bulk density 1200 kg/m^3, Sauter mean diameter 70 µm, or

b) Sand, bulk density 1450 kg/m^3, Sauter mean diameter 170 µm.

The hopper and its connecting pipe to the injection point are purged with pressurized nitrogen pulses to clear any particles from the line. Then cold particles are loaded into the hopper. When cold particles enter the inclined pipe, they mix with the bulk flow of hot solids. Heat exchange between cold and hot particles then creates colder zones inside the test section. Thermocouples at the different planes track the downward movement of these colder zones inside the bulk flow of hot solids. Temperature signals are recorded at a frequency of 50 Hz.

2.4 Heat transfer between hot and cold particles

The mass of cold particles injected is much less than the total mass of the bulk hot solids to ensure that:

- They do not significantly affect the overall hydrodynamics of the system, and
- Their injection does not appreciably alter the overall heat balance of the system.

The mass and enthalpy of the packet are estimated to be 0.1% and 0.0025% of the total bed inventory, respectively. These two values, being very low, justify the above statements regarding the negligible impact of cold particles' addition on the steady-state operation of the system. However, too small an amount of cold particles, after injection, would approach the bulk solids temperature before reaching the thermocouples. If this should happen, the thermocouples would not be able to detect a temperature change, and the thermal-tracing technique would not work. Hence, estimates were made of the times needed for cold particles to reach several temperatures after coming in contact with hot particles. These estimates are based on a simple model where each injected packet of cold particles forms multiple spherical "clusters" upon entry into the moving bed. Since it was not possible to measure

either the size or the number of clusters formed from a certain mass of injected particles, 1 to 1000 clusters were considered for estimation at each of several given temperatures.

Because of the high temperature of the hot particles in the pilot unit, it was advantageous to use inert sand particles at room temperature as cold particles rather than dry ice, which was difficult to handle and to prepare for injection.

When bulk hot solids descend through the solids transfer pipe, the particles drag some combustion gases with them. In addition, a small stream of nitrogen is used to aid the flow of hot solids, especially at the pipe bends. All these gases eventually flow upward relative to the solids through the interstitial spaces of the moving bed. For simplicity, their combined effects are modeled with the gas properties taken as those of air. When cold particles are injected into a moving bed of bulk hot solids, they also come in contact with upward relative flow of interstitial gases. Catalyst particles were the bed material for a few of the experiments. They are modeled as sand particles of the same size and bulk density.

The injected cold tracer particles, being small in amount, are overpowered by the momentum of the continuous flow of bulk hot solids passing through the transfer pipe. The cold particles lose their velocity at the point of injection and virtually adopt the velocity of the moving packed bed of solids. Then, there is no relative velocity between the cold tracer particles and the surrounding hot particles in the moving bed. Since the same type of particles as the bed particles is used as the tracer particles, there is no difference between their voidages in the moving bed. The gas flows upward through both the cluster of cold particles and through the surrounding hot particles in the same fashion. The composition of the

combustion gas dragged down by the particles does not change with temperature. Also, the nitrogen gas used to enhance the mobility of solids inside the pipe is inert. Therefore, the addition of the same type of particles as tracer into the moving bed does not initiate any reaction inside the test section.

Regarding the supply of nitrogen gas to enhance the solids' mobility inside the pipe, the aim has always been to prevent the solids blockage, with as little nitrogen as possible. Although the proportion of nitrogen gas which actually flowed upward remains unknown, it can be inferred that this part was just sufficient to maintain the flow of solids and did not cause the voidage in the test section to exceed the minimum fluidization voidage. In the absence of a measured value, the minimum fluidization voidage is assumed in the analysis.

Several simplifying assumptions are adopted for the calculations:

- Individual particles are assumed to be perfect spheres of varying sizes.
- Injected cold particles form a number of clusters of spherical shape and identical size due to shear forces inside the moving bed.
- There is no relative velocity between the injected cluster of cold particles and the surrounding hot particles. However, hot gas passes through the moving packed bed.
- The moving packed bed (the surrounding hot particles and clusters of injected cold particles) has the same voidage as a bed of these particles at minimum fluidization (ε_{mf}).
- Interstitial gas flows through the cluster at a relative velocity equal to the minimum fluidization velocity divided by the corresponding voidage (U_{mf}/ε_{mf}).

- The temperatures of a cluster and the interstitial gas which passes through it reach equilibrium by the time the gas reaches and leaves the top of the cluster.
- Negligible reaction and negligible overall heat loss take place in the moving packed bed.

The presence of one of these clusters in the bulk hot solids of the moving bed is illustrated in Figure 2.5.

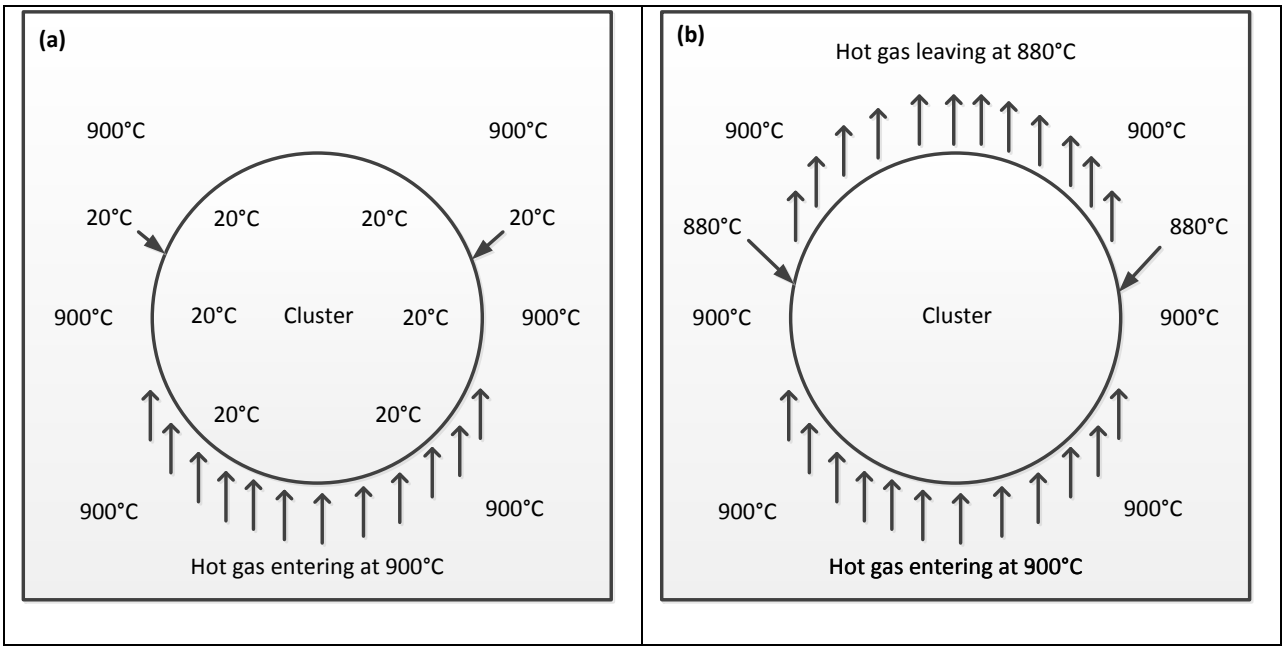

Figure 2.5: One of the clusters of cold particles surrounded by hot bed at 900°C: (a) the cluster immediately after entering the hot bed, and (b) the cluster after attaining thermal equilibrium with the exiting gas.

In reality, neither the individual particles nor the clusters are perfect spheres. Clusters might be of different shapes, or a mixture of various shapes, and it is likely that cluster sizes vary. Therefore, a single injection of cold particles may produce clusters of a variety of sizes and shapes.

The temperatures of the moving bed considered for tests with catalyst and sand are 600°C and 900°C. The moving bed and its interstitial gases have the same temperature. As mentioned above, the injected cold particles in each test are of the same type of particles as the bed material. The mass of injected room-temperature particles was 100 g for each test. The rise in cluster temperature is attributed to three modes of heat transfer between the injected cold particles and the bulk hot particles. The dominant one at 600°C is forced convection from the hot gas entering at bed temperature and passing through the interstices of the cluster. Other contributing modes are natural convection and radiation from the surrounding bed at 600°C. Both forced convection and radiation dominate at 900°C.

The temperature dependence of the dynamic viscosities of air constituents (nitrogen and oxygen) are taken from correlations reported by Kaushal et al. [40]. The dynamic viscosity of air is then calculated using the correlations developed by Wilke [41]. The correlations for air's heat capacity and thermal conductivity are obtained from Felder & Rousseau [42] and Kadoya et al. [43], respectively.

Equation (2.4) provides Gabor's [44] empirical correlation which is used to estimate the thermal conductivity of the cluster. This correlation was chosen since no alternative correlation was found from a literature search. Since the thermal conductivity of gas is much lower than that of the solids for almost all gas-solids combinations, the thermal conductivity of gas exerts more influence on the cluster's overall thermal conductivity compared to the contribution of the thermal conductivity of the solids.

$$\frac{0.9065}{k_{cluster}} = \frac{0.13}{k_{gas}} + \frac{0.667}{k_{solid}} \tag{2.4}$$

As the cluster is surrounded by hot particulate bulk material, it experiences natural convection heat transfer between itself and the gas in the bed. The impact of radiation heat transfer from hot particles in the bed to the cluster is incorporated with that of natural convection heat transfer based on

$$h_{nc+rad}A_{cluster}(T_{bed} - T_{cluster}) = h_{nc}A_{cluster}(T_{bed} - T_{cluster}) + \epsilon_{solid}\sigma A_{cluster}(T_{bed}^4 - T_{cluster}^4) \tag{2.5}$$

The emissivity of sand (ϵ_{solid}) is 0.76, and the Stefan–Boltzmann constant (σ) is $5.67X10^{-8}$ W/m^2-K^4.

The Grace [45] correlation, which is widely used in the field of fluidization, is utilized to estimate the minimum fluidization velocity (U_{mf}) of the particles, i.e.

$$Re_{mf} = \sqrt{C_1^2 + C_2 Ar} - C_1 \tag{2.6}$$

where, $Re_{mf} = \frac{U_{mf}\rho_{gas}d_p}{\mu_{gas}}$ and $Archimedes\ number, Ar = \frac{(\rho_{solid} - \rho_{gas})\rho_{gas}gd_p^3}{\mu_{gas}^2}$

with C_1 and C_2 taken as 27.2 and 0.0408, respectively.

Finally, heat gained by the solids in the cluster during differential time (dt) is equal to the sum of:

a) heat released from the interstitial gas passing through the cluster by forced convection during dt, and
b) heat released from surrounding particles by natural convection and radiation during dt.

i.e.

$$\rho_{solid}.\frac{4}{3}\pi r_{cluster}^{3}.\left(1-\varepsilon_{mf}\right).C_{p,solid}.\frac{d}{dt}[T_{cluster}(t)] = \rho_{gas}.\pi r_{cluster}^{2}.U_{mf}.C_{p,gas}[T_{bed}-T_{cluster}(t)] + h_{nc+rad}.4\pi r_{cluster}^{2}.[T_{bed}-T_{cluster}(t)] \quad (2.7)$$

The first term on the right side of this equation represents forced convection heat transfer from the hot gas to the particles inside the cluster. Application of the lumped capacitance model for this heat transfer is appropriate when the Biot number is less than 0.1. Cengel [46] argued that the lumped capacitance model can still be applied with the criterion Bi < 0.1 not satisfied if high accuracy is not a major concern. The Biot number for this case was estimated to be 0.8. Since the complex dispersion pattern of cold tracer particles among the hot particles in the bed would affect the accuracy of this model anyway, the need for applying a more complex heat transfer model was not felt. This equation is integrated such that a cluster's temperature rises from an initial value of 20°C to several final values so that the estimated times needed to reach these values are obtained.

The results are presented in Figures 2.5 and 2.6 for bed temperatures of 600°C and 900°C, respectively.

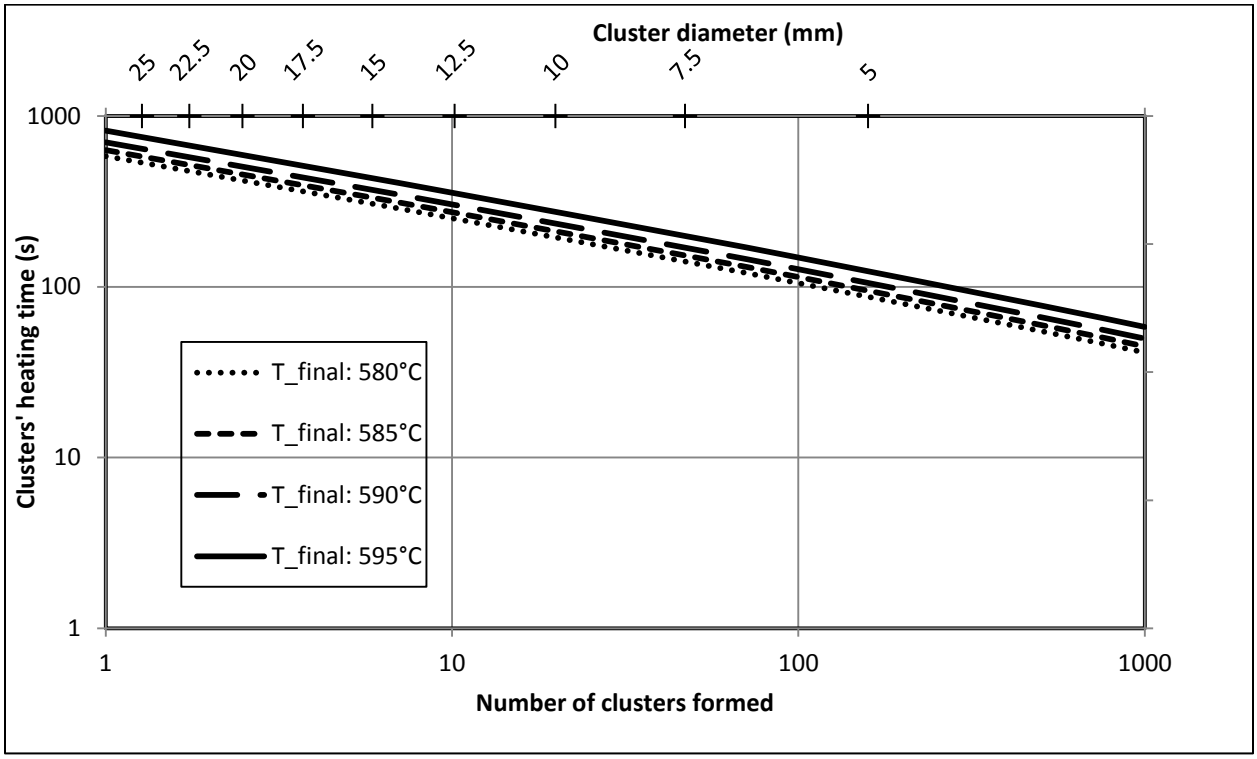

Figure 2.6: Effect of number and size of clusters on heating time from ambient temperature to four final temperatures. (Cold particles: 100 g, T_{bed}: 600°C, ρ_{bulk}: 1200 kg/m^3, d_p: 70 µm.)

As expected, the cluster size decreases as the number of clusters increases for a fixed mass of cold particles. The cluster heating time decreases for all final temperatures, with an increase in the number of clusters formed because smaller clusters heat up more quickly than larger ones of identical composition subjected to the same environment. If 1000 clusters of bulk density 1200 kg/m^3 and size 70 µm form from 100 g of particles, the estimated heating time ranges from 41-58 s to reach temperatures of 580-595°C when the bed temperature is 600°C. If 100 g of particles of bulk density 1450 kg/m^3 and size 170 µm fragment into the same number of clusters, the heating time is estimated to be 25-34 s for final temperatures of 880-895°C and a bed temperature of 900°C.

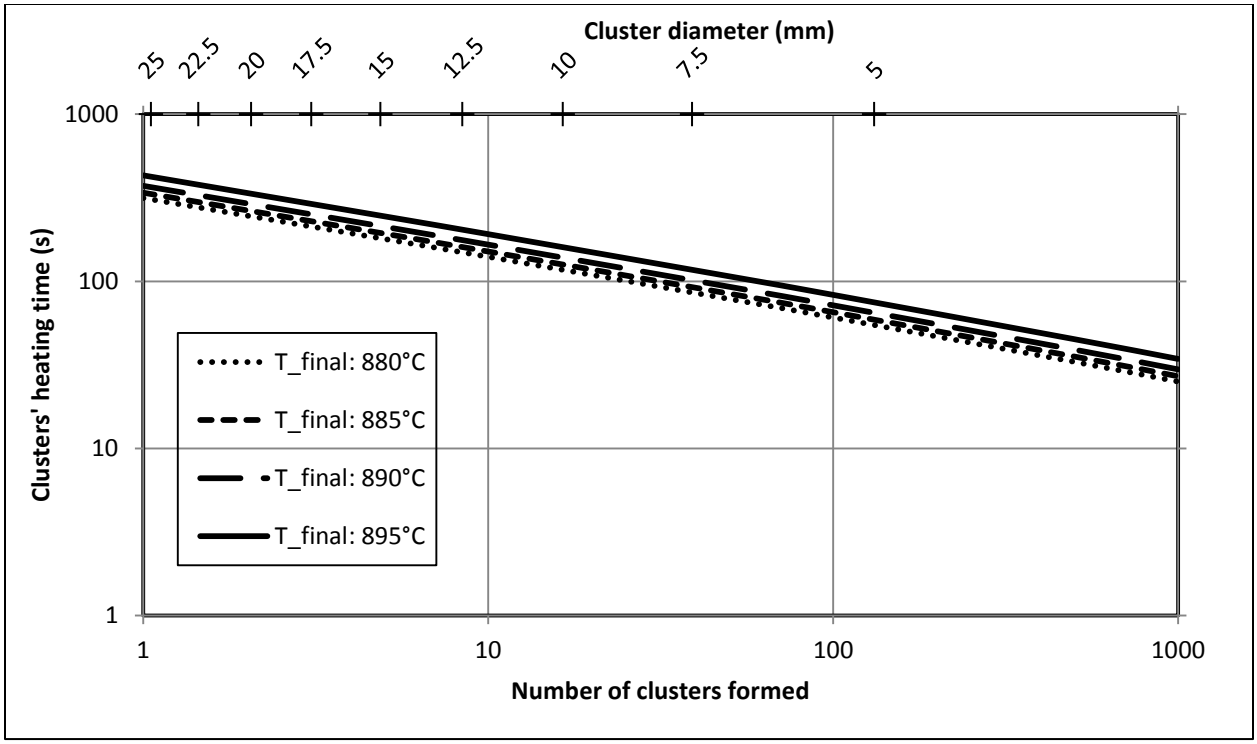

Figure 2.7: Effect of cluster number and size on heating time from room temperature to four final temperatures. (Cold particles: 100 g, T_{bed}: 900°C, ρ_{bulk}: 1450 kg/m^3, d_p: 170 µm.)

Figure 2.8 presents the time needed for the solids to travel from the point of injection where cold particles meet a bulk flow of hot particles to the level of the lowest thermocouple installed in the test section, a distance of 356 mm.

Travel times are calculated for solids fluxes of 20-120 kg/m^2-s in the riser, equivalent to 25-151 kg/m^2-s in the transfer pipe between the riser's cyclone and gasifier. As expected, the travel time decreases as the solids flux increases. The ranges of travel duration are 3 to 17 s and 3 to 21 s for 70 and 170 µm particles, respectively.

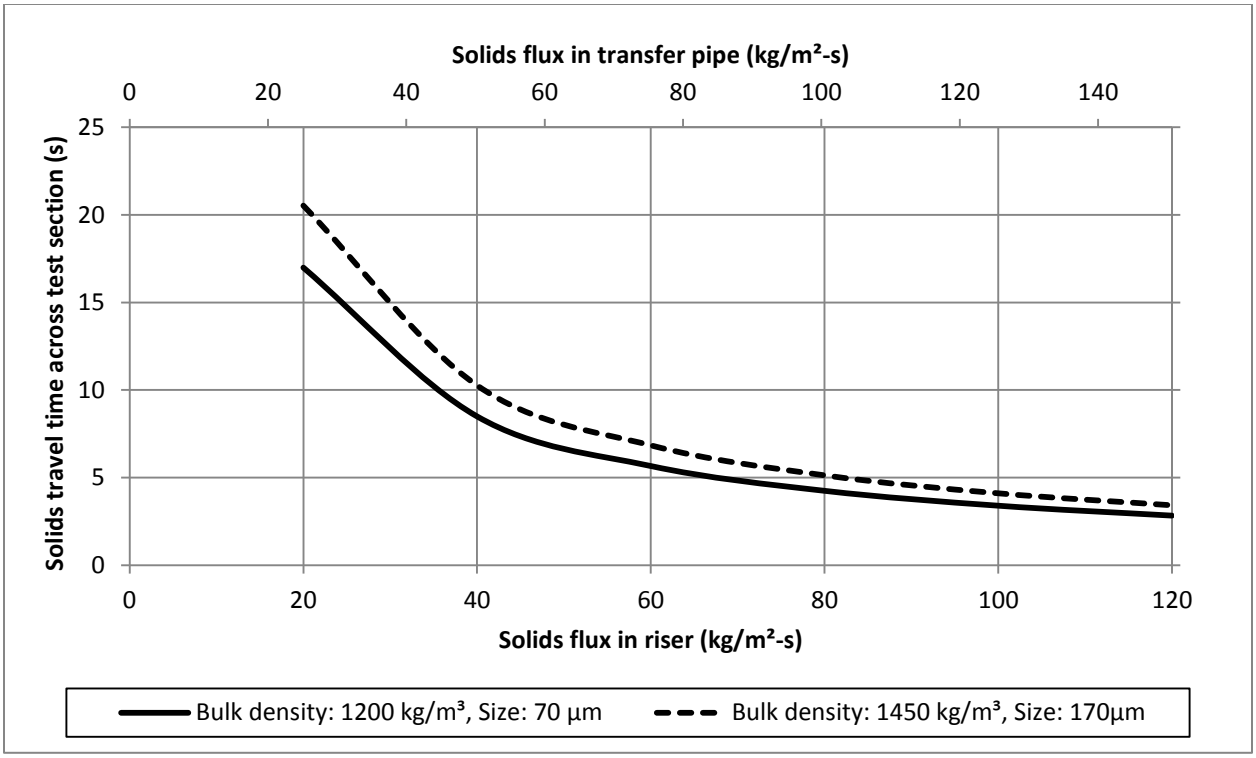

Figure 2.8: Solids travel times across test section of height 356 mm for typical solids flux in the DFB plant.

By comparing cluster heating times with their travel times inside the moving solids for the same operating conditions, it can be seen that clusters are unable to closely approach the bed temperature before passing the last thermocouple of the test section. The longest travel time is obtained at the lowest solids flux considered. For 70 µm particles moving downward at a flux of 20 kg/m^2-s, the travel time is 17 s, whereas for 170 µm particles the corresponding time is 21 s. On the other hand, the shortest heating time is found for the largest number of clusters at the lowest final temperature. For 1000 clusters of 70 µm particles to reach 580°C, the heating time is 41 s. The same number of clusters at 170 µm with a final temperature would require 25 s to heat up to 880°C. These findings have important implications for design and operation of measurement device using thermal tracing technique showing that even if 100 g of injected particles fragment into as many as 1000 clusters, they would still be

capable of providing an easily measurable temperature difference in the experimental measurement interval.

2.5 Data analysis, results and discussion

The raw data obtained from two adjacent thermocouples without and with the injection of cold tracer particles are presented in Figure 2.9 which clearly shows that the signal can easily be distinguished from the background fluctuations.

The temperature signals from pairs of thermocouples with the same penetration into the pipe at two adjacent levels were compared with each other using the cross-correlation technique. Then a plot of cross-correlation coefficient as a function of time shift was obtained. The time shift at which the cross-correlation coefficient attains a maximum value is considered to be the time needed for the solids to travel the distance between the two levels. The solids flux or circulation rate can then be calculated from Equations (2.1) and (2.2). Since each pair of thermocouples produces a value of solids flux, nine values are obtained from each injection of cold particles. Each of these nine values of solids flux corresponds to a fraction of the cross-sectional area of the test section. The total flux is then estimated from the average of the individual values. In order to improve statistical accuracy of the process, three consecutive injections of cold particles were made within a span of five minutes. The sampling time for cold particle injection was 15 s. Finally, all solids fluxes were averaged to obtain a single value for this batch of injections. The code written in MATLAB for data processing is provided in Appendix B.

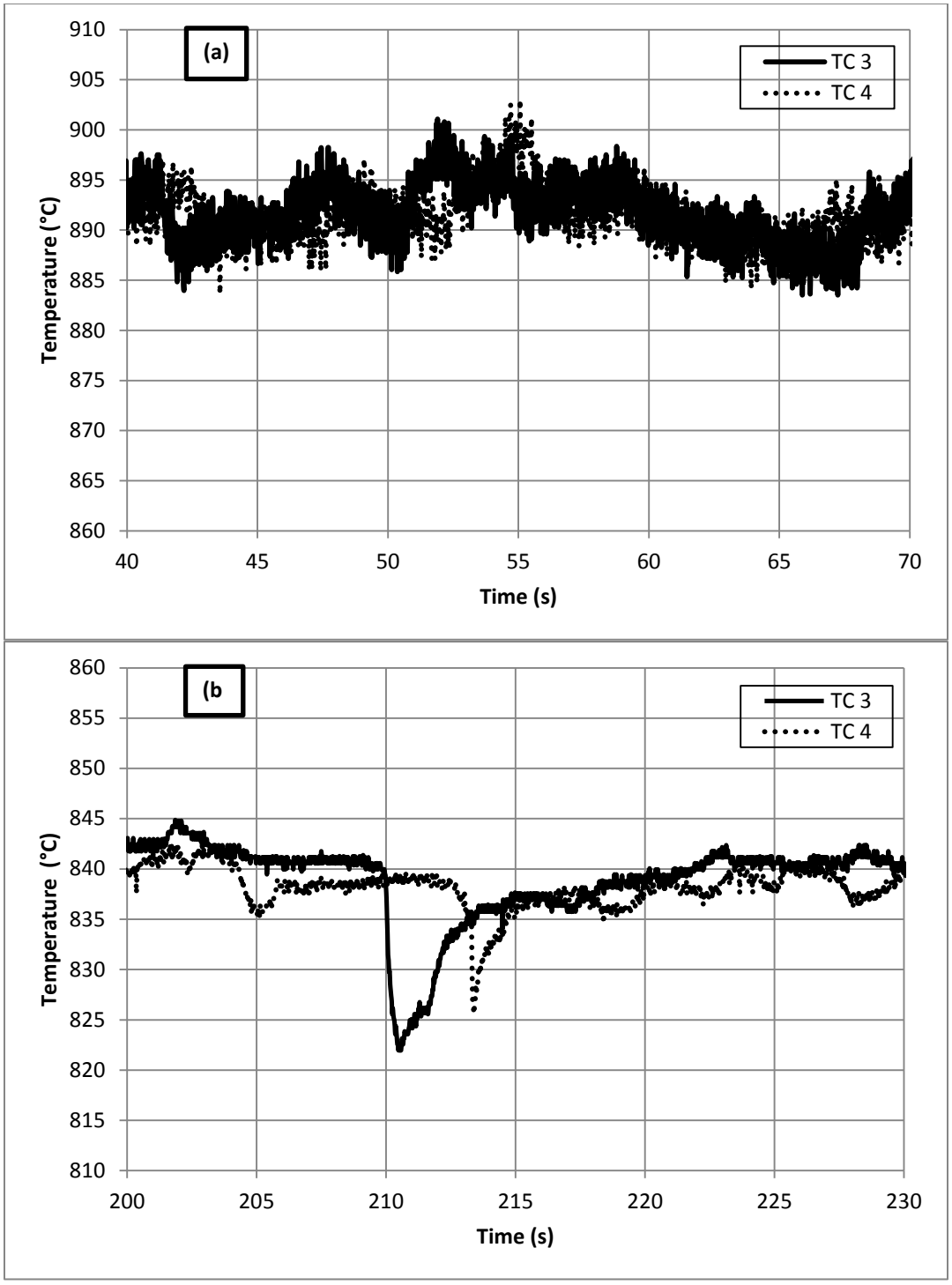

Figure 2.9: Raw signals obtained from thermocouples 3 and 4: (a) with no tracer injection, and (b) with injection of 100 g cold tracer particles. (Bulk density: 1450 kg/m^3, Size: 170 µm.)

As the junctions of the thermocouples are exposed to the measurement environment where moving packed bed of particles at high temperature passes by, it was found that not all of the 12 thermocouples worked properly at all times. If a thermocouple failed at high temperature, it could not be replaced until the plant was shut down. Therefore, the data are based on the actual number of thermocouples working properly during measurement, rather than on the total number of installed thermocouples. The lowest number of working thermocouples in a test was 7. Thus the range of working thermocouple pairs was from 5 to 9 for injection of cold tracer particles.

A set of criteria has been developed to screen out values which cannot be justified physically. For a value of solids flux obtained from any pair of thermocouples to be accepted for subsequent processing, it had to meet all of the following requirements:

- Maximum cross-correlation coefficient > 0.6;
- The maximum coefficient is taken from a clear distinct peak in a plot of cross-correlation coefficient against time shift;
- The plot contains no deep ‘abyss’.

For those values of solids flux which met these criteria, it was further required that:

- For any of the three injections of cold particles, at least one-third of working thermocouple pairs produced usable results.

- The overall pressure balance of the system indicated the presence of moving packed bed solids flow in the transfer pipe between the CFB combustor and BFB gasifier throughout the duration of the batch test of three injections.

Due to complex mixing and flow structure of solids in the test section, several plots of cross-correlation coefficient vs. signal time shift yielded more than one peak. Some others produced deep valleys, with or without a peak nearby. All these plots of questionable shapes were carefully avoided. There were many other plots which appeared to give good shapes, but the data were poorly cross-correlated with coefficients ≤ 0.6. These plots were also screened out. We note that Werther et al. [47] used similar criteria and accepted only those data for which the cross-correlation coefficient was greater than 0.6, whereas Militzer et al. [48] and Liu et al. [39] set their minimum requirement at 0.5 for this coefficient.

The presence of hot solid particles and formation of a moving bed in the lower part of the transfer pipe, where the test section is located, are critical for the successful application of the cold particle tracer technique as moving bed flow must cover the entire test section. The presence of a sufficient amount of hot solids there can be inferred by analyzing the pressure balance of the DFB system over the entire closed path of circulating solids. Hence, absolute pressures at key points of the system are measured during the same 5-minute time span during which each batch of three consecutive tests is performed. The data obtained for each absolute pressure are then averaged over 5 min, with the standard deviation also recorded. The measurement locations of these pressures are shown in Figure 2.10, and a sample pressure balance plot is presented in Figure 2.11. Points 1-6 in Figure 2.11 correspond to the same points in Figure 2.10.

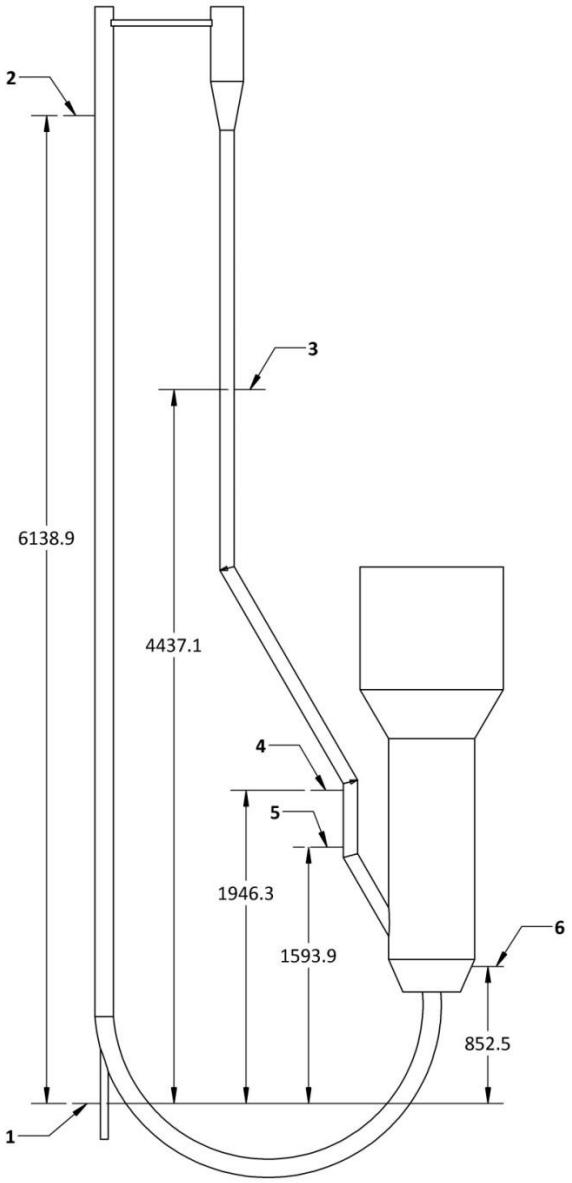

Figure 2.10: Simplified sketch of DFB system showing measurement locations of pressure transducers. (Dimensions are in mm.)

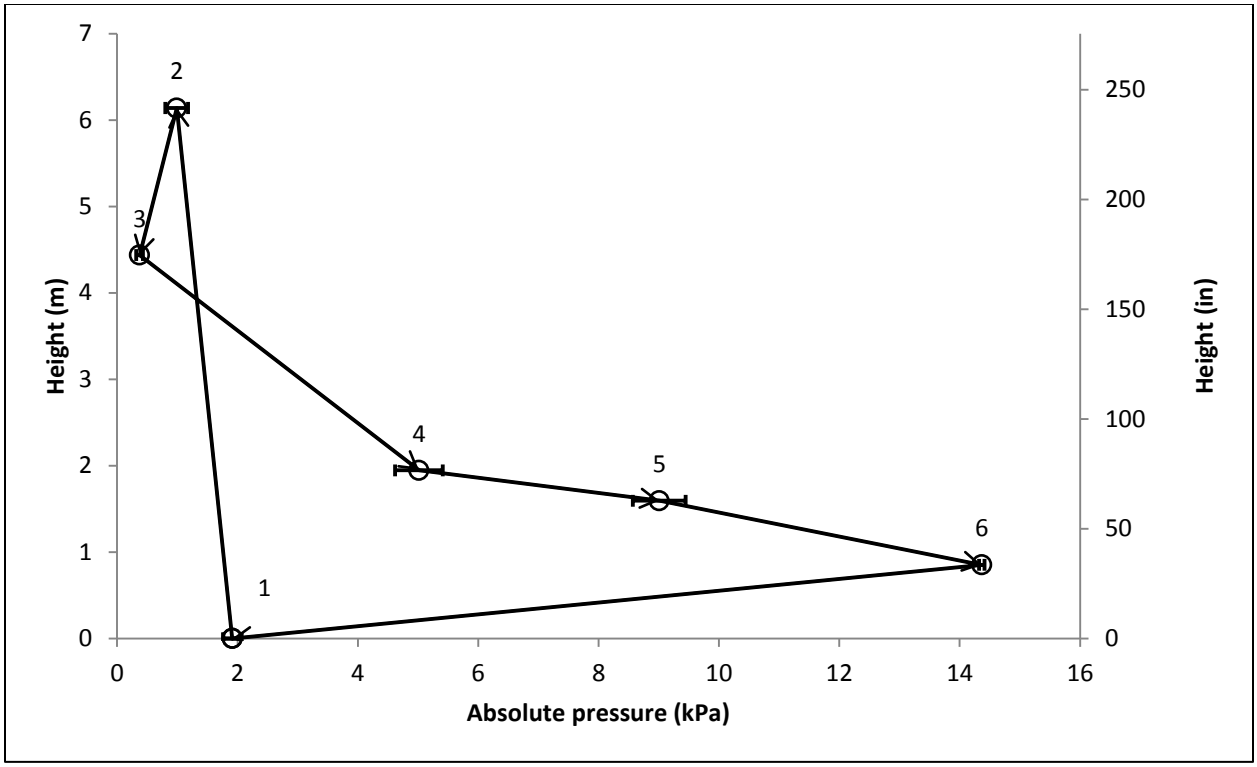

Figure 2.11: Solid circulation loop pressure balance for test batch no. 3, March, 25, 2015.

The test section is situated between points 4 and 5 of Figure 2.10. The pressure drop between these two points for one batch of tests is provided in Figure 2.11. The large pressure drop between points 4 and 5 indicates that the test section was full of hot solid particles, which in turn means that a moving bed occupied the entire test section. In addition, there was a significant pressure drop upstream of the test section, as shown by the slope of the line connecting points 3 and 4 in Figure 2.11. The presence of a considerable amount of solids between points 3 and 4 is possible only if the test section between points 4 and 5 is already full of solids. The relatively low standard deviations at points 4 and 5 suggest that the injections of cold particles altered the structure of moving bed very little. In addition, the extremely low standard deviations at points 1, 2, 3 and 6 confirm that the small packets of injected cold particles did not upset the operational stability of the overall DFB system.

A number of tests were performed over a two-year period. Solids fluxes measured using cold particle tracer technique are presented in Table 2.2. Only results from tests which fulfilled all the criteria discussed above are included. The average solids fluxes and temperatures are accompanied by 90% confidence intervals.

For the tests in which both the bed material and the injected particles were catalyst particles, the solids fluxes were found to be between 49 and 133 kg/m^2-s at temperatures in the test section from 639 to 649°C. More tests were performed with sand particles as both bed material and injected particles. For these particles, the solids flux was measured to be in the range of 16 to 65 kg/m^2-s at temperatures from 612 to 856°C. For one day's data (indicated by asterisks), it was not possible to construct pressure balance covering the full duration of all three tests due to a computer problem that led to accidental loss of pressure data. However, the data of a differential pressure transducer, connected to both ends of the test section and shared with another computer, showed a large pressure drop across the test section, confirming that there were sufficient hot solid particles. Hence, these solids fluxes have been accepted.

The performance of this measurement technique is affected by the complex mixing pattern of injected cold particles into the bulk hot solids flow. The performance was affected by the presence of a bend in the solids transfer pipe just upstream of the test section which made the flow pattern of bulk solids non-uniform across the cross-section of the pipe.

Table 2.2: Measured solids fluxes, their corresponding bed materials, type of injected particles and temperatures.

Bed material & injected particles	Temperature of bulk hot solids (°C)		Solids flux based on riser cross-sectional area (kg/m^2-s)	
	Average	90% confidence interval	Average	90% confidence interval
Catalyst	639	± 4.3	48.9	± 10.0
Catalyst	649	± 0.6	132.7	± 31.3
Catalyst	647	± 0.6	62.5	± 8.5
Sand	775	± 3.8	46.4	± 1.0
Sand	784	± 2.8	22.7	± 9.0
Sand	807	± 4.6	29.4	± 2.0
Sand	612	± 1.0	36.3	± 7.4
Sand	632	± 2.0	15.7	± 0.4
Sand	832	± 2.1	46.6*	± 5.7
Sand	833	± 2.6	55.5*	± 12.5
Sand	840	± 3.2	46.4*	± 8.6
Sand	753	± 2.3	37.3	± 10.6
Sand	767	± 2.2	44.7	± 7.6
Sand	802	± 4.3	41.4	± 5.0
Sand	821	± 1.3	57.2	± 5.5
Sand	826	± 2.4	50.1	± 13.2
Sand	839	± 1.8	65.8	± 12.3
Sand	856	± 0.9	46.3	± 7.0

Note: For the data indicated by asterisks, it was not possible to construct pressure balance due to accidental loss of pressure data of entire DFB system. However, the data of a differential pressure transducer, connected to both ends of test section and shared with another computer, showed a large pressure drop across the test section, confirming that there were sufficient hot solid particles.

A sparger could be designed to disperse cold particles uniformly across the cross-sectional area of the test section, but this was not done because of fear that such a device would alter the flow pattern of bulk solids, disrupting the continuity of the downward moving bed.

Since temperature fluctuations/disturbances exist in high temperature fluidized bed systems, attempts were made to explore whether solids circulation rate could be measured by cross-correlating thermocouple signals with no injection of cold particles. A number of tests were conducted. The criteria presented above for evaluating a plot of cross-correlation coefficient vs. time shift were again applied. The pressure balance in the circulation loop was examined to indicate the presence of solids in the transfer pipe for the duration of each test. The success rate of these attempts was found to be too low to be reported. Nevertheless, the outcomes of these attempts show that the injection of cold particles as tracer is essential for the thermal-tracing technique to work properly.

The performance of the thermal-tracing technique has been shown to be valid at room temperature by comparing with data obtained by measuring the flux by a simple and different method. The lack of other suitable measurement techniques had made it difficult to confirm the validity at high temperature. In order to obtain a comparison, a novel butterfly valve was designed and constructed, as described in the next chapter. An indirect method to estimate the solids circulation rate using energy balance over the gasifier is described in a recent paper by Daniel et al. (manuscript in preparation) is provided in

Appendix C. They estimated the rates to be 45.2 and 55.6 kg/m^2-s in two tests. These values can be compared to 36.3 and 46.4 kg/m^2-s, respectively, reported in Table 2.2, under process conditions similar to those of their two tests, respectively.

The practical potential of the circulation measurement method is apparent from the fact that half of our tests were conducted at temperatures above 800°C, with the highest temperature at which test is conducted being 856°C. It has been shown to work at lower temperatures as well. By automating the injection process of cold particles, the technique could be applied for real-time monitoring of solids flux or circulation rate on a commercial scale.

2.6 Conclusion

A novel method based on thermally tracing the movement of injected packets of cold solids has been developed for measurement of the solids circulation rate in a dual fluidized bed system. An uncertainty analysis was performed to determine the relative importance of each parameter relevant to the estimation of solid circulation rate. Encouraged by the success of preliminary tests in a cold model, a high-temperature test section was constructed and installed in the solid transfer pipe of a DFB pilot plant. A simple model of heat transfer between hot and cold particles was used to design the test section. The thermal-tracing technique successfully measured solid circulation rates over a wide range of temperatures from 20°C to 856°C, and for solids fluxes up to 133 kg/m^2-s. Both Geldart A and B type particles were tested. This technique has no competitor which can work at large-scale systems operating at high temperatures.

3 Development and Application of Butterfly Valve Technique

3.1 Background

In the previous chapter, the development and application of a novel thermal-tracing technique were presented. However, it was not possible to compare the solids circulation rates measured by this technique at high temperature with those of other techniques because of a lack of other suitable techniques which can be applied at high temperature. This chapter considers and presents a butterfly valve technique for application at elevated temperature. The application of a butterfly valve in a circulating fluidized bed system is not new. However, previous applications were limited to circulating bed systems operating at ambient temperature or slightly above ambient. The design and construction of a butterfly valve which is capable of surviving high temperatures typical of industrial systems differs significantly from the valve design for low or ambient temperatures. In that sense, the high-temperature butterfly valve presented in this chapter is considered to be a novel device.

Brereton [36] designed and operated a butterfly valve for the measurement of solids circulation in a room temperature setup. In this technique, the closing of valve's two half-circular plates cause the accumulation of solids on top of it. The change in the height of the top surface of a bed of accumulated solids was then tracked. Since it was a room temperature setup, Brereton [36] was able to use a transparent material for the construction of the column where the valve was installed. The accumulation of solids after closing the valve could be easily monitored in this setup due to the transparency of the construction material. Also, since the valve operated at room temperature, he did not have to consider thermal expansion of the construction material of the valve.

For the purpose of this project, one option could be the use of a butterfly valve suitable for room temperature application, preventing the valve's damage during high-temperature operation of the plant by cooling the valve. A cooling jacket around the pipe which houses the valve might be able to keep the temperature at pipe's surface reasonably low. However, this cooling jacket would not be able to bring down the temperature of valve's plates sufficiently low to prevent damage when the plates would come in contact with solids at high temperature, e.g. 900°C. Therefore, a room-temperature valve with cooling was considered to not be a suitable alternative to a valve that can survive at high temperature without cooling.

In a high-temperature setup, such as the dual fluidized bed pilot plant, the application of butterfly valve technique is complicated due to two factors: i) the impossibility of using a transparent material for construction of the column, and ii) the thermal expansion of the valve's materials of construction with changes in temperature. The downcomer section of the dual fluidized bed pilot plant is made of a high-temperature alloy. Also, it is heavily insulated to prevent loss of heat from the system. This makes visual determination of the top surface of accumulated solids impossible. Hence, a sensor needs to be found which is capable of distinguishing between an empty space and a space full of hot solids. The valve needs to be able to open and close freely at all temperatures. This means that the clearance between the valve's edge and the inner surface of the pipe in which it is installed must be sufficient to accommodate the thermal expansion of both the pipe and the valve at high temperature.

It is important to note that the butterfly valve technique is unlikely to be suitable for measurement of solids circulation rates in commercial-scale plants. The closing of the valve would significantly affect the

steady state operation of the system during the period it remain closed by depriving the downstream reactor from receiving the required amount of solids and also by upsetting the pressure balance in the solid circulation loop. When the valve is reopened, a certain period of time would be needed for the system to return to the steady state condition. The summation of these two times is highly likely to be long enough to discourage the application of the butterfly valve technique. Therefore, the high-temperature butterfly valve was developed in this thesis work only to validate the performance of the thermal-tracing technique at high temperature and not as a competitor.

3.2 Location of the set-up

Both Brereton [36] and Burkell et al. [11] installed their valves to accumulate solids for the measurement of solids circulation rate in the downcomer section of circulating fluidized beds. The solid transfer pipe between the riser and the bubbling bed of the dual fluidized bed pilot plant was the most appropriate location for the installation of the butterfly valve in the present project since the particles travel downward inside that pipe due to gravity. A very small amount of inert nitrogen gas is used to facilitate the flow of solids in the lower part of the transfer pipe. This gas eventually travels upward, but it exerts negligible drag force on the particles anywhere in the solid transfer pipe. Figure 3.1 shows the location of the butterfly valve section in the solid transfer pipe of the dual fluidized bed pilot plant.

There are four sections of the solids transfer pipe – two vertical and two angled. The angled sections are not suitable since the top surface of accumulated solids will not become parallel to the valve's plates.

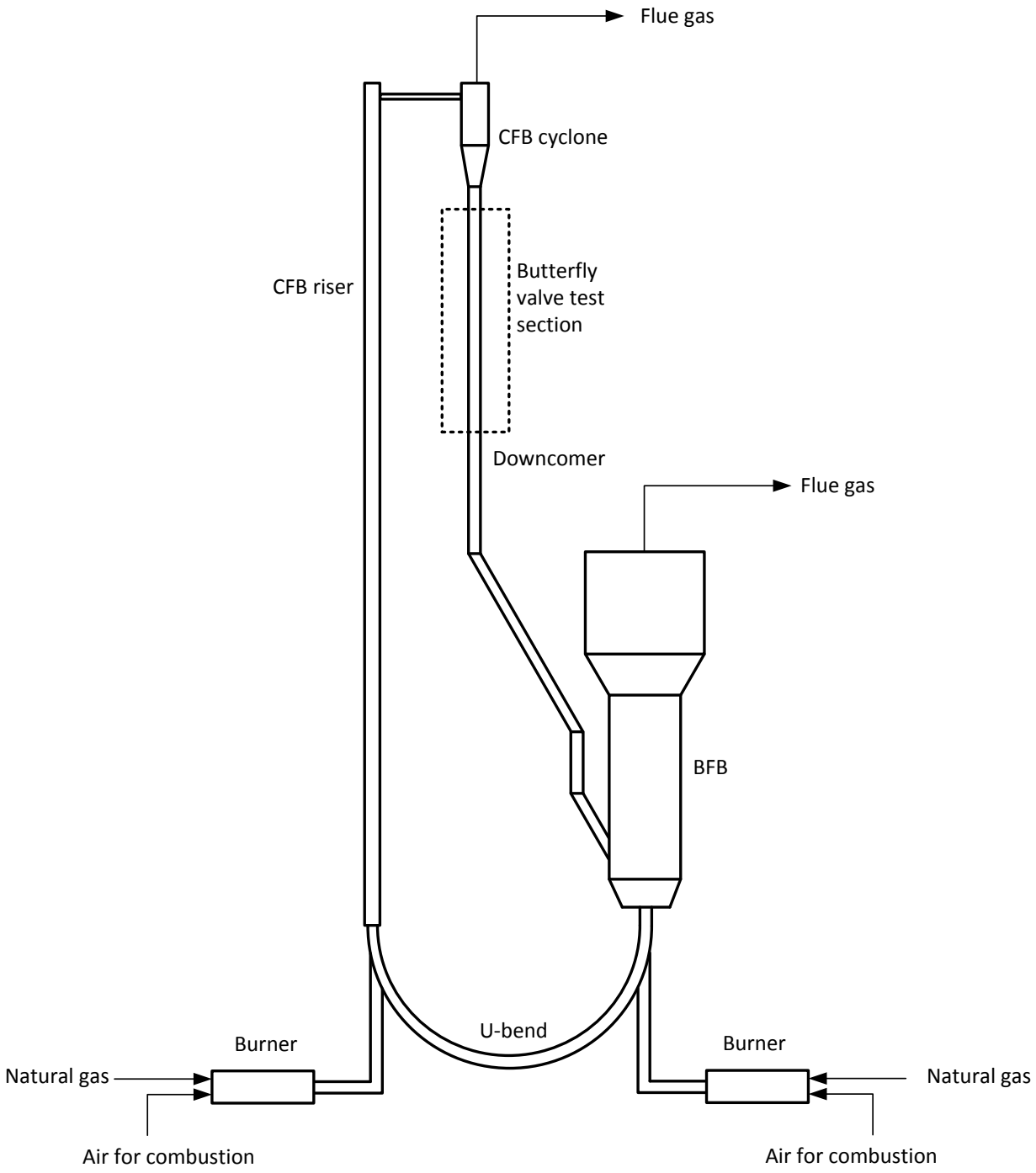

Figure 3.1: Location of butterfly valve in the solid transfer pipe of the dual fluidized bed pilot plant.

The lower vertical section already housed 12 thermocouples and a cold particle injection port for the thermal-tracing test setup. Even if this section were not used for the thermal-tracing test setup, the butterfly valve could not be installed here. This section remains full of a moving bed of solids which would have hindered the closing of the valve. Moreover, it is not long enough to accommodate the valve and the measurement ports. This leaves the upper vertical section for the butterfly valve. There is no moving bed of solids in this section. It is located right below the riser's cyclone, and it is of sufficient length to cover the test section. However, two ports for measuring the pressure and temperature at the lower part of the upper vertical section limited the length available for installing the valve and sensors. Finally, it was decided to fit the entire test section within a length of 857.3 mm.

3.3 Butterfly valve test section

The experimental setup for tests using the butterfly valve technique has four major components. From top to bottom, they are: (i) a port section, (ii) an expander, (iii) a butterfly valve, and (iv) a reducer. Figure 3.2 shows these sections and their dimensions in mm.

The material of construction of the entire test section was stainless steel 310 except for a few small accessories used in the valve itself. Relevant information of these accessories are provided in Section 3.3.3 of this chapter.

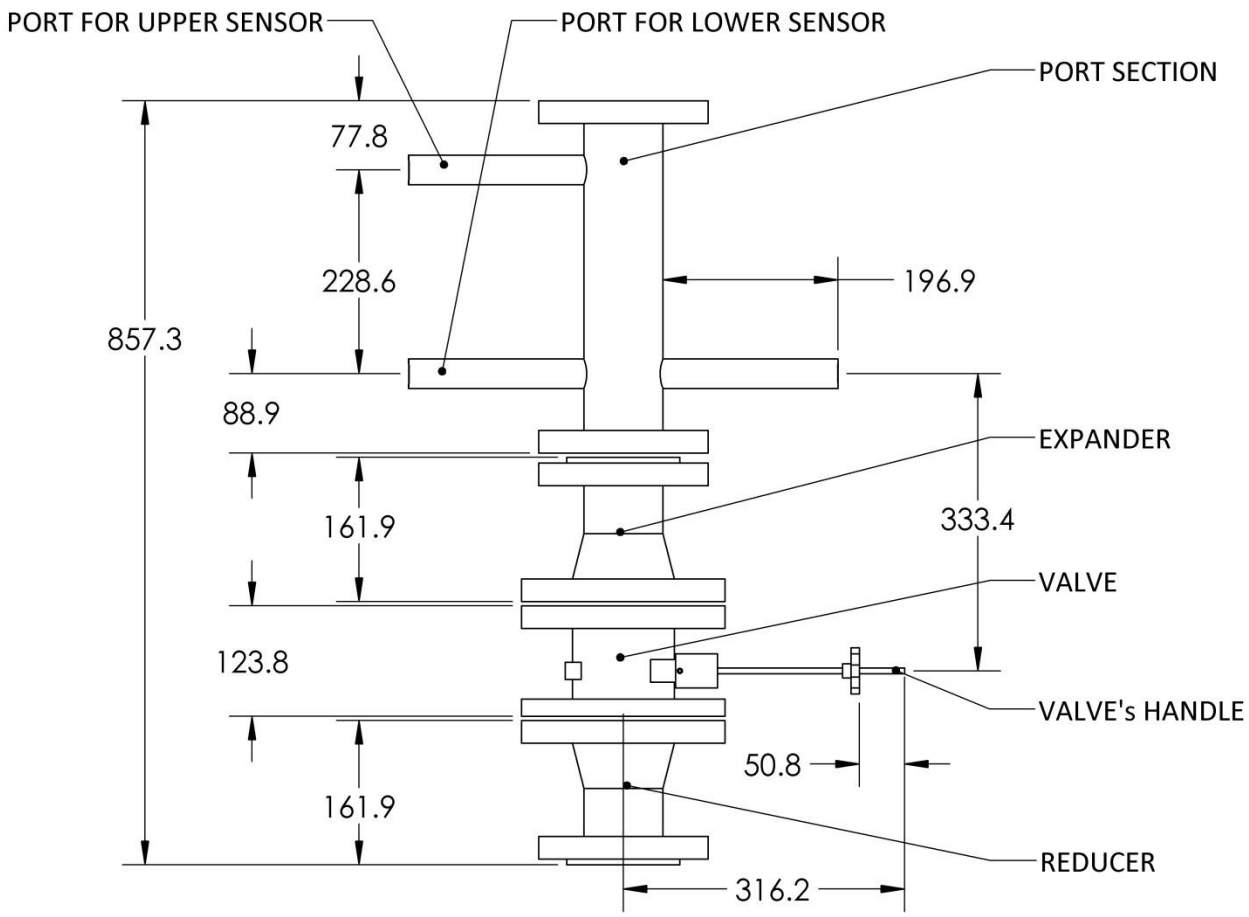

Figure 3.2: Butterfly valve test sections. (Dimensions are in mm.)

Class 150 flanges were used to put the four sections together and then to connect the assembly to the rest of the solids transfer pipe. The pressure rating of these flanges was considered sufficient since the test section would operate at pressures which are only slightly above atmospheric pressure. Slip-on and lap-joint type flanges were chosen, with slip-on flanges in most cases because of their lower cost. The expander and reducer were welded to separate straight pipe sections for installation using lap-joint flanges. The presence of lap-joint flanges in the setup made it possible to rotate the entire test section and/or part of it in an angular direction around the vertical axis if needed in the future.

The flanges at the butterfly valve section have eight holes for bolts equally spaced over a bore circle of 190.5 mm. The other flanges have four holes on a bore circle of 152.4 mm. All bolts have a size of 19.1 mm. The dimensions of the flanges and the bolts fixed the dimension of the gasket installed between adjacent flanges to prevent gas leakage. The gaskets were of type Durlon HT 1000-T316, with thickness 3.2 mm supplied by NE Seal Industrial Products Ltd., Burnaby, BC.

3.3.1 Port section

The port section has three horizontal pipes of internal diameter 24.5 mm (NPS 1, SCH. 80) and length 196.8 mm welded on a vertical pipe of internal diameter 73.7 mm (NPS 3, SCH. 80) and length 395.3 mm. Two of the horizontal pipes were installed on the same vertical plane, but separated by a distance of 228.6 mm. These two pipes house capacitance sensors for detecting the level of accumulated solids. The third horizontal pipe was not used in the test. However, it allowed the insertion of an inspection camera when the plant was not in operation. Also, it could potentially be used for installation of a laser device in case the capacitance sensors had not worked at high temperature.

It was planned to install two capacitance sensors at two different levels, creating an opportunity to measure the times needed for the solids to accumulate above the closed valve to fill up three volumes with each of them bounded by two levels:

- Valve's top surface – lower sensor
- Lower sensor – upper sensor
- Valve's top surface – upper sensor

The use of more than one sensor also serves another purpose. If one sensor shall go out of order during a test, then the test does not need to be abandoned as long as the other one keeps working. This is very important since the preparation for each test required significant time. For hot tests, a long period of time was needed to heat up the system to the desired temperature.

Initially, it was planned that the maximum valve shut-off time would be about 60 s. This duration was what would be needed for the solids to fill up from the valve's top surface to the upper sensor for a solids circulation flux of 10 kg/m2-s. The distance was estimated as 530 mm. The location of the lower sensor was not as critical as that of the upper sensor. The presence of flanges did not allow a location exactly half-way between the valve and the upper sensor. The height of the lower sensor from the valve's top surface was set at 300 mm.

It was considered useful from an operational point of view to estimate the time required for the solids level to reach the top end of test section after closing the butterfly valve. If the solids fill up to the top end, then any additional solids would accumulate inside the cyclone because the gap between the cyclone's bottom and the top end of test section is very small. The cyclone would then not be able to operate effectively, causing a significant amount of solids to leave the circulation loop with the flue gas toward the downstream heat exchangers.

Figure 3.3 shows the times needed to fill up four volumes, each bounded by two levels, for a range of solids circulation flux based on the riser's cross-sectional area.

As expected, the fill-up time decreases with increasing solids circulation flux, with the rate of decrease larger at lower flux than at higher flux. This indicates that an error in measuring the fill-up time at high flux would have a greater impact on the accuracy of results than at lower flux. In addition to being useful for the design of the test section, this figure also acted as a guide for operators to avoid the accumulation of solids in the cyclone.

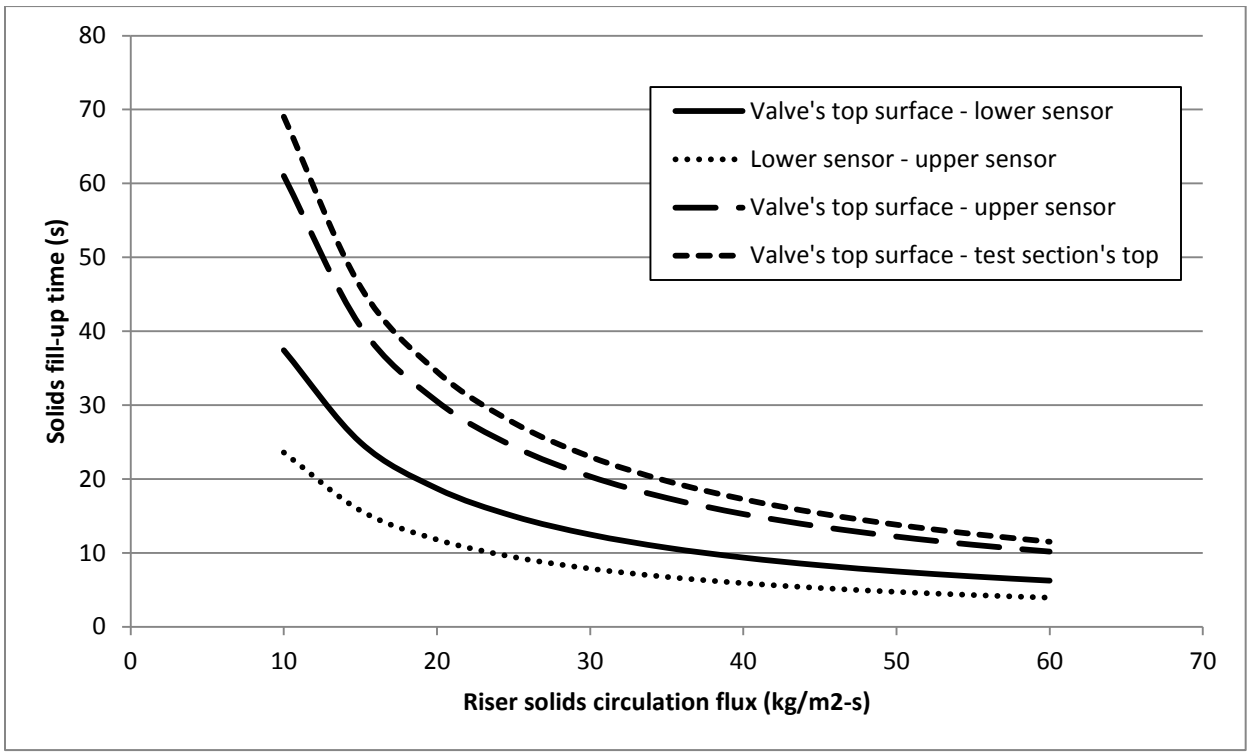

Figure 3.3: Estimated solids fill-up times in the butterfly valve test section (ρ_b = 1450 kg/m^3).

The mass of solids in the pilot plant during the test was approximately 90 kg, whereas the mass of solids required to occupy the space from the valve's top surface to the upper sensor was estimated to be 3.6 kg, i.e. only 4% of the total solids inventory of the system. Therefore, closing of the butterfly valve during the test was considered to be unlikely to significantly affect the hydrodynamics of the system.

3.3.2 Expander and reducer

The pipe used for the butterfly valve itself has an internal diameter of 97.2 mm (NPS 4, SCH. 80). However, the internal diameter of the pipe in the port section and the entire solids transfer pipe from the riser's cyclone to the gasifier is 73.7 mm (NPS 3, SCH. 80). Hence an expander and a reducer are needed to connect the valve with its upstream and downstream, respectively. Their purpose is to ensure a smooth and gradual transition of solids flow area to and from the valve. The expander and reducer are identical in design, but they are mounted in opposite directions.

3.3.3 Butterfly valve

Twenty-eight pages of engineering drawings (see Appendix D) were required to describe all components of the valve for its construction by the departmental workshop. The valve has two identical plates, which remain in vertical positions due to gravity. This keeps the valve open for solids flow through it. When the plates are moved to the horizontal position, the valve is closed and solids accumulate on the plates. Each plate requires a number of identical accessories. Figure 3.4 shows a plate and its accessories in assembled and exploded fashion.

Each plate and its supporting accessories are mounted on a shaft and installed inside the pipe. A handle protrudes from the pipe and the insulation that surrounds it. When this handle is rotated, the rotational force is transmitted to the shaft of the plate through the gear. The shaft and the plate mounted on it then rotate. The gear also synchronizes the rotation of one plate with the other. Two bearings, one at each end of the plate, support its weight and that of the accessories. They also ensure smooth rotation

of the shaft. One end of the plate is completely sealed after the bearing to prevent gas leakage from that end. The other end could not be sealed as the shaft needs to pass through it. Hence, the shaft is wrapped by a packing material to prevent gas leakage. An end cap holds all the accessories in place. Two small keys are used to connect the plate with the shaft.

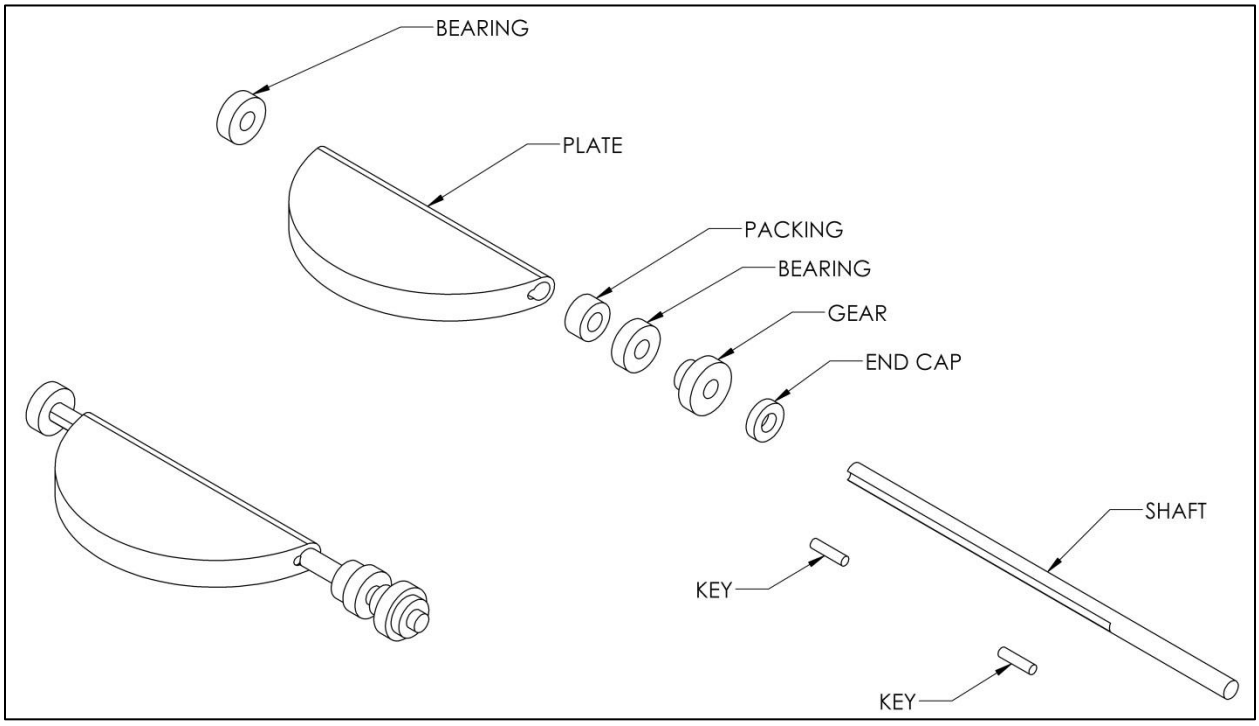

Figure 3.4: One of the two identical plates of the butterfly valve and its accessories (assembled view in the left and exploded view on the right).

The plate, shaft, keys and end cap were all constructed of stainless steel 310. The bearing, packing and gear are purchased from outside companies. Table 3.1 lists their materials of construction, working temperatures, key dimensions, name of manufacturers or suppliers and the product code.

Table 3.1: Key information on bearing, gear and packing.

	Material of construction	Working temperature (°C)	Dimension (mm)	Manufacturer / supplier	Product name / code
Bearing	Ceramic Si_3N_4	900	ID: 6 OD: 15 Width: 5	Boca Bearings, Inc., Boynton Beach, Florida, USA	696 SI3N4
Spur gear (Pin hub)	Stainless steel 303	760	Pitch Dia.: 16.9 OD: 19.1 Bore Dia.: 4.8 Pitch no.: 24 Teeth no.: 16	RPM Mechanical Inc., Burlington, Ontario, Canada	P24S21-16
Packing (Braided)	Wire: Inconel Yarn: Carbon	650	3.2 X 3.2	Grizzly Supplies Ltd., Langley, British Columbia, Canada	SEPCO # 310

It was difficult to locate the bearing, gear and packing material suitable for application at high temperatures typical of the pilot plant. No manufacturer was found who produced metal bearings capable of working at 900°C. Ceramic bearings can handle such a high temperature, but they need to be operated carefully because of their brittle nature. Two of these bearings got broken and needed to be replaced. The original bore diameter of the gear was smaller than the shaft diameter of the valve, with the gear machined in the departmental workshop to enlarge the bore diameter. The maximum working temperature for a packing material found from an extensive search was 650°C. It was decided to keep the temperature of the bearing, gear and packing low by blowing nitrogen gas during hot tests. This nitrogen removed any sand that leaked into the box which houses these items.

A gap is maintained between the two plates to not only allow thermal expansion at high temperature, but also to ensure smooth rotation without touching each other. Similarly, there must be a gap between the edge of plate and the inner wall of the pipe. Otherwise, the plate would touch the inner wall and cannot be operated at high temperature. However, particles would certainly escape through these gaps when the valve is closed. To resolve this issue, a metal structure with a wedge and a tapered inside wall was designed and installed just above the plates inside the pipe. Figure 3.5 shows this structure.

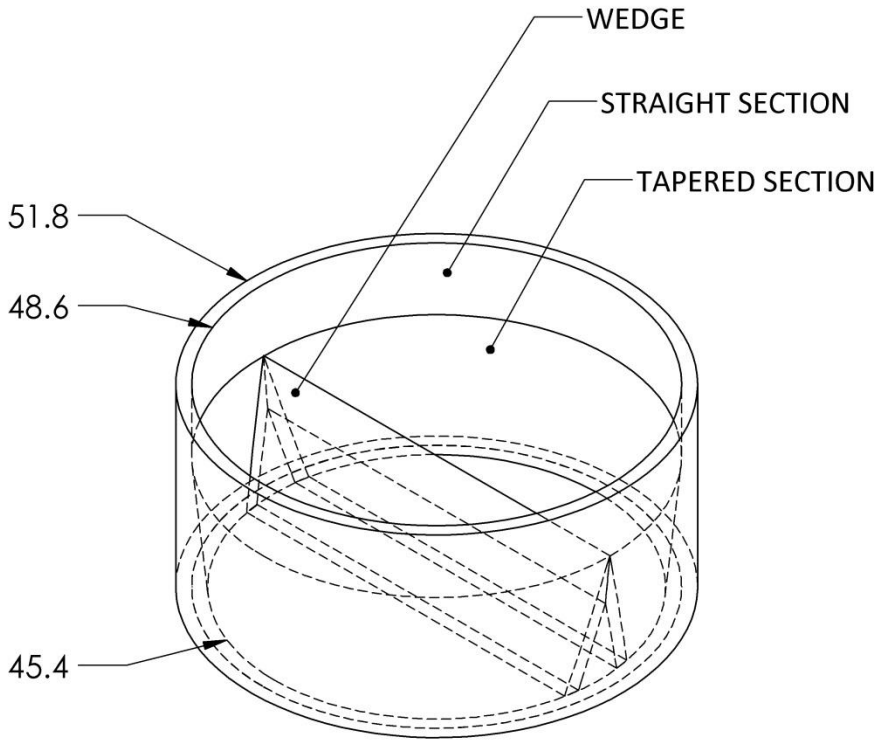

Figure 3.5: Wedge and tapered inside wall to prevent solids escape through the valve. (Radial dimensions are in mm.)

When the valve is closed, the entire gap between the plates at horizontal position falls below the wedge, thereby denying solids passage through the gap. The internal diameter of the bottom end of tapered section is smaller than that of the outer edge of the plate. The plate covers the entire cross-

sectional area at the lower end of the structure between the wedge and inner wall when the valve is in closed position. As a result, the solids cannot enter the gap between the outer edge of a plate and the inner wall of the pipe. The tapered section was constructed by machining a pipe of outside diameter 114.3 mm and thickness of 13.5 mm (NPS 4, SCH. 160).

A section view of the valve in its closed position along a vertical plane going through the axis is provided in Figure 3.6. This figure shows the gap from the plate's edge to the pipe's wall, the gap between two plates, the wedge and the tapered wall.

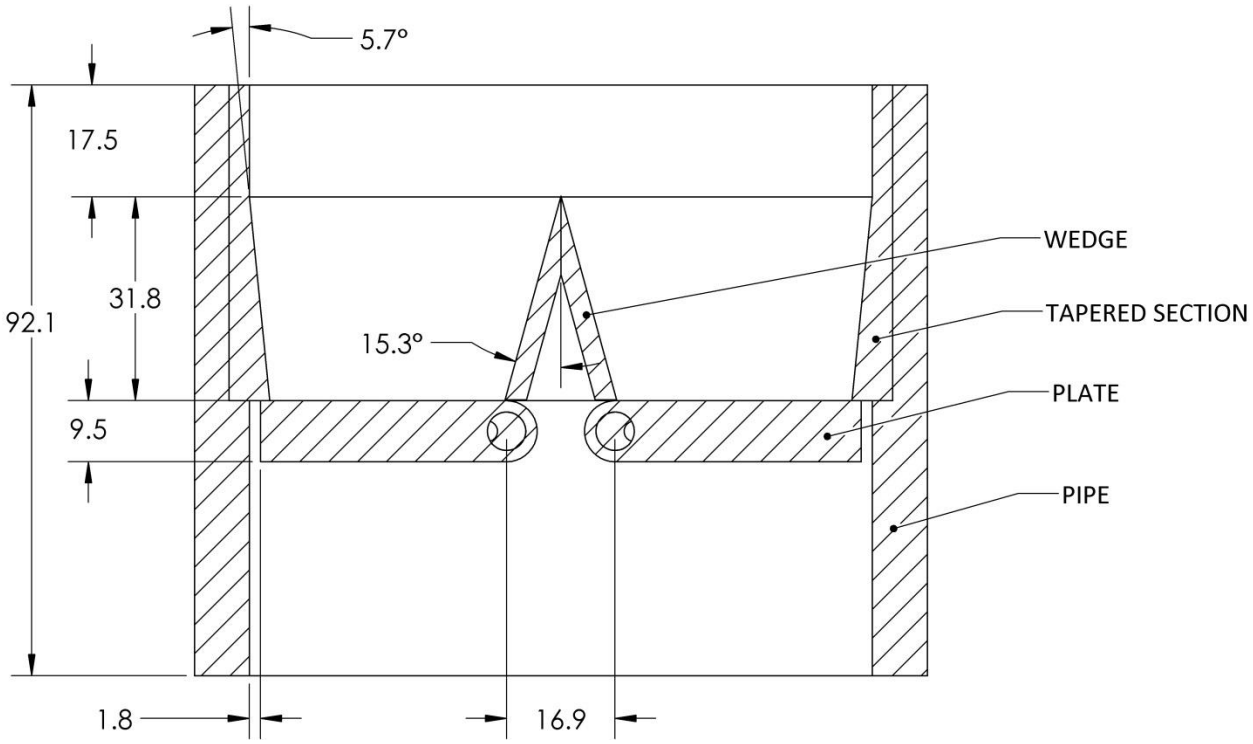

Figure 3.6: Section view of the valve's plates and internal structures. (Dimensions are in mm.)

The pipe available in the market comes with a nominal pipe size (NPS) rating. It is far more economical to design a system with the commercial pipe than with custom-built pipe. The solids transfer pipe

between the combustor and the gasifier has a NPS rating of 3. Hence, most of the butterfly valve test section were designed and constructed with NPS 3 pipe. The butterfly valve itself was initially designed with a NPS 3 pipe in mind.

We used metal rods of an outside diameter 6 mm as shafts for rotating the two plates of the butterfly valve. This size fits the inside diameter of the high-temperature ceramic bearing. No other bearings were found which could serve at high temperatures. With a shaft diameter fixed at 6 mm, it was not possible to select 6.35 mm as the thickness of the plate as this would have left too little material between the outer walls of the shaft and the round edge of the plate. Hence, the next larger size plate, 9.5 mm thickness, was selected.

It was estimated that the two plates of 9.5 mm thickness and the tapered wall would occupy nearly half of the flow area of solids when the valve was in the open position. This was clearly unacceptable. It was highly likely that the reduced flow area would create congestion of solids flow at the valve, especially at higher solids circulation rates. In this situation, not only would the gasifier receive a smaller amount of solids than its requirement, but also the cyclone would flood with solids, leading to considerable solids loss from the circulation loop toward the downstream equipment. Therefore, it was decided not to use NPS 3 pipe where the plates of the valve would be installed and determine the available flow area when a higher NPS rating pipe would be used. The flow areas of the empty pipe and the pipe with plates installed inside were estimated for the NPS 3 and the next three available NPS rating pipes. The resulting flow areas are presented in Figure 3.7.

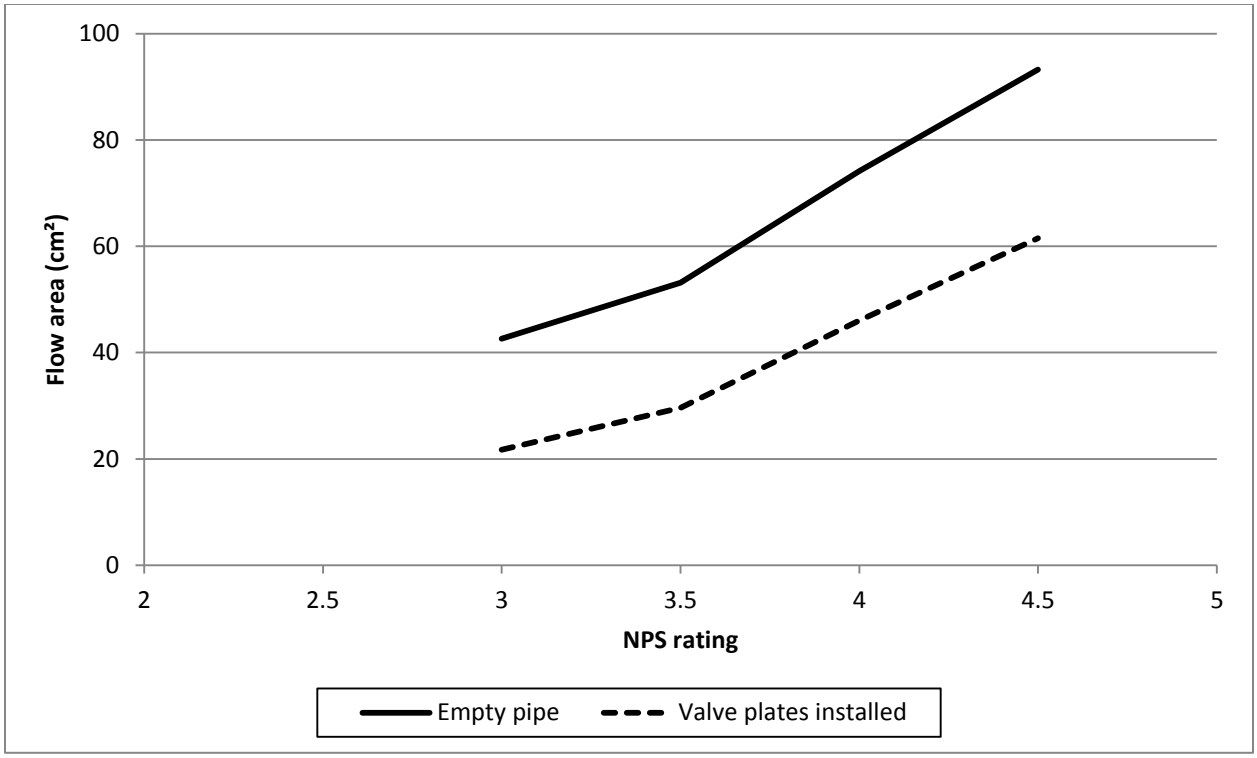

Figure 3.7: Reductions in solids flow area due to installation of valve's plates for different pipe sizes.

With each pipe size, there is a significant loss of the solids flow area due to the installation of the two plates of butterfly valve. However, if the butterfly plates were installed inside a NPS 3.5 pipe, then the solids flow area would become 69.4% of that of NPS 3 pipe with no plates installed,whereas if NPS 4 pipe were used, then there would actually be a slight gain (8%) in flow area compared to that of initial NPS 3 pipe when empty. Therefore, NPS 4 pipe was chosen for the butterfly valve. Note that only the pipe's nominal size was changed from NPS 3 to NPS 4; the schedule number of the pipe remained unchanged at 80.

3.4 Capacitance sensors

Two capacitance sensors were used to track the height of accumulated solids when the butterfly valve was closed. They were retrofitted and calibrated for this project by the manufacturer, Ace Instruments Inc., Port Coquitlam, BC. Each sensor comes with a control box for reading and adjusting the output. A cable connects the sensor to the control box.

Werther and Molerus [49] developed a needle-type capacitance sensor for measuring the local solids concentration around the tip of a needle probe. Similar probes were utilized by Almstedt and Olsson [50] to measure the bubble rise velocities in a pressurized fluidized bed combustor. Brereton [36] used similar capacitance sensors to monitor the local voidage in a circulating fluidized bed combustion unit and found the sensors capable of predicting the core-annulus flow pattern in the riser.

The two sensors used in this project were identical to each other in design. Their calibration and operation procedures were also the same. A thin metal rod is placed inside a ceramic tube which is then installed in a metal tube. The length of the ceramic tube is equal to that of the metal tube. However, the rod is longer than the two tubes, and hence it looks like a needle protruding from the probe assembly. The metal tube not only supports the assembly, but also generates a fixed capacitance. The capacitance of the needle varies depending on the presence of particles in the measurement volume. When the concentration of particles in the vicinity of the needle changes, there is a change in the dielectric constant, which in turn alters the capacitance of the system. The responses are processed by an attached circuit, and the final output voltage is sent to the control box, giving an analog display with a range of 0-5 Volt, a gain knob, a nulling knob and a filter switch.

When the filter function is activated by switching it on, the fluctuation in the output signal is dampened to provide a stable reading in the display. The nulling function is used to set the reading to zero voltage before each test. The purpose of the gain function is to increase or decrease the extent of the system's response for a fixed environment. When the output voltage is larger than 5 V, the gain function is used to bring the response within the 0-5 V range. On the other hand, when the output voltage is too small to read conveniently in the display, the gain function is utilized to magnify the voltage response.

The unit was calibrated by the manufacturer, and the reading was set to 0 for particle-free air. Then the probes were installed in the pilot plant. When the plant was heated to the test temperature, a significant drift of the output voltage from the zero reading was observed, despite there being no circulation of solids at that moment. This drift could get reduced if sufficient time (several hours) was given for the system to adjust to the new temperature. However, it was not practical to maintain a near perfect steady-state temperature of the pilot plant for such a long duration. Also, this waiting period would limit the number of tests that could be conducted in a single run of the plant. This is important since the preparation, clean-up and troubleshooting required several weeks for each run of the plant. Therefore, the nulling function was used to bring back the voltage reading to zero whenever the drift occurred. This practice likely reduced the accuracy of the output response somewhat.

In an ideal scenario, the calibration of the unit should consider not only the presence or absence of particles but also the temperature at which the unit is expected to perform. This means the following sequence needs to be followed: (i) calibrate the unit outside the plant at the desired temperature, (ii) install the unit in the test section, (iii) heat the plant to the desired temperature, (iv) perform the test,

(v) shut down the plant, and (vi) remove the unit for calibration at a different temperature for the next test. This sequence was found to be impractical as it did not allow tests to be conducted at multiple temperatures in a single run of the plant. Therefore, it was decided not to calibrate the unit for a particular temperature. Instead the nulling function was utilized to set the reading to zero before conducting each test in a single run of the plant.

The circuit attached to the probe must be maintained at room temperature, regardless of the operating temperature of the probe. During high-temperature tests, heat transfer occurred by conduction through the probe from the tip end to the circuit end. Since a large portion of the probe remained outside the insulation of the test section, most of the heat was dissipated to the surrounding air through convection. The dissipation process was enhanced many times by blowing the ambient air using a fan. This left very little heat to reach the box that houses the circuit by conduction. However, the heat radiated from the plant was highly likely to reach the circuit's box. In order to minimize this form of heat transfer, the box was wrapped with aluminum foil so that its reflectivity was very high.

3.5 Experimental procedure

The butterfly valve technique and the thermal-tracing technique were applied independently and one immediately after the other, each requiring about 4 minutes to measure the solids circulation rate between the circulating bed riser and the bubbling bed reactors. For the hot tests described in this chapter, it was not necessary for the pilot plant to operate in a gasification mode since operation at the combustion mode was sufficient for the purpose of this project. The operation in a combustion mode requires fewer operators and less time to heat up the plant to the test temperature compared to

operation in a gasification mode. In the combustion mode, natural gas was burned with excess air in the burners upstream of the circulating bed riser and the bubbling bed reactor, with no biomass used for gasification or combustion. The hot flue gas increased the temperature of inert bed material inside both vessels. The circulation rate of the inert solids was then measured at the desired elevated temperature. For the cold tests, the procedure was simpler as there was no need to burn natural gas.

The general experimental procedure for the butterfly valve and thermal-tracing measurements is described below with the flow rates based on normal temperature (20°C) and pressure (1 atm):

1. Start saving the plant's operation data in the computer used to monitor the process parameters.
2. Start supplying nitrogen to the biomass feeder at 0.3 m^3/h to prevent entry of gas and solids into it from the bubbling bed.
3. Start air supplies to the CFB burner and BFB burner at 78.7 m^3/h and 56.7 m^3/h, respectively.
4. Start nitrogen supply through the three small ports for aeration at the U-bend to help the movement of solids from the BFB to the CFB riser. The total rate of aeration was fixed for a test, but varied from test to test in the cold runs.
5. Monitor process parameters and make sure that a steady-state, particularly with regard to solids circulation, has been achieved. If needed, provide aeration using nitrogen gas at a very small rate (in the range of 0.1 – 0.4 m^3/h) at the solids transfer pipe to help solids flow through it.
6. Start purging the gear box of the butterfly valve at 13.1 cm^3/h to prevent accumulation of any particles which may escape into it through the holes for shafts and/or keep its temperature low.

7. Switch on the burners for CFB and BFB; adjust the flow rate of natural gas to 2.6 m^3/h for each of them.
8. Wait for about 10 minutes to allow the burners to start-up and establish a stable flame.
9. Check the concentration of oxygen in the flue gas leaving each reactor using an online gas analyzer. An oxygen concentration of 10-15% indicates the presence of an optimum amount of air for efficient combustion.
10. Flush the hopper for cold particles injection and its connecting pipe to the BFB reactor with pressurized nitrogen pulses of an absolute pressure of 122 kPa.
11. Start data acquisition in a second computer used to collect temperature data from twelve thermocouples at a frequency of 50 Hz. The program stops automatically after 5 minutes.
12. Load cold particles into the hopper and then inject them into the thermal-tracing test section.
13. Repeat Step 12 two more times so that three tests using the thermal-tracing technique are performed within 5 minutes at the same conditions.
14. Close the butterfly valve and simultaneously start the stopwatch.
15. Record the times needed for the top surface of accumulated solids to reach the lower capacitance sensor and then the upper sensor.
16. Open the butterfly valve as soon as the solids level reaches the upper capacitance sensor to resume solids flow through the transfer pipe.
17. Repeat steps 14-16 twice immediately so that there are three tests using the butterfly valve technique.
18. Move to a different operating condition and apply both the thermal-tracing (steps 10-13) and the butterfly valve (steps 14-17) technique to measure the solids circulation rate. During a cold

run of the plant, the only varying parameter is the aeration rate at the U-bend. Similarly, all parameters remain unchanged during a hot run except the temperatures across the plant.

19. Conduct tests at several operating conditions according to plan made prior to the run.
20. Shut down both burners in the case of a hot test. This automatically terminates the flow of natural gas.
21. Close the supply valves for CFB burner air, BFB burner air, aeration nitrogen at the U-bend and solids transfer pipe, and purge nitrogen at the butterfly valve.
22. Continue the nitrogen flow for purging the biomass feeder for at least 8 h, to flush out any combustible gases which might have been left at the end of the run. The nitrogen flow also prevents air entry into the system through the two flue gas exits streams during the flushing period. A total of 8 h of purging significantly lowers the temperature of plant and thereby eliminates hot spots in the system.
23. Close the supply valve of purge nitrogen.
24. Stop saving plant data.

Note that steps 7-9, 20, and 22-23 are ignored for the cold tests.

Several runs of the pilot plant were needed to develop the operating procedure described above. In the initial runs, the natural gas burners had been switched on before starting the circulation of solids by aerating the solids in the U-bend with nitrogen. When there is no circulation of solids, there is negligible heat loss from the solids transfer pipe. The energy saved by not circulating the solids facilitated the heating up of both fluidized bed vessels and the bed materials to the desired temperatures. However, it

also led to condensation at the solids transfer pipe of moisture generated from the combustion of natural gas in the burners. When the solids circulation was started a few hours later, some of the solids contacted water droplets condensed on the inside wall of pipe and accumulated since the start-up of the burners. As a result, the solids mobility inside the pipe was greatly reduced, often causing stoppage of the solids motion. With less or no solids returning to the bubbling bed, both the pressure and temperature of the bed were badly affected in turn making it impossible to maintain steady-state operation of the pilot plant. In order to restore the smooth flow of solids in the transfer pipe, often a thermocouple was removed and air at high-pressure was supplied through the port, clearing the congestion of solids and unblocking the pipe. This procedure (removal of thermocouple from its port, connection of hose to this port, supply of pressurized air, removal of hose and reconnection of thermocouple) required at least 20 minutes.

To avoid this problem, it was decided later to start circulating solids using a small aeration rate before switching on the burners. The continuous flow of solids through the transfer pipe prevents the condensation of water. This new practice extended the heat-up time to reach the desired temperature in both reactor vessels. However, the extra time lost in the heating process was more than balanced by the time saved from having to deal with solids blockage in the transfer pipe.

3.6 Results and discussion

An equal number of batches of tests were conducted at each test condition by independently applying the butterfly valve technique and the thermal-tracing technique. It was possible to conduct three batches of tests using each of these techniques at a single operating condition during the cold run of

plant. However, similar arrangement was not possible during the hot run of plant as the solids temperature at the test sections changed with time. Hence, a single batch of tests using each of the techniques was completed at a single operating condition during a hot run.

The solids circulation rates measured using the butterfly valve technique are compared with those measured using the thermal-tracing technique in this section. The error bars in the figures denote 90% confidence interval of the reported data. The rates obtained during cold tests are presented in Figure 3.8 as a function of the total aeration rate at the U-bend.

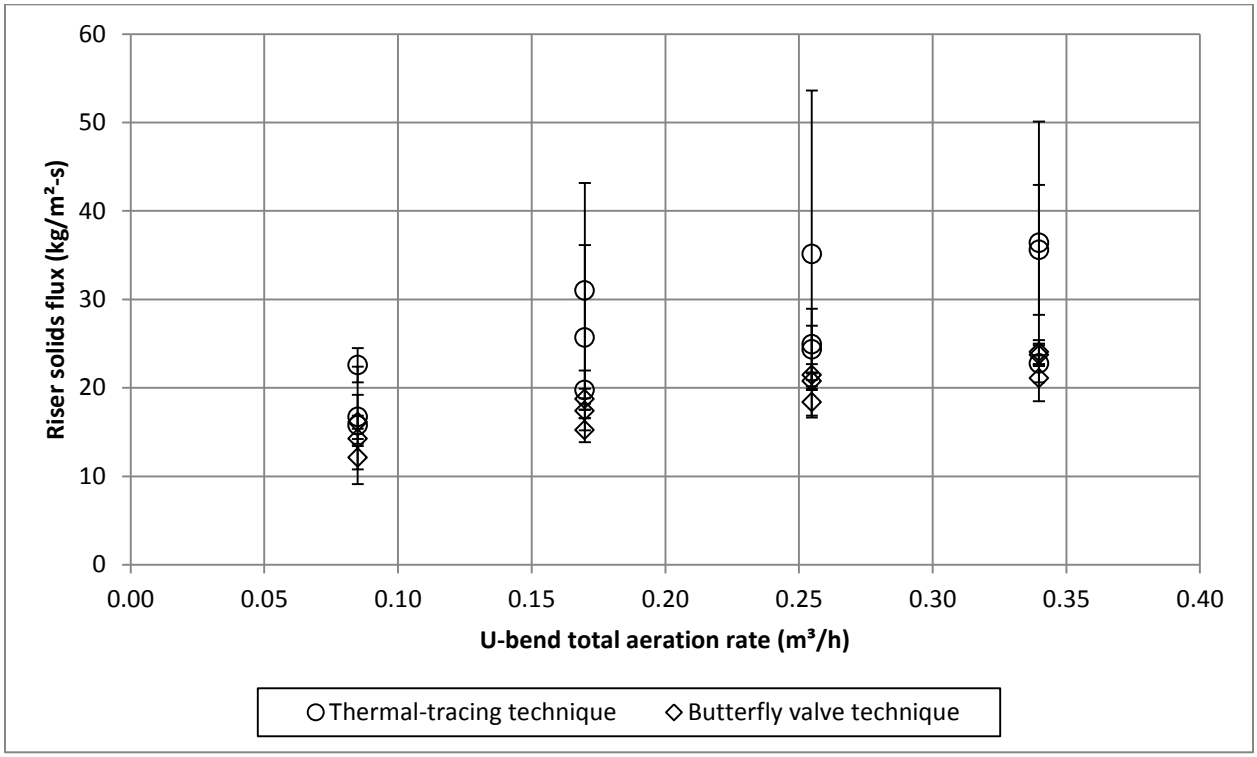

Figure 3.8: The solids circulation fluxes directly measured with the use of two independent techniques at constant superficial gas velocity of 3.4 m/s in the riser.

The three fluxes measured by the butterfly valve technique at each of the aeration rates were found to be similar, with a maximum spread of 31.9% between the maximum and minimum values. These findings indicate a higher degree of reproducibility of the data obtained from the butterfly valve technique compared to the thermal-tracing technique at room temperature.

The error bars for the fluxes measured by the thermal-tracing technique are larger than those associated with the butterfly valve technique. At each of the first two aeration rates, all three fluxes obtained from the thermal-tracing technique are found within a limited range, with the highest flux within maxima of 43.1% and 56.9% higher than for the lowest flux at these two aeration rates. However, for each of the last two aeration rates, two of the fluxes almost coincide, whereas the third was at a distance.

The total aeration rate at the U-bend was held constant during the hot tests. This is because the range over which this rate could be varied during high-temperature operation of the pilot plant was small. The lower end of the range was fixed by the lowest flow rate of nitrogen that the flow meter could measure. On the other end, any higher flow rate of nitrogen could send too much solids for the butterfly valve to handle comfortably, leading to loss of solids from the circulation loop.

The temperature at each part of the pilot plant was changed during the hot tests, causing the superficial gas velocity there to vary. Figure 3.9 shows the solids circulation fluxes measured by applying both the thermal-tracing technique and the butterfly valve technique at different temperatures in the riser. The measured solids flux did not change very much with increasing temperature. This probably happened

due to the fact that the solids circulation rate is determined by the pressure balance among the whole system which was mainly influenced by solids inventory. For a given solids inventory in the system, the pressure drops across the bubble bed gasifier and the riser changed little with bed temperature. Further discussion in this regard is provided in the next chapter.

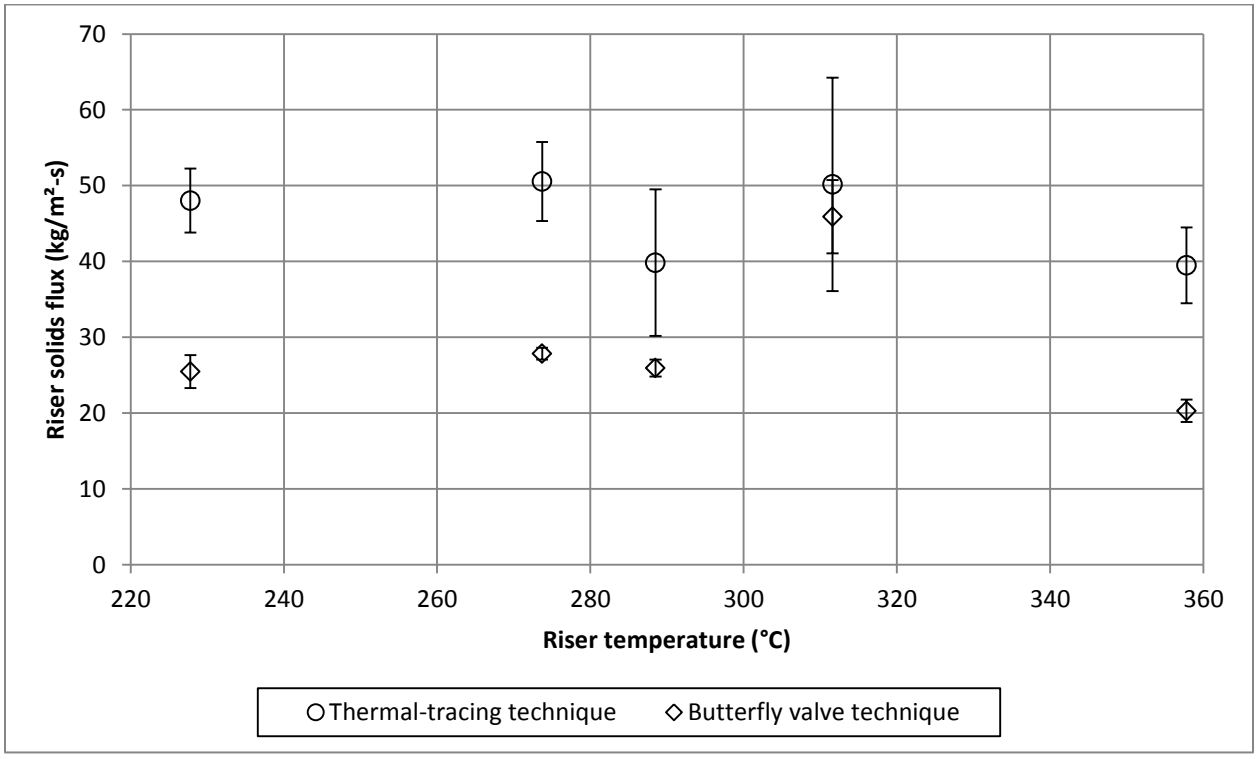

Figure 3.9: Solids circulation fluxes from two independent techniques at a constant aeration rate of 0.08 m^3/h at the U-bend. (Inlet flow rate of air at riser's NG burner for the test at 358°C was 12.5% lower than for the other tests.)

Similar to the cold test results, the error bars for the data points obtained by the butterfly valve technique are much smaller than the bars for the data points of the thermal-tracing technique. At each temperature, there is a difference between the solid circulation fluxes measured by the two techniques. However, the difference is not the same for each temperature. The maximum difference occurred for

358°C where the flux measured by the thermal-tracing technique is 94.5% higher than that measured by the butterfly valve technique. Both techniques have limitations which can be considered to be responsible for the differences. In addition to the complex mixing pattern of cold tracer particles in the hot solids' flow, the velocity profile of the bulk hot solids was affected during the thermal-tracing measurements by a bend in the pipe just upstream of the test section. For the butterfly valve technique, it was not practically possible to calibrate the capacitance sensor for each test condition. Moreover, there was a single capacitance sensor at a plane that penetrated up to the center of the pipe in which the solids accumulated. The solids captured by the cyclone fall randomly into the butterfly valve test section, with no control over how the solids distributed on the top surface of the accumulated solids. It is very likely that the top surface was not flat so that the sensor was unable to fully capture the profile of solids level by measuring from one point. Manual operation of the butterfly valve and the time recording devices no doubt led to additional errors.

The thermal-tracing technique assumes a moving bed density in the test section equal to the bulk density of loose-packed solids. This is a reasonable assumption since the solids move downward by gravity inside the transfer pipe between the riser and the bubbling bed and their quantity is large enough to form a moving bed inside the pipe. In addition, it has been found during the pilot plant's operation that the bed's movement often stops when there is no aeration to help the flow of solids. This is only possible with the presence of a bed, and not if the solids were falling freely.

Another option is to estimate the voidage at thermal-tracing test section using the data obtained from a differential pressure transducer connected to the both ends of the section. This new voidage is used to

estimate the moving bed density in the test section and then this density is utilized to recalculate the solids circulation flux. Figure 3.10 compares these new fluxes with the fluxes obtained based on the butterfly valve technique at cold conditions.

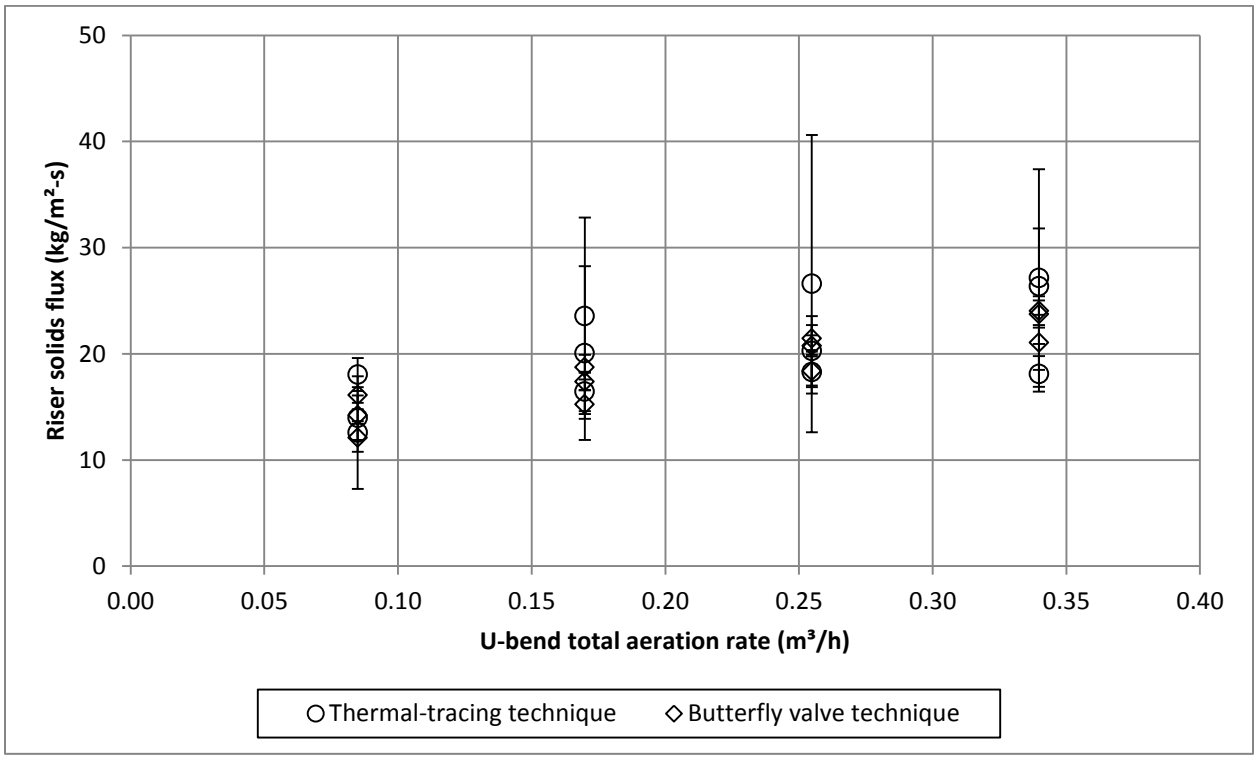

Figure 3.10: Solids circulation fluxes obtained from two techniques at room temperature with measured voidage applied to the data from the thermal-tracing technique. (Riser superficial gas velocity: 3.4 m/s.)

Although these measured values of voidage were able to reduce the difference between some of the fluxes obtained from applying the two techniques, the difference became larger for other fluxes. Overall, the differences decreased somewhat. The recalculated fluxes in the hot tests and their counterparts measured with the help of the butterfly valve are presented in Figure 3.11 as a function of riser temperature measured by a thermocouple installed near the riser's exit. No thermocouple installed

at another location in the riser provided reliable readings for all the hot tests. Hence, the temperatures of all the thermocouples were not averaged over the riser's height.

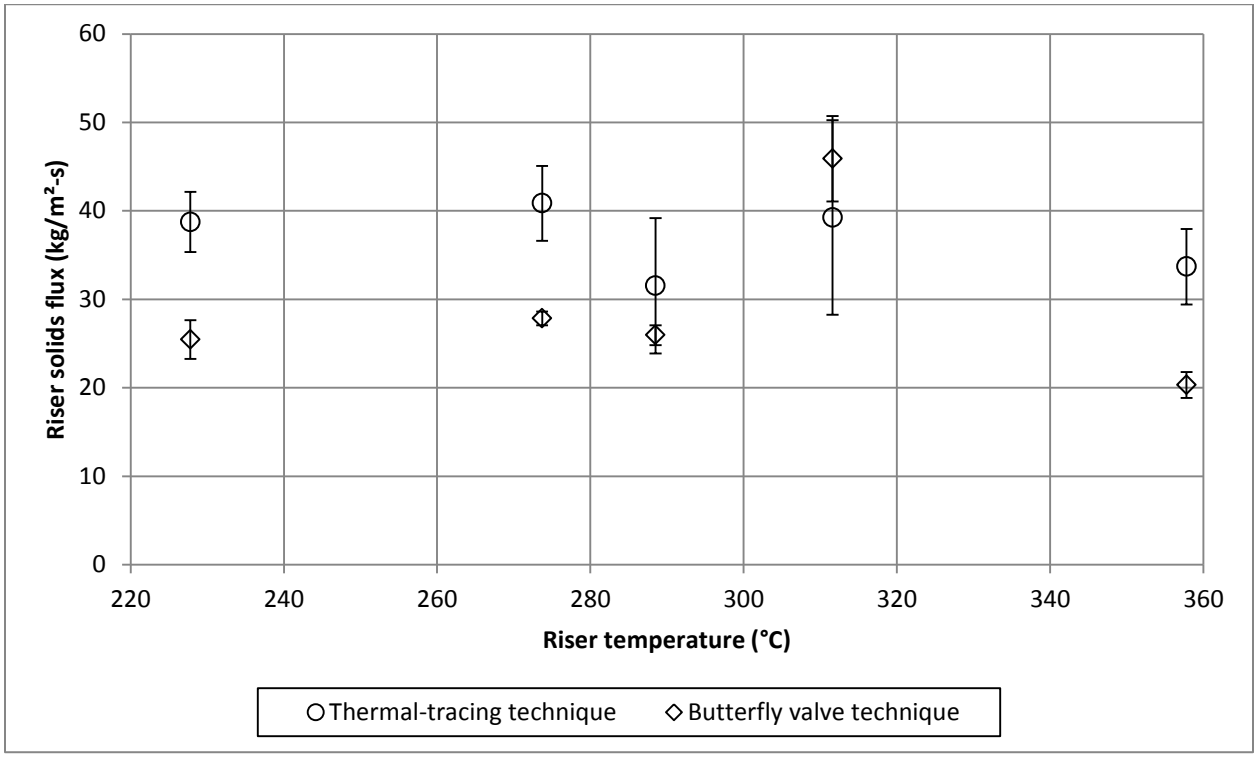

Figure 3.11: Solids circulation fluxes in hot tests with measured voidage applied to the data from the thermal-tracing technique. (U-bend aeration rate: 0.08 m^3/h; inlet flow rate of air at riser's NG burner for the test at 358°C was 12.5% lower than for the other tests.)

The measured values of voidage for the hot tests reduced the differences between the fluxes from the two techniques at all but one operating temperature of the riser. The maximum difference is found for the test at 358°C. This difference is 65.9%, whereas the difference was 94.5% before using the measured voidage. It is important to note that the voidage was measured using pressure data at both ends of the test section. The accuracy of the pressure measured at the top end was affected by the presence of a bend in the transfer pipe, causing a disturbance of the solids velocity profile. Moreover, the connection

of the pipe used for cold tracer injection was not far from this point. This injection pipe remained empty except for brief times when the tracer was injected, creating an opportunity for the pressure to differ somewhat from the top differential transducer connection. A small flow of nitrogen was used to prevent solids blockage inside the pipe. The inlet point of nitrogen was close to the bottom of the transducer. Hence, it is likely that the nitrogen flow affected the accuracy of measurement of pressure at this end.

Since no systematic investigation was carried out to determine the impacts of the bend and the nitrogen flow on the measured voidage, it was decided not to use the recalculated value of flux in the following chapters. Instead the original flux directly measured without recalculation is utilized.

When estimating the solids circulation flux between adjacent thermocouples, it was assumed that the injection of the packet of cold tracer particles momentarily upset the flow rate of the moving packed bed of hot solids at the injection point, but did not create a significant irreversible step change in the hot solids flow vs. time profile at that point, which is mostly true when the tracer flow rate is negligibly small compared to the solids flow rate in the standpipe. Therefore, it only caused a small reversible step change in the form of a pulse that disappeared very quickly, and the flow of solids returned to its pre-pulse rate, even before reaching the thermocouples in the top level of the test section. The duration over which the pulse impacted the solids flow vs. time profile (<1 s) was significantly shorter than the duration of solids travel through the thermal-tracing test section (>2 s). As a result, the solids flow rate measured by any pair of thermocouples in the test section is assumed to have remained unaffected by

injection of a packet of cold tracer particles. This situation is called 'Case 1' for ease of description in Figures 3.12 and 3.13.

Another possibility is that the duration over which the injection of the packet of cold tracer particles impacted the solids flow vs. time profile was larger than the duration of solids travel through the test section. This might happen with large pulse injection and slow damping due to the poor dispersion of cold solids. As a result, a part of the flow rate of solids measured by a pair of thermocouples in the test section was due to the passing packet of cold tracer particles. This part would have to be deducted from the measured flow rate to obtain the actual flow rate in the transfer pipe without the cold tracer particles. By assuming that the injection and spreading time of the injected cold tracer particles is in the same order as the travel time over the entire measurement section (Δt) measured by the pair of thermocouples, the solids circulation flux can be estimated by:

$$G_{s,no\ tracer}\left(\frac{kg}{m^2.s}\right) = G_{s,measured}\left(\frac{kg}{m^2.s}\right) - \frac{0.1\ (kg)}{\Delta t\ (s) \times A\ (m^2)} \tag{3.1}$$

This situation is referred to as 'Case 2'. Figure 3.12 compares the solids circulation fluxes estimated using the two cases with those obtained from using butterfly valve at room temperature tests. Each data point in this figure represents the average of three data measurements collected at the same operating condition. This is done to enhance the clarity of the figure since the location of many data points in a small space would make it difficult to see their differences. As expected, the solids circulation fluxes estimated by assuming the second case are lower and closer, compared to case 1, to the fluxes obtained

from the butterfly valve technique. The highest flux at an aeration rate was within a maximum of 41.9% higher than the lowest flux at that rate for the first case. This percentage reduced to 13.6% for case 2.

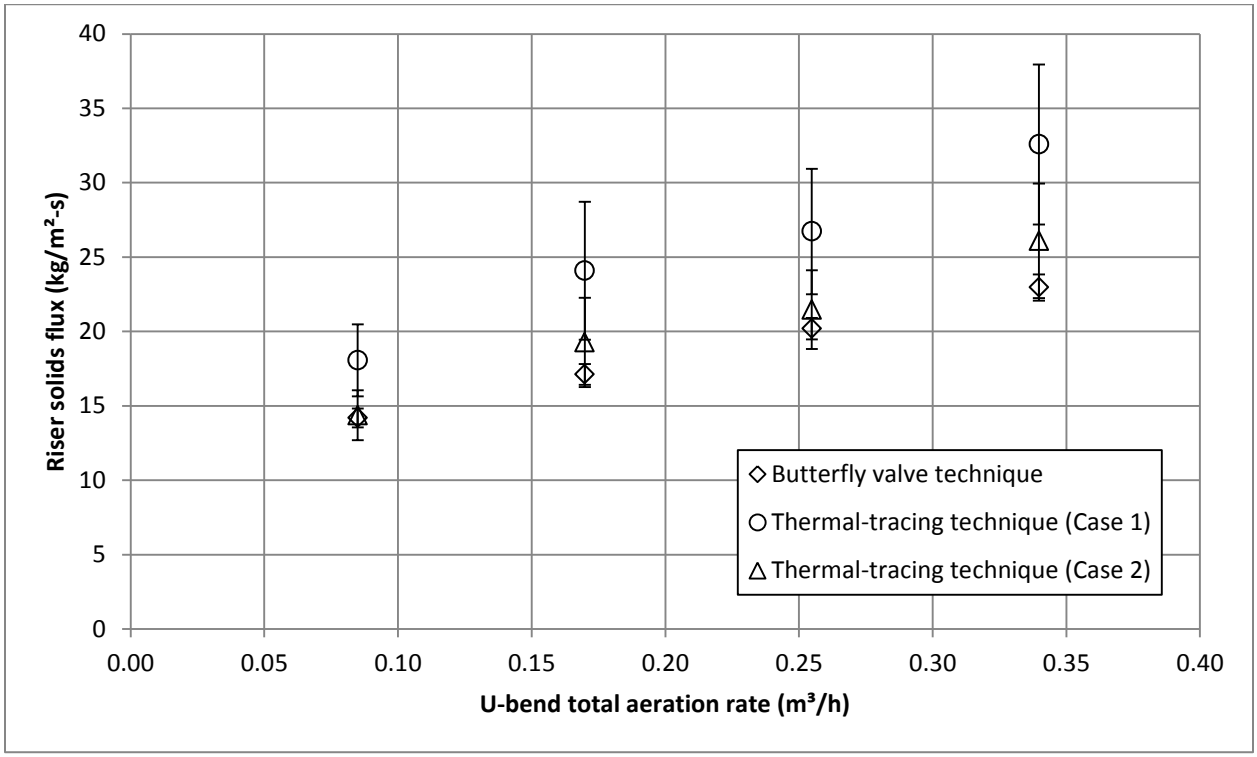

Figure 3.12: Comparison of the solids circulation fluxes obtained from using butterfly valve technique with those obtained from considering the impact of cold tracer's addition in two cases during the cold tests. (Riser superficial gas velocity: 3.4 m/s.)

The solids circulation fluxes measured by applying the thermal-tracing technique at high temperatures for the two cases are compared with the fluxes measured by the butterfly valve technique in Figure 3.13. Out of the two cases, the fluxes estimated by the second case are closer to those of the butterfly valve for all but one temperature. At this temperature, both cases led to almost the same difference with the butterfly valve data point. Whereas the highest flux at a temperature was found to be within a

maximum of 94.5% higher than the lowest flux at that temperature in the first case, the maximum value became 63.2% for the case 2.

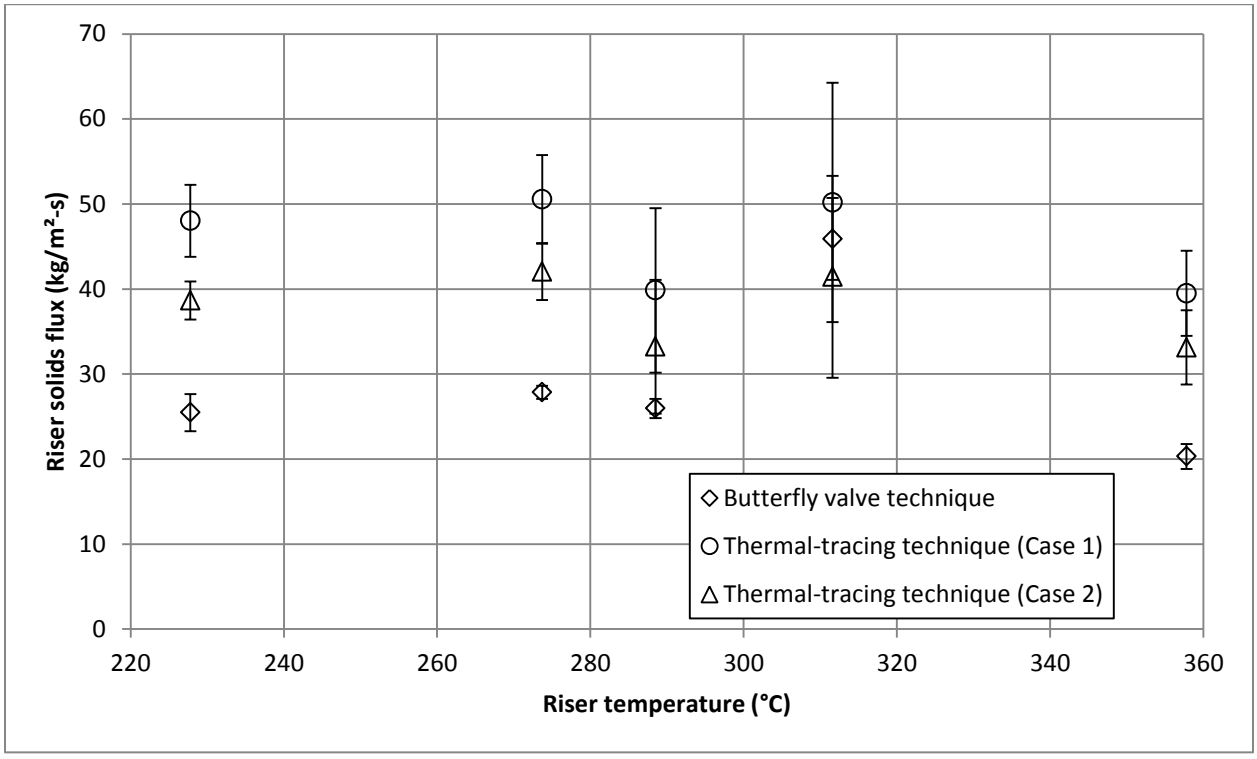

Figure 3.13: Comparison of the solids circulation fluxes obtained from butterfly valve technique with those obtained from considering the impact of cold tracer's addition in two cases during the hot tests. (U-bend aeration rate: 0.08 m3/h; inlet flow rate of air at riser's NG burner for the test at 358°C was 12.5% lower than for the other tests.)

In summary, if the cold tracer pulse was too brief to reach any pair of thermocouples in the measurement section (case 1), the values of calculated solids circulation flux from correlating two thermocouples did not require any correction. In case 2 on the other hand, if the cold tracer did not get dampened quickly, the injected tracer would influence the measurements long enough to affect every pair of thermocouples. Equation (3.1) is then needed to correct the measured solids circulation flux in the transfer line. The corrected solids circulation rate allowing for the propagation of the pulse of cold

tracer particles is shown to have improved agreement between the solids circulation fluxes measured by the thermal-tracing and the butterfly valve techniques.

The actual solids circulation rate should be bounded by Case 1, without any disturbance, and Case 2, allowing for a pulse-like increase from injected tracer particles, but it would require detailed dispersion modeling of the dispersion of injected tracer particles to ascertain the exact impact of the addition of cold tracer particles on the hot solids flow in the thermal-tracing test section. Therefore, without a proper method to correct the impact of tracer injection, the flux directly measured by assuming the first case is utilized in the following chapter.

4 Solids Circulation Rates from Pressure and Energy Balances

4.1 Background

In the two previous chapters, the development and application of a novel thermal-tracing technique and its validation at high temperature using a butterfly valve were illustrated. The operation of the entire pilot plant was necessary to conduct experiments described in those chapters. In this chapter, we make use of the pilot plant's operational data to estimate solids circulation rates and compare with the rates reported in the two previous chapters. The rates are determined in this chapter using two indirect techniques. The first of these techniques is based on a balance of pressure between the riser and the bubbling bed as the solids continuously circulate between these two vessels in a closed loop. The second technique utilizes a balance of all input and output energy streams to and from the bubbling bed reactor vessel. Whereas the pressure balance technique can be applied to both cold and hot tests, the energy balance technique is limited to hot tests only. To our knowledge, no similar work has been reported in the open literature, although it has been practised in the industry.

A number of correlations were utilized for estimating the solids circulation rate using the pressure balance and the energy balance technique. These correlations were chosen based on their popularity, i.e. their frequent use in the fluidization literature.

4.2 Pressure balance modelling

In this section, we perform a pressure balance calculation to estimate solid circulation rate in the riser and the bubbling bed. The hydrodynamic properties relevant for the process are estimated at first. Then the correlations for determining absolute pressures at the bottoms of riser and bubbling bed are given. Finally, the subtraction of one of the bottom pressures from other yields a single equation with two unknown parameters, one of which is solid circulation flux. The value of the other unknown parameter is optimized with the help of experimental findings.

4.2.1 Key assumptions

The operating conditions of the dual fluidized bed pilot plant are such that ideal-gas behaviour of real gases can be assumed, since the operating temperature is quite high, and at the same time the operating pressure is only slightly higher than the ambient pressure [51]. Therefore, the gases inside the plant are assumed to follow the ideal gas law. When natural gas enters the burner, it is mixed with an amount of air which provides more than enough oxygen to react with all the hydrocarbons in the natural gas. The internal volume of the burner allows adequate residence time of the gas mixture to ensure that the combustion reaction is completed.

The particles that escape from the riser's cyclone during the plant's operation were collected from the downstream equipment after shutting down the plant and found to be a few kilograms per hour. This is a very small amount compared to the total solids inventory of about 100 kg. The amount of particles

which escape during each solids circulation test was <1% of the total amount of solids circulating in the system.

A number of simplifying assumptions have been made throughout the estimation processes. The key assumptions are:

- All pure gases and gas mixtures obey the ideal gas law.
- Complete combustion of natural gas occurs in the presence of excess air fed to each burner.
- The number of particles not captured by the cyclones and other factors such as attrition are not significant enough to change the hydrodynamics of the system within the time frame of each test.
- All bubbles at a given cross-section (height) in the bubbling bed have the same size, so that the average diameter of the bubbles changes in the axial direction only.

4.2.2 Estimation of hydrodynamic parameters

4.2.2.1 Flow rates of air and natural gas

The circulating fluidized bed (CFB) riser and the bubbling fluidized bed (BFB) draw input air from separate streams. In each stream, the input air passes through a rotameter before entering a natural gas burner. The burner does not operate during cold tests; instead, the air merely travels through it to reach the respective fluidized bed to act as fluidizing agent. For hot tests, on the other hand, the burner is generating heat from the combustion of natural gas to raise the temperature of both fluidized beds. This

natural gas passes through another rotameter. The combustion of natural gas in the burner produces hot flue gas which fluidizes the particles downstream.

There are four rotameters in total to measure the inlet flow rates of CFB riser air, riser natural gas, BFB air and BFB natural gas. No natural gas is used in the cold tests, and therefore the two rotameters for natural gas flows are not required during cold tests. Each of the rotameters is attached to a pressure gauge.

The ambient temperature and pressure, 20°C and 101.3 kPa, are used as base conditions for all calculations. The typical composition of natural gas is 95% methane, 3% other alkanes such as ethane, propane, butane and pentane and 2% nitrogen [52]. Since the amount other alkanes in total are very small compared to that of methane, they are lumped together with methane for the ease of calculation. Therefore, natural gas is considered to contain 98% methane and 2% nitrogen. The standard correlations to convert a rotameter reading to actual flow rate are given in Appendix E.

4.2.2.2 Superficial gas velocity for cold and hot tests

Ideal gas law is used to convert an actual flow rate of air at base condition to its equivalent flow rate at the riser's operating condition for the cold tests. This is straightforward since no natural gas was used. However, in a hot test, the natural gas undergoes complete combustion in the presence of excess air in the burner and flue gas is produced in the process.

$$CH_4 + 2O_2 \rightarrow CO_2 + 2H_2O \quad (4.1)$$

The molar flow rate of each constituent gas in the input air and natural gas is estimated. Then atomic balances are performed across the burner to calculate the molar flow rate of each constituent gas in the output flue gas. This molar flow rate is converted to volumetric flow rate at the riser's operating condition. The summation of the volumetric flow rate of each constituent gas provides the total volumetric flow rate in the riser from which the superficial gas velocity is calculated.

The superficial gas velocities in the bubbling bed for cold and hot tests are estimated in the same way.

4.2.2.3 Density and viscosity of gas mixture

The density of gas mixture in the riser and bubbling bed is calculated from

$$\rho_{mix} = \sum_{i=1}^{n} x_i . MW_i \quad (4.2)$$

where x_i is the mole fraction of a component i in the mixture and MW_i is its molecular weight.

Kaushal et al. [40] estimated the viscosity of a pure gas (unit: Pa-s) as a function of temperature using

$$\mu_i = (a_1 T^3 + a_2 T^2 + a_3 T + a_4) \times 10^{-6} \quad (4.3)$$

The values of the coefficients (a_1, a_2, a_3 and a_4) are reported in Appendix F.

Equation (4.4), developed by Wilke [41], gives the viscosity of a mixture of pure gases.

$$\mu_{mix} = \sum_{i=1}^{n} \frac{x_i . \mu_i}{\sum_{j=1}^{N} x_i . \phi_{ij}} \tag{4.4}$$

where,

$$\phi_{ij} = \frac{\left[1 + \left(\mu_i/\mu_j\right)^{1/2} \left(MW_j/MW_i\right)^{1/4}\right]^2}{\left[8\left(1 + MW_i/MW_j\right)\right]^{1/2}}$$

4.2.2.4 Particle terminal velocity in riser

First, a drag coefficient is assumed. Then, terminal velocity and Reynolds number are calculated from

$$U_t = \left[\frac{4}{3} . \frac{g d_p}{C_D} . \frac{\rho_p - \rho_{mix}}{\rho_{mix}}\right]^{1/2} \tag{4.5}$$

$$Re_t = \frac{d_p U_t \rho_{mix}}{\mu_{mix}} \tag{4.6}$$

Clift et al. [53] recommended drag correlations as a function of Reynolds number. These correlations are used to obtain a drag coefficient which is compared with the assumed one. If these two coefficients differ, a new drag coefficient is assumed and the entire process is repeated until the difference reduces to 0.001.

4.2.2.5 Bed voidage in riser

The saturation carrying capacity of gas mixture (G_s^*) is estimated using the correlation reported by Bai et al. [54]:

$$\frac{G_s^* d_p}{\mu_{mix}} = 0.125 \left(\frac{U}{\sqrt{g d_p}}\right)^{1.85} Ar^{0.63} \left(\frac{\rho_p - \rho_{mix}}{\rho_{mix}}\right)^{-0.44} \tag{4.7}$$

where,

$$Ar = \frac{(\rho_p - \rho_{mix})\rho_{mix} g d_p^3}{\mu_{mix}^2} \tag{4.8}$$

Bi and Zhu [55] approximated saturation voidage far ahead of riser's exit using:

$$\varepsilon^* = 1 - \frac{G_s^*}{\rho_p (U - U_t)} \tag{4.9}$$

The empirical correlation reported by Bai et al. [54] is utilized to estimate voidage at the bottom (ε_d) and the top exit (ε_e) of the riser.

$$\frac{1 - \varepsilon_d}{1 - \varepsilon^*} = 1 + 0.00614 \left(\frac{U \rho_p}{G_s}\right)^{-0.23} \left(\frac{\rho_p - \rho_{mix}}{\rho_{mix}}\right)^{1.21} \left(\frac{U}{\sqrt{g D_{Riser}}}\right)^{-0.383} for\ G_s > G_s^* \tag{4.10}$$

$$\frac{1-\varepsilon_d}{1-\varepsilon^*} = 1 + 0.103\left(\frac{U\rho_p}{G_s}\right)^{1.13}\left(\frac{\rho_p - \rho_{mix}}{\rho_{mix}}\right)^{-0.013} \; for\; G_s \leq G_s^*$$

$$\frac{1-\varepsilon_e}{1-\varepsilon^*} = 4.04(1-\varepsilon^*)^{0.214} \tag{4.11}$$

The one-dimensional entrainment model of Kunii and Levenspiel [56] is adopted to estimate the average voidage (ε) in the riser:

$$(1-\varepsilon) = (1-\varepsilon_d) + \frac{1}{aH_{Riser}}\left[(\varepsilon_e - \varepsilon_d) - (\varepsilon^* - \varepsilon_d)ln\left(\frac{\varepsilon^* - \varepsilon_d}{\varepsilon^* - \varepsilon_e}\right)\right] \tag{4.12}$$

Here, 'a' is a decay constant whose value can vary from 0.3 to 2.5 according to Kunii and Levenspiel [57]. In this thesis, an optimum value of decay constant is used. The optimization process is described in Section 4.2.3.2.

4.2.2.6 Expanded bed height and voidage in bubbling bed

The Grace [45] correlation is used to estimate the minimum fluidization velocity of the particles:

$$Re_{mf} = \sqrt{C_1^2 + C_2 Ar} - C_1 \tag{4.13}$$

where,

$$Re_{mf} = \frac{d_p U_{mf} \rho_{mix}}{\mu_{mix}} \tag{4.14}$$

and C_1 and C_2 are taken as 27.2 and 0.0408, respectively.

The minimum fluidization voidage for the particles is considered as 0.45.

Initially, a height is assumed for the expanded bed. A representative height at which the calculation of hydrodynamic parameters needs to be performed is set at 40% of the expanded bed height. The average diameter of bubbles at the representative height is estimated by the correlation developed by Darton et al. [58].

$$d_b = 0.54\left(U - U_{mf}\right)\left[z_{Rep} + 4\sqrt{\frac{A_{BFB}}{N_{or}}}\right]^{0.8} g^{-0.2} \tag{4.15}$$

N_{or}, the number of orifices in the distributor plate in the case under study is 72.

Davidson and Harrison [59] developed a correlation for calculating the average bubble velocity that considers the velocity of an isolated bubble, as well as a term accounting for bubble interactions:

$$U_b = 0.71\sqrt{g d_b} + \left(U - U_{mf}\right) \tag{4.16}$$

The bed fraction occupied by bubbles is estimated from

$$\varepsilon_b = \frac{\left(U - U_{mf}\right)}{U_b} \tag{4.17}$$

Finally, the expanded bed voidage and pressure drop (in Pa) are estimated by

$$\varepsilon = \varepsilon_b + (1 - \varepsilon_b)\varepsilon_{mf} \tag{4.18}$$

$$\Delta P = \left(\rho_p - \rho_{mix}\right)(1 - \varepsilon)gH_{bed} \tag{4.19}$$

The pressure drop across the bubbling bed is continuously measured by a differential pressure transducer. If the estimated pressure drop differs from the measured one, then a new height of the expanded bed is assumed and all the subsequent calculations are repeated until the estimated pressure drop is within 0.1% of the measured pressure drop. The corresponding expanded bed height and bed voidage are then taken.

4.2.3 Solid circulation flux from pressure balance

4.2.3.1 Balance of pressure between riser and bubbling bed

The absolute pressures at the bottoms of riser and bubbling bed can be determined using

$$P_{Riser} = \left[\rho_p(1 - \varepsilon)gH + \rho_{mix}\,\varepsilon gH + \Delta P_{acc} + \Delta P_{fg} + \Delta P_{fp} + \Delta P_{cyc}\right]_{Riser} \tag{4.20}$$

$$P_{BFB} = \left[\rho_p(1-\varepsilon)gH + \rho_{mix}\,\varepsilon gH + \Delta P_{acc} + \Delta P_{fg} - \Delta P_{fp} + \Delta P_{cyc}\right]_{BFB} \quad (4.21)$$

It is important to note that the height, H, of BFB in Equation (4.21) denotes the height of the expanded bed in it, whereas the height of riser in Equation (4.20) is its physical height. In both of these equations, the first term in the right side makes the largest contribution as it represents the pressure drop in the vessel due to the presence of particles. The second term is for the pressure drop due to gas flow. The low density of gas mixture causes the contribution of this term to be insignificant. The other terms represent pressure drops due to particle acceleration, wall friction from both gas and particles and the pressure drop across the cyclone. At high gas velocities and high solid circulation rates, the frictional effects can become significant.

The particles acceleration term can be neglected at solids low circulation rates; but it should be considered at high circulation fluxes. Particles can be considered to accelerate from zero velocity at the entrance to the fully developed velocity at the exit. As a first approximation, Bi and Zhu [55] estimated the pressure drop by

$$\Delta P_{acc} = \frac{G_s^2 \rho_p}{2} \quad (4.22)$$

The pressure drop due to gas-wall friction is estimated by the Fanning equation

$$\Delta P_{fg} = 2 f_g \varepsilon \rho_{mix} U^2 \frac{H}{D} \tag{4.23}$$

where, the friction coefficient, is given by

$$f_g = \begin{cases} \dfrac{16}{Re} & for\ Re \leq 2300 \\ \dfrac{0.079}{Re^{0.313}} & for\ Re > 2300 \end{cases} \tag{4.24}$$

The empirical correlation developed by Kono and Saito [60] is utilized to estimate the pressure drop due to particle-wall friction:

$$\Delta P_{fp} = 2 f_p \frac{H}{D} . \frac{G_s^2}{\rho_p (1-\varepsilon)} \tag{4.25}$$

where, the friction coefficient, f_p is given by

$$f_p = \frac{0.0285 \sqrt{gD}}{\dfrac{G_s}{\rho_p (1-\varepsilon)}} \tag{4.26}$$

Note the negative sign placed before this term in Equation (4.21) as there is a net downward movement of particles at the walls of a bubbling bed.

According to Rhodes and Geldart [61], the pressure drop across a typical cyclone attached to a fluidized bed can be approximated by

$$\Delta P_c = \frac{1}{2}\xi \rho_{mix} U^2 \tag{4.27}$$

with, the friction coefficient, ξ taken as 50.

When calculating the pressure drops due to particle acceleration and particle-wall friction in the bubbling bed, the net solid circulation flux across the bubbling bed ($G_{s,BFB}$) is replaced by the flux in riser ($G_{s,Riser}$) according to

$$G_{s,Riser} A_{Riser} = G_{s,BFB} A_{BFB} \tag{4.28}$$

Subtraction of Equation (4.21) from Equation (4.20) yields

$$\begin{aligned} P_{Riser} - P_{BFB} = &\left[\rho_p(1-\varepsilon)gH + \rho_{mix}\,\varepsilon gH + \Delta P_{acc} + \Delta P_{fg} + \Delta P_{fp} + \Delta P_{cyc}\right]_{Riser} \\ &- \left[\rho_p(1-\varepsilon)gH + \rho_{mix}\,\varepsilon gH + \Delta P_{acc} + \Delta P_{fg} - \Delta P_{fp} + \Delta P_{cyc}\right]_{BFB} \end{aligned} \tag{4.29}$$

Direct measurement of pressure at the bottoms of riser and bubbling bed produce the value for the left side of Equation (4.29). The deposition of fine particles that escape from each of these two vessels on the corresponding filter bags during a single test is small. There are twelve filter bags installed at a baghouse in the downstream of each vessel. The desired gauge pressure in the downstream of each

vessel up to the baghouse is zero. However, the deposition of fine particles over a long period of plant's operation causes this gauge pressure to increase significantly (e.g. 2-3 kPa). This pressure acts as a back pressure on the operating pressure of the corresponding vessel. Then, a part of the bottom pressure measured by a transducer comes from the undesired pressure build up in the downstream. Hence, the downstream pressure is deducted from the measured one to obtain a bottom pressure which discounts the contribution of escaped particles. These final values are used in Equation (4.29).

After the substitutions of Equations (4.22) to (4.28) into Equation (4.29), there remain two unknowns: the solid circulation flux in the riser ($G_{s,Riser}$) and the decay constant (a). The decay constant appears in Equation (4.12) and appropriate value of this constant need to be assigned in order to determine the solid circulation flux.

4.2.3.2 Optimization of decay constant

The decay constant (a) used in Equation (4.12) represents the change is voidage with height in the entrainment region of the riser. The dense region at the bottom of riser is considered to have a uniform voidage (ε_d) which can be estimated using Equation (4.10). On the other end, the exit region of riser can be assigned another uniform voidage (ε_e) which is calculated using Equation (4.11). The entrainment region is situated between these two regions and it is here the voidage experiences an exponential decay from ε_d to ε_e across H_e (the length of the region):

$$\frac{\varepsilon^* - \varepsilon_e}{\varepsilon^* - \varepsilon_d} = e^{-aH_e} \tag{4.30}$$

Kunii and Levenspiel [57] compiled a wide range of experimental data reported in the literature for high-velocity fluidized beds and found that the decay constant can assume values between 0.3 and 2.5. They did not work out any correlation for the estimation of this constant. Later, Bi and Zhu [55] found a value of a=0.5 to be reasonable to utilize in their model which they validated against the experimental data obtained from using two kinds of Geldart A particles and one kind of Geldart B particles.

In this work, it was decided to find an optimum value of decay constant that works for both hot and cold tests. For each of the 17 tests, a range of values of the decay constant was considered. The decay constant is needed to estimate the average voidage in the riser using Equation (4.12) which is then used in Equation (4.29) to estimate the solids circulation flux. This way a solids circulation flux in the riser is obtained by using each of the values of decay constant in the range considered. The root-mean-square (RMS) deviation of estimated fluxes from their corresponding fluxes measured by applying thermal-tracing technique is calculated for each value of the decay constant. Equation (4.31) presents the formula utilized here with n=17 (i.e. 17 data points from the experiments). The constant which gives the minimum value of the RMS deviation is selected as the optimum value of a, which is equal to 0.67.

$$RMS\ deviation = \sqrt{\frac{\sum_{i=1}^{n}\left(G_{s,measured,i} - G_{s,estimated,i}\right)^2}{n}} \tag{4.31}$$

4.3 Energy balance modelling

In this section, I perform an energy balance calculation over the bubbling bed reactor to estimate the net flow rate of solid passing through it. The heat transfer parameters are estimated at first. Then, heat loss through reactor wall and insulation is calculated. Finally, an equation that includes each input and output energy streams is solved to obtain the solid circulation rate in the system.

4.3.1 Key assumptions

There was neither any effort to remove heat from the outer surface of the bubbling bed reactor vessel nor any attempt to maintain the surface of the vessel at a particular temperature. The operating team accepted that some heat would be lost and planned accordingly. Inside the vessel, the temperature was not uniform over the surface. However, the axial temperature gradient in the dense bed was found to be negligible. In the freeboard, the temperature was measured at a single point. There was a difference between the average temperature of the dense bed and the freeboard temperature. The resulting heat transfer from the dense bed to the freeboard was not determined as this would be negligible compared to the total heat loss from inside the vessel in the radial direction through the walls and then by natural convection to the ambient atmosphere.

The bubbles in the bed cause rapid and extensive vertical mixing of particles in bubbling fluidized beds. Because of the high bed-to-surface heat transfer coefficient expected in the bubbling bed, the resistance to heat transfer from the interior of the bubbling bed to the inner wall of the vessel was extremely low compared to that from the inner wall to the ambient air by natural convection.

The combustion of natural gas in the burner produces flue gas which comes in contact with a small amount of nitrogen gas while passing through the circulating fluidized bed or bubbling fluidized bed reactor vessels. Because of the inert nature of nitrogen, it is assumed to participate in no reactions affecting the flue gas composition.

Several simplifying assumptions have been adopted:

- Ambient air is free to circulate around the bubbling bed reactor vessel. Heat is lost in two modes from the vessel's outer walls: natural convection and radiation. No heat is lost from the outer surfaces due to forced convection of air.
- Heat loss occurs from inside the BFB vessel through the reactor wall and insulation to the ambient atmosphere in the radial direction only.
- The resistance to heat transfer from the interior of bubbling bed to the inner wall is negligible compared to the resistance between the inner and the outer walls. This is also applicable for the pipes that connect BFB vessel with NG burner.
- The composition of flue gas generated in each NG burner does not alter when passing through its downstream vessel i.e. riser or bubbling bed.
- In the bubbling bed reactor vessel, there is no axial temperature gradient in the dense bed nor in the freeboard. However, the representative temperatures of the dense bed and freeboard differ from one another.

4.3.2 Estimation of heat transfer parameters

4.3.2.1 Heat capacity and thermal conductivity of gas and solid particles

The heat capacity (unit: kJ/mol-K) of a pure gas or even a gas mixture such as air is commonly reported as a function of temperature in the form of

$$C_p = b_1 + b_2 T + b_3 T^2 + b_4 T^3 \tag{4.32}$$

The values of the coefficients for the relevant gases of interest in this thesis appear in Appendix F.

The heat capacity of bed material (sand) does not vary significantly with temperature and therefore is taken as 0.8 kJ/mol-K for all calculations.

Kadoya et al. [43] developed a method for the calculation of thermal conductivity, k, of dry air at any temperature, writing

$$k(T_r, \rho_r) = \Lambda[k'(T_r) + \Delta k(\rho_r)] \tag{4.33}$$

$$k'(T_r) = m_1 T_r + m_2 T_r^{0.5} + m_3 T_r^0 + m_4 T_r^{-1} + m_5 T_r^{-2} + m_6 T_r^{-3} + m_7 T_r^{-4} \tag{4.34}$$

$$\Delta k(\rho_r) = n_1 \rho_r + n_2 \rho_r^2 + n_3 \rho_r^3 + n_4 \rho_r^4 + n_5 \rho_r^5 \tag{4.35}$$

$$T_r = \frac{T}{132.5}, \rho_r = \frac{\rho}{314.3} \; and \; \Lambda = 25.9778 \times 10^{-3} \frac{W}{m.K} \tag{4.36}$$

The values of the coefficients (m_i and n_i) are reported in Appendix F.

4.3.2.2 Natural convection heat transfer coefficient at the outer wall of BFB

The density, viscosity, heat capacity and thermal conductivity of the thin layer of air next to the outer wall of the column are determined at the film temperature which is an average of the temperatures of ambient air and the outer wall.

First, the Rayleigh number is obtained from Prandtl and the Grashhof numbers:

$$Ra = Pr.Gr = \frac{\mu_{air} C_{p,air}}{k_{air}} . \frac{g\beta\left(T_{surface} - T_{ambient}\right)L_c^3}{\nu_{air}^2} \tag{4.37}$$

where, volume expansion coefficient, $\beta = 1/T_{film}$.

Cengel [46] gathered empirical correlations for calculating the average Nusselt number for natural convection over surfaces of different shapes and orientations. They give the following criterion for treating a vertical cylinder as a vertical plate:

$$D \geq \frac{35 L_c}{Gr^{1/4}} \tag{4.38}$$

where, D = cylinder diameter and L_c is the characteristic length.

The correlations for Nusselt number for a vertical flat plate, horizontal plate with hot bottom surface and horizontal cylinder are provided, respectively, by

$$Nu = \left\{0.825 + \frac{0.387Ra^{1/6}}{[1 + (0.492/Pr)^{9/16}]^{8/27}}\right\}^2 \quad (4.39)$$

$$Nu = 0.27Ra^{1/4}, for\ Ra: 10^5 - 10^{11} \quad (4.40)$$

$$Nu = \left\{0.6 + \frac{0.387Ra^{1/6}}{[1 + (0.559/Pr)^{9/16}]^{8/27}}\right\}^2 for\ Ra \leq 10^{12} \quad (4.41)$$

Note that the Nusselt number is defined by

$$Nu = \frac{h_{nc}L_c}{k_{air}} \quad (4.42)$$

where h_{nc} is the natural convection heat transfer coefficient.

4.3.2.3 Radiation heat transfer coefficient at outer wall of BFB

The heat transfer to the ambient air due to radiation from this surface is then estimated

$$Q_{rad} = h_{rad} A_{surface} \left(T_{\infty} - T_{surafce}\right) = \epsilon_{surface} \sigma A_{surface} \left(T_{surface}^4 - T_{\infty}^4\right) \quad (4.43)$$

where, the Stefan–Boltzmann constant, σ = 5.67 × 10−8 W/m^2-K^4 and $\epsilon_{surface}$ is the emissivity of the outer surface of the reactor. The outer surface of the bubbling bed reactor is quite dark because of being oxidized in ambient atmosphere over many years of use and hence its emissivity is taken as 0.9.

4.3.3 Heat loss from bubbling bed reactor system

4.3.3.1 Geometry of the system

Thermal energy is lost from the interior of bubbling bed to the ambient air through layers of insulation and the metal frame of the vessel. Neither the thickness nor the number of layers of insulation is uniform across the vessel. In addition, the temperature difference between the dense bed and the freeboard region inside the vessel is significant. Therefore the vessel is divided into five sections and heat transfer calculations are performed for each of them.

The hot flue gas generated from combustion of natural gas at the burner enters the BFB vessel through the windbox. Heat transfer process at that point is complex as the U-bend passes through the centre of the windbox. Therefore, it was decided to consider the flue gas at the burner exit as the inlet gas to the system, with heat losses from the pipe sections between the burner and windbox also estimated.

Table 4.1 lists all the sections in the system and shows each section's characteristic dimension (length in all but one case), inner wall radius and the thicknesses of construction and insulation materials. Figure 4.1 is used to identify the sections in the system.

Only the top plate has a diameter as its characteristic dimension. The bottom cylindrical part contains the dense region of the bubbling bed. The height of the expanded bed is selected as its characteristic length. The remaining height of this section is lumped with that of the top conical section. For each of the two conical sections, the average of the radii at both ends of the cone is taken to simplify the calculation. An F-shaped pipe section, an expansion bellow and two reducers are installed to connect NG burner to BFB windbox. There are two smaller expansion bellows in the F-section. However, their common diameter is almost similar to the pipe diameter in the section. Hence, these two bellows are taken as ordinary pipes. For ease of calculation, the F-shaped section is considered as a straight pipe with a length equal to the combined length of all the parts in the section. Although physically separated by a bellow, the two reducers are merged together to create a single one and its average diameter is calculated following the way used for BFB conical sections. The average diameter is found to be almost same as that of the bellow. Then the expansion bellow and the two reducers are lumped together to obtain a single diameter and a single length for this assembly. Note that orientations of all BFB sections are vertical except the top plate which is horizontal, whereas the orientations of F-section, reducers and bellows are horizontal except for a very small length of F-section which is vertical.

Table 4.1: BFB sections and their dimensions.

Section	Charac-teristic length	Radius of inner wall	Thicknesses of construction and insulation materials from inside wall to outside wall surface				
			60% alumina brick	Board insulator	Carbon steel	Stainless steel 310	Mineral wool
Top plate	N/A, Diameter: 914.4 mm (36”)	N/A	101.6 mm (4”)	-	9.5 mm (0.375”)	-	-
Top cylinder	762 mm (30”)	346.1 mm (13.625”)					
Top cone	1676.4 mm – expanded bed height	252.4 mm (9.9375”)					
Bottom cylinder	Expanded bed height	152.4 mm (6”)	92.1 mm (3.625”)	25.4mm (1”)	9.5 mm (0.375”)	-	-
Bottom cone	209.6 mm (8.25”)	93.7 mm (3.6875”)	127 mm (5”)	-	9.5 mm (0.375”)	-	-
Windbox	38.1 mm (1.5”)	160.3 mm (6.3125”)	-	-	4.8 mm (0.1875”)	-	114.3 mm (4.5”)
Connecting pipe F-section	1695.9 mm (66.375”)	20.4 mm (0.805”)	-	-	-	3.7 mm (0.145”)	76.2 mm (3”)
Connecting pipe reducers & bellows	460.4 mm (18.125”)	40.8 mm (1.605”)	-	-	-	3.7 mm (0.145”)	88.9 mm (3.5”)

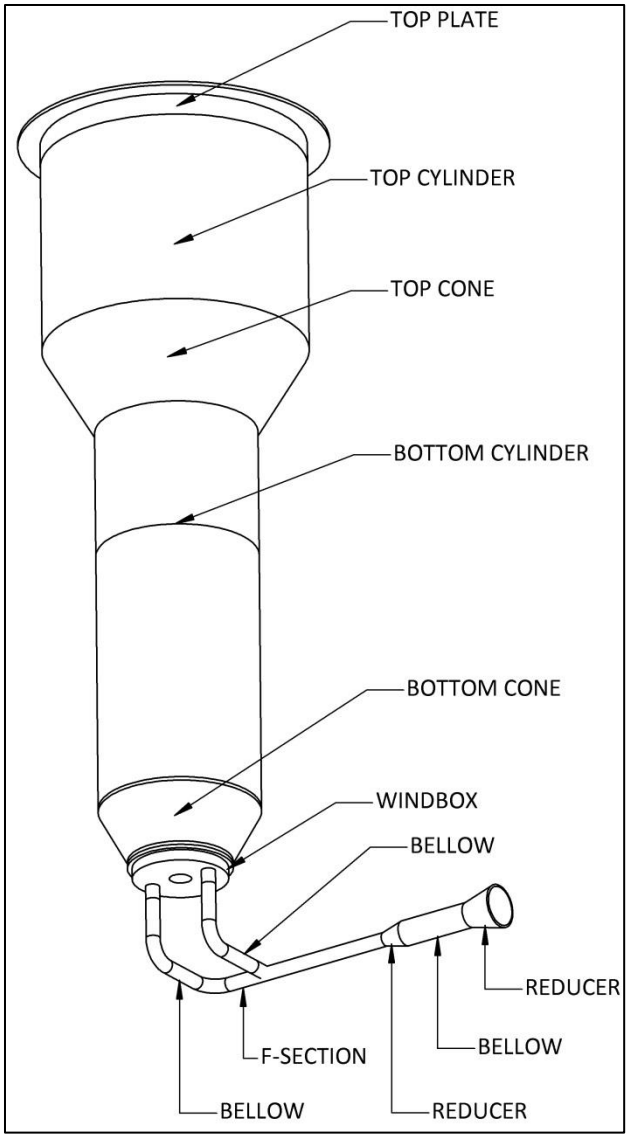

Figure 4.1: Simplified sketch of BFB sections. (Connecting flanges, measurement ports, and inlets and outlets of gas mixtures or solids are not shown.)

4.3.3.2 Thermal resistance network

The temperature inside any section of the system is much higher that the ambient temperature. This difference in temperature creates a driving force for heat loss from every section of the system. However, heat transfer meets resistance during:

- Convection and radiation from the interior of bubbling bed to the inner wall,
- Conduction through the layers of insulations and metals, and
- Convection and radiation from the outer wall through the ambient air.

The resistance to heat transfer from the interior of bubbling bed to the inner wall is ignored. The heat transfers from the outer wall by convection and radiation through air occur in parallel so that

$$\frac{1}{R_{nc+rad}} = \frac{1}{R_{nc}} + \frac{1}{R_{rad}} = \frac{1}{1/h_{nc}A} + \frac{1}{1/h_{rad}A} \tag{4.44}$$

The resistance to heat transfer during conduction through a multilayer assembly of insulation and metal is given by

$$R_{cond} = \begin{Bmatrix} \sum_{i=1}^{n} \frac{ln\frac{r_i}{r_{i-1}}}{2\pi L k_i} & for\ vertical\ cylinders \\ \sum_{i=1}^{m} \frac{\Delta L_i}{k_i A} & for\ horozontal\ plates \end{Bmatrix} \tag{4.45}$$

where, 'r_i' and 'r_{i-1}' are the outside and inside radii of a cylindrical layer, respectively, and ΔL is the thickness of a flat layer.

4.3.3.3 Heat loss from a section

The equivalent (convection and radiation at the outer wall) resistance and the conduction resistance are in series. The heat loss from a section is calculated using

$$Q_{loss} = \frac{T_{inside} - T_{ambient}}{R_{nc+rad} + R_{cond}} \tag{4.46}$$

Because of steady-state, the amount of heat energy that passes through air is the same as the heat loss. We estimate the temperature of the outer wall of a section:

$$Q_{loss} = \frac{T_{surface} - T_{ambient}}{R_{nc+rad}} \tag{4.47}$$

An iterative process is employed to conduct the calculation of heat loss. At first, an arbitrary temperature is assumed for the outer surface of the assembly of insulations and metal. Then, Equations (4.37) to (4.47) are used to calculate the temperature of this surface. The iteration stops when the difference between the assumed and the estimated temperatures reduces to 0.001. The corresponding value of heat loss is taken for subsequent calculations.

4.3.4 Solid circulation flux from energy balance

It is possible to determine the solids circulation rate through the bubbling bed reactor from the change in temperature of the solids and an energy balance, assuming steady state conditions. This method does not work for cold tests because the solids do not change their temperature. An energy balance at steady state over the bubbling bed leads to

$$\dot{m}_{solids} = \frac{Q_{flue,in} - Q_{flue,out} - Q_{purge} - Q_{loss}}{C_{p,solids}\left(T_{solids,in} - T_{solids,out}\right)} \tag{4.48}$$

The thermal energy contents of the inlet and outlet flue gas are estimated at the entrance of the connecting pipe (of NG burner and BFB) and at BFB exit, respectively. A small flow of nitrogen (5 litres/min) is continuously injected into the bubbling bed reactor vessel through the biomass feeding port to prevent solids entry into the feed hopper. A portion of the thermal energy input to the bubbling bed is used to raise the temperature of the purge nitrogen from the ambient temperature to the bubbling bed's temperature. Each of these three thermal energies is calculated with the use of

$$Q = \sum_{i} \dot{m}_i C_{p,i} (T - T_{ambient}) \tag{4.49}$$

where, 'i' is the constituent gas in the mixture.

The addition of heat loss from each section of Table 4.1 gives the total loss of thermal energy from the BFB vessel and preceding pipe connections through their walls. The denominator of the right side of

Equation (4.48) comes from the use of Equation (4.49) to account the thermal energies of incoming and outgoing solids.

Because of the steady-state operation of the dual fluidized bed system, the flow rates of solids through the bubbling bed and the riser are equal to each other. Hence the solids circulation flux can be estimated based on the cross-sectional area of riser for direct comparison with fluxes obtained from other methods:

$$G_s = \frac{\dot{m}_{solids}}{A_{Riser}} \tag{4.50}$$

4.4 Results and discussion

The solid circulation rates based on the thermal-tracing and butterfly valve techniques presented in the previous chapter, are compared with corresponding rates estimated using the indirect technique(s) described in this chapter. As mentioned earlier, the energy balance technique is not applicable during cold operation of the plant. However, every attempt to apply this technique during a hot run was successful. The pressure balance technique was successful in estimating the solids circulation rates during all cold and hot runs. Similarly, the butterfly valve technique's success rate was 100% for both hot and cold runs. In comparison, the thermal-tracing technique's success rate was 68%, considering both hot and cold tests, i.e. 68% of the data generated by injecting cold tracer particles during these tests were able to satisfy the criteria developed to filter out unjustifiable data.

The error bars shown in the figures of this chapter reflect 90% confidence interval of the reported data. The error bars are applied to those solid circulation rates which are directly measured. Figure 4.2 shows the fluxes obtained in the cold tests with the application of two direct measurement techniques and an indirect technique at four different aeration rates in the U-bend located between the bubbling bed and the riser. All other operating parameters including volumetric flow rates of air into the bubbling bed and the riser were not changed during the cold experiments.

In general, the fluxes based on pressure balance technique are found to be closer to those resulting from the butterfly valve technique than to the fluxes of thermal-tracing technique. Most of the fluxes estimated by the pressure balance technique are in good agreement with those measured by the thermal-tracing technique. However, some fluxes show minor deviations, especially at higher aeration rates. It should be noted that none of the techniques is devoid of source of error.

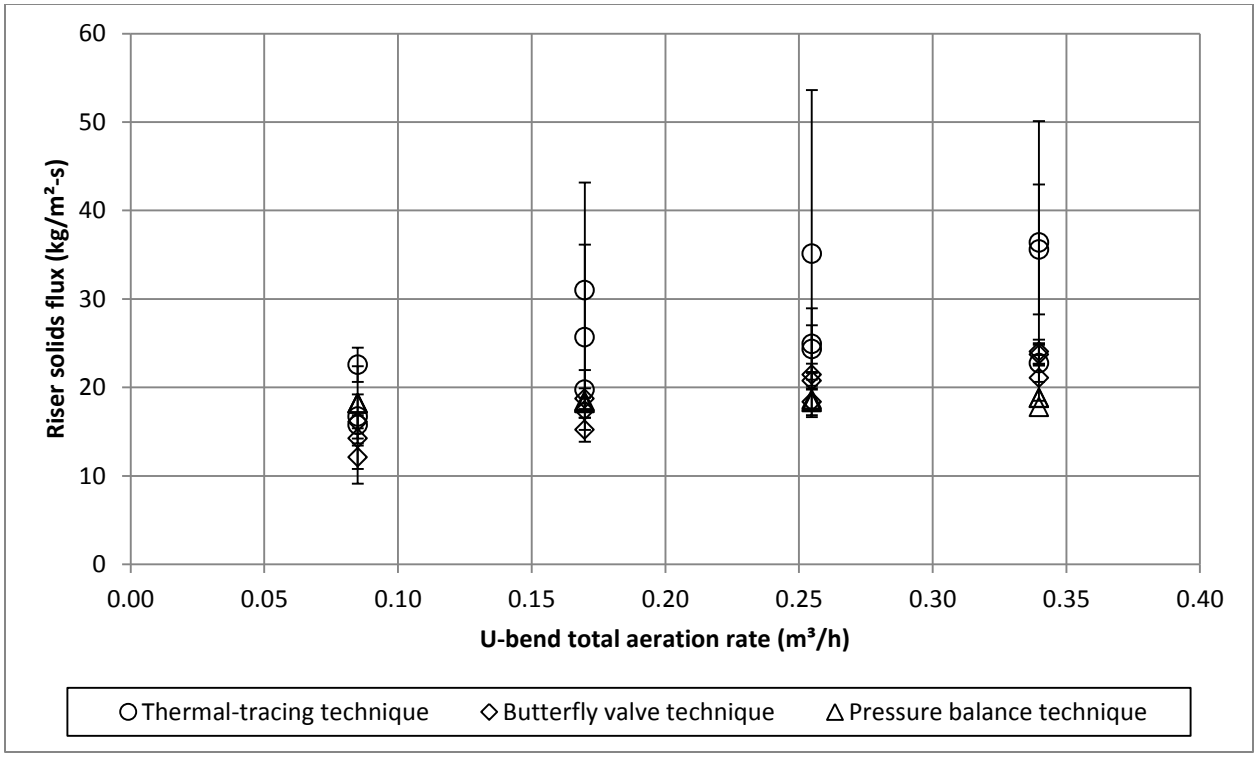

Figure 4.2: Comparison of solid circulation fluxes in the cold tests estimated at different aeration rates in the U-bend using 3 independent techniques with a constant superficial gas velocity of 3.4 m/s in the riser.

Figure 4.2 does not reveal any strong correlation between changes in the aeration rate at the U-bend and the solids circulation flux. The aeration at the U-bend facilitates the flow of solids from bubbling bed to the riser. A more important parameter is the difference in pressure between the bottoms of the bubbling bed and the riser which provide the driving force for solids leaving the bubbling bed to flow to the riser through the U-bend. Figure 4.3 presents the cold test results at constant superficial gas velocity in the riser with the pressure difference plotted on the horizontal axis. This figure does not suggest any significant impact of the change of pressure difference on the solids circulation flux. This may be because the range of pressure difference in these tests was narrow.

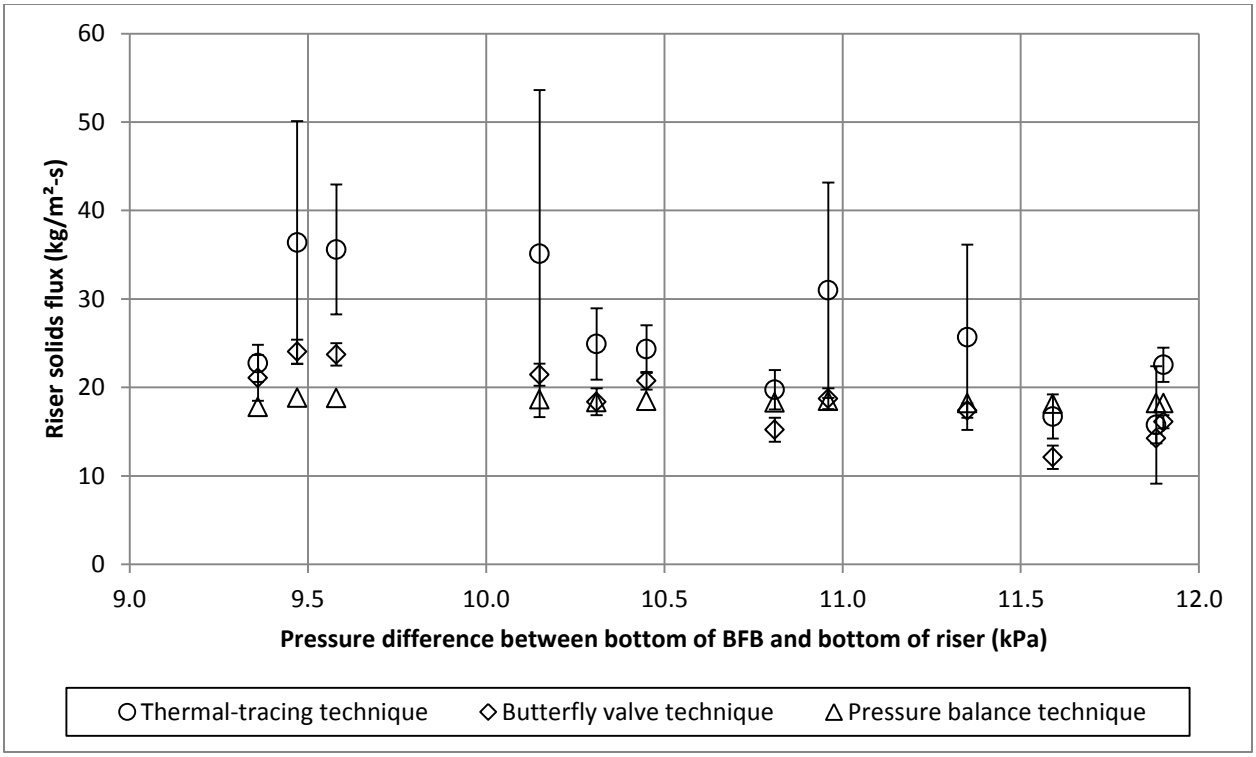

Figure 4.3: Impact of pressure difference between BFB and riser on solids circulation flux in cold tests obtained from using 3 independent techniques at a fixed superficial gas velocity of 3.4 m/s in the riser.

In the hot tests, it was possible to apply all four techniques at the same time for the determination of solids circulation flux. Figure 4.4 shows the fluxes at five temperatures with the same aeration rate at the U-bend. The fluxes differ from one another to some extent at each temperature, with the butterfly valve technique producing the lowest flux at four of the five temperatures. The combination of the limitations of these techniques are likely to cause these differences. However, the agreements can be considered reasonable, since there is no accurate technique for determining solids circulation rates at high temperatures.

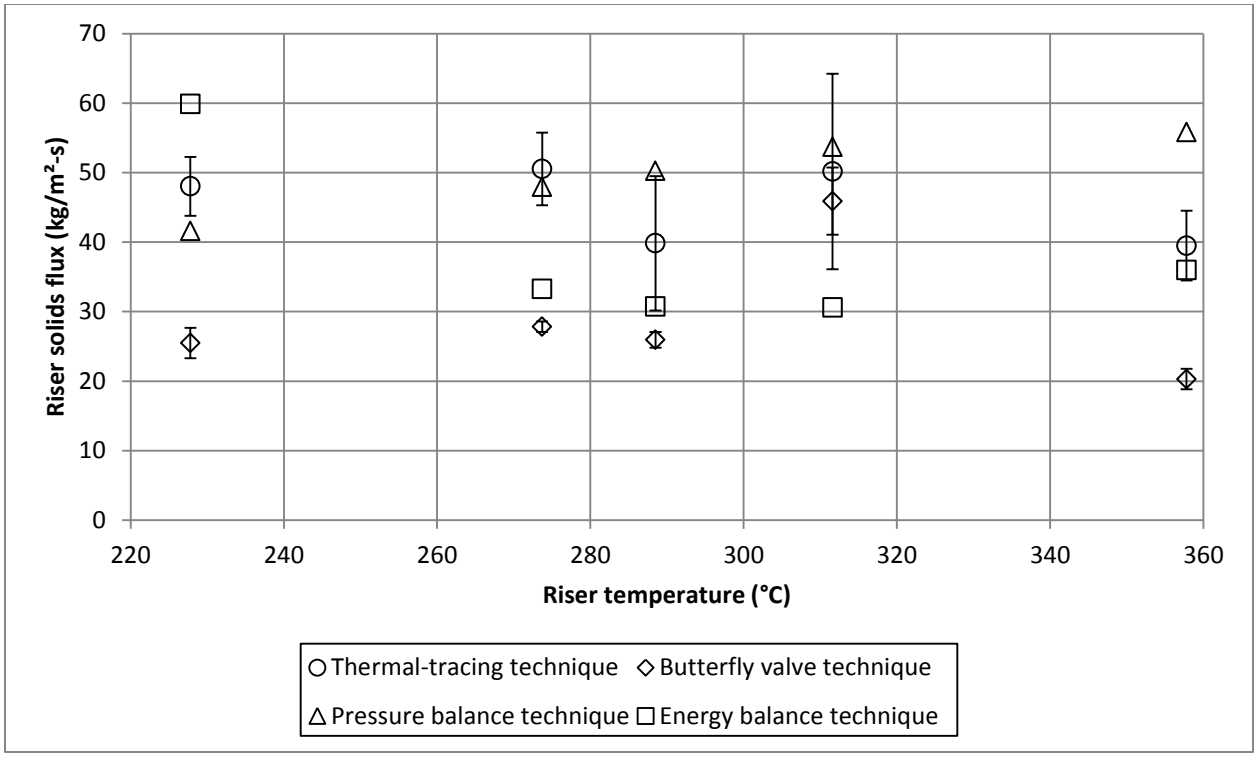

Figure 4.4: Comparison of solids circulation fluxes in the hot tests estimated at different temperatures in the riser using 4 independent techniques with a constant aeration rate of 0.08 m^3/h at the U-bend. (Inlet flow rate of air at riser's NG burner for the test at 358°C was 12.5% lower than for the other tests.)

According to Figure 4.4, the change in temperature appears to have little effect on the solids circulation flux. Figure 4.5 explores the effect of the change of pressure difference between the bottoms of the bubbling bed and the riser on the solid circulation flux in the hot tests. Note that the range of pressure difference is too small to expect any appreciable change in the solids circulation flux.

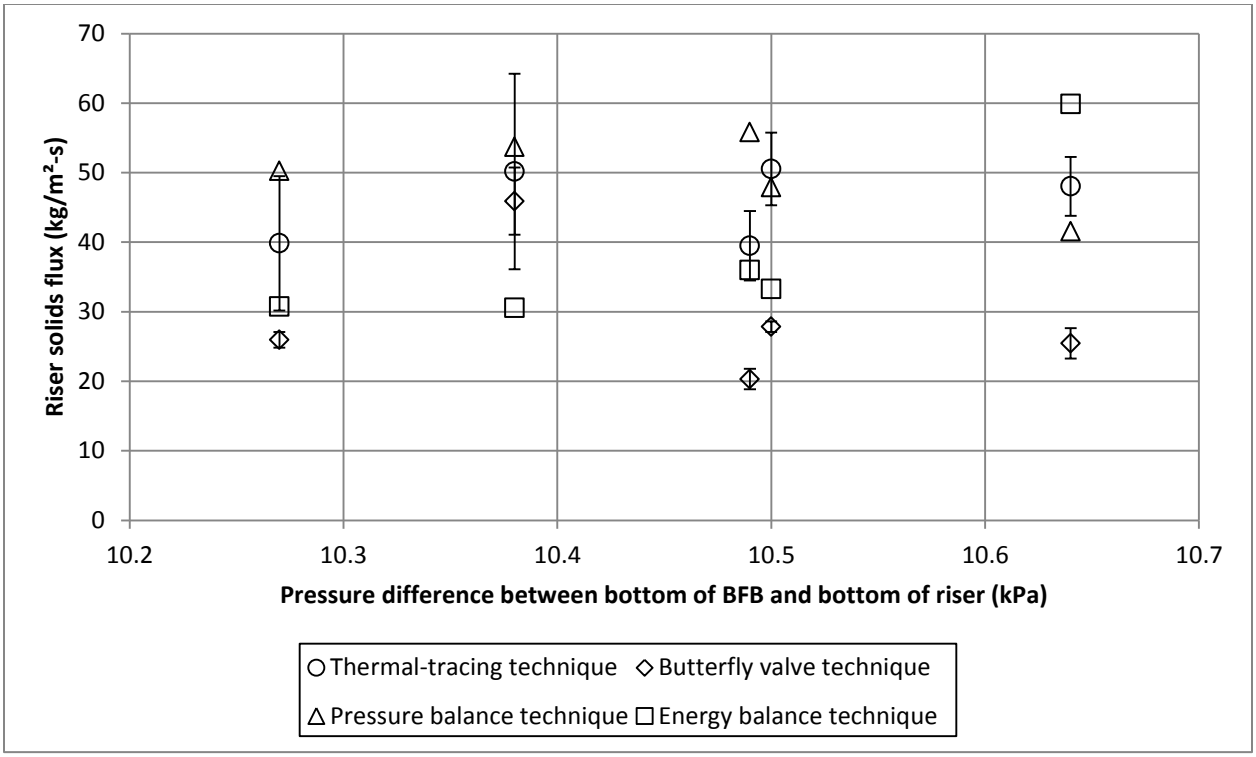

Figure 4.5: Impact of pressure difference between BFB and riser on solids circulation flux in the hot tests obtained from using 4 independent techniques at a fixed aeration rate of 0.08 m^3/h at the U-bend.

When the volumetric flow rate of inlet air to the NG burner for CFB riser was fixed, an increase in the riser temperature made the volumetric flow rate of flue gas there to rise, which in turn caused the superficial gas velocity to increase. Four hot tests were conducted at the same volumetric flow rate of the inlet air. The solids circulation fluxes from these four hot tests are plotted against the riser superficial gas velocity in Figure 4.6. The flux did not change significantly with superficial gas velocity for the limited velocity range covered. This has happened due to the limitation imposed by two operating parameters, the aeration at the U-bend and the pressure difference between the bottoms of the bubbling bed and riser, on the arrival of solids at the entrance of riser. Since the first parameter remained unchanged and the second parameter varied little, the supply of solids at the bottom of riser

did not change appreciably. An increase in superficial gas velocity cannot increase solids circulation rate in the riser when the supply of solids is limited.

The operating envelopes in which the cold and hot tests were performed were not large enough to permit any meaningful investigation of the impact of change in the aeration rate at U-bend, the pressure difference between the bottoms of the bubbling bed and the riser, and the superficial gas velocity in riser on the solids circulation flux. However, they were sufficient to compare the solids circulation fluxes obtained from applying four independent techniques.

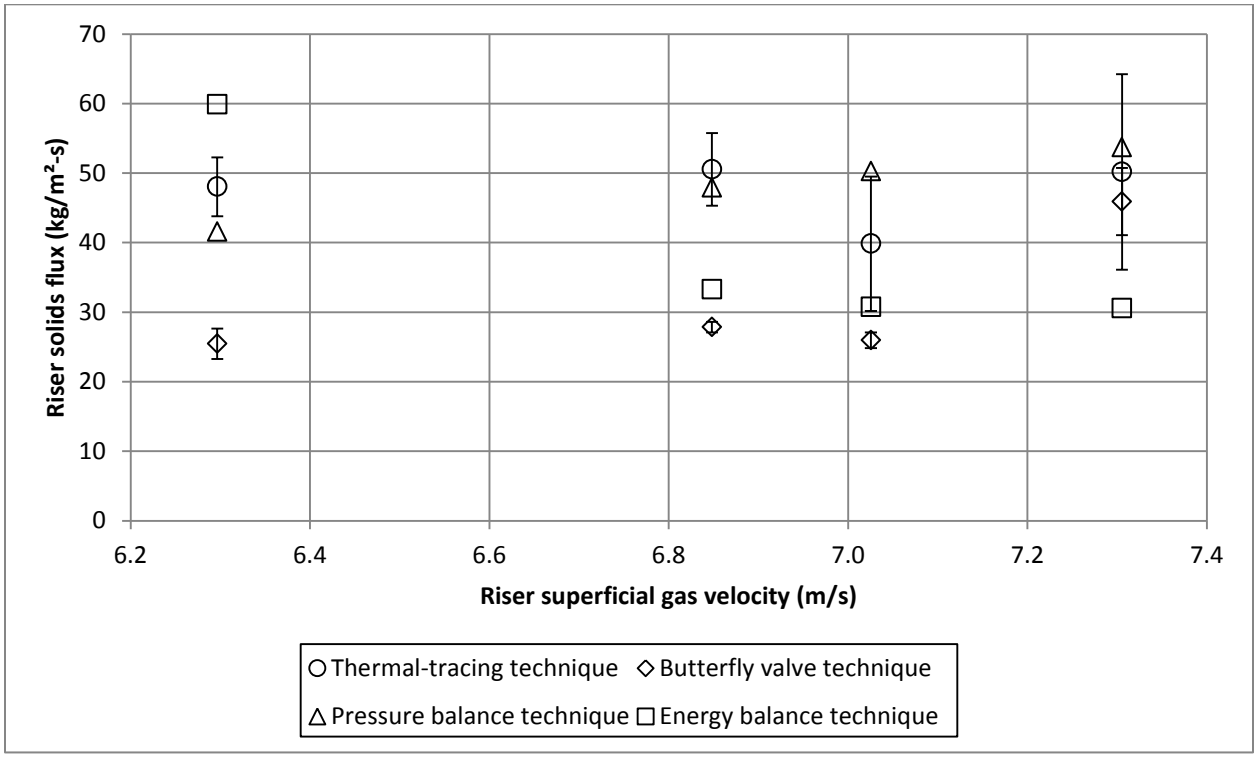

Figure 4.6: Effect of riser superficial gas velocity on solids circulation flux in the hot tests obtained from using 4 independent techniques with a fixed air flow rate of 1.3 m^3/min at the inlet of riser's NG burner and a fixed aeration rate of 0.08 m^3/h at the U-bend.

The accuracy of the pressure balance technique is affected by the utilization of several empirical correlations which were originally developed using different particles. During the estimation of the flow rates of inlet air and natural gas streams and heat loss from the system, a room temperature of 20°C has been used. However, it could not be strictly maintained at all times due to the poor ventilation system of the laboratory.

One of the assumptions for the heat loss calculation is the natural movement of room air around the bubbling bed reactor vessel. However, the vessel is surrounded by other components which made the flow pattern of air too complicated to determine accurately for the purpose of this work. In addition, several fans blew air to keep nearby areas free from the build-up of any leaked gas. Their use might have induced a small proportion of forced convection of air around the bubbling bed reactor vessel. The heat losses through flanges, pressure and temperature measurements ports, nitrogen purging connections and bubbling bed's support structures have also been overlooked as their contributions are likely to be small. There are minor deviations in the insulation thickness at places like pipe bends and flange connections. Such a deviation from uniform thickness at a section is not reflected in the calculation. If it were possible to accurately determine the impacts of these factors, it would have resulted a slightly higher value of total heat loss from the system. This could make the solid circulation rates estimated by using energy balance technique to decrease marginally. However, their agreement with the rates determined using the other three techniques would not have been changed significantly. This is because some data points in the Figures 4.4-4.6 which were obtained from using energy balance technique would have gone farther from those obtained from using other techniques, while some other would have done the opposite.

5 Conclusions and Recommendations

The overall goal of this project is to advance the technology for direct measurement of solids circulation rates in dual fluidized bed systems, helping to develop such systems for large-scale industrial applications in the future. Since the solids circulation rate is a critical hydrodynamic parameter affecting the system performance, its accurate determination has important implications for the scale-up, design and operation of a dual fluidized bed gasification plant. Search in the literature did not reveal any reported techniques suitable for this job.

In this thesis, the development and application of a novel thermal-tracing technique for measuring the solids circulating rate between the two fluidized beds of the pilot plant have been described. The development of a novel butterfly valve technique to validate the thermal-tracing technique at high temperature is also described. In addition, estimation of the solids circulation rates based on extensive operating data of the pilot plant using a pressure balance method and an energy balance method are outlined. The solids circulation rates obtained from these three techniques generally supports the rates measured by the thermal-tracing technique.

Beyond the dual fluidized bed gasification process, the thermal-tracing technique can be applied to measure the solids circulation rate in other circulating fluidized bed processes such as fluid catalytic cracking (FCC) and carbon capture through calcination and carbonation in parallel reactors. The greatest strength of this technique lies in its ability to provide measurements at high temperatures where alternative techniques are unsuitable or impractical.

5.1 Conclusions

- In preliminary experiments, solids circulation rates were measured by two independent techniques at room temperature. The results obtained from these techniques agreed well with each other, and this agreement provided a strong basis for the development of a novel thermal-tracing technique for application at high temperatures.
- The heat transfer between the moving bulk hot solids (either catalyst or sand) and injected cold tracer particles was modeled. The model confirmed that the cold tracer particles did not attain the temperature of bulk solids before leaving the thermal-tracing test section. The findings helped to justify the chosen dimensions in the design and construction of the high-temperature test section.
- The pressure balance across the solids circulation loop confirmed the presence of sufficient solids in the thermal-tracing test section. It was included in a set of criteria developed to filter out physically unexplainable data.
- A number of tests were conducted without the injection of cold tracer particles to determine whether or not the fluctuations in temperature signal are sufficient for the measurement of solids circulation rate. The poor outcome demonstrated that there is no substitute for cold tracer injection.
- The solids circulation rate between the two fluidized beds of the pilot plant was successfully measured by applying the novel thermal-tracing technique during high-temperature operation of the gasifier. It was possible to conduct a significant number of these tests at temperatures

higher than 800°C. Both Geldart A and B type particles were tested. The highest temperature at which the rate was measured was 856°C.

- Despite some differences between the solid circulation fluxes measured by using the butterfly valve and the thermal-tracing techniques, these fluxes were generally found to be in reasonable agreement with each other. If an experimentally measured voidage is applied to the data obtained from the use of the thermal-tracing technique, the overall difference is decreased.
- Given the difficulty of determining the solids circulation rates, the fluxes from all four methods described in this thesis are considered to show reasonable agreement.
- Each of the four methods has its limitations. The combined effects of their limitations are thought to be responsible for the differences among the fluxes determined by these techniques.
- With a fixed air flow rate at the inlet of natural gas burner and a fixed rate of aeration at the U-bend, the solids circulation flux did not change appreciably with changes in riser superficial gas velocity in the range of operating conditions covered by the hot tests. In the cold tests, no strong relation was observed between the changes in the aeration rate of the U-bend and the solids circulation flux. The change in the pressure difference between the bottoms of bubbling bed and circulating bed riser did not significantly impact the solids circulation flux for both hot and cold tests in the operating range used in this project.

5.2 Recommendations for future work

The following recommendations are made for further development of the thermal-tracing technique:

- The solids transfer pipe of any new dual fluidized bed plant should have a sufficiently long vertical section where the solids descend in moving packed bed flow, without any bend in the transfer pipe close to the thermal-tracing test section.
- The process of injecting cold tracer particles should be automated so that the total time needed to complete three consecutive injections can be minimized. This automatic injection process can be integrated with the data acquisition and processing programs. This will allow virtually real-time monitoring of the solids circulation rate in the plant.
- Efforts should be made to fabricate multipoint thermocouples with each junction exposed to the measurement environment. Replacing the existing single-point thermocouple with a multipoint one will increase the number of data points at a cross-sectional area.
- The cold tracer injection system (hopper, flow meter, pressure relief valve, gauge and regulator) should be installed as close to the thermal-tracing test section as permitted by safety considerations. This will reduce the travel time of tracer particles from the hopper to the test section, increasing accuracy.
- Research should be performed on the mixing pattern of the cold tracer particles with the bulk hot solids inside the solids transfer pipe. An improved way of dispersing the tracer particles uniformly over the pipe's cross-sectional area would enhance the performance of the thermal-tracing technique.

- The individual and/or combined impacts of the following parameters on the solids circulation rate should be investigated over a wide range of each parameter:
    - Superficial gas velocity in the riser,
    - Total aeration rate at the U-bend, and
    - Difference in pressure between the bottoms of the riser and bubbling bed.
- The possibility of using cold gas as tracer should be investigated. This could be useful for any future processes which would not allow the addition of particles during operation.
- A single type of particles was used as the bed material in each test of this project. The performance of the thermal-tracing technique should be investigated using a bed material composed of two or more types of particles. This would be relevant for any future processes where the primary solids in the bed would not attain desired mobility on its own, and therefore would have to be mixed with another type of solids.

References

[1] U.S. and world population clock, (2017). https://www.census.gov/popclock/ (accessed September 26, 2017).

[2] BP statistical review of world energy 2017, London, 2017. https://www.bp.com/content/dam/bp/en/corporate/pdf/energy-economics/statistical-review-2017/bp-statistical-review-of-world-energy-2017-full-report.pdf.

[3] IPCC, 2013: Climate Change 2013: The Physical Science Basis. Contribution of Working Group I to the Fifth Assessment Report of the Intergovernmental Panel on Climate Change, Cambridge, 2014. http://www.ipcc.ch/report/ar5/wg1/.

[4] Global Forest Resources Assessment 2015, Rome, 2016.

[5] K. Maniatis, Progress in Biomass Gasification: An Overview, in: Prog. Thermochem. Biomass Convers., 2008: pp. 1–31.

[6] X.T. Bi, X. Liu, High density and high solids flux CFB risers for steam gasification of solids fuels, in: Fuel Process. Technol., 2010: pp. 915–920.

[7] P. Basu, B. Acharya, P. Kushal, Design methods for fluidised bed gasifiers: comparison of three approaches, J. Energy Inst. 83 (2010) 32–40.

[8] H. Hofbauer, H. Stoiber, G. Veronik, Gasification of organic material in a novel fluidized bed system, in: Proc. 1st SCEJ Symp. Fluid., Tokyo, 1995.

[9] Y. Li, Z. Chen, P. Watkinson, X. Bi, J.R. Grace, C.J. Lim, N. Ellis, A Novel Dual-bed for Steam Gasification of Biomass, Biomass Convers. Biorefinery. (2017).

[10] N.H. Florin, A.T. Harris, Enhanced hydrogen production from biomass with in situ carbon dioxide

capture using calcium oxide sorbents, Chem. Eng. Sci. 63 (2008) 287–316.

[11] J.J. Burkell, J.R. Grace, J. Zhao, C.J. Lim, Measurement of solids circulation rates in circulating fluidized beds, in: P. Basu, J.F. Large (Eds.), Circ. Fluid. Bed Technol. II, Pergamon, Oxford, 1988: pp. 501–509.

[12] L.R. Glicksman, D. Westphalen, C. Brereton, J. Grace, Verification of the Scaling Laws for Circulating Fluidized Beds, in: P. Basu, M. Horio, M. Hasatani (Eds.), Circ. Fluid. Bed Technol. III, Pergamon, Nagoya, 1990: pp. 119–124.

[13] J.R. Muir, C.M.H. Brereton, J.R. Grace, C.J. Lim, Line-and sinker measurement of solids circulation rate in a CFB combustor, in: U. Arena, R. Chirone, M. Miccio, P. Salatino (Eds.), Fluid. XI, Engineering Conferences International, New York, 2004: pp. 315–322.

[14] C.E. Davies, B.J. Harris, A Device for Measuring Solids Flowrates: Characteristics, and Applications in a Circulating Fluidized Bed, in: Fluid. VII, Engineering Foundation, New York, 1992: pp. 741–748.

[15] A. Kreuzeder, C. Pfeifer, H. Hofbauer, Fluid-dynamic investigations in a scaled cold model for a dual fluidized bed biomass steam gasification process: Solid flux measurements and optimization of the cyclone, Int. J. Chem. React. Eng. 5 (2007).

[16] J.C. Ludlow, E.R. Monazam, L.J. Shadle, Improvement of continuous solid circulation rate measurement in a cold flow circulating fluidized bed, Powder Technol. 182 (2008) 379–387.

[17] C.E. Davies, S.J. Tallon, E.S. Webster, Applications of active acoustics in particle technology, Particuology. 8 (2010) 568–571.

[18] N. Ellis, C.J. Lim, P.A. Reyes, J.I. Soletti, J.R. Grace, Acoustic emissions method for solids mass flux measurements, in: 21st Int. Conf. Fluid. Bed Combust., Naples, 2012: pp. 681–688.

[19] E.R. Monazam, R. Panday, L.J. Shadle, Estimate of solid flow rate from pressure measurement in circulating fluidized bed, Powder Technol. 203 (2010) 91–97.

[20] G.S. Patience, J. Chaouki, B.P.A. Grandjean, Solids flow metering from pressure drop measurement in circulating fluidized beds, Powder Technol. 61 (1990) 95–99.

[21] X. Song, H. Bi, C.J. Lim, J.R. Grace, E. Chan, B. Knapper, C. McKnight, Hydrodynamics of the reactor section in fluid cokers, Powder Technol. 147 (2004) 126–136.

[22] K.S. Lim, P. Peeler, T. Joyce, A. Zakhari, R. Close, Estimation of solids circulation rate in a large pilot-scale CFB, in: J.R. Grace, J. Zhu, H. de Lasa (Eds.), Circ. Fluid. Bed Technol. VII, Niagara Falls, 2002: pp. 169–176.

[23] E. Grieco, L. Marmo, Predicting the pressure drop across the solids flow rate control device of a circulating fluidized bed, Powder Technol. 161 (2006) 89–97.

[24] E.R. Monazam, L.J. Shadle, A transient method for characterizing flow regimes in a circulating fluid bed, Powder Technol. 139 (2004) 89– 97.

[25] B.T. Chorpening, M. Spencer, J. Charley, R.C. Stehle, D.W. Greve, Microwave Doppler Sensing of Sliding or Intermittent Particle Flows, 2016 Multiph. Flow Sci. Work. (2016). https://mfix.netl.doe.gov/workshop-files/2016/mfs/Microwave Doppler - Multiphase flow meeting 2016 -v5b.pdf (accessed October 26, 2016).

[26] W. Wu, A.L. Gerhart, Z. Chen, P.A. Dellenback, P.K. Agarwal, A device for measuring solids flowrate in a circulating fluidized bed, Powder Technol. 120 (2001) 151–158.

[27] M. Lech, Mass flow rate measurement in vertical pneumatic conveying of solid, Powder Technol. 114 (2001) 55–58.

[28] P. Bodelin, Y. Molodtsof, A. Delebarre, Flow structure investigations in a CFB, in: A.A. Avidan

(Ed.), Circ. Fluid. Bed Technol. IV, Hidden Valley, California, USA, 1993: pp. 118–122.

[29] M. Kuramoto, D. Kunii, T. Furusawa, Flow of dense fluidized particles through an opening in a circulation system, Powder Technol. 47 (1986) 141–149.

[30] J. Liu, B. Huan, Turbine meter for the measurement of bulk solids flowrate, Powder Technol. 82 (1995) 145–151.

[31] R.J. Dry, R.B. White, T. Joyce, Correlation of solids circulation rate in circulating fluidized bed systems, in: A.A. Avidan (Ed.), Circ. Fluid. Bed Technol. IV, Hidden Valley, California, USA, 1993: pp. 621–627.

[32] S. Roy, A. Kemoun, M. Al-Dahhan, M.P. Dudukovic, A method for estimating the solids circulation rate in a closed-loop circulating fluidized bed, Powder Technol. 121 (2001) 213–222.

[33] S. Bhusarapu, P. Fongarland, M.H. Al-Dahhan, M.P. Dudukovic´, Measurement of overall solids mass flux in a gas-solid Circulating Fluidized Bed, Powder Technol. 148 (2004) 158–171.

[34] J.A. Medrano, M. Nordio, G. Manzolini, M. van Sint Annaland, F. Gallucci, On the measurement of solids circulation rates in interconnected fluidized beds: Comparison of different experimental techniques, Powder Technol. 302 (2016) 81–89.

[35] D.C. Guio-Perez, F. Dietrich, J.N. Ferreira Cala, T. Proll, H. Hofbauer, Estimation of solids circulation rate through magnetic tracer tests, Powder Technol. 316 (2017) 650–657.

[36] C. Brereton, Fluid Mechanics of High Velocity Fluidized Beds, The University of British Columbia, 1987.

[37] M.H. Rahman, Yield Stresses of Mixtures with Bimodal Size Distributions, University of Alberta, 2011.

[38] T.M. Knowlton, Standpipes and Nonmechanical Valves, in: W.-C. Yang (Ed.), Chapter 21 Handb.

Fluid. Fluid-Particle Syst., Marcel Dekker, Inc, New York, 2003.

[39] J. Liu, J.R. Grace, X. Bi, Novel Multifunctional Optical-Fiber Probe: I. Development and Validation, AIChE. 49 (2003) 1405–1420.

[40] P. Kaushal, T. Pröll, H. Hofbauer, Model for biomass char combustion in the riser of a dual fluidized bed gasification unit: Part 1 - Model development and sensitivity analysis, Fuel Process. Technol. 89 (2008) 651–659.

[41] C.R. Wilke, A Viscosity Equation for Gas Mixtures, J. Chem. Phys. 18 (1950) 517.

[42] R.M. Felder, R.W. Rousseau, Elementary Principles of Chemical Processes, 2nd ed., Wiley, 1986.

[43] K. Kadoya, N. Matsunaga, A. Nagashima, Viscosity and Thermal-Conductivity of Dry Air in the Gaseous-Phase, J. Phys. Chem. Ref. Data. 14 (1985) 947–970.

[44] J.D. Gabor, Wall-to-Bed Heat Transfer in Fluidized and Packed Beds, Chem. Eng. Prog. Symp. Ser. 66 (1970) 76–86.

[45] J.R. Grace, Fluidized-Bed Hydrodynamics, in: G. Hetsroni (Ed.), Sect. 8.1 Handb. Multiph. Syst., Hemisphere, Washington, 1982: p. 8:5-64.

[46] Y.A. Cengel, Heat Transfer: A Practical Approach, 2nd ed., McGraw-Hill, 2002.

[47] J. Werther, B. Hage, C. Rudnick, A comparison of laser Doppler and single-fibre reflection probes for the measurement of the velocity of solids in a gas-solid circulating fluidized bed, Chem. Eng. Process. Process Intensif. 35 (1996) 381–391.

[48] J. Militzer, J.P. Hebb, G. Jollimore, K. Shakourzadeh, Solid particle velocity measurements, in: Fluid. VII, Engineering Foundation, New York, 1992: pp. 763–769.

[49] J. Werther, O. Molerus, The local structure of gas fluidized beds - I. A statistically based monitoring system, Int. J. Multiph. Flow. 1 (1973) 103–122.

[50] A.E. Almstedt, E. Olsson, Measurements of bubble behaviour in a pressurized fluidized bed burning coal, using capacitance probes, in: 7th Int. Conf. Fluid. Bed Combust., ASME, Philadelphia, 1982: pp. 89–98.

[51] Y.A. Cengel, M. Boles, Thermodynamics: An Engineering Approach, 5th ed., McGraw-Hill, 2006.

[52] Material safety data sheet for natural gas, Enbridge, Inc. (2015). https://www.enbridgegas.com/assets/docs/2015 MSDS Natural Gas - English.pdf%0A (accessed July 26, 2017).

[53] M.E. Clift, R., Grace, J.R., Weber, Bubbles, Drops and Particles, Academic Press, London, 1978.

[54] D. Bai, A.S. Issangya, J.-X. Zhu, J.R. Grace, Analysis of the overall pressure balance around a high-density circulating fluidized bed, Ind. Eng. Chem. Res. 36 (1997) 3898–3903.

[55] H. Bi, J.-X. Zhu, Static Instability Analysis of Circulating Fluidized Beds and Concept of High Density Risers, AIChE J. 39 (1993) 1272–1280.

[56] D. Kunii, O. Levenspiel, Fluidization Engineering, 2nd ed., Butterworth-Heinemann, Stoneham, 1991.

[57] D. Kunii, O. Levenspiel, Entrainment of solids from fluidized beds I. Hold-up of solids in the freeboard II. Operation of fast fluidized beds, Powder Technol. 61 (1990) 193–206.

[58] R.C. Darton, R.D. LaNauze, J.F. Davidson, D. Harrison, Bubble growth due to coalescence in fluidised beds, Trans. Inst. Chem. Eng. 55 (1977) 274–280.

[59] J.F. Davidson, D. Harrison, Behavior of a continuously bubbling fluidized bed, Chem. Eng. Sci. 21 (1966) 731–738.

[60] H. Konno, S. Saito, Pneumatic conveying of solids through straight pipes, J. Chem. Eng. Japan. 2 (1969) 211–217.

[61] M.J. Rhodes, D. Geldart, Model for the Circulating Fluidized Bed, Powder Technol. 53 (1987) 155–162.

[62] Heat transfer coefficient, (2017). https://en.wikipedia.org/wiki/Heat_transfer_coefficient (accessed September 14, 2017).

[63] C. Chatfield, The analysis of time series, Chapman and Hall, New York, 1984.

[64] G.E. Caldwell, L. Li, Coefficient of cross correlation and the time domain correspondence, J. Electromyogr. Kinesiol. 9 (1999) 385–389.

Appendices

Appendix A: Analysis of thermocouple's response time and cross-correlation technique

The key design information of the thermocouples is given in Table A.1.

Table A.1: Key specifications of thermocouples.

Manufacturer	Omega Engineering Inc., Laval, Quebec, Canada
Model	KQXL-18E-18
Type	K
Junction type	Exposed
Junction (head) diameter	1.6 mm (1/16")
Length	457.2 mm (18")
Sheath Diameter	3.2 mm (1/8")

The temperature measured by a thermocouple installed in the thermal-tracing test section remains almost constant, with negligible fluctuations before the injection of cold tracer particles. When the tracer particles are injected, they form clusters, as described in Section 2.4. When one of these clusters comes in contact with a thermocouple, it causes an instantaneous change in temperature there. If the Biot number is less than 0.1, the thermocouple follows a simple "lumped capacitance model", and the

dynamic response of a temperature sensor such as thermocouple (TC), subject to an instantaneous temperature change, can be modeled as a first-order system. The 'response time' or 'time constant' is then defined as the time needed to reach 63.2% of final temperature change.

Since it would be difficult and hazardous to create the exact measurement environment of temperature 900°C outside the pilot plant, the results of a time response study conducted by the manufacturer are utilized to calculate the response time of the thermocouple used in the thermal-tracing test section. The manufacturer found the response time of a thermocouple of the type used in our study to be 0.19 s when plunged into hot or cold water.

If the thermocouple is dipped into quiescent water, heat transfer between them changes the internal energy of the thermocouple:

$$m_{TC,head} C_{p,TC,head} \frac{d}{dt}\left(T_{TC,head}\right) = h_{conv,water} A_{TC,head}\left(T_{\infty,water} - T_{TC,head}\right) \quad \text{(A.1)}$$

Rearrangement of this equation gives,

$$\frac{m_{TC,head} C_{p,TC,head}}{h_{conv,water} A_{TC,head}} \frac{d}{dt}\left(T_{TC,head}\right) + T_{TC,head} = T_{\infty,water} \quad \text{(A.2)}$$

The response time of the thermocouple when immersed into the water,

$$\tau_{TC,water} = \frac{m_{TC,head} C_{p,TC,head}}{h_{conv,water} A_{TC,head}}$$

Then,

$$m_{TC,head} C_{p,TC,head} = \tau_{TC,water} h_{conv,water} A_{TC,head} \quad \text{(A.3)}$$

Here, the heat transfer coefficient due to natural convection in water at room temperature is taken as 500 W/m^2-K [62].

When a cluster of cold particles passes a thermocouple, it can be considered that the thermocouple is immersed into that cluster instantaneously. The change in the internal energy of the thermocouple's junction during differential time (dt) is equal to the sum of:

a) Heat transfer between the thermocouple's junction and the interstitial gases of the cluster through natural convection and radiation during dt, and
b) Heat transfer between the thermocouple's junction and the cluster through conduction

i.e.

$$m_{TC,head}C_{p,TC,head}\frac{d}{dt}\left(T_{TC,head}\right) = h_{nc+rad}A_{TC,head}\left(T_{cluster}-T_{TC,head}\right)+k_{cluster}L_c\left(T_{cluster}-T_{TC,head}\right) \quad \text{(A.4)}$$

However, this lumped capacitance model of heat transfer is applicable when the Biot number, *Bi*, is less than 0.1, where

$$Bi = \frac{h_{nc+rad}L_c}{k_{TC,head}}$$

The thermal conductivity of the thermocouple's junction, $k_{TC,head}$, is 24.47 W/m-K. This value is supplied by the manufacturer. The characteristic length (L_c) of the thermocouple's junction or head is its diameter, assuming spherical shape.

Rearranging Equation (A.4) yields,

$$\frac{m_{TC,head}C_{p,TC,head}}{h_{nc+rad}A_{TC,head}+k_{cluster}L_c}\frac{d}{dt}\left(T_{TC,head}\right)+T_{TC,head}=T_{cluster} \quad \text{(A.5)}$$

The response time of the thermocouple for its contact with a cluster,

$$\tau_{TC,cluster} = \frac{m_{TC,head}C_{p,TC,head}}{h_{nc+rad}A_{TC,head}+k_{cluster}L_c}$$

The values of the thermal conductivity of the cluster, the combined convective and radiative heat transfer coefficient and $m_{TC,head}C_{p,TC,Head}$ are obtained using Equations (2.4), (2.5) and (A.3), respectively.

A response time is estimated for different numbers of sand particles per cluster considered in Section 2.4. The corresponding response times are provided in Table A.2.

Table A.2: Response times of the thermocouple in the cluster.

Number of clusters formed when 100 g of cold particles are injected	Response time (s)	Biot number (-)
1	0.74	0.0068
5	0.73	0.0070
10	0.72	0.0071
50	0.69	0.0074
100	0.68	0.0076
500	0.63	0.0082
1000	0.61	0.0085

Each of these response times is smaller than a typical travel time between thermocouples of 2.34 s (Section 2.1) and $Bi < 0.1$ in all cases. Since a cluster may spread a little when travelling between two successive thermocouples, the difference between the impacts of response times on these thermocouples' outputs can be considered negligible. However, one of the criteria to accept a value of

solids circulation flux obtained from a pair of thermocouple is that the maximum cross-correlation coefficient be higher than 0.6.

According to Chatfield [63] and Caldwell and Li [64], the cross-correlation coefficient of two time series x and y with an identical number of data points, N, is defined as

$$r_{xy}(k) = \frac{c_{xy}(k)}{\sqrt{c_{xx}(0)c_{yy}(0)}} \tag{A.6}$$

where,

$$c_{xy}(k) = \sum_{t=1}^{N-k} (x_t - \bar{x})\,(y_{t+k} - \bar{y}) + \sum_{t=N-k+1}^{N} (x_t - \bar{x})\,(y_{t-N+k} - \bar{y}), if\ k = 1,2,\dots,N$$

$$c_{xy}(k) = \sum_{t=1}^{N} (x_t - \bar{x})\,(y_t - \bar{y}), if\ k = 0$$

$$c_{xx}(0) = \sum_{t=1}^{N} (x_t - \bar{x})^2$$

$$c_{yy}(0) = \sum_{t=1}^{N} (y_t - \bar{y})^2$$

A coefficient is obtained by shifting one signal with respect to the other. This time shift is represented by 'k' in the correlations provided above. When the patterns of these two signals obtain their best possible match in the process of changing the time shift (k), the cross-correlation coefficient (r_{xy}) attains the maximum value.

An exposed junction thermocouple produces sharper pattern in its time vs. temperature signal due to the addition of cold tracer particles when compared to the pattern obtained from a grounded or ungrounded junction thermocouple. This sharp pattern enhances the probability of obtaining a higher value of maximum cross-correlation coefficient. This is important since the maximum value of cross-correlation coefficient in this project was required to be 0.6 or higher. There are some values found by cross-correlating thermocouple signals which were slightly higher than 0.6. If ordinary thermocouples were used, those values might have become smaller than 0.6, and therefore, not considered for subsequent analysis to estimate the solids circulation flux. This argument shows the usefulness of using the exposed-junction thermocouple instead of an ordinary thermocouple with slower response time.

Appendix B: MATLAB code for processing thermocouples' data

The code was written to process the temperature data collected from twelve thermocouples installed at the thermal-tracing test section. Cross-correlation is performed between the data of two adjacent thermocouples. The maximum cross-correlation coefficient is identified for this pair. The time shift at this coefficient is used to estimate the solids circulation rate. The code is given below:

```
clc

% Bulk density, kg/m3
rho_b = 1450;

% Input Frequency
f = 50;

% Distance between levels, meter
L12 = 2/39.37;
L23 = 4/39.37;
L34 = 4/39.37;

% ID of Pipe and Riser, inch
Dp = 3.068;
Dr = 3.438;

% Number of rows
N = size (data,1);

%%%%%%%%%%%%%%%%%%%%%%%%%%%%%%%%%%%%%%%%%%%%%%%%%%%%%%%%%%%
%%%%%%%%%%%%%%%
%TC01 & TC02
%%%%%%%%%%%%%%%%%%%%%%%%%%%%%%%%%%%%%%%%%%%%%%%%%%%%%%%%%%%
%%%%%%%%%%%%%%%

% Mean of T1 & T2
T1M = mean (data(:,2));
T2M = mean (data(:,3));

% Calculate C_xx & C_yy
```

```
C_xx = 0;
C_yy = 0;
for i = 1:N
   C_xx_1 = (data(i,2)-T1M)^2;
   C_yy_1 = (data(i,3)-T2M)^2;
C_xx = C_xx + C_xx_1;
C_yy = C_yy + C_yy_1;
end

% Calculate C_xy_0
C_xy_0 = 0;
for i = 1:N
   C_xy_0_1 = (data(i,2)-T1M)*(data(i,3)-T2M);
C_xy_0 = C_xy_0 + C_xy_0_1;
end

% Calculate r_xy_0
r_xy_0_12 = C_xy_0/(C_xx*C_yy)^0.5;

% Calculate r_xy as a function of k values
j = 0;
for k12 = 0.02:0.02:5;

   % For storing the k values
   j = j+1;

   N1 = data(end,1)-data(1,1);
   C_xy_1 = 0;
   C_xy_2 = 0;

   % To deal with jitter, 1/f is used in stead of actual time
   for t = 0:(1/f):(N1-k12);

        % Read x_t
        i1 = 1:N;
        temp1 = abs((data(1,1)+t)-data(i1,1));
        [index1 index1] = min(temp1);
        x_t = data(index1,2);

        % Read y_t_k
        i2 = 1:N;
        temp2 = abs((data(1,1)+t+k12)-data(i2,1));
        [index2 index2] = min(temp2);
        y_t_k = data(index2,3);
```

```
        C_xy_1_1 = (x_t-T1M)*(y_t_k-T2M);
        C_xy_1 = C_xy_1 + C_xy_1_1;
    end

      for t = (N1-k12+(1/f)):(1/f):N1;

        % Read x_t
        i3 = 1:N;
        temp3 = abs((data(1,1)+t)-data(i3,1));
        [index3 index3] = min(temp3);
        x_t = data(index3,2);

        % Read y_t_k_N
        i4 = 1:N;
        temp4 = abs((data(1,1)+t+k12-N)-data(i4,1));
        [index4 index4] = min(temp4);
        y_t_k_N = data(index4,3);

        C_xy_2_1 = (x_t-T1M)*(y_t_k_N-T2M);
        C_xy_2 = C_xy_2 + C_xy_2_1;
      end

        C_xy = C_xy_1 + C_xy_2;
        % Generate r_xy vs k values
        r_xy_12(j) = C_xy/(C_xx*C_yy)^0.5;
        k12_1(j) = k12;
end

% Display the values for maximum cross correlation coefficient and
% corresponsing value for time shift
R_max_12 = max(r_xy_12);
index_desired = find(max(r_xy_12)==r_xy_12(1,:));
K_R_max_12 = k12_1(1,index_desired);

desired_line_x = [K_R_max_12 K_R_max_12];
desired_line_y = [0 R_max_12];
subplot(3,3,1),plot(0,r_xy_0_12,k12_1,r_xy_12,desired_line_x,desired_line_y,'--')
xlabel('Time shift (Sec)');
ylabel('Cross correlation coefficient');
title('T1-T2');
text(K_R_max_12,R_max_12,(num2str([K_R_max_12 R_max_12])),'VerticalAlignment','bottom');
```

```
%%%%%%%%%%%%%%%%%%%%%%%%%%%%%%%%%%%%%%%%%%%%%%%%%%%%%%%%%%%%%%%%%%%%%
%%%%%%%%%%%%%%%%%%
%TC02 & TC03
%%%%%%%%%%%%%%%%%%%%%%%%%%%%%%%%%%%%%%%%%%%%%%%%%%%%%%%%%%%%%%%%%%%%%
%%%%%%%%%%%%%%%%%%

% Mean of T1 & T2
T1M = mean (data(:,3));
T2M = mean (data(:,4));

% Calculate C_xx & C_yy
C_xx = 0;
C_yy = 0;
for i = 1:N
   C_xx_1 = (data(i,3)-T1M)^2;
   C_yy_1 = (data(i,4)-T2M)^2;
C_xx = C_xx + C_xx_1;
C_yy = C_yy + C_yy_1;
end

% Calculate C_xy_0
C_xy_0 = 0;
for i = 1:N
   C_xy_0_1 = (data(i,3)-T1M)*(data(i,4)-T2M);
C_xy_0 = C_xy_0 + C_xy_0_1;
end

% Calculate r_xy_0
r_xy_0_23 = C_xy_0/(C_xx*C_yy)^0.5;

% Calculate r_xy as a function of k values
j = 0;
for k23 = 0.02:0.02:5;

   % For storing the k values
   j = j+1;

   N1 = data(end,1)-data(1,1);
   C_xy_1 = 0;
   C_xy_2 = 0;

   % To deal with jitter, 1/f is used in stead of actual time
   for t = 0:(1/f):(N1-k23);
```

```
        % Read x_t
        i1 = 1:N;
        temp1 = abs((data(1,1)+t)-data(i1,1));
        [index1 index1] = min(temp1);
        x_t = data(index1,3);

        % Read y_t_k
        i2 = 1:N;
        temp2 = abs((data(1,1)+t+k23)-data(i2,1));
        [index2 index2] = min(temp2);
        y_t_k = data(index2,4);

        C_xy_1_1 = (x_t-T1M)*(y_t_k-T2M);
        C_xy_1 = C_xy_1 + C_xy_1_1;
    end

    for t = (N1-k23+(1/f)):(1/f):N1;

        % Read x_t
        i3 = 1:N;
        temp3 = abs((data(1,1)+t)-data(i3,1));
        [index3 index3] = min(temp3);
        x_t = data(index3,3);

        % Read y_t_k_N
        i4 = 1:N;
        temp4 = abs((data(1,1)+t+k23-N)-data(i4,1));
        [index4 index4] = min(temp4);
        y_t_k_N = data(index4,4);

        C_xy_2_1 = (x_t-T1M)*(y_t_k_N-T2M);
        C_xy_2 = C_xy_2 + C_xy_2_1;
    end

        C_xy = C_xy_1 + C_xy_2;
        % Generate r_xy vs k values
        r_xy_23(j) = C_xy/(C_xx*C_yy)^0.5;
        k23_1(j) = k23;
end

% Display the values for maximum cross correlation coefficient and
% corresponsing value for time shift
R_max_23 = max(r_xy_23);
index_desired = find(max(r_xy_23)==r_xy_23(1,:));
```

```
K_R_max_23 = k23_1(1,index_desired);

desired_line_x = [K_R_max_23 K_R_max_23];
desired_line_y = [0 R_max_23];
subplot(3,3,2),plot(0,r_xy_0_23,k23_1,r_xy_23,desired_line_x,desired_line_y,'--')
xlabel('Time shift (Sec)');
ylabel('Cross correlation coefficient');
title('T2-T3');
text(K_R_max_23,R_max_23,(num2str([K_R_max_23 R_max_23])),'VerticalAlignment','bottom');

%%%%%%%%%%%%%%%%%%%%%%%%%%%%%%%%%%%%%%%%%%%%%%%%%%%%%%%
%%%%%%%%%%%%%%
%TC03 & TC04
%%%%%%%%%%%%%%%%%%%%%%%%%%%%%%%%%%%%%%%%%%%%%%%%%%%%%%%
%%%%%%%%%%%%%%

% Mean of T1 & T2
T1M = mean (data(:,4));
T2M = mean (data(:,5));

% Calculate C_xx & C_yy
C_xx = 0;
C_yy = 0;
for i = 1:N
   C_xx_1 = (data(i,4)-T1M)^2;
   C_yy_1 = (data(i,5)-T2M)^2;
C_xx = C_xx + C_xx_1;
C_yy = C_yy + C_yy_1;
end

% Calculate C_xy_0
C_xy_0 = 0;
for i = 1:N
   C_xy_0_1 = (data(i,4)-T1M)*(data(i,5)-T2M);
C_xy_0 = C_xy_0 + C_xy_0_1;
end

% Calculate r_xy_0
r_xy_0_34 = C_xy_0/(C_xx*C_yy)^0.5;

% Calculate r_xy as a function of k values
j = 0;
for k34 = 0.02:0.02:5;
```

```
% For storing the k values
j = j+1;

N1 = data(end,1)-data(1,1);
C_xy_1 = 0;
C_xy_2 = 0;

% To deal with jitter, 1/f is used in stead of actual time
for t = 0:(1/f):(N1-k34);

    % Read x_t
    i1 = 1:N;
    temp1 = abs((data(1,1)+t)-data(i1,1));
    [index1 index1] = min(temp1);
    x_t = data(index1,4);

    % Read y_t_k
    i2 = 1:N;
    temp2 = abs((data(1,1)+t+k34)-data(i2,1));
    [index2 index2] = min(temp2);
    y_t_k = data(index2,5);

    C_xy_1_1 = (x_t-T1M)*(y_t_k-T2M);
    C_xy_1 = C_xy_1 + C_xy_1_1;
end

  for t = (N1-k34+(1/f)):(1/f):N1;

    % Read x_t
    i3 = 1:N;
    temp3 = abs((data(1,1)+t)-data(i3,1));
    [index3 index3] = min(temp3);
    x_t = data(index3,4);

    % Read y_t_k_N
    i4 = 1:N;
    temp4 = abs((data(1,1)+t+k34-N)-data(i4,1));
    [index4 index4] = min(temp4);
    y_t_k_N = data(index4,5);

    C_xy_2_1 = (x_t-T1M)*(y_t_k_N-T2M);
    C_xy_2 = C_xy_2 + C_xy_2_1;
  end
```

```
        C_xy = C_xy_1 + C_xy_2;
        % Generate r_xy vs k values
        r_xy_34(j) = C_xy/(C_xx*C_yy)^0.5;
        k34_1(j) = k34;
end

% Display the values for maximum cross correlation coefficient and
% corresponsing value for time shift
R_max_34 = max(r_xy_34);
index_desired = find(max(r_xy_34)==r_xy_34(1,:));
K_R_max_34 = k34_1(1,index_desired);

desired_line_x = [K_R_max_34 K_R_max_34];
desired_line_y = [0 R_max_34];
subplot(3,3,3),plot(0,r_xy_0_34,k34_1,r_xy_34,desired_line_x,desired_line_y,'--')
xlabel('Time shift (Sec)');
ylabel('Cross correlation coefficient');
title('T3-T4');
text(K_R_max_34,R_max_34,(num2str([K_R_max_34 R_max_34])),'VerticalAlignment','bottom');

%%%%%%%%%%%%%%%%%%%%%%%%%%%%%%%%%%%%%%%%%%%%%%%%%%%%%%%%%%
%%%%%%%%%%%%%%%
%TC05 & TC06
%%%%%%%%%%%%%%%%%%%%%%%%%%%%%%%%%%%%%%%%%%%%%%%%%%%%%%%%%%
%%%%%%%%%%%%%%%

% Mean of T1 & T2
T1M = mean (data(:,6));
T2M = mean (data(:,7));

% Calculate C_xx & C_yy
C_xx = 0;
C_yy = 0;
for i = 1:N
   C_xx_1 = (data(i,6)-T1M)^2;
   C_yy_1 = (data(i,7)-T2M)^2;
C_xx = C_xx + C_xx_1;
C_yy = C_yy + C_yy_1;
end

% Calculate C_xy_0
C_xy_0 = 0;
for i = 1:N
   C_xy_0_1 = (data(i,6)-T1M)*(data(i,7)-T2M);
```

```
C_xy_0 = C_xy_0 + C_xy_0_1;
end

% Calculate r_xy_0
r_xy_0_56 = C_xy_0/(C_xx*C_yy)^0.5;

% Calculate r_xy as a function of k values
j = 0;
for k56 = 0.02:0.02:5;

   % For storing the k values
   j = j+1;

   N1 = data(end,1)-data(1,1);
   C_xy_1 = 0;
   C_xy_2 = 0;

   % To deal with jitter, 1/f is used in stead of actual time
   for t = 0:(1/f):(N1-k56);

        % Read x_t
        i1 = 1:N;
        temp1 = abs((data(1,1)+t)-data(i1,1));
        [index1 index1] = min(temp1);
        x_t = data(index1,6);

        % Read y_t_k
        i2 = 1:N;
        temp2 = abs((data(1,1)+t+k56)-data(i2,1));
        [index2 index2] = min(temp2);
        y_t_k = data(index2,7);

        C_xy_1_1 = (x_t-T1M)*(y_t_k-T2M);
        C_xy_1 = C_xy_1 + C_xy_1_1;
   end

     for t = (N1-k56+(1/f)):(1/f):N1;

        % Read x_t
        i3 = 1:N;
        temp3 = abs((data(1,1)+t)-data(i3,1));
        [index3 index3] = min(temp3);
        x_t = data(index3,6);
```

```
        % Read y_t_k_N
        i4 = 1:N;
        temp4 = abs((data(1,1)+t+k56-N)-data(i4,1));
        [index4 index4] = min(temp4);
        y_t_k_N = data(index4,7);

        C_xy_2_1 = (x_t-T1M)*(y_t_k_N-T2M);
        C_xy_2 = C_xy_2 + C_xy_2_1;
      end

        C_xy = C_xy_1 + C_xy_2;
        % Generate r_xy vs k values
        r_xy_56(j) = C_xy/(C_xx*C_yy)^0.5;
        k56_1(j) = k56;
end

% Display the values for maximum cross correlation coefficient and
% corresponsing value for time shift
R_max_56 = max(r_xy_56);
index_desired = find(max(r_xy_56)==r_xy_56(1,:));
K_R_max_56 = k56_1(1,index_desired);

desired_line_x = [K_R_max_56 K_R_max_56];
desired_line_y = [0 R_max_56];
subplot(3,3,4),plot(0,r_xy_0_56,k56_1,r_xy_56,desired_line_x,desired_line_y,'--')
xlabel('Time shift (Sec)');
ylabel('Cross correlation coefficient');
title('T5-T6');
text(K_R_max_56,R_max_56,(num2str([K_R_max_56 R_max_56])),'VerticalAlignment','bottom');

%%%%%%%%%%%%%%%%%%%%%%%%%%%%%%%%%%%%%%%%%%%%%%%%%%%%%%%%%%%%%
%%%%%%%%%%%%%%%
%TC06 & TC07
%%%%%%%%%%%%%%%%%%%%%%%%%%%%%%%%%%%%%%%%%%%%%%%%%%%%%%%%%%%%%
%%%%%%%%%%%%%%%

% Mean of T1 & T2
T1M = mean (data(:,7));
T2M = mean (data(:,8));

% Calculate C_xx & C_yy
C_xx = 0;
C_yy = 0;
for i = 1:N
```

```
   C_xx_1 = (data(i,7)-T1M)^2;
   C_yy_1 = (data(i,8)-T2M)^2;
C_xx = C_xx + C_xx_1;
C_yy = C_yy + C_yy_1;
end

% Calculate C_xy_0
C_xy_0 = 0;
for i = 1:N
   C_xy_0_1 = (data(i,7)-T1M)*(data(i,8)-T2M);
C_xy_0 = C_xy_0 + C_xy_0_1;
end

% Calculate r_xy_0
r_xy_0_67 = C_xy_0/(C_xx*C_yy)^0.5;

% Calculate r_xy as a function of k values
j = 0;
for k67 = 0.02:0.02:5;

   % For storing the k values
   j = j+1;

   N1 = data(end,1)-data(1,1);
   C_xy_1 = 0;
   C_xy_2 = 0;

   % To deal with jitter, 1/f is used in stead of actual time
   for t = 0:(1/f):(N1-k67);

        % Read x_t
        i1 = 1:N;
        temp1 = abs((data(1,1)+t)-data(i1,1));
        [index1 index1] = min(temp1);
        x_t = data(index1,7);

        % Read y_t_k
        i2 = 1:N;
        temp2 = abs((data(1,1)+t+k67)-data(i2,1));
        [index2 index2] = min(temp2);
        y_t_k = data(index2,8);

        C_xy_1_1 = (x_t-T1M)*(y_t_k-T2M);
        C_xy_1 = C_xy_1 + C_xy_1_1;
```

```
   end

      for t = (N1-k67+(1/f)):(1/f):N1;

         % Read x_t
         i3 = 1:N;
         temp3 = abs((data(1,1)+t)-data(i3,1));
         [index3 index3] = min(temp3);
         x_t = data(index3,7);

         % Read y_t_k_N
         i4 = 1:N;
         temp4 = abs((data(1,1)+t+k67-N)-data(i4,1));
         [index4 index4] = min(temp4);
         y_t_k_N = data(index4,8);

         C_xy_2_1 = (x_t-T1M)*(y_t_k_N-T2M);
         C_xy_2 = C_xy_2 + C_xy_2_1;
      end

         C_xy = C_xy_1 + C_xy_2;
         % Generate r_xy vs k values
         r_xy_67(j) = C_xy/(C_xx*C_yy)^0.5;
         k67_1(j) = k67;
end

% Display the values for maximum cross correlation coefficient and
% corresponsing value for time shift
R_max_67 = max(r_xy_67);
index_desired = find(max(r_xy_67)==r_xy_67(1,:));
K_R_max_67 = k67_1(1,index_desired);

desired_line_x = [K_R_max_67 K_R_max_67];
desired_line_y = [0 R_max_67];
subplot(3,3,5),plot(0,r_xy_0_67,k67_1,r_xy_67,desired_line_x,desired_line_y,'--')
xlabel('Time shift (Sec)');
ylabel('Cross correlation coefficient');
title('T6-T7');
text(K_R_max_67,R_max_67,(num2str([K_R_max_67 R_max_67])),'VerticalAlignment','bottom');

%%%%%%%%%%%%%%%%%%%%%%%%%%%%%%%%%%%%%%%%%%%%%%%%%%%%%
%%%%%%%%%%%%%%
%TC07 & TC08
```

```
%%%%%%%%%%%%%%%%%%%%%%%%%%%%%%%%%%%%%%%%%%%%%%%%%%%%%%%%%%%%%%%%%%%%%%%%%%%%%%%%%%%%%%%%%%
%%%%%%%%%%%%%%%%%%%%%%%

% Mean of T1 & T2
T1M = mean (data(:,8));
T2M = mean (data(:,9));

% Calculate C_xx & C_yy
C_xx = 0;
C_yy = 0;
for i = 1:N
   C_xx_1 = (data(i,8)-T1M)^2;
   C_yy_1 = (data(i,9)-T2M)^2;
C_xx = C_xx + C_xx_1;
C_yy = C_yy + C_yy_1;
end

% Calculate C_xy_0
C_xy_0 = 0;
for i = 1:N
   C_xy_0_1 = (data(i,8)-T1M)*(data(i,9)-T2M);
C_xy_0 = C_xy_0 + C_xy_0_1;
end

% Calculate r_xy_0
r_xy_0_78 = C_xy_0/(C_xx*C_yy)^0.5;

% Calculate r_xy as a function of k values
j = 0;
for k78 = 0.02:0.02:5;

   % For storing the k values
   j = j+1;

   N1 = data(end,1)-data(1,1);
   C_xy_1 = 0;
   C_xy_2 = 0;

   % To deal with jitter, 1/f is used in stead of actual time
   for t = 0:(1/f):(N1-k78);

       % Read x_t
       i1 = 1:N;
       temp1 = abs((data(1,1)+t)-data(i1,1));
```

```
        [index1 index1] = min(temp1);
        x_t = data(index1,8);

        % Read y_t_k
        i2 = 1:N;
        temp2 = abs((data(1,1)+t+k78)-data(i2,1));
        [index2 index2] = min(temp2);
        y_t_k = data(index2,9);

        C_xy_1_1 = (x_t-T1M)*(y_t_k-T2M);
        C_xy_1 = C_xy_1 + C_xy_1_1;
    end

    for t = (N1-k78+(1/f)):(1/f):N1;

        % Read x_t
        i3 = 1:N;
        temp3 = abs((data(1,1)+t)-data(i3,1));
        [index3 index3] = min(temp3);
        x_t = data(index3,8);

        % Read y_t_k_N
        i4 = 1:N;
        temp4 = abs((data(1,1)+t+k67-N)-data(i4,1));
        [index4 index4] = min(temp4);
        y_t_k_N = data(index4,9);

        C_xy_2_1 = (x_t-T1M)*(y_t_k_N-T2M);
        C_xy_2 = C_xy_2 + C_xy_2_1;
    end

        C_xy = C_xy_1 + C_xy_2;
        % Generate r_xy vs k values
        r_xy_78(j) = C_xy/(C_xx*C_yy)^0.5;
        k78_1(j) = k78;
end

% Display the values for maximum cross correlation coefficient and
% corresponsing value for time shift
R_max_78 = max(r_xy_78);
index_desired = find(max(r_xy_78)==r_xy_78(1,:));
K_R_max_78 = k78_1(1,index_desired);

desired_line_x = [K_R_max_78 K_R_max_78];
```

```
desired_line_y = [0 R_max_78];
subplot(3,3,6),plot(0,r_xy_0_78,k78_1,r_xy_78,desired_line_x,desired_line_y,'--')
xlabel('Time shift (Sec)');
ylabel('Cross correlation coefficient');
title('T7-T8');
text(K_R_max_78,R_max_78,(num2str([K_R_max_78 R_max_78])),'VerticalAlignment','bottom');

%%%%%%%%%%%%%%%%%%%%%%%%%%%%%%%%%%%%%%%%%%%%%%%%%%%%%%%%%%%%%%%%
%%%%%%%%%%%%%%%
%TC09 & TC10
%%%%%%%%%%%%%%%%%%%%%%%%%%%%%%%%%%%%%%%%%%%%%%%%%%%%%%%%%%%%%%%%
%%%%%%%%%%%%%%%

% Mean of T1 & T2
T1M = mean (data(:,10));
T2M = mean (data(:,11));

% Calculate C_xx & C_yy
C_xx = 0;
C_yy = 0;
for i = 1:N
   C_xx_1 = (data(i,10)-T1M)^2;
   C_yy_1 = (data(i,11)-T2M)^2;
C_xx = C_xx + C_xx_1;
C_yy = C_yy + C_yy_1;
end

% Calculate C_xy_0
C_xy_0 = 0;
for i = 1:N
   C_xy_0_1 = (data(i,10)-T1M)*(data(i,11)-T2M);
C_xy_0 = C_xy_0 + C_xy_0_1;
end

% Calculate r_xy_0
r_xy_0_0910 = C_xy_0/(C_xx*C_yy)^0.5;

% Calculate r_xy as a function of k values
j = 0;
for k0910 = 0.02:0.02:5;

   % For storing the k values
   j = j+1;
```

```
N1 = data(end,1)-data(1,1);
C_xy_1 = 0;
C_xy_2 = 0;

% To deal with jitter, 1/f is used in stead of actual time
for t = 0:(1/f):(N1-k0910);

    % Read x_t
    i1 = 1:N;
    temp1 = abs((data(1,1)+t)-data(i1,1));
    [index1 index1] = min(temp1);
    x_t = data(index1,10);

    % Read y_t_k
    i2 = 1:N;
    temp2 = abs((data(1,1)+t+k0910)-data(i2,1));
    [index2 index2] = min(temp2);
    y_t_k = data(index2,11);

    C_xy_1_1 = (x_t-T1M)*(y_t_k-T2M);
    C_xy_1 = C_xy_1 + C_xy_1_1;
end

  for t = (N1-k0910+(1/f)):(1/f):N1;

    % Read x_t
    i3 = 1:N;
    temp3 = abs((data(1,1)+t)-data(i3,1));
    [index3 index3] = min(temp3);
    x_t = data(index3,10);

    % Read y_t_k_N
    i4 = 1:N;
    temp4 = abs((data(1,1)+t+k0910-N)-data(i4,1));
    [index4 index4] = min(temp4);
    y_t_k_N = data(index4,11);

    C_xy_2_1 = (x_t-T1M)*(y_t_k_N-T2M);
    C_xy_2 = C_xy_2 + C_xy_2_1;
  end

    C_xy = C_xy_1 + C_xy_2;
    % Generate r_xy vs k values
    r_xy_0910(j) = C_xy/(C_xx*C_yy)^0.5;
```

```
        k0910_1(j) = k0910;
end

% Display the values for maximum cross correlation coefficient and
% corresponsing value for time shift
R_max_0910 = max(r_xy_0910);
index_desired = find(max(r_xy_0910)==r_xy_0910(1,:));
K_R_max_0910 = k0910_1(1,index_desired);

desired_line_x = [K_R_max_0910 K_R_max_0910];
desired_line_y = [0 R_max_0910];
subplot(3,3,7),plot(0,r_xy_0_0910,k0910_1,r_xy_0910,desired_line_x,desired_line_y,'--')
xlabel('Time shift (Sec)');
ylabel('Cross correlation coefficient');
title('T09-T10');
text(K_R_max_0910,R_max_0910,(num2str([K_R_max_0910
R_max_0910])),'VerticalAlignment','bottom');

%%%%%%%%%%%%%%%%%%%%%%%%%%%%%%%%%%%%%%%%%%%%%%%%%%%%%%%%%%%%%%
%%%%%%%%%%%%%%
%TC10 & TC11
%%%%%%%%%%%%%%%%%%%%%%%%%%%%%%%%%%%%%%%%%%%%%%%%%%%%%%%%%%%%%%
%%%%%%%%%%%%%%

% Mean of T1 & T2
T1M = mean (data(:,11));
T2M = mean (data(:,12));

% Calculate C_xx & C_yy
C_xx = 0;
C_yy = 0;
for i = 1:N
   C_xx_1 = (data(i,11)-T1M)^2;
   C_yy_1 = (data(i,12)-T2M)^2;
C_xx = C_xx + C_xx_1;
C_yy = C_yy + C_yy_1;
end

% Calculate C_xy_0
C_xy_0 = 0;
for i = 1:N
   C_xy_0_1 = (data(i,11)-T1M)*(data(i,12)-T2M);
C_xy_0 = C_xy_0 + C_xy_0_1;
end
```

```
% Calculate r_xy_0
r_xy_0_1011 = C_xy_0/(C_xx*C_yy)^0.5;

% Calculate r_xy as a function of k values
j = 0;
for k1011 = 0.02:0.02:5;

   % For storing the k values
   j = j+1;

   N1 = data(end,1)-data(1,1);
   C_xy_1 = 0;
   C_xy_2 = 0;

   % To deal with jitter, 1/f is used in stead of actual time
   for t = 0:(1/f):(N1-k1011);

        % Read x_t
        i1 = 1:N;
        temp1 = abs((data(1,1)+t)-data(i1,1));
        [index1 index1] = min(temp1);
        x_t = data(index1,11);

        % Read y_t_k
        i2 = 1:N;
        temp2 = abs((data(1,1)+t+k1011)-data(i2,1));
        [index2 index2] = min(temp2);
        y_t_k = data(index2,12);

        C_xy_1_1 = (x_t-T1M)*(y_t_k-T2M);
        C_xy_1 = C_xy_1 + C_xy_1_1;
   end

     for t = (N1-k1011+(1/f)):(1/f):N1;

        % Read x_t
        i3 = 1:N;
        temp3 = abs((data(1,1)+t)-data(i3,1));
        [index3 index3] = min(temp3);
        x_t = data(index3,11);

        % Read y_t_k_N
        i4 = 1:N;
```

```
        temp4 = abs((data(1,1)+t+k1011-N)-data(i4,1));
        [index4 index4] = min(temp4);
        y_t_k_N = data(index4,12);

        C_xy_2_1 = (x_t-T1M)*(y_t_k_N-T2M);
        C_xy_2 = C_xy_2 + C_xy_2_1;
      end

        C_xy = C_xy_1 + C_xy_2;
        % Generate r_xy vs k values
        r_xy_1011(j) = C_xy/(C_xx*C_yy)^0.5;
        k1011_1(j) = k1011;
end

% Display the values for maximum cross correlation coefficient and
% corresponsing value for time shift
R_max_1011 = max(r_xy_1011);
index_desired = find(max(r_xy_1011)==r_xy_1011(1,:));
K_R_max_1011 = k1011_1(1,index_desired);

desired_line_x = [K_R_max_1011 K_R_max_1011];
desired_line_y = [0 R_max_1011];
subplot(3,3,8),plot(0,r_xy_0_1011,k1011_1,r_xy_1011,desired_line_x,desired_line_y,'--')
xlabel('Time shift (Sec)');
ylabel('Cross correlation coefficient');
title('T10-T11');
text(K_R_max_1011,R_max_1011,(num2str([K_R_max_1011
R_max_1011])),'VerticalAlignment','bottom');

%%%%%%%%%%%%%%%%%%%%%%%%%%%%%%%%%%%%%%%%%%%%%%%%%%%%%%%%
%%%%%%%%%%%%%
%TC11 & TC12
%%%%%%%%%%%%%%%%%%%%%%%%%%%%%%%%%%%%%%%%%%%%%%%%%%%%%%%%
%%%%%%%%%%%%%

% Mean of T1 & T2
T1M = mean (data(:,12));
T2M = mean (data(:,13));

% Calculate C_xx & C_yy
C_xx = 0;
C_yy = 0;
for i = 1:N
  C_xx_1 = (data(i,12)-T1M)^2;
```

```
   C_yy_1 = (data(i,13)-T2M)^2;
C_xx = C_xx + C_xx_1;
C_yy = C_yy + C_yy_1;
end

% Calculate C_xy_0
C_xy_0 = 0;
for i = 1:N
   C_xy_0_1 = (data(i,12)-T1M)*(data(i,13)-T2M);
C_xy_0 = C_xy_0 + C_xy_0_1;
end

% Calculate r_xy_0
r_xy_0_1112 = C_xy_0/(C_xx*C_yy)^0.5;

% Calculate r_xy as a function of k values
j = 0;
for k1112 = 0.02:0.02:5;

   % For storing the k values
   j = j+1;

   N1 = data(end,1)-data(1,1);
   C_xy_1 = 0;
   C_xy_2 = 0;

   % To deal with jitter, 1/f is used in stead of actual time
   for t = 0:(1/f):(N1-k1112);

        % Read x_t
        i1 = 1:N;
        temp1 = abs((data(1,1)+t)-data(i1,1));
        [index1 index1] = min(temp1);
        x_t = data(index1,12);

        % Read y_t_k
        i2 = 1:N;
        temp2 = abs((data(1,1)+t+k1112)-data(i2,1));
        [index2 index2] = min(temp2);
        y_t_k = data(index2,13);

        C_xy_1_1 = (x_t-T1M)*(y_t_k-T2M);
        C_xy_1 = C_xy_1 + C_xy_1_1;
   end
```

```
      for t = (N1-k1112+(1/f)):(1/f):N1;

         % Read x_t
         i3 = 1:N;
         temp3 = abs((data(1,1)+t)-data(i3,1));
         [index3 index3] = min(temp3);
         x_t = data(index3,12);

         % Read y_t_k_N
         i4 = 1:N;
         temp4 = abs((data(1,1)+t+k1112-N)-data(i4,1));
         [index4 index4] = min(temp4);
         y_t_k_N = data(index4,13);

         C_xy_2_1 = (x_t-T1M)*(y_t_k_N-T2M);
         C_xy_2 = C_xy_2 + C_xy_2_1;
      end

         C_xy = C_xy_1 + C_xy_2;
         % Generate r_xy vs k values
         r_xy_1112(j) = C_xy/(C_xx*C_yy)^0.5;
         k1112_1(j) = k1112;
end

% Display the values for maximum cross correlation coefficient and
% corresponsing value for time shift
R_max_1112 = max(r_xy_1112);
index_desired = find(max(r_xy_1112)==r_xy_1112(1,:));
K_R_max_1112 = k1112_1(1,index_desired);

desired_line_x = [K_R_max_1112 K_R_max_1112];
desired_line_y = [0 R_max_1112];
subplot(3,3,9),plot(0,r_xy_0_1112,k1112_1,r_xy_1112,desired_line_x,desired_line_y,'--')
xlabel('Time shift (Sec)');
ylabel('Cross correlation coefficient');
title('T11-T12');
text(K_R_max_1112,R_max_1112,(num2str([K_R_max_1112
R_max_1112])),'VerticalAlignment','bottom');

%%%%%%%%%%%%%%%%%%%%%%%%%%%%%%%%%%%%%%%%%%%%%%%%%%%%%%%%%%%%
%%%%%%%%%%%%%%
%Calculation of Solid Circulation Rate
```

```
%%%%%%%%%%%%%%%%%%%%%%%%%%%%%%%%%%%%%%%%%%%%%%%%%%%%%%%%
%%%%%%%%%%%%%%

%Calculation of velocities, m/s

V12 = L12/K_R_max_12;
V23 = L23/K_R_max_23;
V34 = L34/K_R_max_34;

V56 = L12/K_R_max_56;
V67 = L23/K_R_max_67;
V78 = L34/K_R_max_78;

V0910 = L12/K_R_max_0910;
V1011 = L23/K_R_max_1011;
V1112 = L34/K_R_max_1112;

%Calculation of Gs in pipe, kg/m2-s

GsP12 = V12*rho_b;
GsP23 = V23*rho_b;
GsP34 = V34*rho_b;

GsP56 = V56*rho_b;
GsP67 = V67*rho_b;
GsP78 = V78*rho_b;

GsP0910 = V0910*rho_b;
GsP1011 = V1011*rho_b;
GsP1112 = V1112*rho_b;

%Calculation of Gs in riser, kg/m2-s

GsR12 = GsP12*(Dp/Dr)^2;
GsR23 = GsP23*(Dp/Dr)^2;
GsR34 = GsP34*(Dp/Dr)^2;

GsR56 = GsP56*(Dp/Dr)^2;
GsR67 = GsP67*(Dp/Dr)^2;
GsR78 = GsP78*(Dp/Dr)^2;

GsR0910 = GsP0910*(Dp/Dr)^2;
GsR1011 = GsP1011*(Dp/Dr)^2;
GsR1112 = GsP1112*(Dp/Dr)^2;
```

```
% Collection of all result values in a table
Table = [12 R_max_12 K_R_max_12 V12 GsP12 GsR12;23 R_max_23 K_R_max_23 V23 GsP23 GsR23;34
R_max_34 K_R_max_34 V34 GsP34 GsR34;56 R_max_56 K_R_max_56 V56 GsP56 GsR56;67 R_max_67
K_R_max_67 V67 GsP67 GsR67;78 R_max_78 K_R_max_78 V78 GsP78 GsR78;910 R_max_0910
K_R_max_0910 V0910 GsP0910 GsR0910;1011 R_max_1011 K_R_max_1011 V1011 GsP1011
GsR1011;1112 R_max_1112 K_R_max_1112 V1112 GsP1112 GsR1112];

% Use current time and date in the file
date_time = datestr(now);

% Save all result values in a file
fid = fopen('Gs.txt','at');
fprintf(fid,date_time);
fprintf(fid,'\n');
fprintf(fid,'\n');
fprintf(fid,'TC\t Max XC coeff\t Time Shift(s)\t Velocity(m/s)\t Pipe Gs(kg/m2-s)\t Riser Gs(kg/m2-s)\n');
fprintf(fid,'%4.0f\t %12.4f\t %12.2f\t %12.4f\t %12.1f\t %12.1f\n',Table(1,1:6));
fprintf(fid,'%4.0f\t %12.4f\t %12.2f\t %12.4f\t %12.1f\t %12.1f\n',Table(2,1:6));
fprintf(fid,'%4.0f\t %12.4f\t %12.2f\t %12.4f\t %12.1f\t %12.1f\n',Table(3,1:6));
fprintf(fid,'%4.0f\t %12.4f\t %12.2f\t %12.4f\t %12.1f\t %12.1f\n',Table(4,1:6));
fprintf(fid,'%4.0f\t %12.4f\t %12.2f\t %12.4f\t %12.1f\t %12.1f\n',Table(5,1:6));
fprintf(fid,'%4.0f\t %12.4f\t %12.2f\t %12.4f\t %12.1f\t %12.1f\n',Table(6,1:6));
fprintf(fid,'%4.0f\t %12.4f\t %12.2f\t %12.4f\t %12.1f\t %12.1f\n',Table(7,1:6));
fprintf(fid,'%4.0f\t %12.4f\t %12.2f\t %12.4f\t %12.1f\t %12.1f\n',Table(8,1:6));
fprintf(fid,'%4.0f\t %12.4f\t %12.2f\t %12.4f\t %12.1f\t %12.1f\n',Table(9,1:6));
fprintf(fid,'\n');
fprintf(fid,'\n');
fprintf(fid,'\n');
fprintf(fid,'\n');
fclose(fid);

% Save figure into a file
formatout = 'yyyy_mm_dd_HH_MM_SS';
fname = datestr(now,formatout);
saveas(gcf,fname,'fig');

% Display the results in commande window
disp('  TC   Max XC coeff  Time shift(s)  Velocity(m/s) Pipe Gs(kg/m2-s) Riser Gs(kg/m2-s)')
disp('')
disp(num2str(Table))
```

Appendix C: Manuscript of paper authored by Daniel et al.[2]

ESTIMATION OF SOLID CIRCULATION RATE AND CHAR TRANSFER RATE FROM GASIFIER TO COMBUSTOR IN A DUAL FLUIDIZED BED PILOT PLANT FOR BIOMASS STEAM GASIFICATION

Daniel, L., Shah, U.D., Rahman, M.H., Bi, X.T., Grace, J.R. and Lim, C.J., Department of Chemical and Biological Engineering, University of British Columbia, 2360 East Mall, Vancouver, Canada V6T 1Z3.

Abstract

The operation of a dual fluidized bed (DFB) plant, consisting of a riser as combustor and a bubbling bed as gasifier, for synthesis gas production from solid fuel such as biomass requires the determination of solid circulation rate and char transfer rate from the gasifier to the combustor. The system performance relies on supplying sufficient heat from the combustor to the gasifier via solids circulation between these two reactors. The flow rate of char from gasifier to combustor also needs to be determined to track the heat generated in the combustor which supports endothermic reactions in the gasifier. Direct

[2] The author wrote the manuscript of the paper provided in Appendix C, and also acted as the co-supervisor of Mr. Lius Daniel's Masters research project.

measurements of these two critical parameters are difficult, with the number of reported techniques capable of working at high temperatures extremely small.

A novel method of using mass and energy balances to estimate both solid circulation rate and char transfer rate was developed. These balances are performed over the entire DFB system and over individual reactors. Heat losses to the surrounding are estimated both from energy balance calculations and from direct measurement of the outer surface temperature of the reactor wall and insulation assembly. General agreement has been found between these two methods. Under typical gasification conditions, the solid circulation fluxes were estimated to be 45.2 and 55.6 kg/m^2-s in two independent tests, in good agreement with values obtained from experiments using a thermal-tracing technique. The char transfer rates from the gasifier to combustor were calculated to be 1.2 and 0.6 kg/h, respectively, in reasonable agreement with average biomass feed rates. The new method can be applied to dual gasification systems at any temperature or flow rate.

Introduction

The depletion of fossil fuel resources, rising energy demand, and environmental concerns related to increasing greenhouse gas emissions demand cleaner and sustainable energy sources. Biomass is a promising energy source for the future since it is abundantly available as waste and produces almost zero net carbon emissions. In 2010, the utilization of woody biomass contributed approximately 9% to world energy production and 65% of renewable energy production. It is estimated that biomass could meet 10-40% of the world's primary energy consumption demand if all the resources were utilized [1].

The potential of biomass, however, depends not only on the availability of the biomass resources, but also on its efficient utilization. Therefore, finding the most efficient way to convert biomass into useful energy products is very important.

Biomass particles can be gasified with steam instead of air to avoid nitrogen in the product gas and consequently to ensure a high heating value of the syngas, which can be used in combined heat and power (CHP) production plants or for the synthesis of fuels or value-added chemicals. In addition, injection of a metal oxide sorbent could capture carbon-dioxide to produce high-quality syngas with high hydrogen concentration and negative CO_2 emission, with tar minimized or even eliminated.

Gasification of biomass with steam involves a number of endothermic reactions occurring at temperatures above 700°C. The required heat can be obtained from combustion of part of the char produced in the gasifier. This can be accomplished in two ways – by injecting oxygen to directly burn these char particles in the gasifier or, by burning the char in a separate combustor and circulating an inert heat carrier such as sand to transfer heat to the gasifier from the combustor [2]. The latter is preferred, as the injection of air or oxygen into the gasifier lowers the heating value and purity of the syngas [3], preventing it from direct use for synthesis of biofuels and bio-products. Consequently, the gasification system requires not only a biomass steam gasifier, but also a char combustor. Fluidized bed reactors are appropriate because of their ability to circulate particles between vessels. One promising option is to combine a bubbling fluidized bed (BFB) as the gasifier and a circulating fluidized bed (CFB) riser as the combustor to create a so-called “dual fluidized bed” (DFB) system [4].

The circulation rate of inert heat-carrying bed material (generally known as solid circulation rate) between the two fluidized beds is one of the critical operating parameters of the DFB system as it directly affects hydrodynamics, heat and mass balance in both reactors and thereby strongly influences their performances. The transfer rate of biomass char from BFB gasifier to CFB combustor controls the amount of heat generated in the combustor that is transferred to the gasifier which in turn controls the production of syngas in the gasifier. The determination of these two parameters is essential for design, scale-up and operation of commercial-scale DFB gasification systems.

Techniques for direct measurement of solid circulation rate have been under development for several decades [5–12]. These and other potential techniques were reviewed by Rahman et al. [13], who introduced a thermal-tracing technique which was able to measure solid circulation rates over a wide range of temperatures and flow rates, with the method applied at temperatures up to 856°C.

In this paper, an overall energy balance analysis is applied to commercial reactor systems to estimate the solids circulation rate between reactors, such as in a fluid catalytic cracking reactor and catalyst regenerator or a fluid coking reactor and coke combustor. To our knowledge, there has been no previously reported attempt to estimate both solids circulation rate and char burning rate in a dual fluidized bed reactor system. This paper proposes an indirect method of estimating both the solids circulation rate and char transfer rate using mass and energy balances over the gasifier and combustor. The results are compared with those derived from the thermal-tracing technique developed by Rahman et al. [13]. The application of this method is not limited to particular ranges of circulation, transfer rates or temperatures.

General description of system

A dual fluidized bed reactor system for steam gasification of biomass was built at the University of British Columbia. Figure provides a schematic diagram. An inert bed material continuously circulates between the CFB combustor and BFB gasifier. Sand of average diameter 170 μm and bulk density 1450 kg/m^3 is the inert bed material. When biomass particles are fed into the gasifier and exposed to temperatures as high as 700°C, the moisture of the particles is evaporated. With steam fed to the gasifier, the dry particles decompose and react to produce char and volatile components including tars. The initial devolatilization gases are carbon monoxide (CO), carbon dioxide (CO_2), hydrogen (H_2) and methane (CH_4) [14]. The char constituents are mainly carbon and small amount of ash. Some of the char undergoes heterogeneous gas-solid reactions with steam, producing CO, CO_2, H_2 and CH_4. However, most of the char from the gasifier is transferred to the combustor where it is burned with excess air. The heat generated raises the temperature of sand particles in the combustor. These sand particles carry heat back to the gasifier, and release heat to sustain gasification reactions whose net effects are endothermic. The syngas produced in the gasifier mainly consists of CO, CO_2, H_2, H_2O and CH_4.

Because of heat loss from the pilot system, the combustion of char alone is insufficient to maintain the desired operating temperature of the riser combustor. Natural gas (NG) is therefore combusted in a separate burner and the resulting hot gas is fed to the combustor through the air inlet. The air flow is selected in such a way that it provides adequate oxygen for the complete combustion of not only the natural gas, but also the char. Combustion gases from both these fuels are separated from bed material in the cyclone and leave the system. This flue gas mixture contains CO, CO_2, inert N_2, O_2 and H_2O.

The flow rates of biomass, steam, air and natural gas are metered before entering the system. A number of temperature and pressure sensors are installed across the system. An online flue gas analyzer measures the concentrations of its non-condensable components; whereas the dry composition of syngas is obtained by an online gas chromatograph. A small number of sand particles escape from the closed loop with the flue gas at the cyclone. The rate of sand loss from the system is determined by collecting the sands downstream and an equal amount of fresh sand is continuously added to the system to make up for the loss.

Mass and energy balance

Mass and energy balance analyses are performed over each reactor and over the entire DFB system. These calculations allow the determination of solid circulation in the system and char transfer rate from BFB gasifier to CFB combustor. Figure shows block diagrams for mass and energy balances over the system with information of key operating conditions included for the first test reported below. Figure provides the block diagrams for the second test.

Since the solid circulation rate is the same all over the system because of continuous sand addition to make up for the loss and all sand particles are inert to combustion and gasification reactions, their flow rates are the same at the inlet and outlet of each reactor. Hence, the changes in flow rates are not considered for mass balances over the CFB combustor and BFB gasifier.

For simplicity, the functions of the CFB riser and its supporting natural gas burner are lumped together and shown as a single unit labelled CFB in the diagrams. This makes sense as all the gases produced in the burner must pass through the CFB riser. The typical composition of natural gas is 95% methane, 3% other alkanes such as ethane, propane, butane and pentane, and 2% nitrogen [15]. Since the amounts of other alkanes in total are very small compared to that of methane, they are lumped together with methane for ease of calculation. Therefore, natural gas is considered to contain 98% methane and 2% nitrogen. It is assumed that the natural gas is completely combusted in the unit according to

$$CH_4 + 2O_2 \rightarrow CO_2 + 2H_2O \quad (1)$$

The other fuel which undergoes combustion in the CFB riser is char. To simplify the calculation, it is assumed that char particles entering CFB riser carry negligible ash with them. In the calculation, char is considered as pure carbon. Its combustion is given by:

$$C(char) + O_2 \rightarrow CO_2 \quad (2)$$

Sufficient air is provided to allow complete combustion of char particles. Compressed air is pre-heated to temperatures above 275°C and then fed to the NG burner as sources of O_2 there and for the downstream CFB riser. Air also acts as fluidizing agent in the CFB riser. Ignoring trace elements, the air is treated as a mixture of N_2 and O_2. The pre-heating of air helps the NG burner maintain a high operating temperature in the CFB riser combustor. Properties of air and natural gas at the CFB riser inlet are provided in Table 1. Superheated steam at about 550°C enters the BFB gasifier to supply O_2 for biomass gasification and to fluidize the bed.

Softwood pellets were used as the biomass feed in the experiments; their composition is assumed to be constant. The ultimate analysis of wood pellets is given in Table 2. Since the amounts of nitrogen and sulfur are small, they are not considered in the calculations. The higher heating value (HHV) of the woody biomass is estimated from the correlation reported by Zainal et al. [16]:

$$\boldsymbol{HHV}\left(\frac{\boldsymbol{MJ}}{\boldsymbol{kg}}\right) = \mathbf{0.23}(\mathbf{146.58} \times \boldsymbol{C} + \mathbf{56.878} \times \boldsymbol{H} - \mathbf{51.53} \times \boldsymbol{O} + \mathbf{29.23}) \quad (3)$$

where C, H and O are mass fractions of carbon, hydrogen and oxygen in the biomass on a dry basis.

The heat capacities of the pure compounds which make up the flue gas and the syngas are estimated as functions of temperature from

$$C_p = a + bT + cT^2 + dT^3 \quad (4)$$

with the values of the coefficients were taken from Felder & Rousseau [17]. The heat capacity of sand is considered to be independent of temperature and is taken as 700 J/kg-K for all calculations.

It is assumed that all char particles generated in the BFB gasifier are transferred to the CFB combustor where they react completely with excess O_2. Hence the char transfer rate is taken as equal to the char burn-out rate in the CFB combustor. This rate (m_7) can be calculated by solving molar balances over the CFB riser. The balances for nitrogen, methane, char, oxygen, carbon-di-oxide and water are given by

$$x_{3,N_2} m_3 + x_{4,N_2} m_4 = x_{6,N_2} m_6 \quad (5)$$

$$x_{3,CH_4} m_3 = n_{r1} \times 16 \quad (6)$$

$$m_7 = n_{r2} \times 12 \quad (7)$$

$$x_{4,O_2} m_4 - (2n_{r1} + n_{r2}) \times 32 = x_{6,O_2} m_6 \quad (8)$$

$$x_{6,CO_2} m_6 = (n_{r1} + n_{r2}) \times 44 \quad (9)$$

$$x_{6,H_2O} m_6 = 2n_{r1} \times 18 \quad (10)$$

where n_{r1} and n_{r2} are the extents of reactions given by Equations (1) and (2), respectively. $x_{i,j}$ denotes mole fraction of component j in stream i. m_i stands for the mass flow rate of stream i.

An energy balance over the BFB gasifier, as shown in Figure , is used to calculate the circulation rate of inert bed material between the two reactors:

$$H_{Biomass} + H_{Steam} - H_{Syngas} - H_{Char} - Q_{BFB+U-Bend} = m_{sand} \times C_{p,sand} \times \left(T_{out,BFB} - T_{in,BFB}\right) \quad (11)$$

The only unknown parameter is the mass flow rate of inert solids (m_{sand}) through the reactor. The change in inert solids' enthalpy is represented by the right side of the above equation. The enthalpy of the biomass feed is estimated using Equation (3). The enthalpy of steam is taken at its inlet temperature of 550°C. The composition of syngas is given by an online gas chromatograph, and its enthalpy is found by adding the enthalpies of the constituent gases. The flow rate of char (m_7) determined above allows one to calculate its enthalpy at the gasifier exit. The enthalpies of syngas and char are estimated using their standard heats of formation at 25°C and the sensible heat needed to raise their temperature to the reactor's temperature. The solids circulation flux (G_s) in terms of riser cross-sectional area (A_{CFB}) is obtained using

$$G_s = \frac{m_{sand}}{A_{CFB}} \tag{12}$$

Heat loss

The estimates of solid circulation rate and char transfer rate depend on energy balances for the combustor, the gasifier and other components of the system such as cyclones and connecting pipes. With all input and output streams accounted for, the only item in the energy balance that needs to be determined is the heat loss. It is estimated by two different methods: (a) heat transfer model for heat loss through the reactor wall; and (b) direct measurement of wall surface temperature.

Due to the small inside diameters of the reactors and other sections of the DFB system, it is assumed that the resistance to heat transfer from the interior of bubbling bed to the inner wall is negligible

compared to the resistance of the inner and the outer walls and losses from the outside to ambient air. Except for the gasifier, all other sections can be treated as two concentric cylinders where a metal pipe is surrounded by a layer of insulation. In the gasifier, there are two layers of insulation inside the metal pipe resulting in three concentric cylinders. The top cover of the BFB also has three layers. They are to be treated as circular flat plates or disks. The material of construction is a high-temperature alloy 800HT for all sections, except the gasifier, whose material is carbon steel. Table 3 presents the material of construction, length, wall thickness, insulation material and thickness for each section.

The change of temperature in the axial direction inside any section of the system is found to be very small compared to the temperature difference between that section and its surroundings. Hence, the temperatures measured along the axial direction are averaged to obtain a representative temperature of that reactor and this average temperature is then used to represent the inside wall temperature. Since the difference between temperatures of the inside wall and the ambient atmosphere is quite large, significant heat transfer by radial conduction occurs through multi-layer assembly of section's wall and insulation material. As a result, the outer wall of that section and insulation assembly attain a temperature much higher than the ambient air temperature. At this temperature, heat is dissipated to the surroundings by natural convection and radiation.

In the model, heat transfer from the outer surfaces is considered to occur only by natural convection. The average heat transfer coefficient due to natural convection at the outermost layer is expressed by

$$Nu = \frac{hL}{k} = p\left(\frac{L^3\rho^2 g\beta\Delta T}{\mu^2}.\frac{C_p\mu}{k}\right)^q = p(Gr.Pr)^q \quad (13)$$

The coefficients p and q were obtained from Geankoplis [18]. The correlations for calculating wall temperature and total heat loss from the BFB gasifier are given by

$$Q_{tot,BFB} = \frac{T_{BFB} - 298}{\sum\frac{\Delta x_i}{k_i A_i} + \frac{1}{h_{ol}A_{ol}}} + \epsilon\sigma A_{ol}\left(T_{wall}^4 - 298^4\right) \quad (14)$$

$$T_{wall} = T_{BFB} - Q_{tot}\left(\frac{1}{h_{ol}A_{ol}} + \frac{r_2 - r_1}{k_1 A_{lm,21}} + \frac{r_3 - r_2}{k_2 A_{lm,32}}\right) \quad (15)$$

where Δx_i, k_i and A_i are the thickness, thermal conductivity and surface area of layer i, respectively; h_{ol} is the convective heat transfer coefficient at the outermost surface of area A_{ol}; subscript 1 denotes the innermost layer, 2 the middle layer and 3 the outermost later; A_{lm} stands for the log-mean cross-sectional area of adjacent layers.

For all other sections including the CFB riser, radiation heat loss is neglected in Equation (14) although each has one less layer of insulation. It is shown below that most heat loss from the system occurs in the BFB gasifier as its surface area is quite large. Hence, neglecting radiation heat losses for all other sections does not significantly affect the distribution of heat loss across the system.

Given the importance of heat loss for the heat balance over each section of the DFB system, heat losses were also estimated from direct measurement of surface temperatures in the system using an infrared

thermometer in combination with a K-type thermocouple connected to a hand-held calibrator. The infrared device provided the convenience of measuring temperatures of hot surfaces without actually going very close to them, whereas the hand-held calibrator was used to tune the infrared device.

Wall surface temperatures were obtained from 9 points in the BFB gasifier, 4 in the CFB riser, 2 in the downcomer, 2 at the U-bend and 2 points on the inclined part of the solid transfer pipe. The number of measurement points was limited, as operators were not allowed to enter some locations during the tests for safety reasons. The locations of measurement points are indicated on Figure . Note that not all the 9 points in the BFB gasifier were chosen along the axial direction. 5 out of 7 axial locations had a single point, whereas the rest had more than one point distributed tangentially on the outer surface. This was done to make sure that non-uniform temperature distribution on the outer surface, possible in a large-diameter vessel such as the BFB gasifier, was taken into account. In the CFB riser, there are 2 points at different angles in the tangential direction at both axial positions. Each axial location had a thermocouple installed to log the inside temperature of that section. With temperatures of both inner layer and outer layer directly measured, the total heat that transfers across all layers (metal plus insulation) were easily calculated by combining the thermal resistances of each layer. In this manner, heat loss due to a combination of forced and natural convection could be determined.

Small amount of heat was transferred by forced convection as several fans were directed toward the DFB system to prevent local build-up of CO or CO_2 if there should be accidental leakage of syngas. The model ignored this heat transfer as the location of reactors and other units very close to each other made the flow pattern of external air too complicated to explore for the purpose of this paper.

However, the measured temperature of the outer surface included the impact of this heat transfer. In the model, the heat losses through flanges, pressure and temperature measurement ports, nitrogen purging connections and reactors' support structures were overlooked as their contributions were likely to be small.

Results and discussion

Heat loss from each section of DFB system obtained from the two independent methods outlined above are compared in Figure . Heat losses are estimated by applying the model to the data from two test runs. The measurements of surface temperature were conducted at a later date by operating the system at a temperature similar to the two earlier tests. In the case of the BFB gasifier, CFB riser, downcomer and U-bend, the heat loss found from measurement of surface temperature was similar to those from the model. It was not possible to measure surface temperatures of the CFB cyclone and the exit pipe of CFB NG burner. However, the model shows that the combined heat loss from these sections was only 4.2% of the total heat loss and therefore is considered not large enough to affect the overall heat loss appreciably. According to the model, the heat losses were 28.1% and 25.0% of the total energy inputs into the system by biomass, steam and natural gas in the two test runs.

The model produces overall heat losses of 36.7 kW and 29.6 kW for the two tests whereas surface temperature measurement gave a heat loss of 37.9 kW. From Figures 2 and 3, it can be seen that the operating temperatures of the CFB combustor and BFB gasifier were much higher in Test 1 than in Test 2. This explains why the overall heat loss during Test 1 was higher than during Test 2. A higher operating

temperature in a reactor creates a larger difference between the temperature inside and the ambient temperature outside, and this temperature difference causes greater heat loss from the reactor. Each of the heat losses from the model is found to be lower than that from the measurement of surface temperatures. That the model delivers lower values can be explained by the fact that it did not consider heat transfer by radiation from any section except BFB and by forced convection from any of the sections. Moreover, the model overlooked the heat losses through flanges, measurement ports, thermocouples and reactor support structures.

Both methods found that most of the overall heat loss from the DFB system occurs from the BFB gasifier. The heat loss from the BFB gasifier is three times of that from all other sections combined, because of its large surface area. Both methods considered heat transfer by radiation from the BFB gasifier. However, the model did not take into account heat transfer due to fan-induced forced convection on the outer surface because of the difficulty in estimating the air velocity near the outer surface of the unit.

With heat loss estimated from the two different methods, the solid circulation rate and the char transfer rate from the BFB gasifier to CFB combustor can be estimated because all other heat balance input and output parameters to the DFB system as a whole were measured and are therefore known.

The solid circulation fluxes are estimated to be 45.2 and 55.6 kg/m^2-s in Tests 1 and 2, respectively. Although this energy balance was conducted over the BFB gasifier, the flux is reported using the cross-sectional area of the CFB riser to enable comparison with information available in the literature. Based

on a thermal-tracing method, Rahman et al. (2017) measured these fluxes to be 36.3 and 46.4 kg/m^2-s under process conditions. Although similar in magnitude to those of Tests 1 and 2, respectively, in each case, the flux estimated in this work is higher than the measured flux. This finding cannot be taken as a general trend as the number of data point is very small. Nevertheless, the general agreement between the rates obtained from these two independent methods is quite encouraging as direct measurement of solid circulation rate at high temperature is very difficult. From Figures 2 and 3, the difference between the temperatures of the CFB combustor and BFB gasifier are calculated to be 110°C and 85°C for Tests 1 and 2, respectively. The smaller temperature difference in the second test occurred due to its higher solids circulation rate compared to the first test.

An oxygen balance over the CFB riser shows 1.2 and 0.6 kg/h burn-out rate of char for the Tests 1 and 2, respectively. Since all char particles that enter the CFB riser are fully combusted in the presence of excess O_2, the char transfer rates from BFB gasifier to the CFB combustor are therefore 1.2 and 0.6 kg/h in these tests. This corresponds to char constituting 12% and 6% of the feed biomass by weight in the respective tests. The lower rate in the second test can be attributed to the lower operating temperature in the gasifier which promotes formation of tar which includes some carbon. However, it was not possible to determine the char transfer rate from another method. No relevant information was found from the literature for comparison.

This determination of solid circulation rate in the overall DFB system and char transfer rate from gasifier to combustor using mass and energy balance calculations required accurate measurement of pressures, temperatures, compositions and flow rates of all input and output streams, and process conditions in

the reactors. In the case of the solid circulation rate, there are few direct methods which can be conveniently applied to large-scale systems being operated at high temperatures. There is no reported technique which can directly measure the char transfer rate from the BFB gasifier to the CFB combustor. Although the indirect method presented in this paper requires considerable background information, it is very useful given the difficulties associated with the direct method. Moreover, the application of this indirect method is not limited to any particular range of flow rate or temperature.

Conclusion

A novel method of estimating solid circulation rate in a dual fluidized bed reactor system and char transfer rate from gasification reactor to combustion reactor is presented. This relies on performing mass and energy balances over the entire system and over individual reactors. As an essential component of the energy balance, heat loss was determined in two ways – a heat balance model and measurement of outer surface temperatures. The values were similar to one another. The solid circulation fluxes were found to be 45.2 and 55.6 kg/m^2-s, both values comparing quite well with the fluxes obtained from a novel thermal-tracing technique. This method is not limited to any particular range of flow rate or temperature. The char transfer rates from the gasifier to the combustor were estimated to be 1.2 and 0.6 kg/h, respectively.

Acknowledgement

The authors are grateful to Yonghua Li and Zhiwei Chen for assistance with the experiments. Funding from the Indonesia Endowment Fund for Education, Natural Sciences and Engineering Research Council of Canada, Carbon Management Canada, British Columbia Bioenergy Network, Dow Chemical Company and Highbury Energy Inc. is also acknowledged with gratitude.

Nomenclature

a, b, c & d	Coefficients for calculating heat capacity (-)
A	Area (m^2)
C_p	Heat capacity (kJ/mol-K)
g	Gravitational acceleration (m/s^2)
Gr	Grashof number (-)
G_s	Solid circulation flux (kg/m^2-s)
h	Convective heat transfer coefficient (W/m^2-K)
H	Energy content (kW)
ΔH_c	Heat of combustion (kJ/mol)
HHV	Higher heating value (kW)
k	Thermal conductivity (W/m-K)
L	Characteristic length (m)

m	Mass flow rate (kg/h)
m_s	Solid circulation rate (kg/h)
n	Extent of reaction (kmol/h)
Nu	Nusselt number (-)
p & q	Constants for calculating heat transfer coefficients (-)
Pr	Prandtl number (-)
Q	Heat loss (kW)
r	Radius (m)
T	Temperature (K)
x	Mole fraction (-)
Δx	Thickness of a layer (m)
β	Volumetric coefficient of expansion of fluid (1/K)
ϵ	Surface emissivity (-)
μ	Viscosity (kg/m-s)
ρ	Density (kg/m^3)
σ	Stefan–Boltzmann constant (W/m^2-K^4)

Subscripts

i	Input/output stream
in	Inlet
j	Gas component

lm	Log mean
ol	Outer layer
out	Outlet

References

[1] P. Lauri, P. Havlik, G. Kindermann, N. Forsell, H. Böttcher, M. Obersteiner, Woody biomass energy potential in 2050, Energy Policy. 66 (2014) 19–31.

[2] X.T. Bi, X. Liu, High density and high solids flux CFB risers for steam gasification of solids fuels, in: Fuel Process. Technol., 2010: pp. 915–920.

[3] P. Basu, B. Acharya, P. Kushal, Design methods for fluidised bed gasifiers: comparison of three approaches, J. Energy Inst. 83 (2010) 32–40.

[4] H. Hofbauer, H. Stoiber, G. Veronik, Gasification of organic material in a novel fluidized bed system, in: Proc. 1st SCEJ Symp. Fluid., Tokyo, 1995.

[5] J.J. Burkell, J.R. Grace, J. Zhao, C.J. Lim, Measurement of solids circulation rates in circulating fluidized beds, in: P. Basu, J.F. Large (Eds.), Circ. Fluid. Bed Technol. II, Pergamon, Oxford, 1988: pp. 501–509.

[6] J.R. Muir, C.M.H. Brereton, J.R. Grace, C.J. Lim, Line-and sinker measurement of solids circulation rate in a CFB combustor, in: U. Arena, R. Chirone, M. Miccio, P. Salatino (Eds.), Fluid. XI, Engineering Conferences International, New York, 2004: pp. 315–322.

[7] J.C. Ludlow, E.R. Monazam, L.J. Shadle, Improvement of continuous solid circulation rate

measurement in a cold flow circulating fluidized bed, Powder Technol. 182 (2008) 379–387.

[8] E.R. Monazam, R. Panday, L.J. Shadle, Estimate of solid flow rate from pressure measurement in circulating fluidized bed, Powder Technol. 203 (2010) 91–97.

[9] E.R. Monazam, L.J. Shadle, A transient method for characterizing flow regimes in a circulating fluid bed, Powder Technol. 139 (2004) 89– 97.

[10] A. Kreuzeder, C. Pfeifer, H. Hofbauer, Fluid-dynamic investigations in a scaled cold model for a dual fluidized bed biomass steam gasification process: Solid flux measurements and optimization of the cyclone, Int. J. Chem. React. Eng. 5 (2007).

[11] C.E. Davies, S.J. Tallon, E.S. Webster, Applications of active acoustics in particle technology, Particuology. 8 (2010) 568–571.

[12] N. Ellis, C.J. Lim, P.A. Reyes, J.I. Soletti, J.R. Grace, Acoustic emissions method for solids mass flux measurements, in: 21st Int. Conf. Fluid. Bed Combust., Naples, 2012: pp. 681–688.

[13] M.H. Rahman, X.T. Bi, J.R. Grace, C.J. Lim, Measurement of solids circulation rate in a high-temperature dual fluidized bed pilot plant, Powder Technol. 316 (2017) 658–669.

[14] J.W. Black, K.G. Bircher, K.A. Chisholm, Fluidized bed gasification of solid wastes and biomass: the CIL Program. Thermal conversion of solid wastes and biomass., Am. Chem. Soc. Symp. Ser. 130 (1979) 351–361.

[15] Material safety data sheet for natural gas, Enbridge, Inc. (2015). https://www.enbridgegas.com/assets/docs/2015 MSDS Natural Gas - English.pdf%0A (accessed July 26, 2017).

[16] Z.A. Zainal, R. Ali, C.H. Lean, K.N. Seetharamu, Prediction of performance of a downdraft gasifier using equilibrium modeling for different biomass materials, Energy Convers. Manag. 42 (2001)

1499–1515.

[17] R.M. Felder, R.W. Rousseau, Elementary Principal of Chemical Processes, 3rd ed., John Wiley & Sons, New York, 2000.

[18] C.J. Geankoplis, Transport Processes and Separation Principles, 4th ed., New Jersey, 2003.

[19] M.M. Yu, M.S. Masnadi, J.R. Grace, X.T. Bi, C.J. Lim, Y. Li, Co-gasification of biosolids with biomass: Thermogravimetric analysis and pilot scale study in a bubbling fluidized bed reactor, Bioresour. Technol. 175 (2015) 51–58.

Table 1: Properties of air and natural gas [15] at CFB riser inlet

	Natural gas	Air
Temperature (°C)	25	280 (Test 1) & 300 (Test 2)
Pressure (atm)	1	1
Composition (% mole)	98% CH_4, 2% N_2	79% N_2, 21% O_2

Table 2: Ultimate analysis of wood pellets [19]

	Content (% wt.)	Normalized Content (% wt.) – N & S free
Carbon (C)	47.8	48.4
Hydrogen (H)	6.4	6.5
Oxygen (O)	44.6	45.1
Nitrogen (N)	0.3	-
Sulphur (S)	0.9	-
Total	100	100

Table 3: Material of construction, length, wall thickness, insulation material and thickness for each section

	Material of construction	Wall thickness (mm)	Length (mm)	Insulation material	Insulation thickness (mm)
BFB gasifier	Carbon steel	9.5	2720	60% alumina brick	88.9
				Board insulator	25.4
U-bend	800 HT	5.5	1225	Ceramic & glass fibre	88.9
CFB riser	800 HT	13.5	6800	Ceramic & glass fibre	88.9
NG Burner pipe	800 HT	6.1	660	Ceramic & glass fibre	88.9
CFB Cyclone	800 HT	15.8	768	Ceramic & glass fibre	88.9
Downcomer sections: Upper & lower	800 HT	7.6 & 5.5	2132 & 2337	Ceramic & glass fibre	88.9

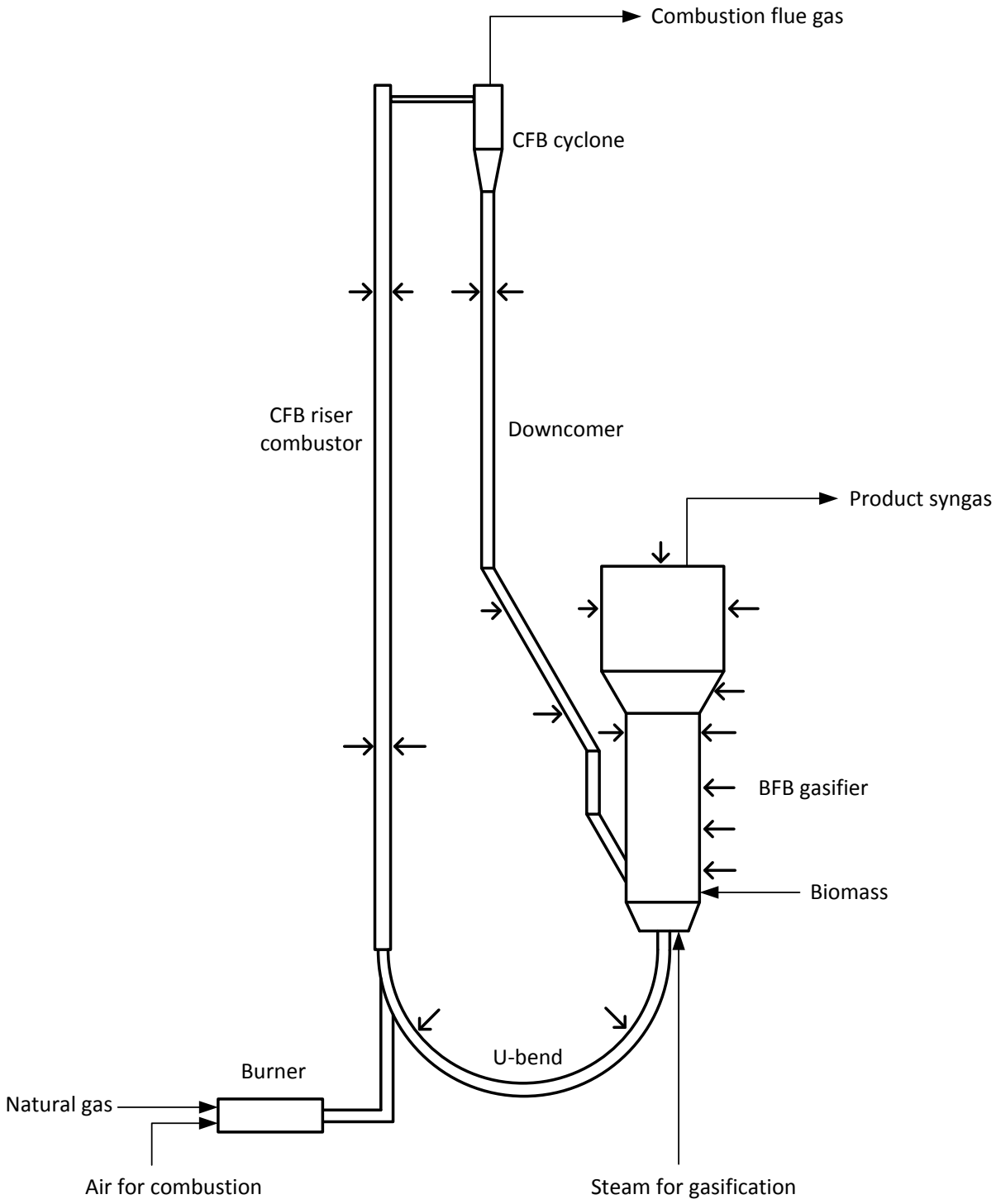

Figure 1: Schematic of DFB pilot plant at the University of British Columbia. Locations of surface temperature measurements are indicated by arrows.

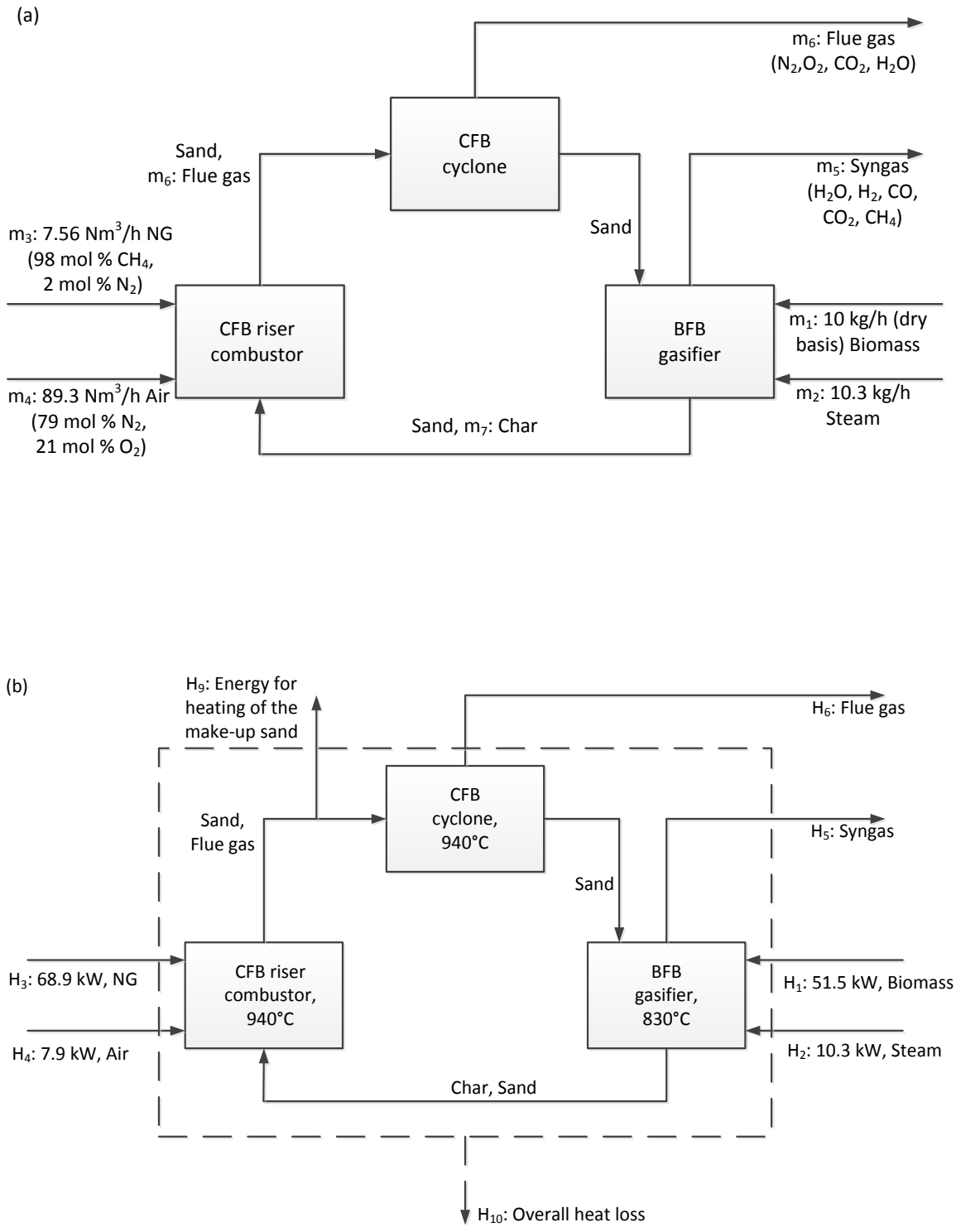

Figure 2: Overall balance over DFB system for Test 1: (a) mass balance; (b) energy balance.

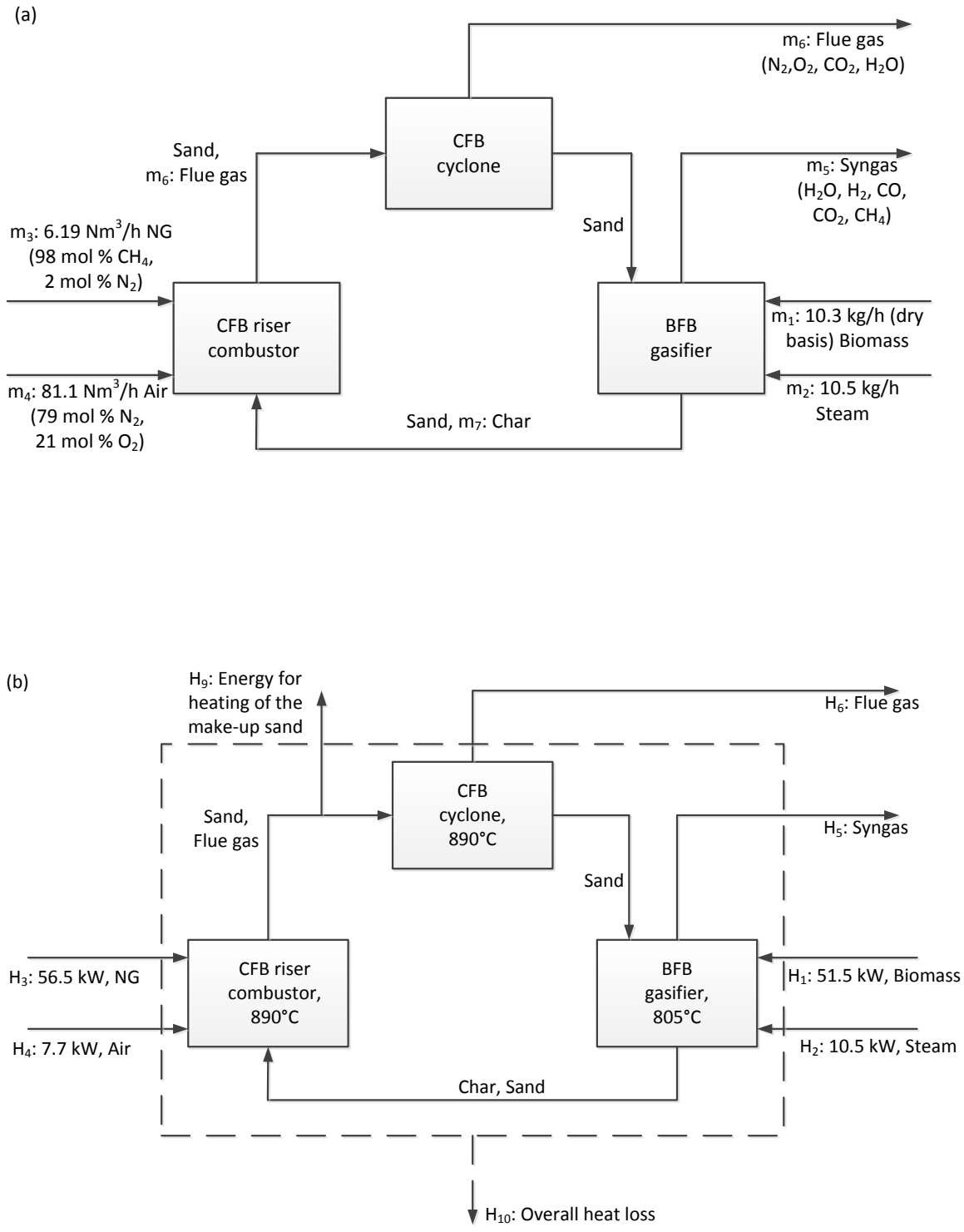

Figure 3: Overall balance over DFB system for Test 2: (a) mass balance; (b) energy balance.

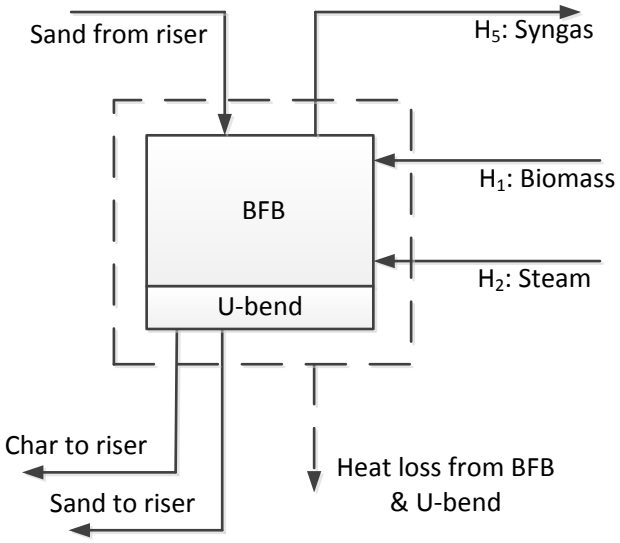

Figure 4: Isolated energy balance over BFB and U-bend to calculate solid circulation rate. (Heat of reactions are included in the estimation of the enthalpies of char and syngas.)

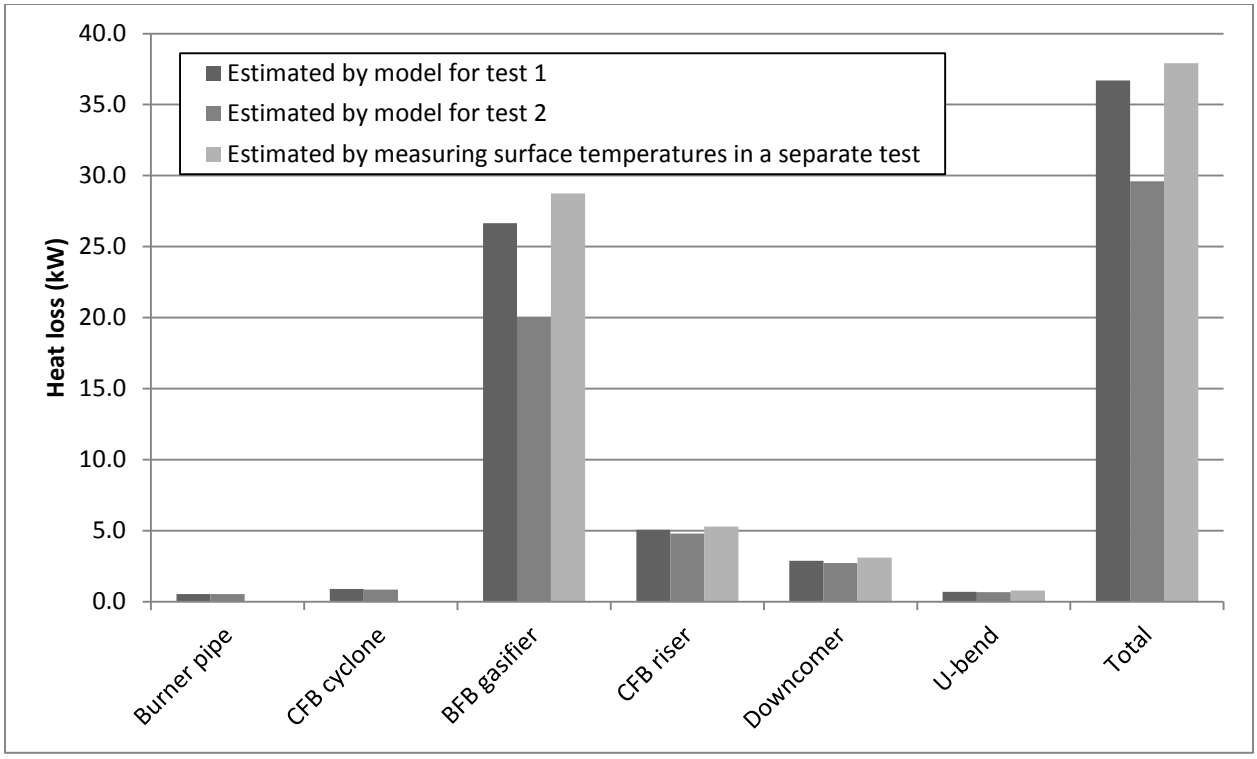

Figure 5: Relative heat losses from different sections of DFB pilot plant using two independent methods. (During surface temperature measurements, the key inside temperatures are T_{CFB}: 890°C, T_{BFB}: 850°C.)

Appendix D: Engineering drawings of butterfly valve

The detained engineering drawings for the construction of butterfly valve and its accessories are provided in this appendix. The imperial units (e.g. length in inch) were used as it was a requirement for construction in the departmental workshop.

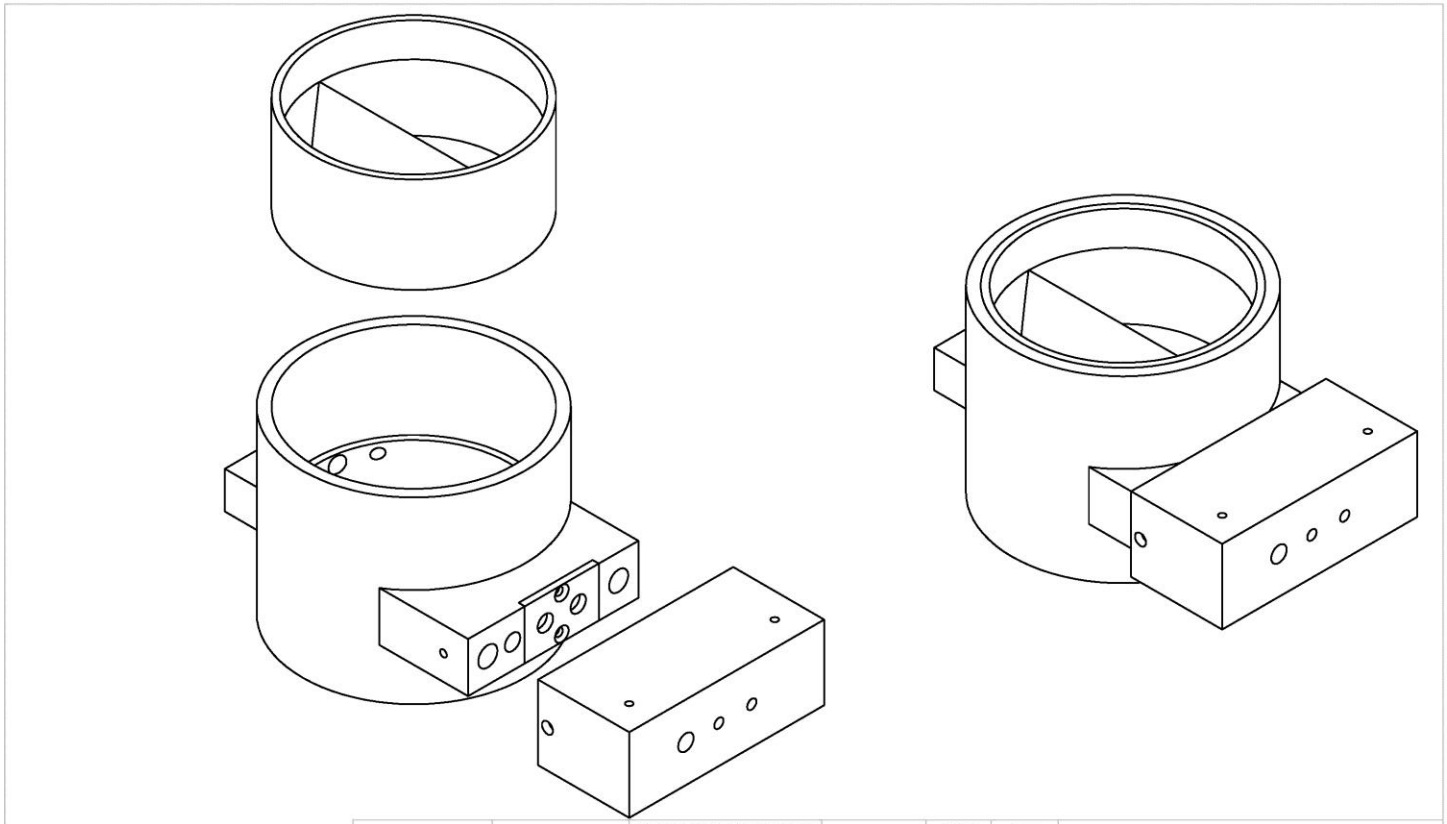

		UNLESS OTHERWISE SPECIFIED:		NAME	DATE
		DIMENSIONS ARE IN INCHES TOLERANCES: FRACTIONAL ± ANGULAR: MACH ± BEND ± TWO PLACE DECIMAL ± THREE PLACE DECIMAL ±	DRAWN		
			CHECKED		
			ENG APPR.		
			MFG APPR.		
		INTERPRET GEOMETRIC TOLERANCING PER:	Q.A.		
		MATERIAL	COMMENTS:		
NEXT ASSY	USED ON	FINISH			
APPLICATION		DO NOT SCALE DRAWING			

TITLE:

SIZE	DWG. NO.	REV
A	20150620-A-exploded	
SCALE: 1:5	WEIGHT:	SHEET 1 OF 2

5 4 3 2 1

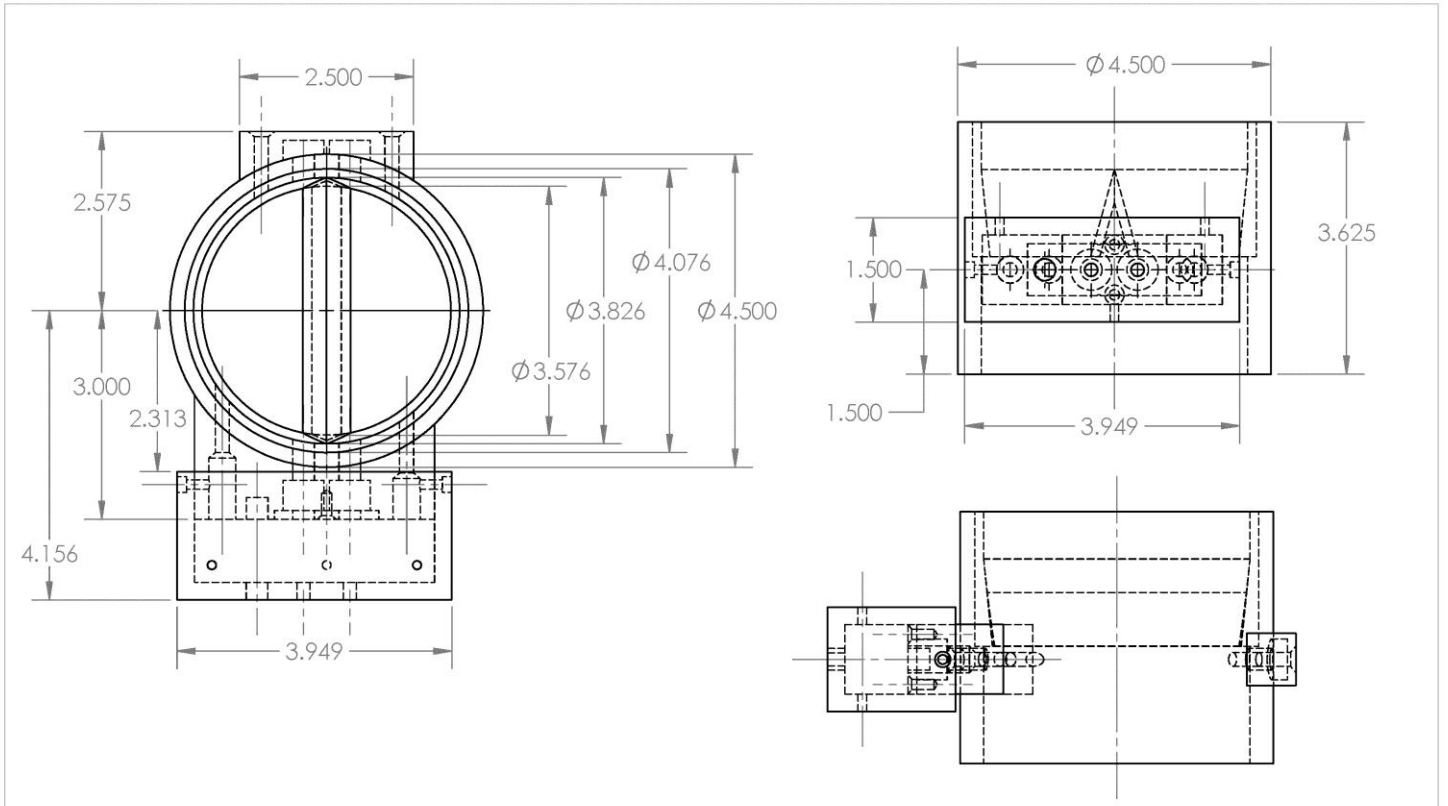

		UNLESS OTHERWISE SPECIFIED:		NAME	DATE
		DIMENSIONS ARE IN INCHES TOLERANCES: FRACTIONAL ± ANGULAR: MACH ± BEND ± TWO PLACE DECIMAL ± THREE PLACE DECIMAL ±	DRAWN		
			CHECKED		TITLE:
			ENG APPR.		
			MFG APPR.		
		INTERPRET GEOMETRIC TOLERANCING PER:	Q.A.		
		MATERIAL	COMMENTS:		SIZE DWG. NO. REV
NEXT ASSY	USED ON	FINISH			2014-0620-A-exploded
APPLICATION		DO NOT SCALE DRAWING			SCALE: 1:5 WEIGHT: SHEET 2 OF 2

5 4 3 2 1

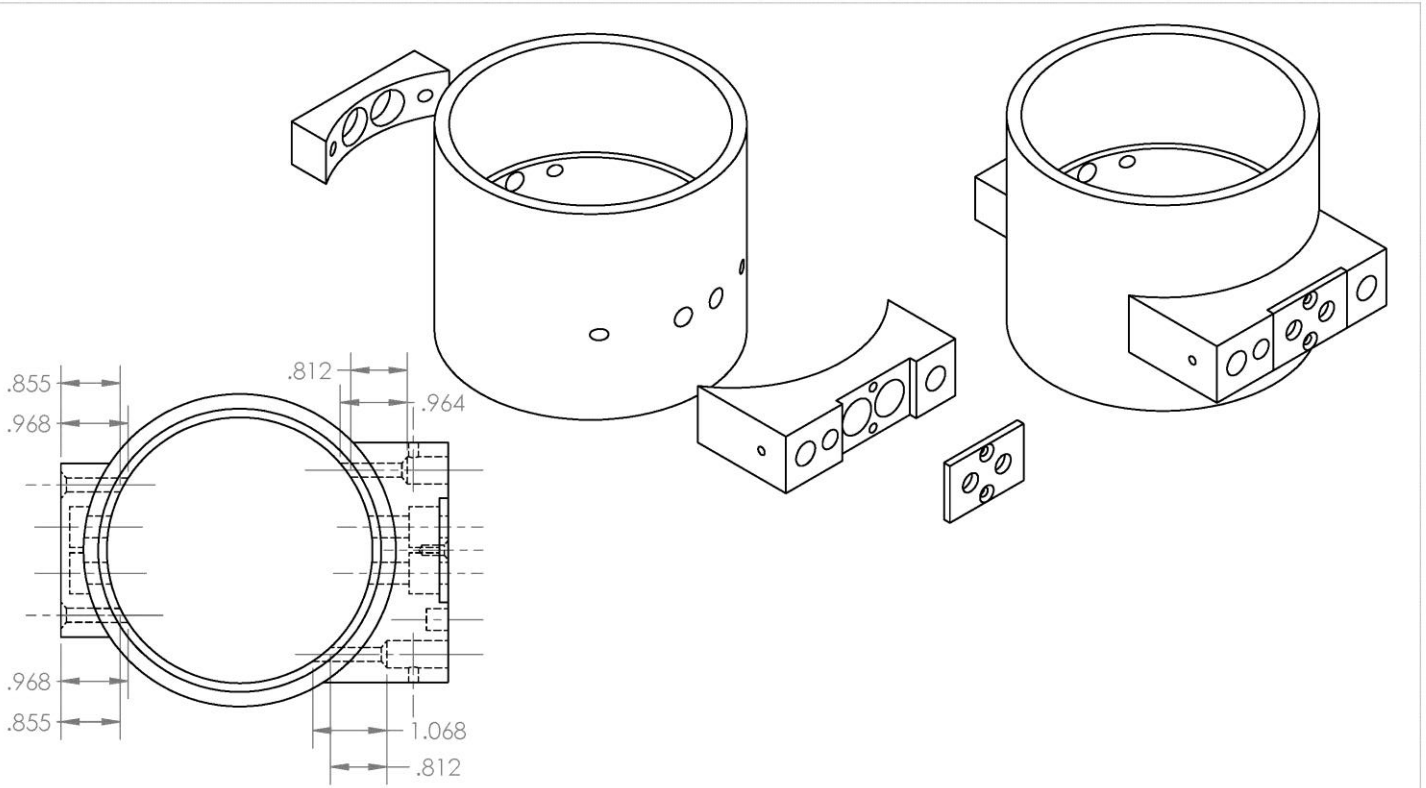

		UNLESS OTHERWISE SPECIFIED:		NAME	DATE
		DIMENSIONS ARE IN INCHES TOLERANCES: FRACTIONAL ± ANGULAR: MACH ± BEND ± TWO PLACE DECIMAL ± THREE PLACE DECIMAL ±	DRAWN		
			CHECKED		
			ENG APPR.		
			MFG APPR.		
		INTERPRET GEOMETRIC TOLERANCING PER:	Q.A.		
		MATERIAL	COMMENTS:		
NEXT ASSY	USED ON	FINISH			
APPLICATION		DO NOT SCALE DRAWING			

TITLE:

SIZE	DWG. NO.	REV
A	20150620-A1-exploded	
SCALE: 1:2	WEIGHT:	SHEET 1 OF 2

5 4 3 2 1

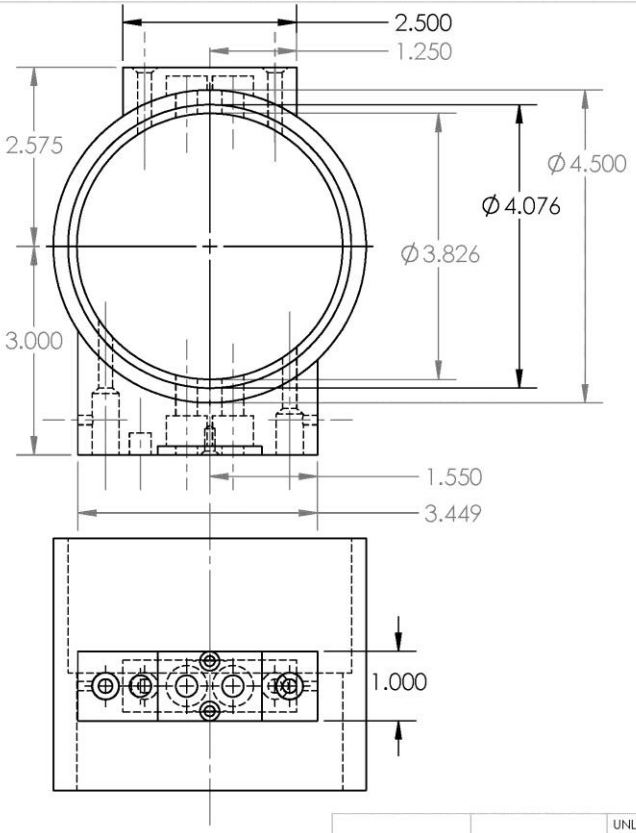

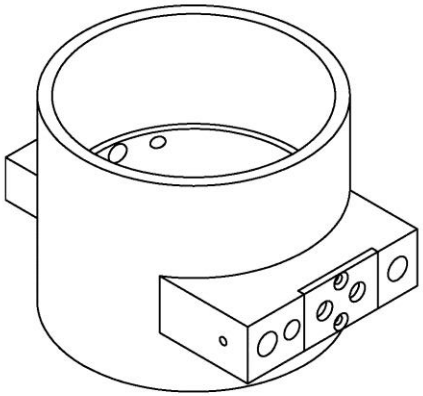

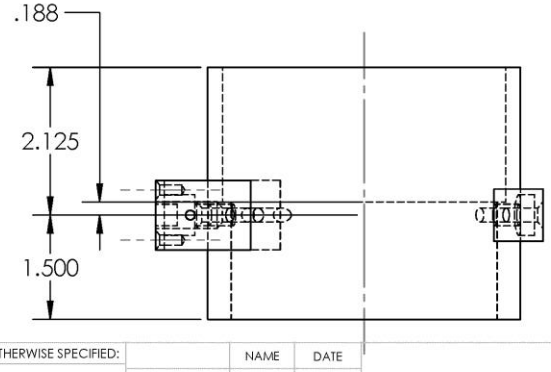

		UNLESS OTHERWISE SPECIFIED:		NAME	DATE
		DIMENSIONS ARE IN INCHES TOLERANCES: FRACTIONAL ± ANGULAR: MACH ± BEND ± TWO PLACE DECIMAL ± THREE PLACE DECIMAL ±	DRAWN		
			CHECKED		
			ENG APPR.		
			MFG APPR.		
		INTERPRET GEOMETRIC TOLERANCING PER:	Q.A.		
		MATERIAL	COMMENTS:		
NEXT ASSY	USED ON	FINISH			
APPLICATION		DO NOT SCALE DRAWING			

TITLE:

SIZE	DWG. NO.	REV
A	20150620-A1-exploded	
SCALE: 1:2	WEIGHT:	SHEET 2 OF 2

5 4 3 2 1

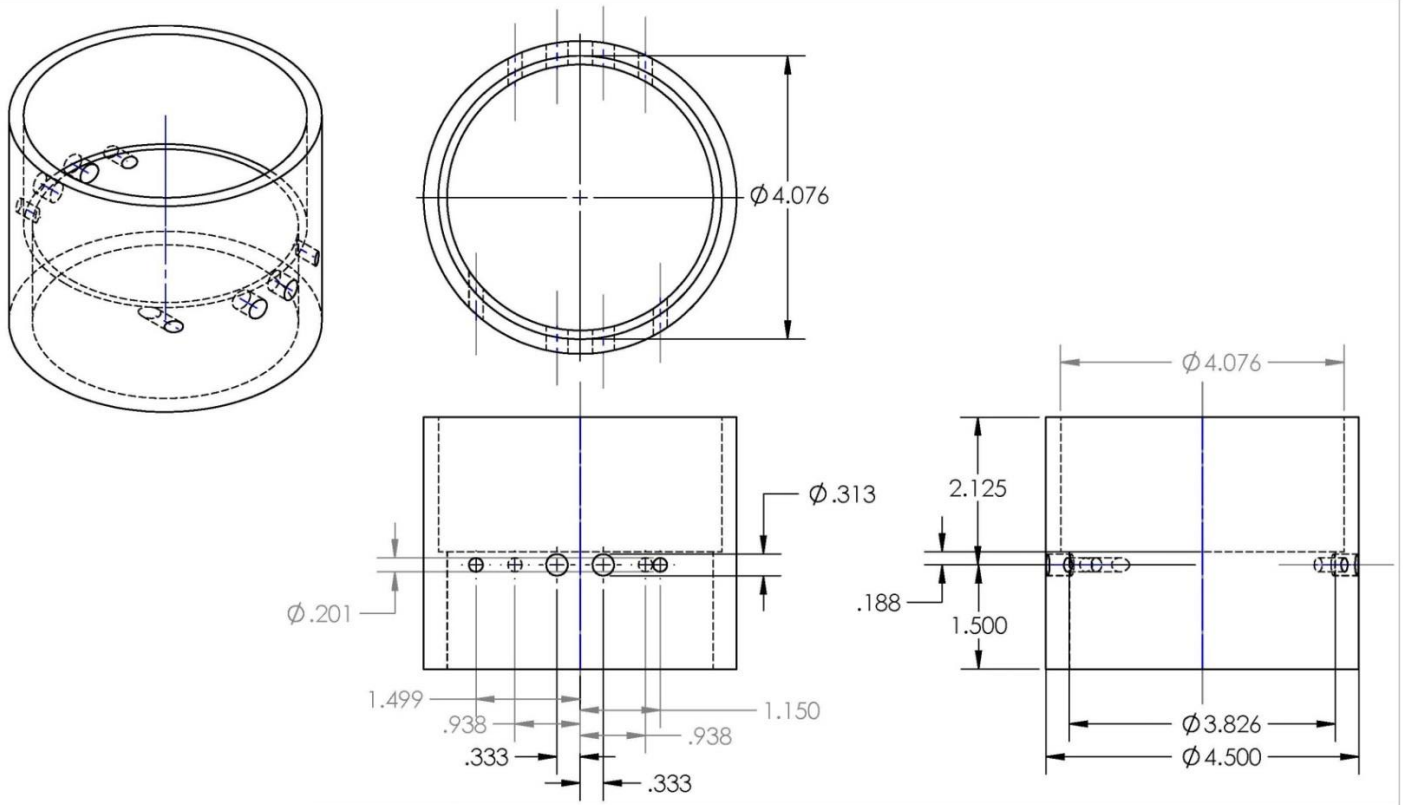

		UNLESS OTHERWISE SPECIFIED:		NAME	DATE
		DIMENSIONS ARE IN INCHES TOLERANCES: FRACTIONAL ± ANGULAR: MACH ± BEND ± TWO PLACE DECIMAL ± THREE PLACE DECIMAL ±	DRAWN		
			CHECKED		
			ENG APPR.		
			MFG APPR.		
		INTERPRET GEOMETRIC TOLERANCING PER:	Q.A.		
		MATERIAL	COMMENTS:		
NEXT ASSY	USED ON	FINISH			
APPLICATION		DO NOT SCALE DRAWING			

TITLE:

SIZE	DWG. NO.	REV
A2	0150204-A1.1	
SCALE: 1:2	WEIGHT:	SHEET 1 OF 1

5 4 3 2 1

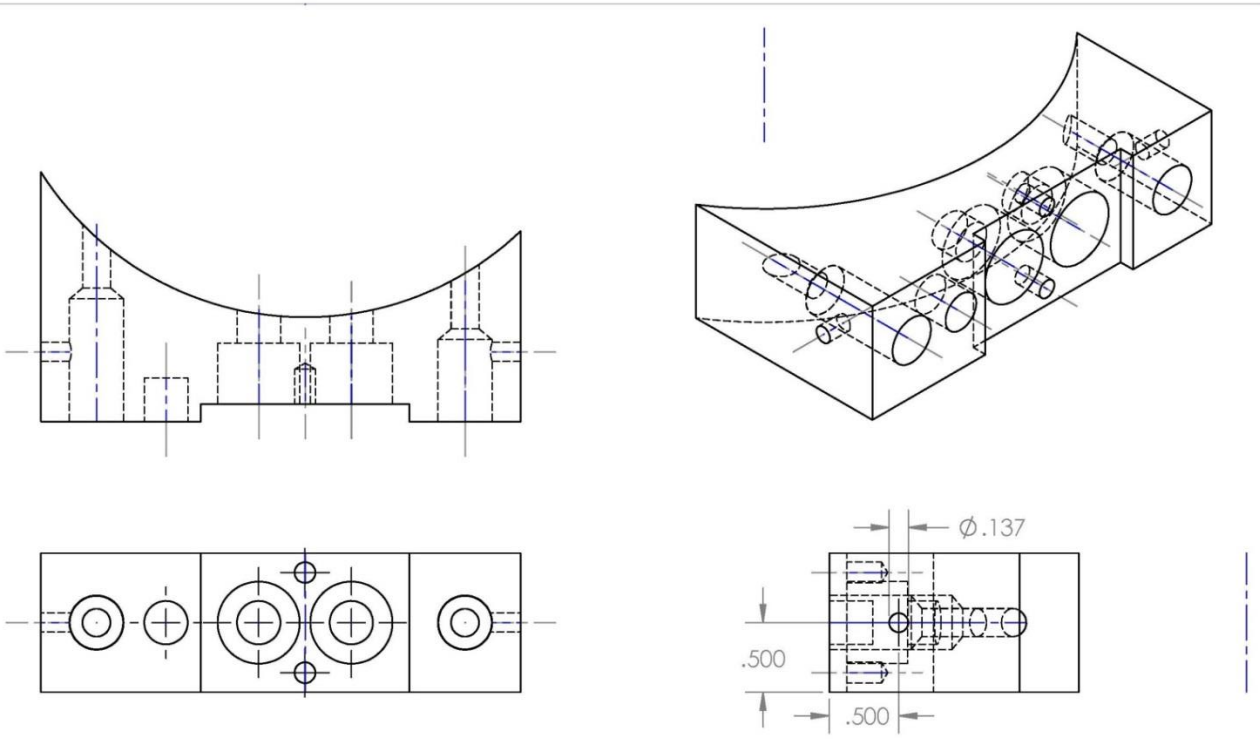

		UNLESS OTHERWISE SPECIFIED:		NAME	DATE
		DIMENSIONS ARE IN INCHES TOLERANCES: FRACTIONAL ± ANGULAR: MACH ± BEND ± TWO PLACE DECIMAL ± THREE PLACE DECIMAL ±	DRAWN		
			CHECKED		TITLE:
			ENG APPR.		
			MFG APPR.		
		INTERPRET GEOMETRIC TOLERANCING PER:	Q.A.		
		MATERIAL	COMMENTS:		SIZE DWG. NO. REV
NEXT ASSY	USED ON	FINISH			A 20150204-A1.2
APPLICATION		DO NOT SCALE DRAWING			SCALE: 1:1 WEIGHT: SHEET 1 OF 3

5 4 3 2 1

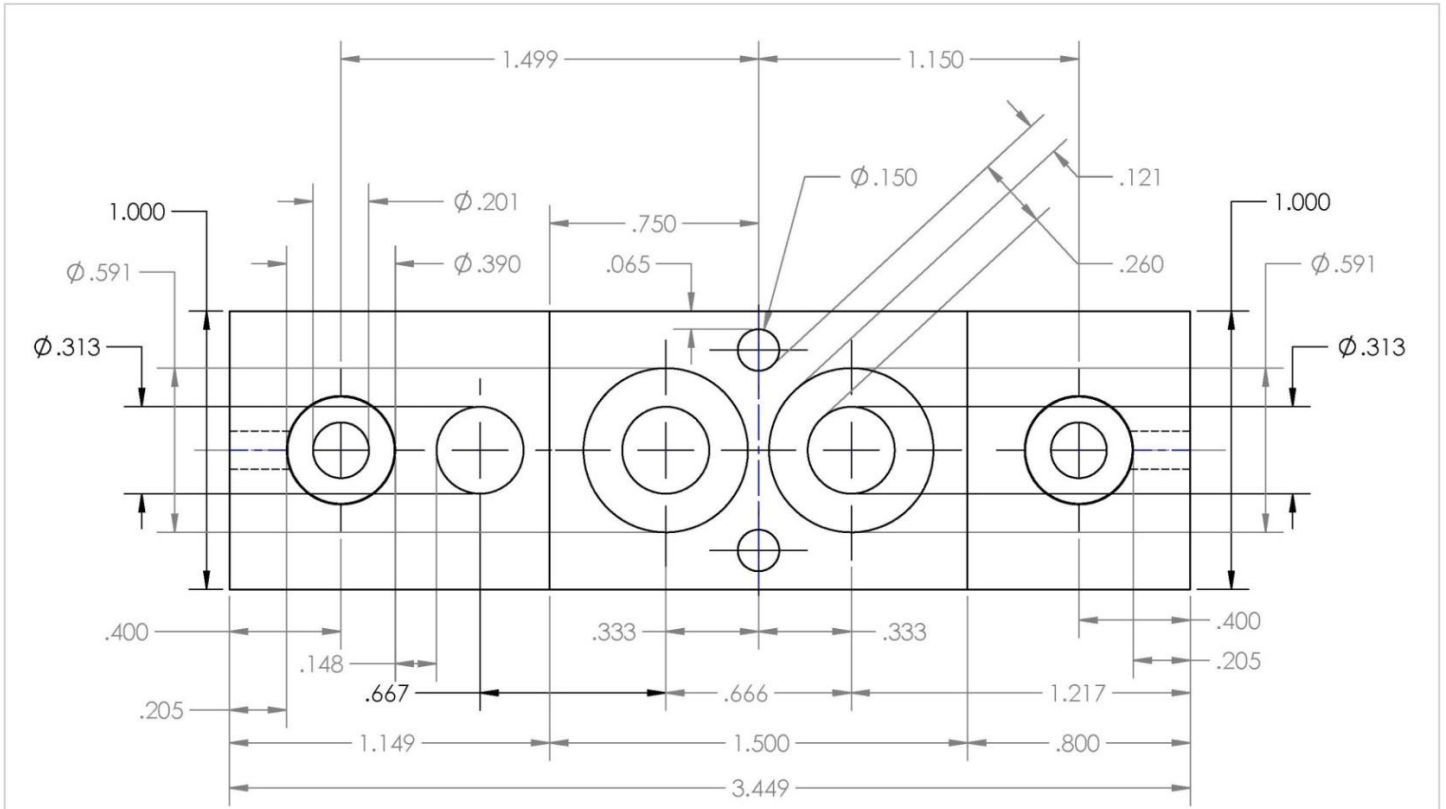

		UNLESS OTHERWISE SPECIFIED:		NAME	DATE
		DIMENSIONS ARE IN INCHES TOLERANCES: FRACTIONAL ± ANGULAR: MACH ± BEND ± TWO PLACE DECIMAL ± THREE PLACE DECIMAL ±	DRAWN		
			CHECKED		
			ENG APPR.		
			MFG APPR.		
		INTERPRET GEOMETRIC TOLERANCING PER:	Q.A.		
		MATERIAL	COMMENTS:		
NEXT ASSY	USED ON	FINISH			
APPLICATION		DO NOT SCALE DRAWING			

PROPRIETARY AND CONFIDENTIAL

THE INFORMATION CONTAINED IN THIS DRAWING IS THE SOLE PROPERTY OF <INSERT COMPANY NAME HERE>. ANY REPRODUCTION IN PART OR AS A WHOLE WITHOUT THE WRITTEN PERMISSION OF <INSERT COMPANY NAME HERE> IS PROHIBITED.

TITLE:

SIZE	DWG. NO.	REV
A2	0150204-A1.2	
SCALE: 1:1	WEIGHT:	SHEET 2 OF 3

5 4 3 2 1

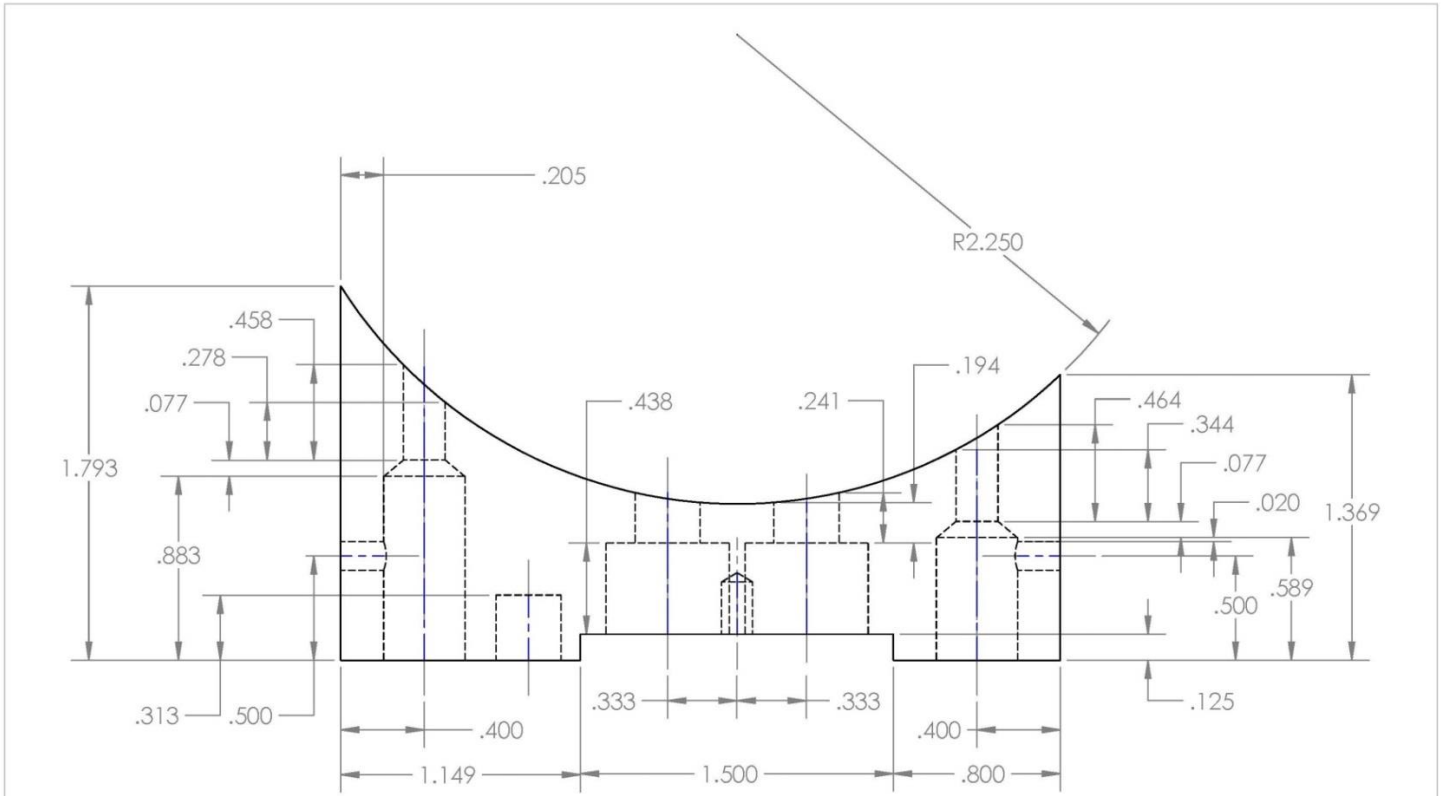

		UNLESS OTHERWISE SPECIFIED:		NAME	DATE
		DIMENSIONS ARE IN INCHES TOLERANCES: FRACTIONAL ± ANGULAR: MACH ± BEND ± TWO PLACE DECIMAL ± THREE PLACE DECIMAL ±	DRAWN		
			CHECKED		
			ENG APPR.		
			MFG APPR.		
		INTERPRET GEOMETRIC TOLERANCING PER:	Q.A.		
		MATERIAL	COMMENTS:		
NEXT ASSY	USED ON	FINISH			
APPLICATION		DO NOT SCALE DRAWING			

PROPRIETARY AND CONFIDENTIAL

THE INFORMATION CONTAINED IN THIS DRAWING IS THE SOLE PROPERTY OF <INSERT COMPANY NAME HERE>. ANY REPRODUCTION IN PART OR AS A WHOLE WITHOUT THE WRITTEN PERMISSION OF <INSERT COMPANY NAME HERE> IS PROHIBITED.

TITLE:

SIZE	DWG. NO.	REV
A2	0150204-A1	2
SCALE: 1:1	WEIGHT:	SHEET 3 OF 3

5 4 3 2 1

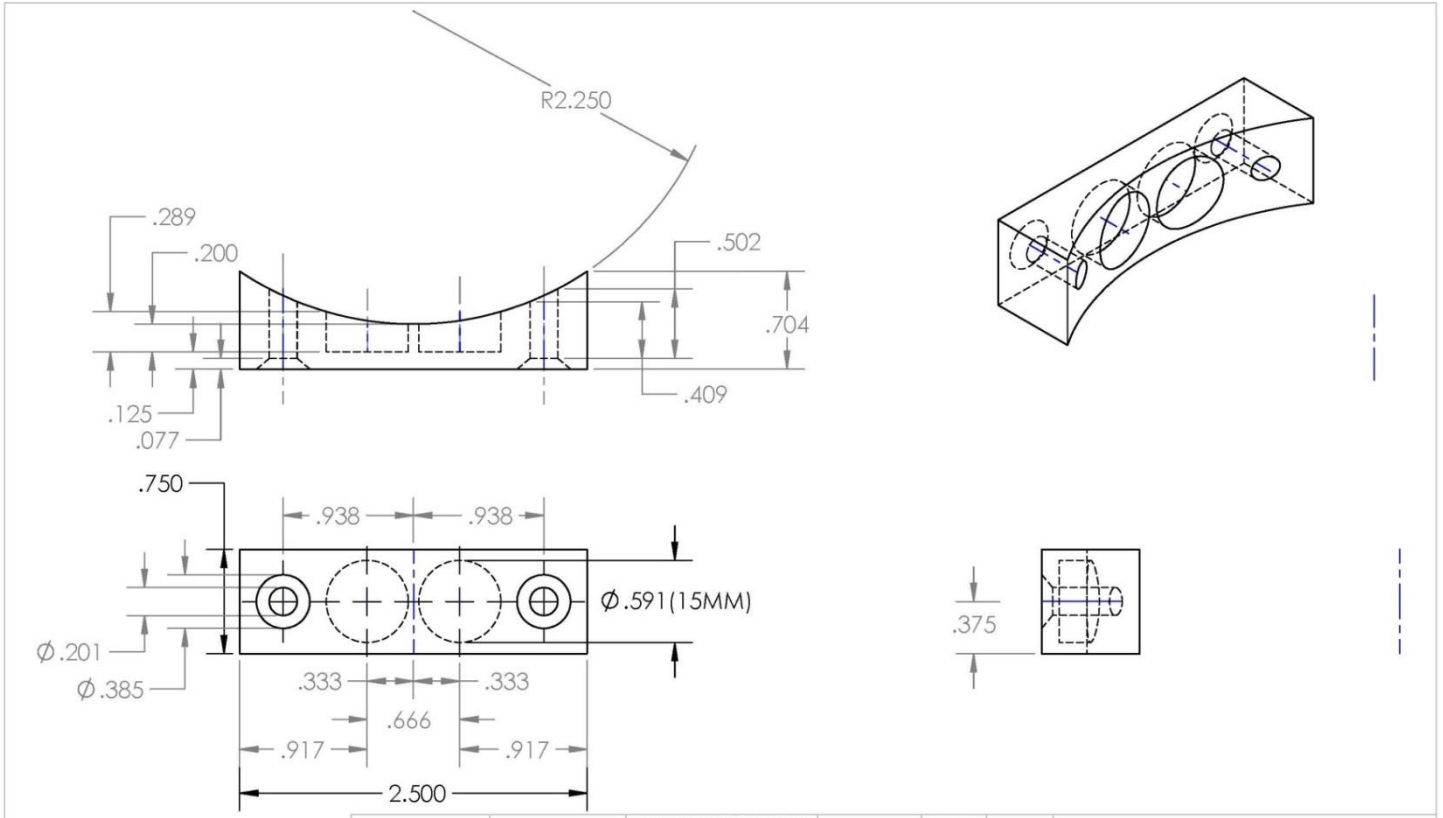

		UNLESS OTHERWISE SPECIFIED:		NAME	DATE
		DIMENSIONS ARE IN INCHES TOLERANCES: FRACTIONAL ± ANGULAR: MACH ± BEND ± TWO PLACE DECIMAL ± THREE PLACE DECIMAL ±	DRAWN		
			CHECKED		
			ENG APPR.		
			MFG APPR.		
		INTERPRET GEOMETRIC TOLERANCING PER:	Q.A.		
		MATERIAL	COMMENTS:		
NEXT ASSY	USED ON	FINISH			
APPLICATION		DO NOT SCALE DRAWING			

TITLE:

SIZE	DWG. NO.	REV
A2	0150204-A1	.3
SCALE: 1:1	WEIGHT:	SHEET 1 OF 1

5 4 3 2 1

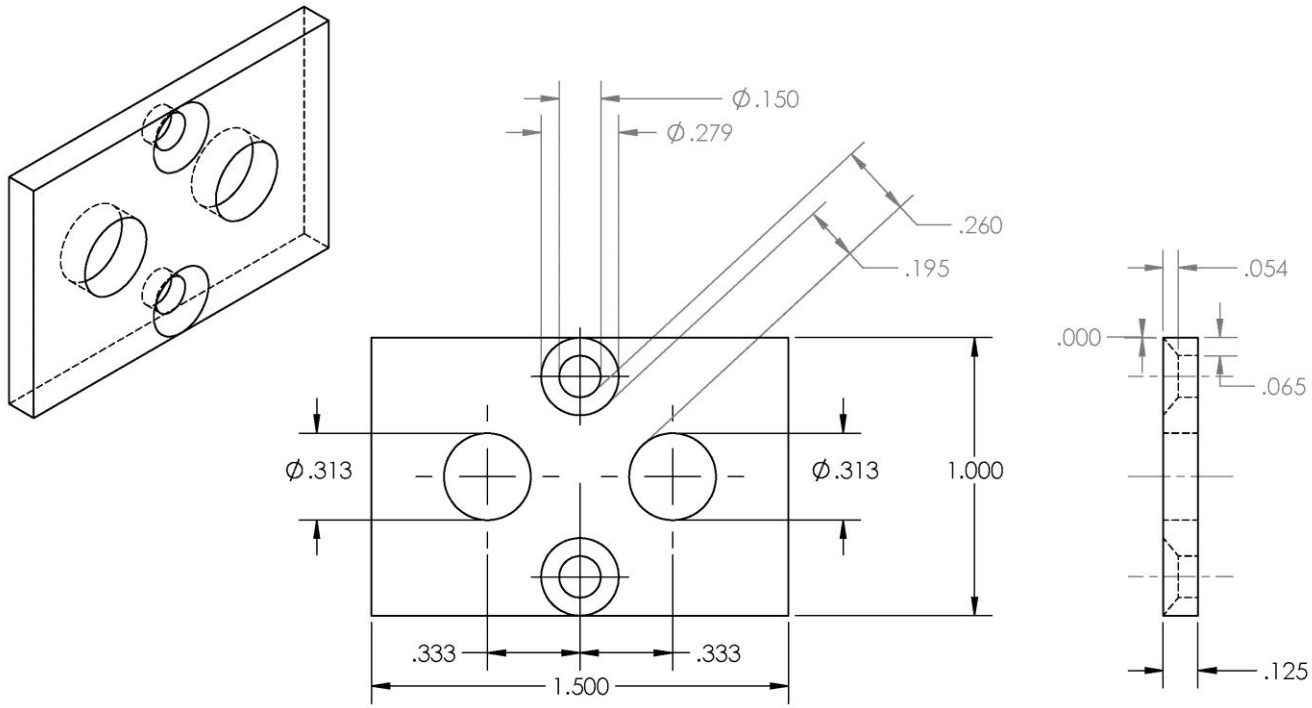

		UNLESS OTHERWISE SPECIFIED:		NAME	DATE
		DIMENSIONS ARE IN INCHES TOLERANCES: FRACTIONAL ± ANGULAR: MACH ± BEND ± TWO PLACE DECIMAL ± THREE PLACE DECIMAL ±	DRAWN		
			CHECKED		
			ENG APPR.		
			MFG APPR.		
		INTERPRET GEOMETRIC TOLERANCING PER:	Q.A.		
		MATERIAL	COMMENTS:		
NEXT ASSY	USED ON	FINISH			
APPLICATION		DO NOT SCALE DRAWING			

TITLE:

SIZE A2 | DWG. NO. 20150204-A1.4 | REV 4

SCALE: 1:1 | WEIGHT: | SHEET 1 OF 1

5 4 3 2 1

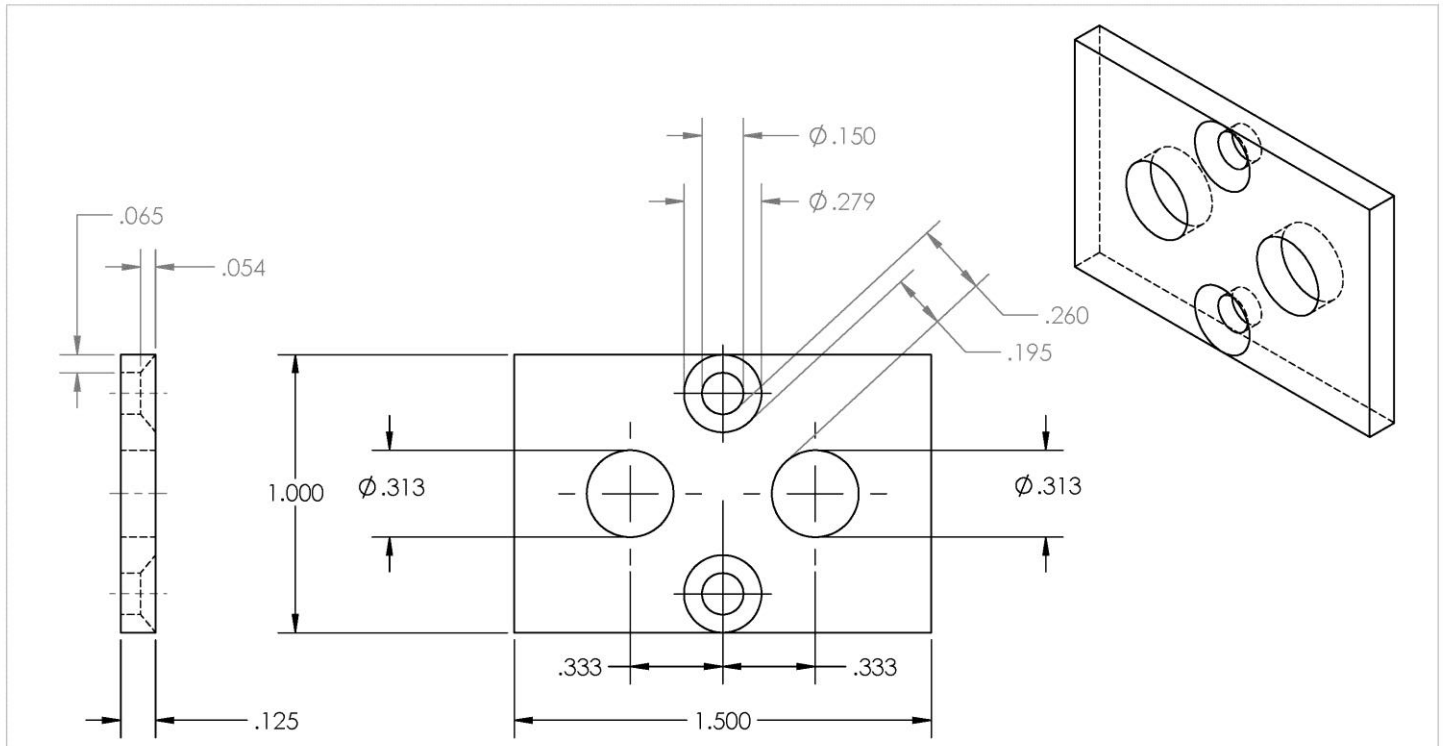

		UNLESS OTHERWISE SPECIFIED:		NAME	DATE
		DIMENSIONS ARE IN INCHES TOLERANCES: FRACTIONAL ± ANGULAR: MACH ± BEND ± TWO PLACE DECIMAL ± THREE PLACE DECIMAL ±	DRAWN		
			CHECKED		
			ENG APPR.		
			MFG APPR.		
		INTERPRET GEOMETRIC TOLERANCING PER:	Q.A.		
		MATERIAL	COMMENTS:		
NEXT ASSY	USED ON	FINISH			
APPLICATION		DO NOT SCALE DRAWING			

TITLE:

SIZE	DWG. NO.	REV
A2	20150204-A1.5	
SCALE: 1:1	WEIGHT:	SHEET 1 OF 1

5 4 3 2 1

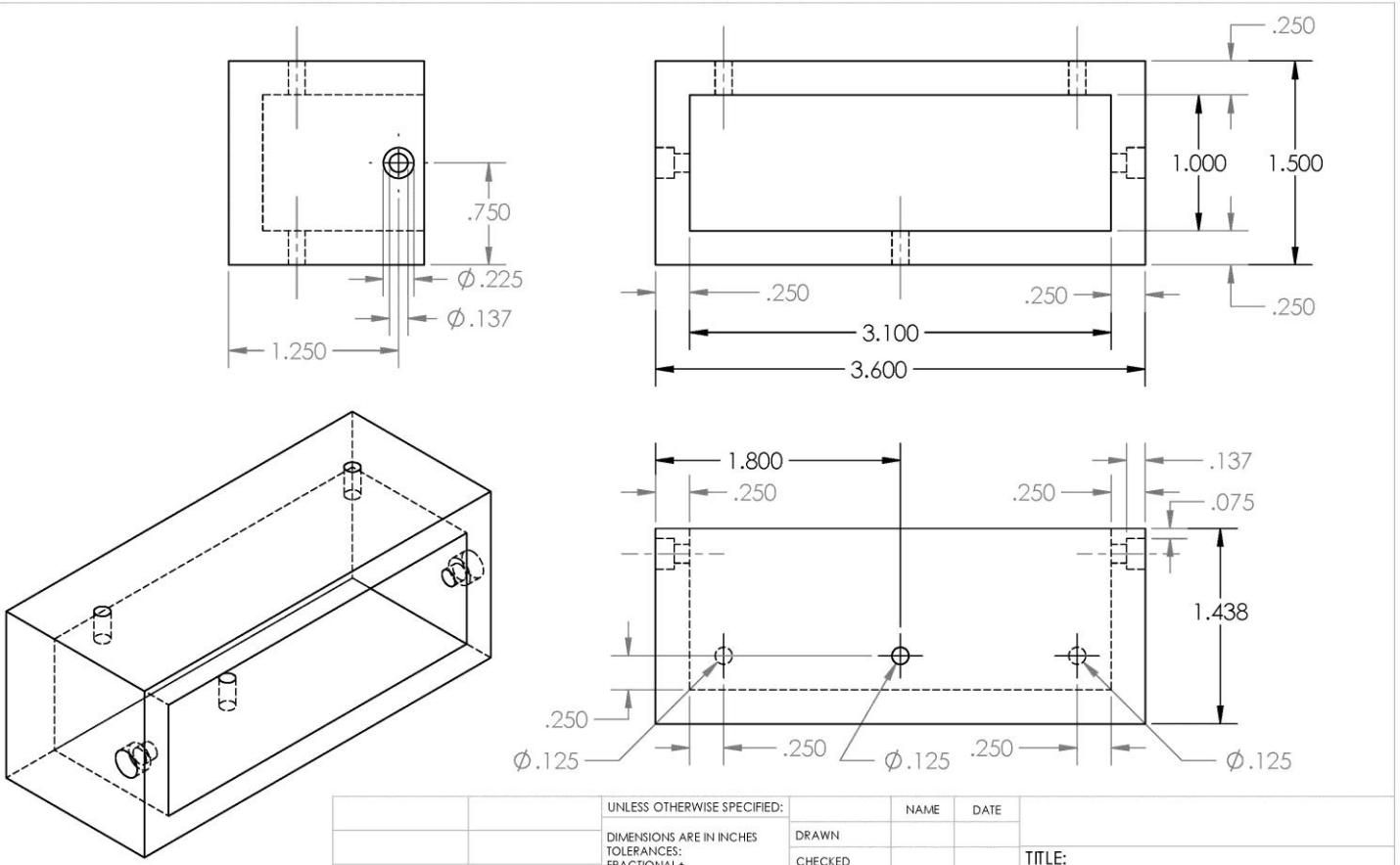

		UNLESS OTHERWISE SPECIFIED:		NAME	DATE
		DIMENSIONS ARE IN INCHES TOLERANCES: FRACTIONAL ± ANGULAR: MACH ± BEND ± TWO PLACE DECIMAL ± THREE PLACE DECIMAL ±	DRAWN		
			CHECKED		
			ENG APPR.		
			MFG APPR.		
		INTERPRET GEOMETRIC TOLERANCING PER:	Q.A.		
		MATERIAL	COMMENTS:		
NEXT ASSY	USED ON	FINISH			
APPLICATION		DO NOT SCALE DRAWING			

TITLE:

SIZE | DWG. NO. | REV

A20150204-A3

SCALE: 1:1 | WEIGHT: | SHEET 1 OF 1

5 4 3 2 1

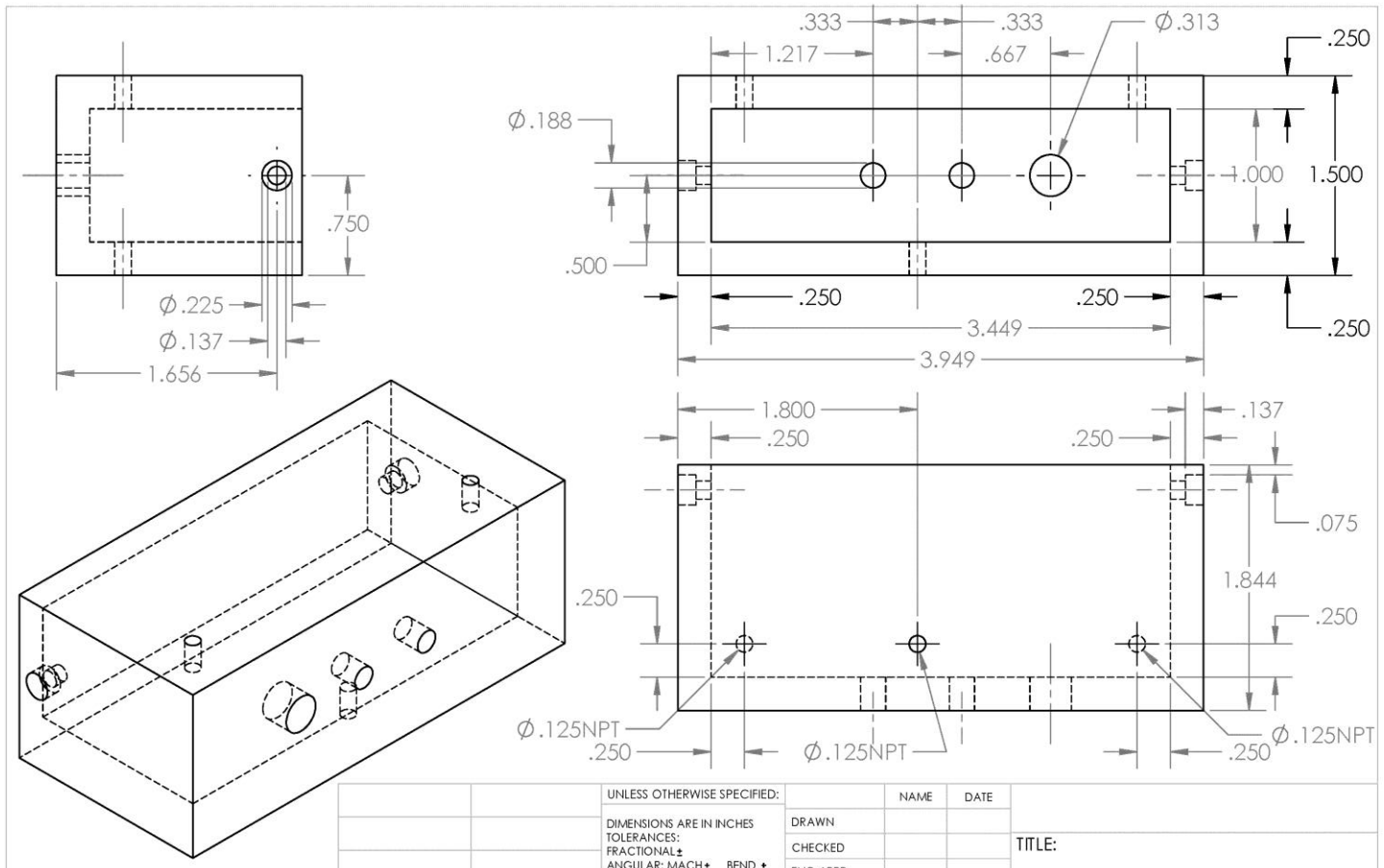

		UNLESS OTHERWISE SPECIFIED:		NAME	DATE
		DIMENSIONS ARE IN INCHES TOLERANCES: FRACTIONAL ± ANGULAR: MACH ± BEND ± TWO PLACE DECIMAL ± THREE PLACE DECIMAL ±	DRAWN		
			CHECKED		
			ENG APPR.		
			MFG APPR.		
		INTERPRET GEOMETRIC TOLERANCING PER:	Q.A.		
		MATERIAL	COMMENTS:		
NEXT ASSY	USED ON	FINISH			
APPLICATION		DO NOT SCALE DRAWING			

PROPRIETARY AND CONFIDENTIAL

THE INFORMATION CONTAINED IN THIS DRAWING IS THE SOLE PROPERTY OF <INSERT COMPANY NAME HERE>. ANY REPRODUCTION IN PART OR AS A WHOLE WITHOUT THE WRITTEN PERMISSION OF <INSERT COMPANY NAME HERE> IS PROHIBITED.

TITLE:

SIZE	DWG. NO.	REV
A	20150204-A4	
SCALE: 1:1	WEIGHT:	SHEET 1 OF 1

5 4 3 2 1

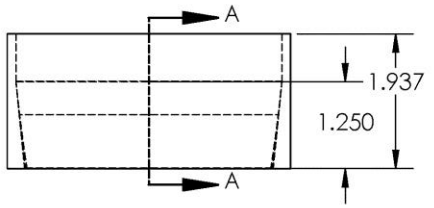

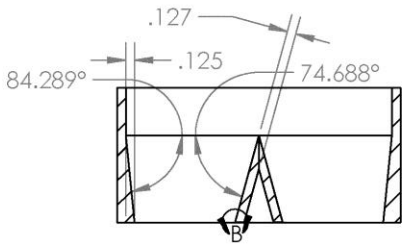

SECTION A-A
SCALE 1 : 2

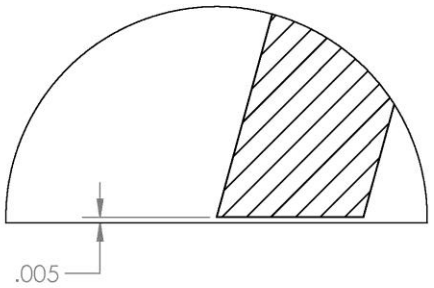

DETAIL B
SCALE 8 : 1

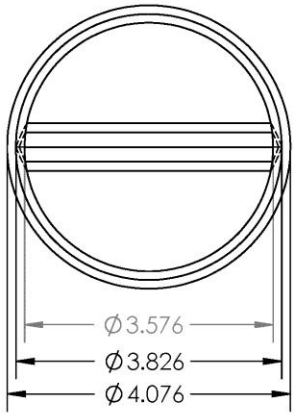

		UNLESS OTHERWISE SPECIFIED:		NAME	DATE
		DIMENSIONS ARE IN INCHES TOLERANCES: FRACTIONAL ± ANGULAR: MACH ± BEND ± TWO PLACE DECIMAL ± THREE PLACE DECIMAL ±	DRAWN		
			CHECKED		
			ENG APPR.		
			MFG APPR.		
		INTERPRET GEOMETRIC TOLERANCING PER:	Q.A.		
		MATERIAL	COMMENTS:		
NEXT ASSY	USED ON	FINISH			
APPLICATION		DO NOT SCALE DRAWING			

TITLE:

SIZE	DWG. NO.	REV
A	20150620-A2-exploded	
SCALE: 1:5	WEIGHT:	SHEET 1 OF 2

5 4 3 2 1

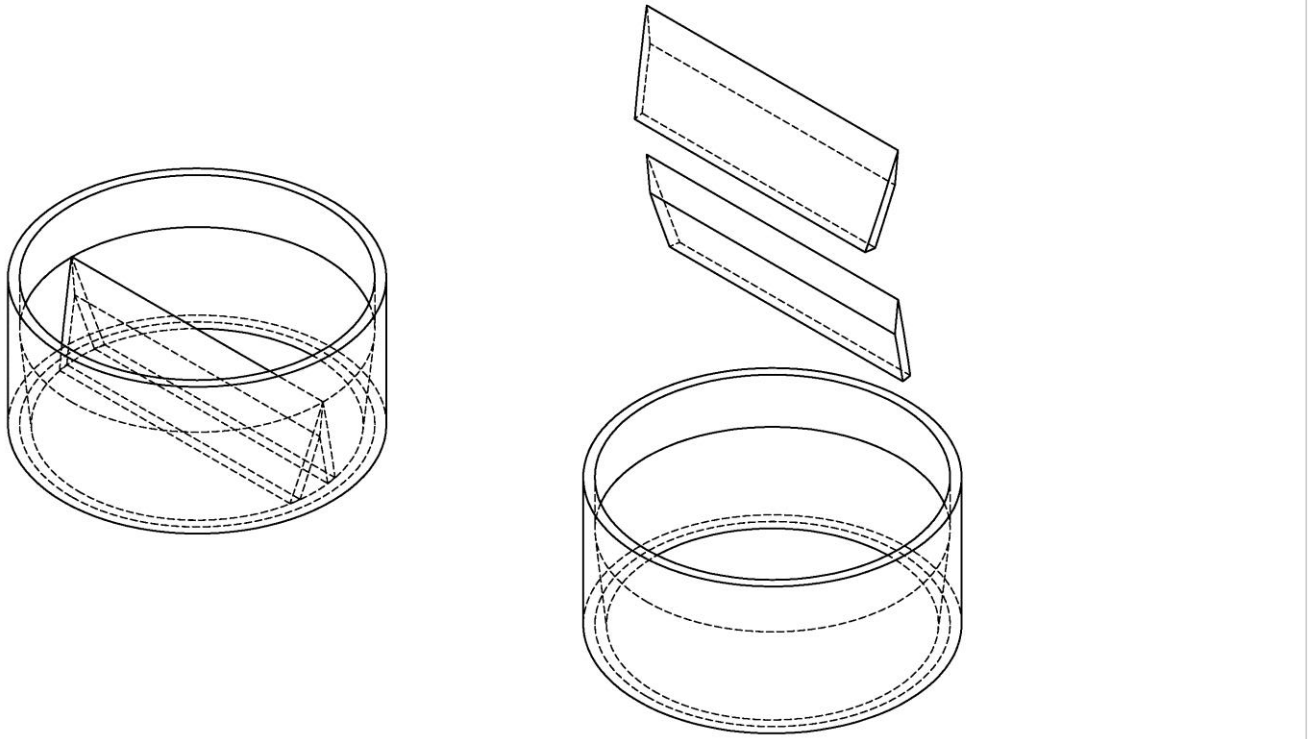

		UNLESS OTHERWISE SPECIFIED:		NAME	DATE
		DIMENSIONS ARE IN INCHES TOLERANCES: FRACTIONAL ± ANGULAR: MACH ± BEND ± TWO PLACE DECIMAL ± THREE PLACE DECIMAL ±	DRAWN		
			CHECKED		
			ENG APPR.		
			MFG APPR.		
		INTERPRET GEOMETRIC TOLERANCING PER:	Q.A.		
		MATERIAL	COMMENTS:		
NEXT ASSY	USED ON	FINISH			
APPLICATION		DO NOT SCALE DRAWING			

TITLE:

SIZE	DWG. NO.	REV
A3	20170620-A2-exploded	
SCALE: 1:5	WEIGHT:	SHEET 2 OF 2

5 4 3 2 1

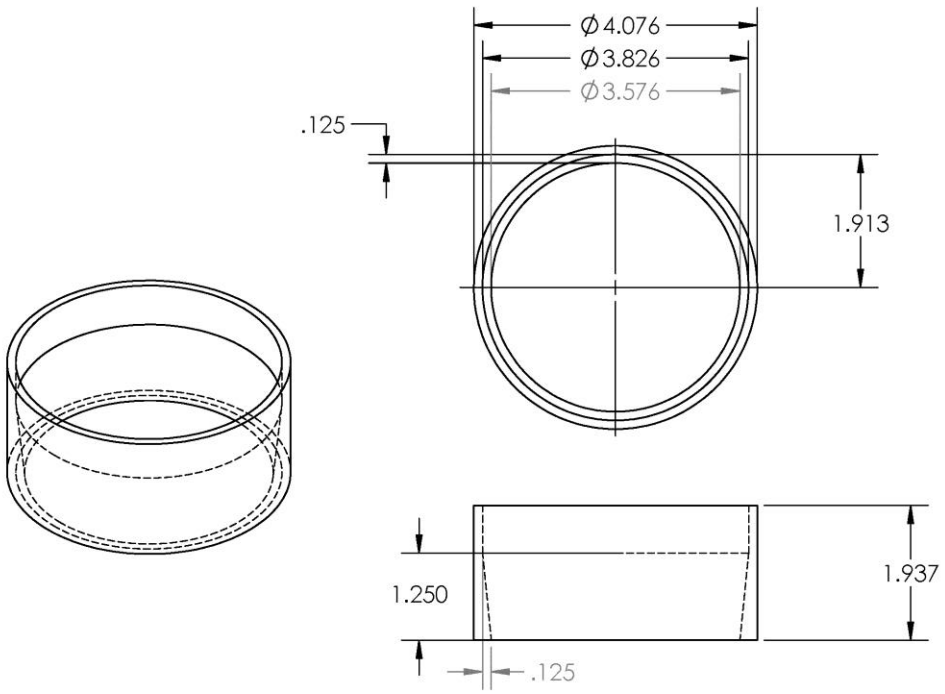

		UNLESS OTHERWISE SPECIFIED:		NAME	DATE
		DIMENSIONS ARE IN INCHES TOLERANCES: FRACTIONAL ± ANGULAR: MACH ± BEND ± TWO PLACE DECIMAL ± THREE PLACE DECIMAL ±	DRAWN		
			CHECKED		
			ENG APPR.		
			MFG APPR.		
		INTERPRET GEOMETRIC TOLERANCING PER:	Q.A.		
		MATERIAL	COMMENTS:		
NEXT ASSY	USED ON	FINISH			
APPLICATION		DO NOT SCALE DRAWING			

TITLE:

SIZE	DWG. NO.	REV
A2	0150204-A2.1	
SCALE: 1:2	WEIGHT:	SHEET 1 OF 1

5 4 3 2 1

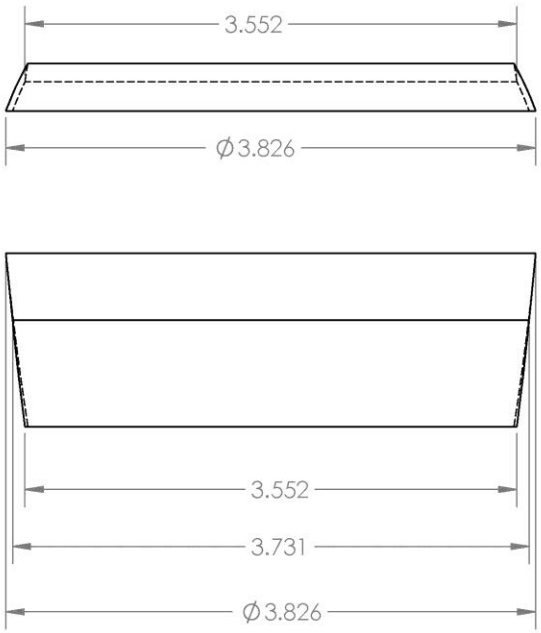

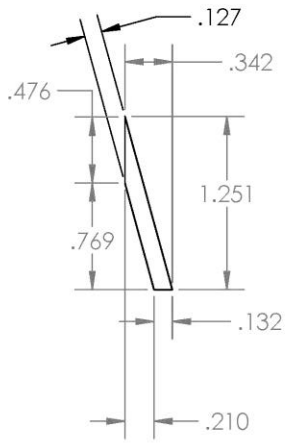

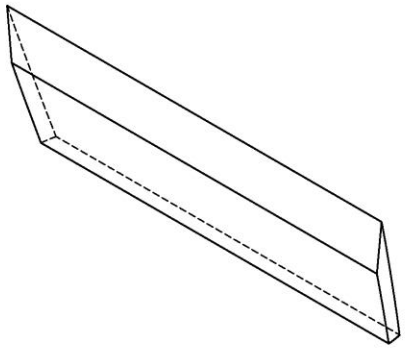

		UNLESS OTHERWISE SPECIFIED:		NAME	DATE
		DIMENSIONS ARE IN INCHES TOLERANCES: FRACTIONAL ± ANGULAR: MACH ± BEND ± TWO PLACE DECIMAL ± THREE PLACE DECIMAL ±	DRAWN		
			CHECKED		
			ENG APPR.		
			MFG APPR.		
		INTERPRET GEOMETRIC TOLERANCING PER:	Q.A.		
		MATERIAL	COMMENTS:		
NEXT ASSY	USED ON	FINISH			
APPLICATION		DO NOT SCALE DRAWING			

TITLE:

SIZE	DWG. NO.	REV
A	20150204-A2.2	
SCALE: 1:1	WEIGHT:	SHEET 1 OF 1

5 4 3 2 1

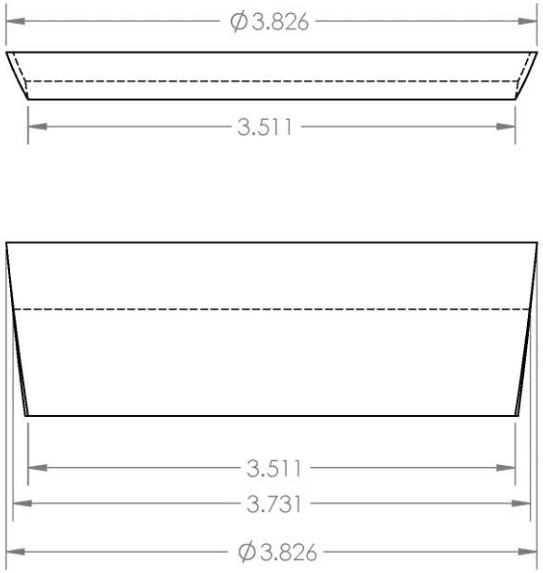

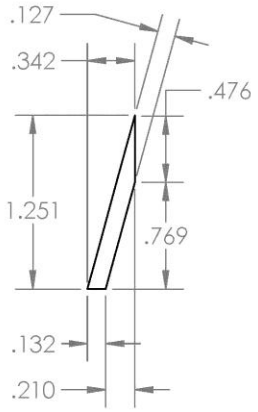

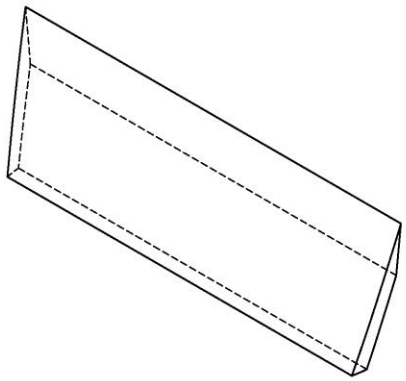

		UNLESS OTHERWISE SPECIFIED:		NAME	DATE
		DIMENSIONS ARE IN INCHES TOLERANCES: FRACTIONAL ± ANGULAR: MACH ± BEND ± TWO PLACE DECIMAL ± THREE PLACE DECIMAL ±	DRAWN		
			CHECKED		
			ENG APPR.		
			MFG APPR.		
		INTERPRET GEOMETRIC TOLERANCING PER:	Q.A.		
		MATERIAL	COMMENTS:		
NEXT ASSY	USED ON	FINISH			
APPLICATION		DO NOT SCALE DRAWING			

TITLE:

SIZE	DWG. NO.	REV
A	20150204-A2.3	
SCALE: 1:1	WEIGHT:	SHEET 1 OF 1

5 4 3 2 1

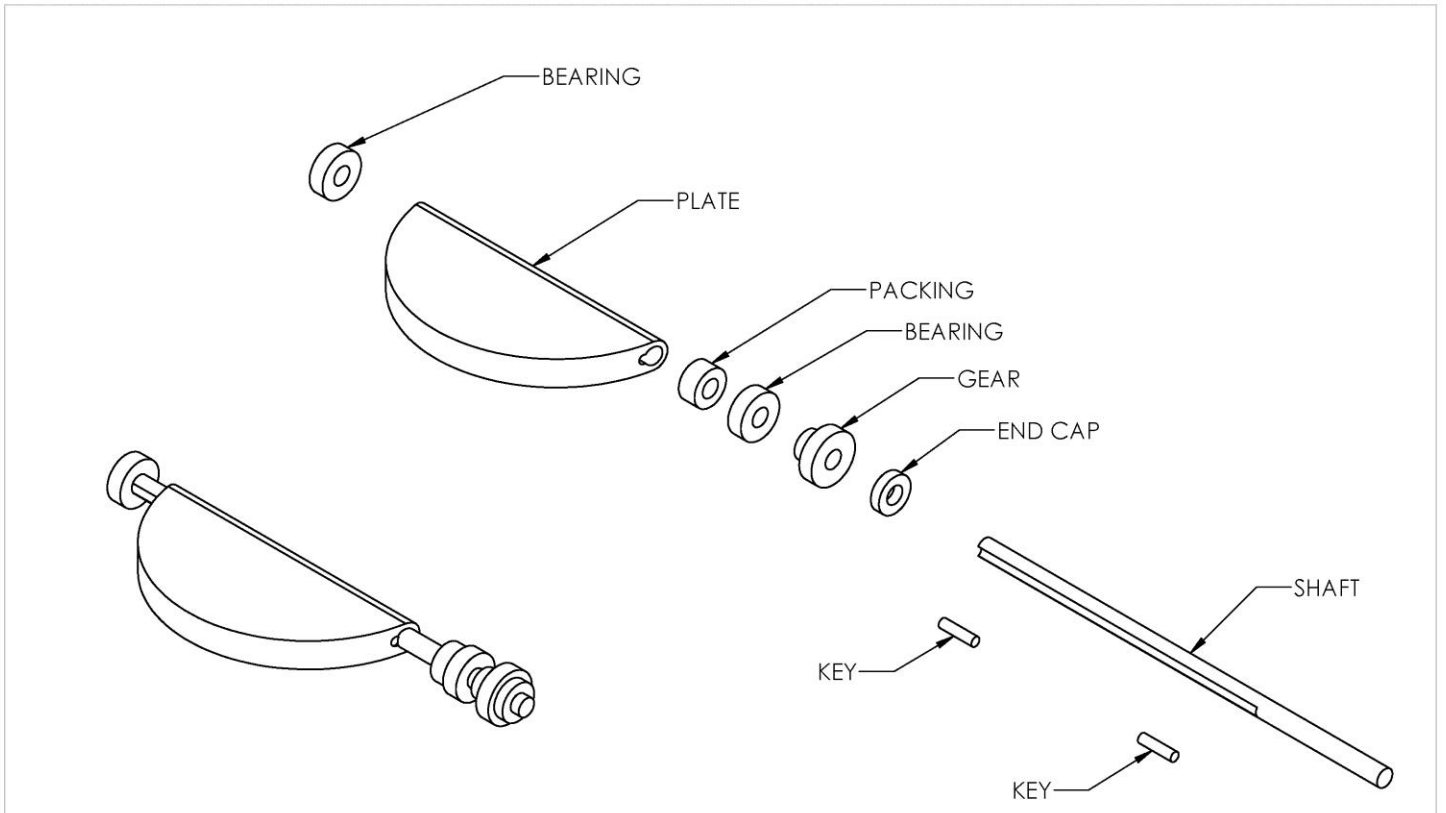

		UNLESS OTHERWISE SPECIFIED:		NAME	DATE
		DIMENSIONS ARE IN INCHES TOLERANCES: FRACTIONAL ± ANGULAR: MACH ± BEND ± TWO PLACE DECIMAL ± THREE PLACE DECIMAL ±	DRAWN		
			CHECKED		
			ENG APPR.		
			MFG APPR.		
		INTERPRET GEOMETRIC TOLERANCING PER:	Q.A.		
		MATERIAL	COMMENTS:		
NEXT ASSY	USED ON	FINISH			
APPLICATION		DO NOT SCALE DRAWING			

TITLE:

SIZE | DWG. NO. | REV

20150620-B-exploded

SCALE: 1:2 | WEIGHT: | SHEET 1 OF 2

5 4 3 2 1

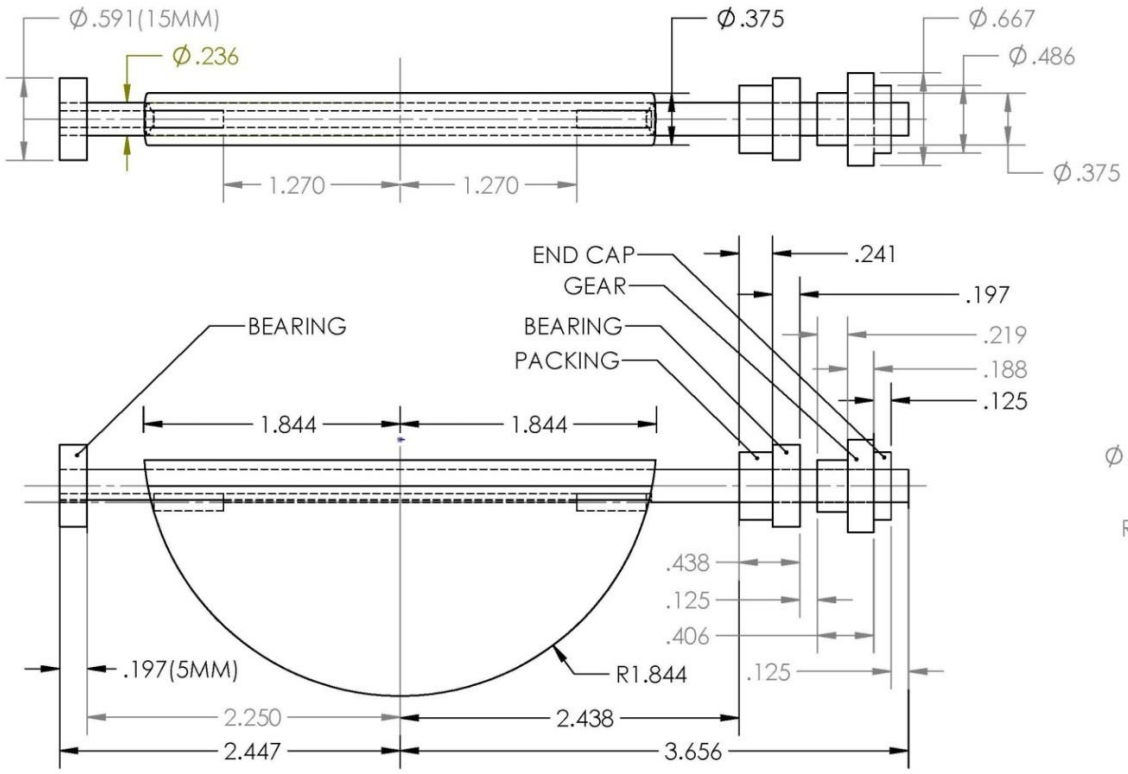

		UNLESS OTHERWISE SPECIFIED:		NAME	DATE
		DIMENSIONS ARE IN INCHES TOLERANCES: FRACTIONAL ± ANGULAR: MACH ± BEND ± TWO PLACE DECIMAL ± THREE PLACE DECIMAL ±	DRAWN		
			CHECKED		TITLE:
			ENG APPR.		
			MFG APPR.		
		INTERPRET GEOMETRIC TOLERANCING PER:	Q.A.		
		MATERIAL	COMMENTS:		SIZE / DWG. NO. / REV
NEXT ASSY	USED ON	FINISH			20150620-B-exploded A
APPLICATION		DO NOT SCALE DRAWING			SCALE: 1:2 WEIGHT: SHEET 2 OF 2

5 4 3 2 1

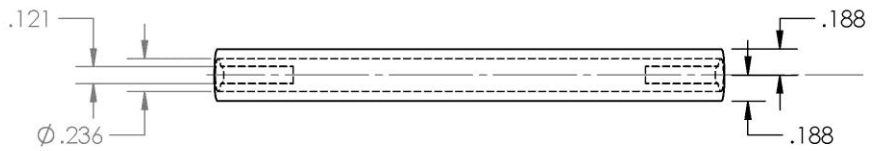

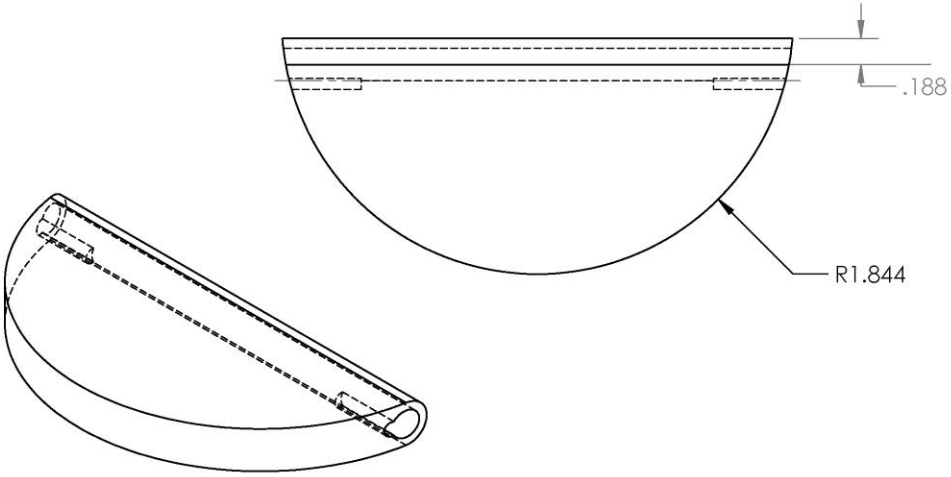

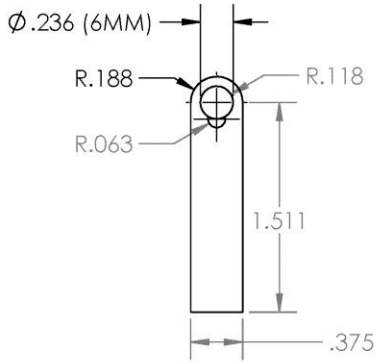

		UNLESS OTHERWISE SPECIFIED:		NAME	DATE
		DIMENSIONS ARE IN INCHES TOLERANCES: FRACTIONAL ± ANGULAR: MACH ± BEND ± TWO PLACE DECIMAL ± THREE PLACE DECIMAL ±	DRAWN		
			CHECKED		
			ENG APPR.		
			MFG APPR.		
		INTERPRET GEOMETRIC TOLERANCING PER:	Q.A.		
		MATERIAL	COMMENTS:		
NEXT ASSY	USED ON	FINISH			
APPLICATION		DO NOT SCALE DRAWING			

TITLE:

SIZE	DWG. NO.	REV
A	20150204-B1	
SCALE: 1:1	WEIGHT:	SHEET 1 OF 1

5 4 3 2 1

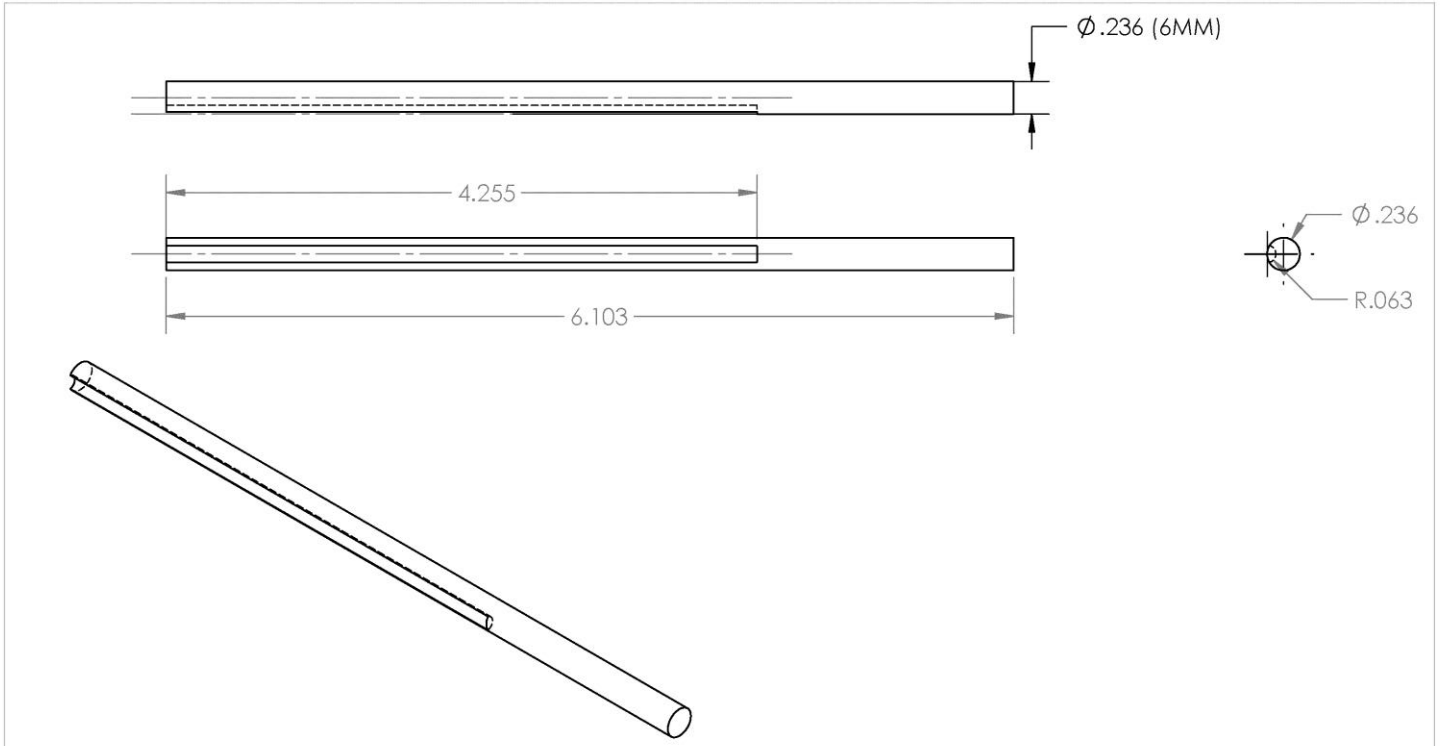

		UNLESS OTHERWISE SPECIFIED:		NAME	DATE
		DIMENSIONS ARE IN INCHES TOLERANCES: FRACTIONAL ± ANGULAR: MACH ± BEND ± TWO PLACE DECIMAL ± THREE PLACE DECIMAL ±	DRAWN		
			CHECKED		
			ENG APPR.		
			MFG APPR.		
		INTERPRET GEOMETRIC TOLERANCING PER:	Q.A.		
		MATERIAL	COMMENTS:		
NEXT ASSY	USED ON	FINISH			
APPLICATION		DO NOT SCALE DRAWING			

PROPRIETARY AND CONFIDENTIAL

THE INFORMATION CONTAINED IN THIS DRAWING IS THE SOLE PROPERTY OF <INSERT COMPANY NAME HERE>. ANY REPRODUCTION IN PART OR AS A WHOLE WITHOUT THE WRITTEN PERMISSION OF <INSERT COMPANY NAME HERE> IS PROHIBITED.

TITLE:

SIZE	DWG. NO.	REV
A2	20150204-B2.1	
SCALE: 1:2	WEIGHT:	SHEET 1 OF 1

5 4 3 2 1

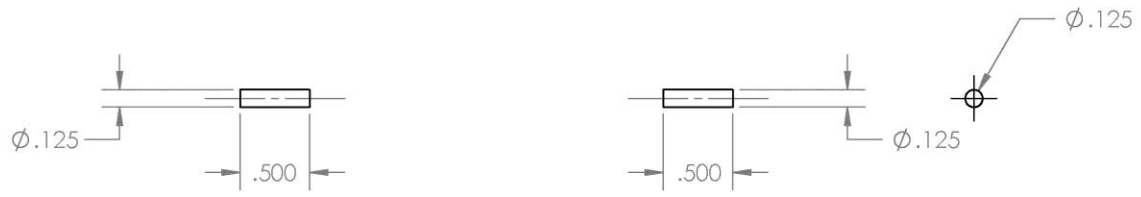

		UNLESS OTHERWISE SPECIFIED:		NAME	DATE
		DIMENSIONS ARE IN INCHES TOLERANCES: FRACTIONAL ± ANGULAR: MACH ± BEND ± TWO PLACE DECIMAL ± THREE PLACE DECIMAL ±	DRAWN		
			CHECKED		
			ENG APPR.		
			MFG APPR.		
		INTERPRET GEOMETRIC TOLERANCING PER:	Q.A.		
		MATERIAL	COMMENTS:		
NEXT ASSY	USED ON	FINISH			
APPLICATION		DO NOT SCALE DRAWING			

TITLE:

SIZE A2 | DWG. NO. 20150204-B2.2 | REV

SCALE: 1:1 | WEIGHT: | SHEET 1 OF 1

5 4 3 2 1

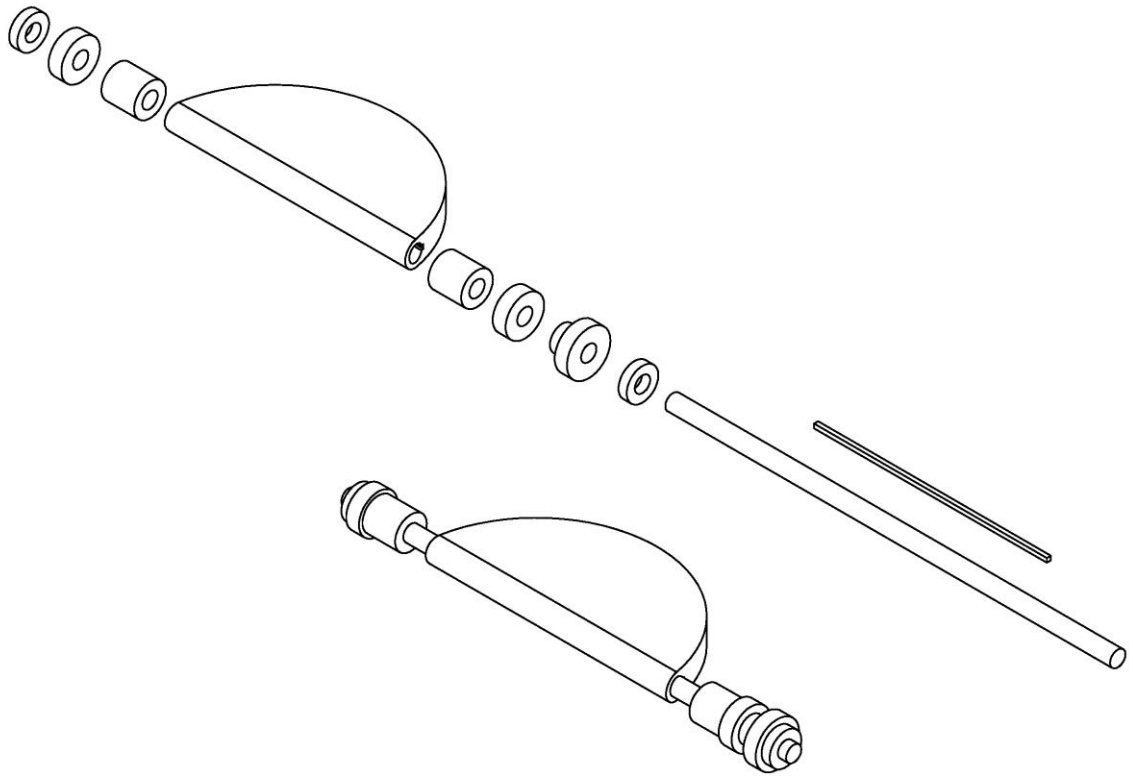

		UNLESS OTHERWISE SPECIFIED:		NAME	DATE
		DIMENSIONS ARE IN INCHES TOLERANCES: FRACTIONAL ± ANGULAR: MACH ± BEND ± TWO PLACE DECIMAL ± THREE PLACE DECIMAL ±	DRAWN		
			CHECKED		
			ENG APPR.		
			MFG APPR.		
		INTERPRET GEOMETRIC TOLERANCING PER:	Q.A.		
		MATERIAL	COMMENTS:		
NEXT ASSY	USED ON	FINISH			
APPLICATION		DO NOT SCALE DRAWING			

TITLE:

SIZE | DWG. NO. | REV

2014-0620-C-exploded

SCALE: 1:5 | WEIGHT: | SHEET 1 OF 1

5 4 3 2 1

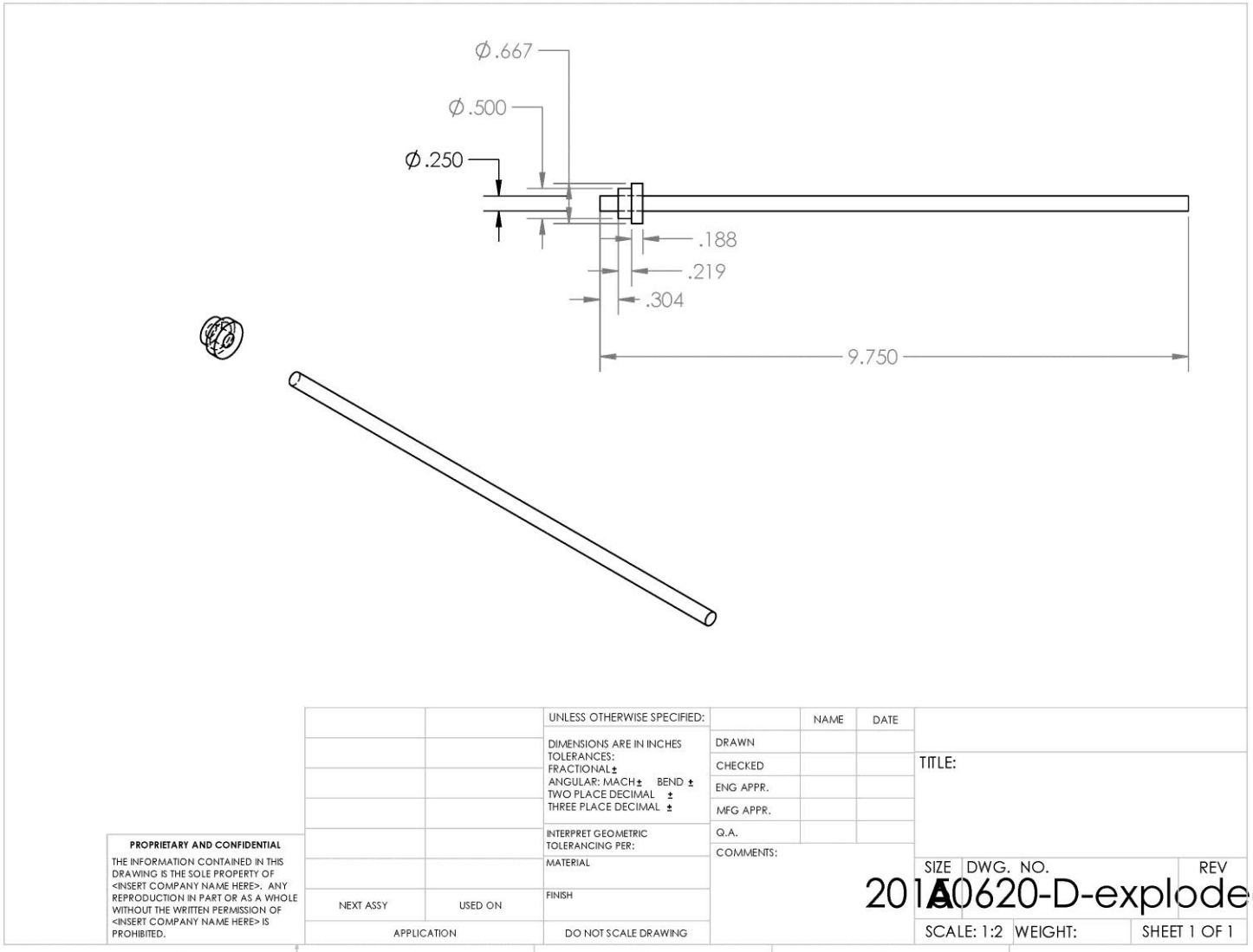

		UNLESS OTHERWISE SPECIFIED:		NAME	DATE
		DIMENSIONS ARE IN INCHES TOLERANCES: FRACTIONAL ± ANGULAR: MACH ± BEND ± TWO PLACE DECIMAL ± THREE PLACE DECIMAL ±	DRAWN		
			CHECKED		
			ENG APPR.		
			MFG APPR.		
		INTERPRET GEOMETRIC TOLERANCING PER:	Q.A.		
		MATERIAL	COMMENTS:		
NEXT ASSY	USED ON	FINISH			
APPLICATION		DO NOT SCALE DRAWING			

TITLE:

SIZE	DWG. NO.	REV
A	20160620-D-exploded	
SCALE: 1:2	WEIGHT:	SHEET 1 OF 1

5 4 3 2 1

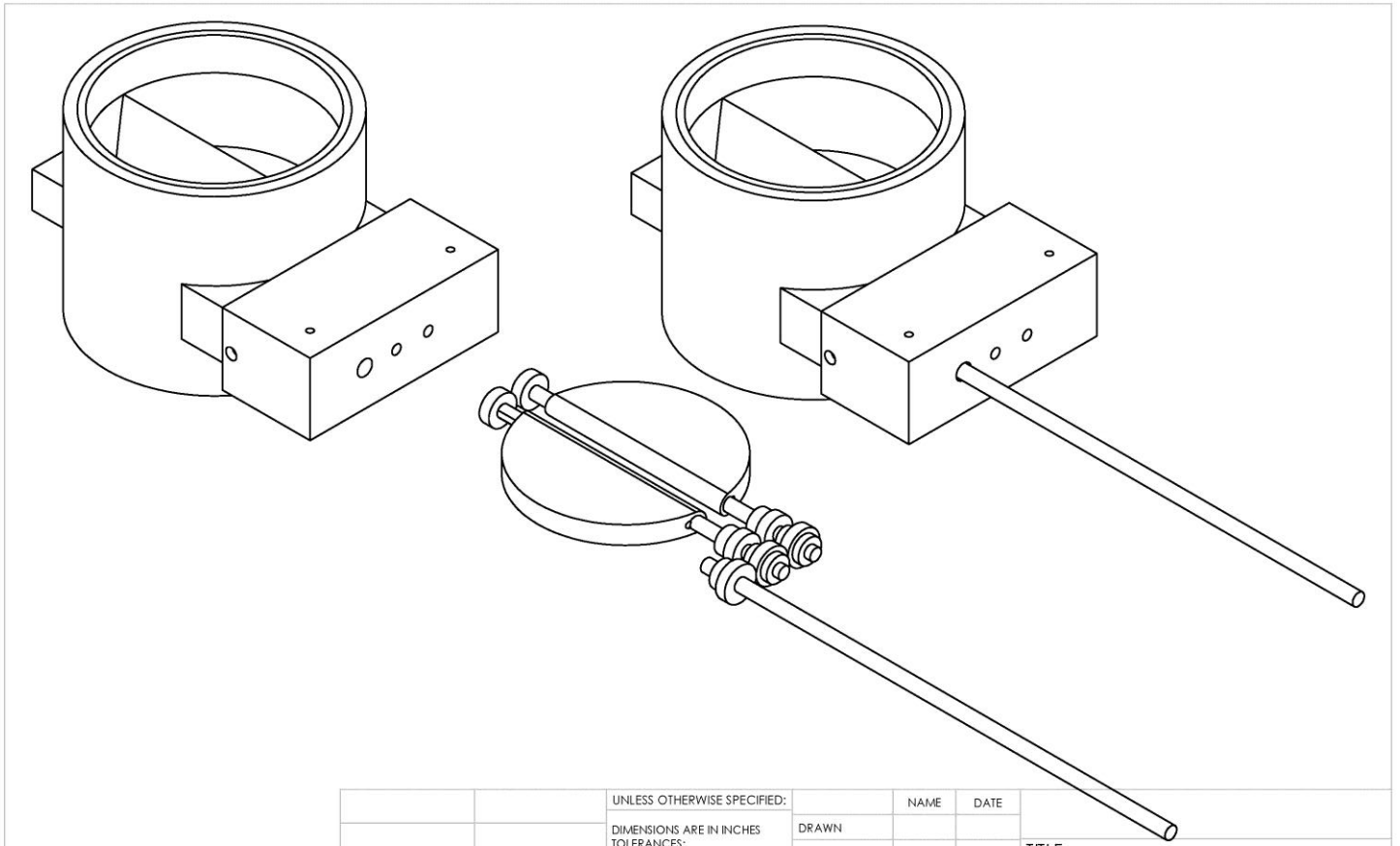

		UNLESS OTHERWISE SPECIFIED:		NAME	DATE
		DIMENSIONS ARE IN INCHES TOLERANCES: FRACTIONAL ± ANGULAR: MACH ± BEND ± TWO PLACE DECIMAL ± THREE PLACE DECIMAL ±	DRAWN		
			CHECKED		
			ENG APPR.		
			MFG APPR.		
		INTERPRET GEOMETRIC TOLERANCING PER:	Q.A.		
		MATERIAL	COMMENTS:		
NEXT ASSY	USED ON	FINISH			
APPLICATION		DO NOT SCALE DRAWING			

TITLE:

SIZE	DWG. NO.	REV
A	20150420-ABCD-explode	
SCALE: 1:5	WEIGHT:	SHEET 1 OF 3

5 4 3 2 1

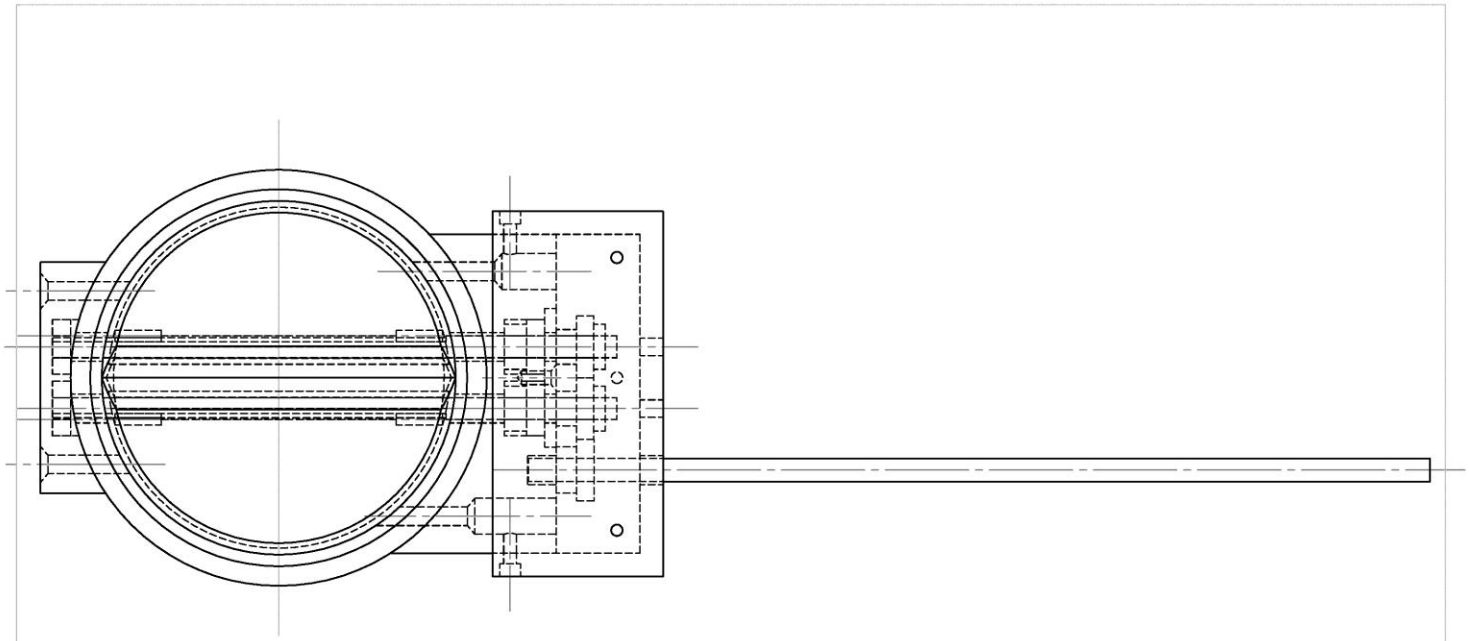

		UNLESS OTHERWISE SPECIFIED:		NAME	DATE
		DIMENSIONS ARE IN INCHES TOLERANCES: FRACTIONAL ± ANGULAR: MACH ± BEND ± TWO PLACE DECIMAL ± THREE PLACE DECIMAL ±	DRAWN		
			CHECKED		
			ENG APPR.		
			MFG APPR.		
		INTERPRET GEOMETRIC TOLERANCING PER:	Q.A.		
		MATERIAL	COMMENTS:		
NEXT ASSY	USED ON	FINISH			
APPLICATION		DO NOT SCALE DRAWING			

TITLE:

SIZE	DWG. NO.	REV
A	20150420-ABCD-explode	
SCALE: 1:5	WEIGHT:	SHEET 2 OF 3

5 4 3 2 1

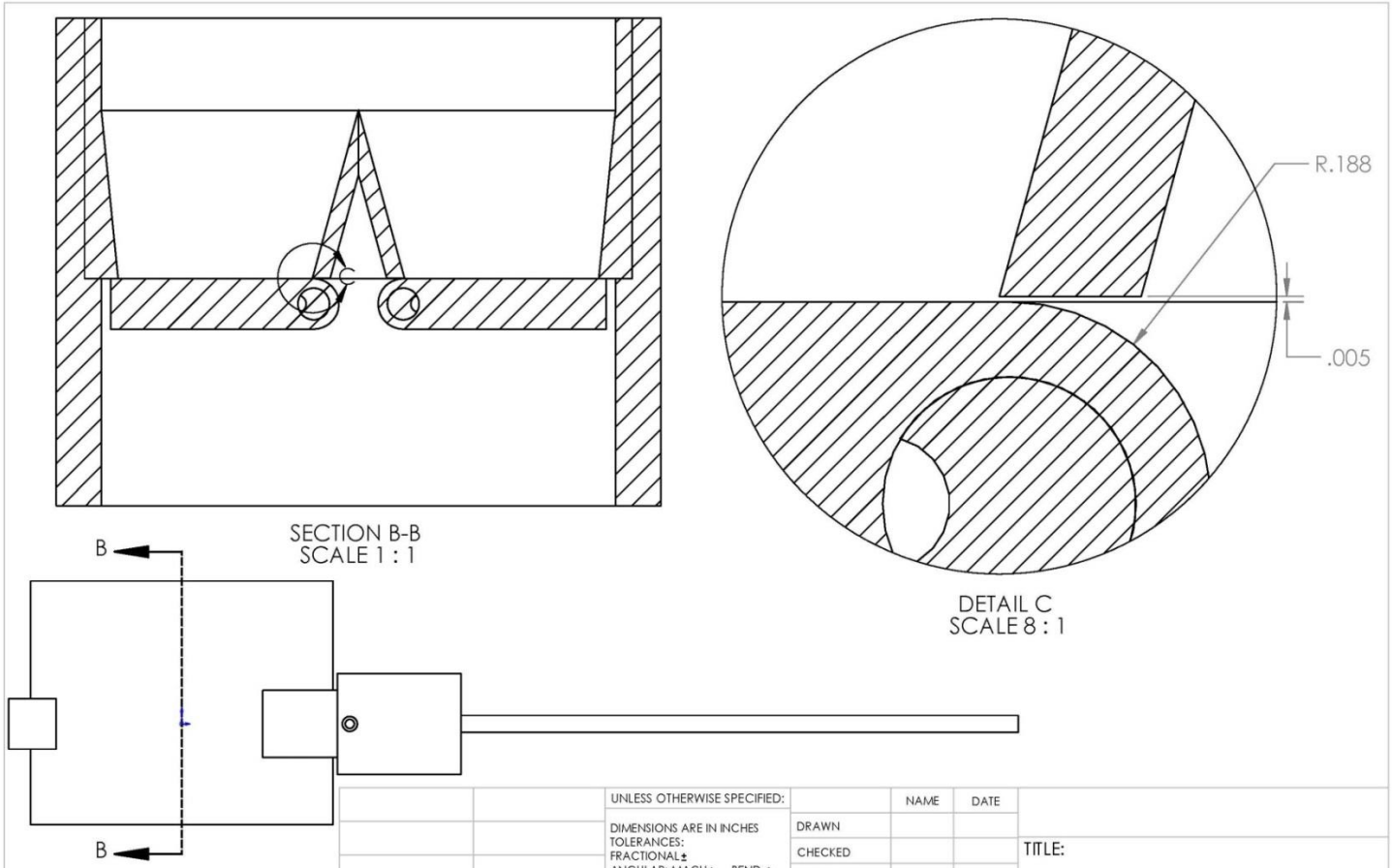
SECTION B-B
SCALE 1 : 1
DETAIL C
SCALE 8 : 1
R.188
.005
B
B
UNLESS OTHERWISE SPECIFIED:
DIMENSIONS ARE IN INCHES
TOLERANCES:
FRACTIONAL ±
ANGULAR: MACH ± BEND ±
TWO PLACE DECIMAL ±
THREE PLACE DECIMAL ±
INTERPRET GEOMETRIC TOLERANCING PER:
MATERIAL
FINISH
DO NOT SCALE DRAWING
NAME
DATE
DRAWN
CHECKED
ENG APPR.
MFG APPR.
Q.A.
COMMENTS:
TITLE:
SIZE
DWG. NO.
REV
20150420-ABCD-explode
A
SCALE: 1:5
WEIGHT:
SHEET 3 OF 3
NEXT ASSY
USED ON
APPLICATION
PROPRIETARY AND CONFIDENTIAL
THE INFORMATION CONTAINED IN THIS DRAWING IS THE SOLE PROPERTY OF <INSERT COMPANY NAME HERE>. ANY REPRODUCTION IN PART OR AS A WHOLE WITHOUT THE WRITTEN PERMISSION OF <INSERT COMPANY NAME HERE> IS PROHIBITED.
5
4
3
2
1

Appendix E: Conversion of rotameter reading to actual flow rate

The flow rate indicated by the rotameter needed to be corrected to obtain the actual flow rate. Since the design pressure of the rotameter is different from the operating pressure shown at the gauge, a pressure correction factor is required:

$$Pressure\ correction\ factor = \sqrt{\frac{Operating\ pressure\ (Gauge\ reading\ in\ psig + 14.7)}{Design\ pressure\ (14.7)}}$$

A density correction factor is needed for measuring flow rates of natural gas as the rotameters employed for this purpose were designed based on air flow. This factor is estimated as

$$Density\ correction\ factor = \sqrt{\frac{Density\ of\ gas\ used\ in\ design\ (air)}{Density\ of\ gas\ being\ measured\ (NG)}}$$

Finally, the actual flow rate is obtained by multiplying the indicated flow rate by one or two of these factors depending on the gas used.

Appendix F: Values of coefficients for estimation of gas properties

Table E1: Values of coefficients for viscosity estimation [40].

	$a_1 \times 10^{-8}$	$a_2 \times 10^{-5}$	$a_3 \times 10^{-2}$	a_4
N_2	1.89690	-4.99074	7.22905	0.16613
O_2	1.39088	-4.49772	7.72693	0.98526
CO_2	0.48702	-2.34095	6.11504	-1.33587
H_2O	-0.59916	1.15667	3.37086	-1.67766

Table E2: Values of coefficients for heat capacity estimation [42].

	$b_1 \times 10^{3}$	$b_2 \times 10^{5}$	$b_3 \times 10^{8}$	$b_4 \times 10^{12}$
H_2	28.84	0.00765	0.3288	-0.8698
CH_4	34.31	5.469	0.3661	-11
CO	28.95	0.411	0.3548	-2.22
N_2	29	0.2199	0.5723	-2.871
O_2	29.1	1.158	-0.6076	1.311
CO_2	36.11	4.233	-2.887	7.464
H_2O	33.46	0.688	0.7604	-3.593

Table E3: Values of coefficients for thermal conductivity estimation [43].

	1	2	3	4	5	6	7
m	0.239503	0.00649768	1	-1.92615	2.00383	-1.07553	0.229414
n	0.402287	0.356603	-0.163159	0.138059	-0.0201725		